Fluid and Structural Modeling of the Disease-Free and Atherosclerotic Human Carotid Bifurcation

by

Hesham F. Younis

B.S. in Mechanical Engineering
American University in Cairo, June 1994

S.M. in Mechanical Engineering
Massachusetts Institute of Technology, June 1997

Submitted to the Department of Mechanical Engineering in Partial Fulfillment of the Requirements for the Degree of

Doctor of Philosophy in Mechanical Engineering

at the

MASSACHUSETTS INSTITUTE OF TECHNOLOGY

February, 2002

Signature of Author _____
Department of Mechanical Engineering
September 14, 2001

Certified by _____
Professor Roger D. Kamm
Thesis Supervisor

Accepted by _____
Professor Ain A. Sonin
Chairman, Department Committee on Graduate Studies

Fluid and Structural Modeling of the Disease-Free and Atherosclerotic Human Carotid Bifurcation

by

Hesham F. Younis

Submitted to the Department of Mechanical Engineering on Sep 14, 2001 in Partial Fulfillment of the Requirements for the Degree of Doctor of Philosophy in Mechanical Engineering

Abstract

Cardiovascular disease is the leading cause of death in the United States. It claims more lives each year than the next 7 leading causes of death combined. Atherosclerosis is a major cause of cardiovascular disease and is an inflammatory process characterized by intimal thickening of arteries and plaque build up. Atherosclerosis can also damage the arterial wall and in turn cause the formation of a thrombus that can partially or totally occlude the diseased artery. If the actual vessel is the carotid artery, this often leads to a stroke.

The focus of this study is to analyze the blood flow and arterial wall motion in the carotid bifurcation, a frequently diseased site of the cerebral circulation. Using ultrasound velocity measurements and magnetic resonance imaging (MRI) data of normal volunteers and patients *in vivo*, realistic blood velocity profiles and wall anatomy geometries are generated and imported into a commercial finite element package, ADINA (Automatic Dynamic Incremental Nonlinear Analysis, Watertown, MA) for computational analysis. Using three types of 3D transient finite element analyses: structure only, rigid walled fluid only and fully coupled fluid-structure interaction, areas of low fluid shear stress and high mechanical strain are identified. These results are compared with experimental evidence collected from the literature as well as histological data of plaque gathered from imaged patients after endarterectomy to identify potential correlations with regions of inflammation.

In normal volunteers, localized high cyclic strains (which have been implicated in the stimulation of endothelial and smooth muscle cells) and high maximum wall shear stress temporal gradients (which are related to the expression of atherogenesis-related genes in endothelial cells) are observed at the flow divider and along the outside wall of the external carotid, both common sites of early inflammation. Localized separated flow regions are observed, especially near the outer wall of the internal carotid (the carotid bulb), in response to the localized abrupt changes in the curvature and cross-sectional area of the artery wall. The oscillation and low mean value of wall shear stress in these regions have been widely correlated to atherogenesis and late stage atherosclerotic inflammation.

Within the 4 patients studied (P1, P2, P3 and P4), the results indicate that strong correlations exist in the vicinity of the carotid bulb, immediately downstream of observed stenoses, although the sign of the correlation coefficient seems to depend on the severity of the stenosis. The results in the two patients (P1 and P2) with non-constricting ($< 50\%$) stenoses, show that the wall shear stress (oscillatory shear index) in P1 at that location generally observes strong negative (positive) correlations with smooth muscle cell (SMC), lipid and collagen presence, but no correlation to macrophage presence and vice versa in P2, which experiences solely strong correlations with macrophage presence. This is evidence that the inflammatory process, is continuing downstream of the stenosis. In P3 (*80%* stenosis), the WSS at that location correlates *positively* with SMC, lipids, macrophages and collagen. The difference is believed to be due to the extensive re-modeling and the advanced stenosis present. No statistically significant correlations were found in the case of P4, the last patient studied.

It is well-known that heart rate, blood pressure and flow or pressure waveforms at a given location can vary considerably during the course of normal, daily activity. This study also considers these variations and examines the differences in hemodynamics produced by varying heart rate in a fully coupled fluid-structure 3D finite element model of the carotid bifurcation. Results show that even for a 50% increase in heart rate, as would occur during a vigorous walk, significant differences in the fluid mechanical parameters of interest occur. The lowest values of wall shear stress occur at the carotid bulb, and almost double by the 50% increase in heart rate associated with moderate exercise. Values for the maximum wall shear stress temporal gradient also double along the carotid bulb.

Finally, a 2D sensitivity analysis of arterial wall and plaque properties is also conducted to determine the effect of variable material properties on the stress in this type of arterial modeling, via finite element analysis. The results show that the stresses within the arterial wall, fibrous plaque, calcified plaque, and lipid pool have low sensitivities for a $\pm$10% variation in Young's modulus, E. The sensitivity due to the variation in E is consistent between isotropic (linear and nonlinear), isotropic linear with residual strains, and transversely isotropic models. Therefore, stress analysis may be used with confidence that the material properties contribute relatively small errors in the prediction of stresses in the wall. Either isotropic or anisotropic models provide useful estimates, however the predictions in regions of stress concentration (e.g., the site of rupture) are somewhat more sensitive to the specific model used, differing by up to 30% in the present example and almost halving when residual stresses are included.

Thesis Supervisor: Roger D. Kamm
Title: Professor of Mechanical Engineering
Thesis Committee:
Prof. Roger D. Kamm, (Thesis Supervisor)
Prof. Alan J. Grodzinsky
Dr. Richard T. Lee, Brigham and Women's Hospital

Acknowledgments

I wish to thank Professor Roger D. Kamm for his guidance and insight which strongly contributed to the completion of this work. I am indebted to his contributions which shaped my graduate education and greatly appreciate the opportunity he has given me. I am also especially grateful to Mohammad Kaazempur-Mofrad, PhD and Ray Chan, PhD for their invaluable technical contributions in various stages of this research. I could not have come this far without their help.

I would also like to thank many of my other colleagues for their help and contributions throughout this work: Alexandra Chau, Lucia Contreras, Denise Hinton, PhD, Chanil Chung, PhD, Ana Isasi, Linda Kim, Deepa Santhumayor, Hayden Huang and Galina Sukhova, PhD. UROP students Shobha Williamson and Yee Lam worked on a large part of chapter 7; it could not have been completed without them.

I am grateful to my friends and colleagues in the fluids lab, in particularly Mark Bathe for his continuous input and explanations of finite element modeling and on how to use ADINA. I am also appreciative to the customer support people of ADINA R&D for their guidance and help. Thanks to Dr. Rich Lee, MD for his invaluable insight, that helped me draw useful conclusions throughout the research. Thanks to Dr. Bob Lees, MD and the crew at the Boston Heart Foundation for hosting me in their lovely Kendall square clinic for so long.

My friends here have been my support mechanism for so many years and I could not have gone this far without them; they are the true reason why I will always cherish my stay here in Boston. Osamah el Rifai, Amr and Waleed Farahat, Omar Roushdy, Mostafa el Far, Mostafa Hafez, Nagi el Abassi, James Moran (wellllllllllllllllllllllll), Maribel Vazquez, Ahmed el Shimi, Ahmed Farid, Nihal Allam, Noha Sayed el Ahl and last but not least, Fanny Lacassagne. Our conversations and times together will stay with me for as long as I live. A special thanks to Lucia Contreras for her patience and kindness throughout my writing of this thesis. Even though not with me in Boston, but always with me in spirit, my brother Ehab and my close friends Alex Tabet and Hisham Farahat were always extremely supportive of me. A final word of thanks to my Spanish professors here at MIT: Margarita Ribas-Groeger and Soledad Fox. I am not kidding when I say that Spanish I and II were the most enjoyable classes I took at MIT. As for my other classes, I want to thank two of the best lecturers I have ever come across for their clarity and energy: Profs. Alan Grodzinsky and John Leinhard.

I do not even know where to start to thank my parents, Farouk and Tawhida, for their support throughout my graduate education; their kindness and continuous encouragement made the completion of this thesis not only possible, but very comfortable. I dedicate this thesis to them. Finally and by far most importantly, I would like to thank Allah (swt) for the patience and power He gave me to finish this thesis.

Financial support from the National Heart, Lung, and Blood Institute (HL 61794) is gratefully acknowledged.

I. Introduction

I.1. Motivation

Cardiovascular disease claims approximately 950,00 lives in the United States every year, accounting for 40% of all deaths occurring per year. Cardiovascular disease claims more lives each year than the next seven leading causes of death combined [1]. Atherosclerosis is a major cause of cardiovascular disease. It is an inflammatory process characterized by intimal thickening of arteries and plaque accumulation. When advanced, this plaque can reduce the amount of blood flowing through the artery leading to ischemia and loss of function. The disease process in atherosclerosis can also lead to rupture of the arterial wall and in turn cause the formation of a blood clot or thrombus that can either partially or totally occlude the diseased artery [2]. When this happens in the arteries leading to the brain, the result is cerebral thrombosis, the most common type of stroke. Cerebral thrombosis is a type of ischemic stroke [3] where the blood flow to part of the brain is blocked. The results can be devastating, ranging from loss of feeling, diminished eyesight, paralysis on one side of the body to sudden death. Stroke causes 16% of deaths from cardiovascular disease, and is the United States' number 3 killer. The focus of this study is to enhance our understanding of the biomechanical factors that promote inflammation in the unstable atherosclerotic lesion with emphasis on the carotid bifurcation (see figure 1), a commonly diseased site of the circulation.

I.1.1. The Initiation and Progression of Atherosclerosis

Atherosclerosis is believed to be initiated by endothelial dysfunction from a variety of causes including elevated and modified LDL cholesterol (low-density lipoprotein), free radicals caused by cigarette smoking, hypertension and possibly infectious microorganisms. Endothelial dysfunction leads to changes in the normal homeostatic properties of the endothelium such as increased permeability and adhesiveness of the endothelium to leukocytes and platelets [4] that contribute to the inflammatory response observed in the early stages of the disease.

If the offending agents are not removed or neutralized, the inflammatory response continues. Fatty streaks appear in the lesion [5] consisting of lipid-laden monocytes and macrophages (foam cells) and T lymphocytes. Monocytes that migrate through the artery wall differentiate and become macrophages. Inflammation can also stimulate smooth-muscle migration. The resulting mass of cells forms an intermediate lesion. Up to a certain point, the lumen area remains unchanged; the arterial wall can still expand its outer diameter to accommodate the thickening.

As macrophage and smooth muscle cell accumulation by migration and proliferation continues, the lesion grows. At some point the artery can no longer expand to accommodate the changes and the now advanced lesion progresses into the lumen. As it does, a fibrous cap might form that walls it off from the blood. The enclosed mass contains a mixture of leukocytes, lipids, and debris, which may form a necrotic core. The lesion may continue to grow through leukocyte adhesion and infiltration that tend to occur at the shoulders of the cap [4].

Several studies have shown that macrophages may stimulate metalloproteinase (MMP) production in the lesions [6-8]. MMPs such as collagenases, elastases, and stromelysins may cause degradation of the fibrous cap. Depending on the local stresses, typically highest at the shoulders of the lesion due to stress concentrations there [9-11], an event referred to as plaque rupture may occur. A schematic of these different stages throughout the disease is shown in figure 2. Plaque rupture is followed by platelet aggregation and thrombosis (figure 3).

I. 2. Hypotheses tested

I.2.1. Low/oscillatory fluid dynamic shear stress correlates with regions of atherosclerotic inflammation (3D rigid wall fluid simulations and fluid-structure simulations)

There is a long standing hypothesis that correlates fluid dynamic forces and atherosclerotic disease. Many analytical, numerical and experimental studies have been conducted. Much of what inspired these studies is the observation that atherosclerotic disease is focal, typically occurring at sites of complex hemodynamics. These include arterial bifurcations, junctions and/or regions of high curvature.

Fry [12, 13] was the first to postulate that high wall shear stresses would cause damage to the arterial wall; endothelial disruption or denudation could lead to atherosclerosis. Since then, however, it has become widely accepted that low or oscillatory shear stress rather than high shear stress contribute to atherogenesis [14-16].

Previous studies have shown that regions of low or oscillatory shear stress cause monocyte adhesion to the endothelial wall, the first stage in progression of the disease. Low shear stress leads to the expression of VCAM-1, a monocyte adhesion molecule [17], increased and prolonged NF-kappa B activity, a regulator of some endothelial cell adhesion molecules [18] and a reduction in NO release (augmented levels inhibit monocyte adhesion [19, 20]).

Extensive numerical work helped to identify such regions of low shear stress for stenosed arteries, healthy and diseased bifurcations (for an extensive review, see Berger and Jou [21]). With many such studies conducted, it is somewhat surprising that none have rigorously tested the validity of the low shear stress hypothesis by using *in vivo* data. Very few researchers, (e.g. Stroud [22]) have used realistic geometries to represent the diseased arterial wall. Most studies also neglected arterial wall motion.

A major goal of this present thesis is thus to test the hypothesis that low or oscillatory shear correlates to atherosclerotic inflammation using 3D computational analyses based on realistic flow profiles and geometries by input of actual data gathered from *in vivo* magnetic resonance images of healthy and diseased arteries. Histology from diseased arteries harvested from patients after endarterectomy provide a conclusive method to correlate regions of monocyte deposition/macrophage accumulation to regions of low fluid dynamic shear stress. This is addressed in chapters 5 and 6.

I.2.2. Cyclic strain amplitude in the carotid bifurcation correlates to atherogenesis (3D structural simulations)

Previous studies have shown that mechanical strain controls the release of fibroblast growth factor-2 (FGF-2), an agent implicated in early smooth muscle cell migration and proliferation), and monocyte chemoattractant protein 1 (MCP-1), a chemokine involved in monocyte recruitment into the arterial wall and atherosclerotic lesions, as well as endothelial cell proliferation, morphologic change and migration. In this thesis, we calculate the physiologic cyclic strains in the carotid bifurcation, a common site of disease. Realistic three dimensional geometries of healthy arteries are constructed and used for finite element analysis. The arterial wall is treated as homogenous, isotropic, and undergoing large strain, large displacement deformations. Our results show that the highest variations in cyclic strain are found in regions where early inflammation is typically observed, but could not be predicted by the low shear stress hypothesis: the carotid apex and outer wall of the external carotid. This is addressed in chapters 3 and 5.

I.2.3. Incorporating the effect of heart rate variability (e.g. moderate exercise) in numerical simulations can have a significant impact on fluid mechanical variables of interest (3D fluid-structure interaction simulations)

Many investigators have examined the effects of varying fluid dynamic parameters in blood flow simulations of vessel bifurcations, junctions and grafts. Among the effects often incorporated are the non-Newtonian properties of blood, treatment of blood as a two phase medium, inclusion of arterial wall compliance and combinations thereof. Although these studies are of insight, much of this previous work has been done for a

single set of flow conditions. This section of the thesis takes into account that human activity throughout the day varies significantly and simulates this by varying the heart rate in a fully coupled fluid-structure interaction 3D finite element model of a carotid bifurcation. The results show that even for a 50% increase in heart rate, as is that of a person walking at a faster than normal pace, significant differences in the fluid mechanical parameters of interest appear: the lowest values of wall shear stress (WSS) occurred at the carotid bulb, and were almost doubled by the 50% increase in heart rate associated with moderate exercise. The values of the maximum wall shear stress temporal gradient (WSSTG), another potentially relevant parameter in atherogenesis, also doubled. This is addressed in chapter 4.

I.2.4. The variability of measured plaque material parameters impacts the strain distributions more than the stress distribution (2D structural simulations)

Accurate estimates of stress in an atherosclerotic lesion require knowledge of the material properties of its components (e.g., normal wall, fibrous plaque, calcified regions, lipid pools) that can only be approximated. Thus there is considerable uncertainty in these computational predictions. The purpose of this section of the thesis is to test the sensitivity of predicted levels of stress and strain to the parameter values of plaque via finite element analysis. The results show that the currently known parameters of the arterial wall, fibrous plaque, calcified plaque, and lipid pool have low sensitivities for a $\pm$10% variation in Young's modulus, E. The variation in E is consistent between isotropic (linear and nonlinear), isotropic linear with residual strains, and transversely isotropic models. Therefore, stress analysis may be used with confidence that the material properties contribute relatively small errors in the prediction of stresses in the wall. Either isotropic or anisotropic models provide useful estimates, however the predictions in regions of stress concentration (e.g., the site of rupture) are somewhat more sensitive to the specific model used, differing by up to 30% in the present example. This is addressed in chapter 7.

I.3. Techniques Employed

I.3.1. Imaging Techniques

Magnetic resonance imaging to determine accurate arterial/plaque wall was carried out on healthy volunteers and patients at Massachusetts General Hospital (MGH). The same patients were scheduled for carotid endarterectomy to provide histology specimens. MR Imaging of tissue is performed using one of three currently available techniques: T1, T2 or phase contrast. Centerline velocities are obtained using ultrasound measurements.

Collaborators at MGH are currently using a 1.5 T imager capable of in plane resolutions as high as 0.39 mm/pixel of slices 2 mm apart.

Once generated, the wall data are processed through SolidWorks (SolidWorks Corporation, Concord, MA), a solid modeler, (figure 4) to create a 3-D representation of the carotid bifurcation. The length of the region imaged is typically 6 cm long; 3 cm proximal and distal to the point of bifurcation. The velocity data is used to generate Womersley flow profiles at the common and internal carotids and applied as boundary conditions to the fluid nodes of the finite element mesh as a function of time along the cardiac cycle. The boundary conditions are specified at two branches of the bifurcation (common and internal) and step one of the simulation performed. Flow profiles at the output of the external carotid artery at the end of this step were then used as an input boundary condition to the second computational step, while retaining the Womersley flow at the common carotid and imposing a traction-free boundary condition at the internal carotid. This second step was then considered the final computed solution as in Perktold et. al. [23].

I.3.2. FEM techniques

ADINA, version 7.4 (Automatic Dynamic Incremental Nonlinear Analysis, Watertown, MA), a commercially available finite element package is used in all the computational calculations herein. ADINA is capable of performing fully coupled, three dimensional, non-linear FSI analyses. The simulations include all of the above mentioned effects and

incorporate a non-linear, isotropic, hyperelastic model for the 3D simulations of the healthy arterial wall and three types of plaque models for the 2D structure-only simulations: isotropic linear, transversely isotropic linear and hyperelastic isotropic non-linear. Blood is treated as an incompressible, Newtonian fluid (an assumption that has repeatedly been shown to hold well for large arteries [21, 23], where shear rates generally exceed 100 s^{-1}) and the flow assumed laminar.

The arterial solid response is modeled using the standard Lagrangian formulation for large displacements and large strains [24]. An isotropic form of the strain energy density function for the (nearly) incompressible artery wall is specified [25]:

$$W = \frac{a}{b}\left(e^{\frac{b}{2}(I_1-3)} - 1 \right) \tag{1}$$

where a and b are elastic constants that reflect the elastic properties and tissue composition; I_1 is the first invariant of the strain tensor. In the Taylor series expansion, a has the significance of the elastic modulus. This exponential form is appropriate for arterial mechanics since it portrays the well-known strain-stiffening behavior of collagen.

Since the plaque is much stiffer than the artery wall and the strains are much smaller, it was initially modeled using linear elastic analyses. For transversely isotropic materials, the complete set of elastic parameters needed for each type of plaque is [11, 26] :

$$E_r, E_\theta, \nu_{r\theta}, \nu_{\theta z}, G_{r\theta} \tag{2}$$

Continuity and the full Navier-Stokes equations are solved for the fluid. In order to incorporate the effect of a moving wall, the Arbitrary Lagrangian Eulerian (ALE) formulation [27] is used.

Iteration between the fluid and solid solvers ensures a fully coupled structure-fluid interaction analysis satisfying the requirements of force equilibrium and velocity and

displacement compatibility at each time step in the analysis. The user controls the number of iterations to be performed as well as the iteration tolerances [28] needed for convergence.

The use of a free meshing algorithm greatly simplifies the task of meshing a complex geometry such as the full 3-D carotid artery bifurcation. In addition, the most reliable form of importing data into ADINA, parasolid files, generates complex solid bodies, which can only be meshed using free meshing. ADINA is only capable of mapped meshing on simple bodies that are topologically equivalent to volumes [29]. ADINA's default mesher, the Delaunay mesher, is faster and more robust than its advancing front mesher and is capable of automatically refining the mesh in problem areas. It is not necessary to use the same mesh in the fluid and solid domains.

Free meshing dictates the use of tetrahedral elements (or triangular elements in 2D). To date, no algorithm has been developed for brick elements (or rectangular elements in 2D), [30]. This problem is handled in all analyses performed by refining the mesh until the solution converges. Code validation was accomplished by comparing FEM results to the analytical solutions for the unsteady pipe flow problem (for the fluid domain) and the inflation of a hyperelastic cylinder (for the arterial wall domain) before proceeding to model the complex flows/strains of the carotid bifurcation. All our 3D simulations were conducted using free meshing, while the 2D simulations were conducted using mapped meshing.

I.4. References

1. AHA (1997) 1998 Heart and Stroke Statistical Update. American Heart Association, Dallas, TX.
2. Schoen, F.J. (1994) The Heart. In *Robbins Pathologic Basis of Disease* (R. S. Cotran, V. Kumar and S. L. Robbins, eds), Saunders, Philadelphia 517-582.
3. AHA (1996) Heart and Stroke Facts. American Heart Association, Dallas, TX.
4. Ross, R. (1999) Atherosclerosis--an inflammatory disease. *N Engl J Med* **340**, 115-26.
5. Napoli, C., D'Armiento, F.P., Mancini, F.P., Postiglione, A., Witztum, J.L., Palumbo, G., Palinski, W. (1997) Fatty streak formation occurs in human fetal

aortas and is greatly enhanced by maternal hypercholesterolemia. Intimal accumulation of low density lipoprotein and its oxidation precede monocyte recruitment into early atherosclerotic lesions. *J Clin Invest* **100**, 2680-90.

6. Shah, P.K., Falk, E., Badimon, J.J., Fernandez-Ortiz, A., Mailhac, A., Villareal-Levy, G., Fallon, J.T., Regnstrom, J., Fuster, V. (1995) Human monocyte-derived macrophages induce collagen breakdown in fibrous caps of atherosclerotic plaques. Potential role of matrix-degrading metalloproteinases and implications for plaque rupture. *Circulation* **92**, 1565-9.
7. Galis, Z.S., Sukhova, G.K., Lark, M.W., Libby, P. (1994) Increased expression of matrix metalloproteinases and matrix degrading activity in vulnerable regions of human atherosclerotic plaques. *J Clin Invest* **94**, 2493-503.
8. Schonbeck, U., Mach, F., Sukhova, G.K., Murphy, C., Bonnefoy, J.Y., Fabunmi, R.P., Libby, P. (1997) Regulation of matrix metalloproteinase expression in human vascular smooth muscle cells by T lymphocytes: a role for CD40 signaling in plaque rupture? *Circ Res* **81**, 448-54.
9. Richardson, P.D., Davies, M.J., Born, G.V. (1989) Influence of plaque configuration and stress distribution on fissuring of coronary atherosclerotic plaques. *Lancet* **2**, 941-4.
10. Loree, H.M., Kamm, R.D., Stringfellow, R.G., Lee, R.T. (1992) Effects of fibrous cap thickness on peak circumferential stress in model atherosclerotic vessels. *Circ Res* **71**, 850-8.
11. Cheng, G.C., Loree, H.M., Kamm, R.D., Fishbein, M.C., Lee, R.T. (1993) Distribution of circumferential stress in ruptured and stable atherosclerotic lesions. A structural analysis with histopathological correlation. *Circulation* **87**, 1179-87.
12. Fry, D.L. (1968) Acute vascular endothelial changes associated with increased blood velocity gradients. *Circ Res* **22**, 165-97.
13. Fry, D.L. (1969) Certain histological and chemical responses of the vascular interface to acutely induced mechanical stress in the aorta of the dog. *Circ Res* **24**, 93-108.
14. Caro, C.G., Fitz-Gerald, J.M., Schroter, R.C. (1971) Atheroma and arterial wall shear. Observation, correlation and proposal of a shear dependent mass transfer mechanism for atherogenesis. *Proc R Soc Lond B Biol Sci* **177**, 109-59.
15. Ku, D.N., Giddens, D.P., Zarins, C.K., Glagov, S. (1985) Pulsatile flow and atherosclerosis in the human carotid bifurcation. Positive correlation between plaque location and low oscillating shear stress. *Arteriosclerosis* **5**, 293-302.
16. Friedman, M.H., Hutchins, G.M., Bargeron, C.B., Deters, O.J., Mark, F.F. (1981) Correlation of human arterial morphology with hemodynamic measurements in arterial casts. *J Biomech Eng* **103**, 204-7.
17. Gonzales, R.S., Wick, T.M. (1996) Hemodynamic modulation of monocytic cell adherence to vascular endothelium. *Ann Biomed Eng* **24**, 382-93.
18. Mohan, S., Mohan, N., Sprague, E.A. (1997) Differential activation of NF-kappa B in human aortic endothelial cells conditioned to specific flow environments. *Am J Physiol* **273**, C572-8.
19. Tsao, P.S., Lewis, N.P., Alpert, S., Cooke, J.P. (1995) Exposure to shear stress alters endothelial adhesiveness. Role of nitric oxide. *Circulation* **92**, 3513-9.

20. Tsao, P.S., Buitrago, R., Chan, J.R., Cooke, J.P. (1996) Fluid flow inhibits endothelial adhesiveness. Nitric oxide and transcriptional regulation of VCAM-1. *Circulation* **94**, 1682-9.
21. Berger, S.A., Jou, L.D. (2000) Flows in Stenotic Vessels. *Annual Review of Fluid Mechanics* **32**, 347-384.
22. Stroud, J.S. (2000) Numerical simulations of blood flow in stenotic vessels. University of California at Berkeley, Berkeley.
23. Perktold, K., Resch, M., Florian, H. (1991) Pulsatile non-Newtonian flow characteristics in a three-dimensional human carotid bifurcation model. *J Biomech Eng* **113**, 464-75.
24. Bathe, K.J. (1996) *Finite element procedures*. Prentice Hall, Englewood Cliffs, N.J.
25. Delfino, A., Stergiopulos, N., Moore, J.E., Jr., Meister, J.J. (1997) Residual strain effects on the stress field in a thick wall finite element model of the human carotid bifurcation. *J Biomech* **30**, 777-86.
26. Jones, R.M. (1975) Macromechanical Behavior of a Lamina. In *Mechanics of Composite Materials*McGraw-Hill Book Co., New York 31-57.
27. Bathe, K.J., Zhang, H., Ji, S. (1999) Finite element analysis of fluid flows fully coupled with structural interactions. *Computers and Structures* **72**, 1-16.
28. ADINA (1997) ADINA Theory and Modeling Guides. ADINA R&D Inc, Watertown, MA.
29. ADINA (1999) ADINA System Newsletter. , Volume 2ADINA R&D Inc., Watertown, MA.
30. Bathe, K.J. (1999) Computer methods in engineering, lecture notes. , Cambridge, MA.
31. Hansen, J.T. (1998) *Essential Anatomy Dissector: Following Grant's Method.* Williams & Wilkins, Baltimore, MD.

I.5. Figures

I.5.1 Figure Captions

Figure 1. Anatomy of arteries in the neck, taken from Hansen [31]

Figure 2. Stages in the inflammatory atherosclerotic process, taken from Ross [4]

Figure 3. Sequential progression of coronary artery lesion morphology, from Shoen [2].

Figure 4. Procedure to be used to import MRI data from source into finite element package. Note that both fluid and solid domains are generated.

I.5.2. Figures

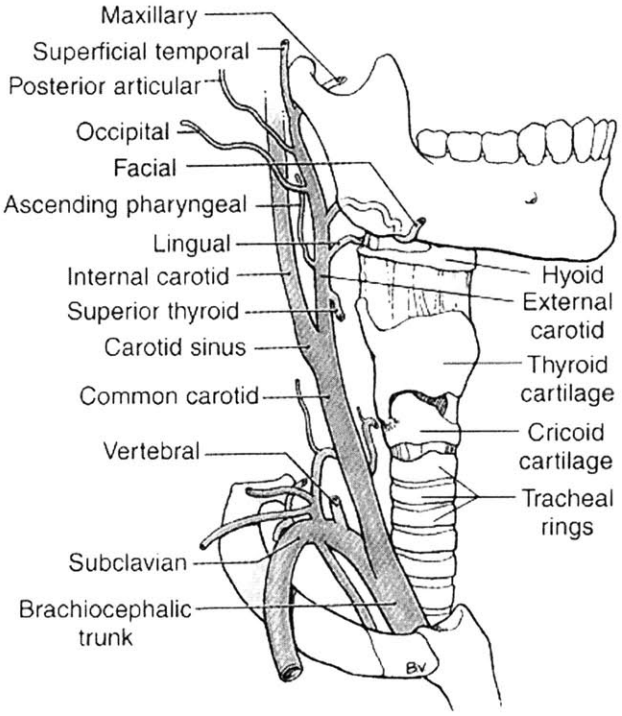

Figure 1

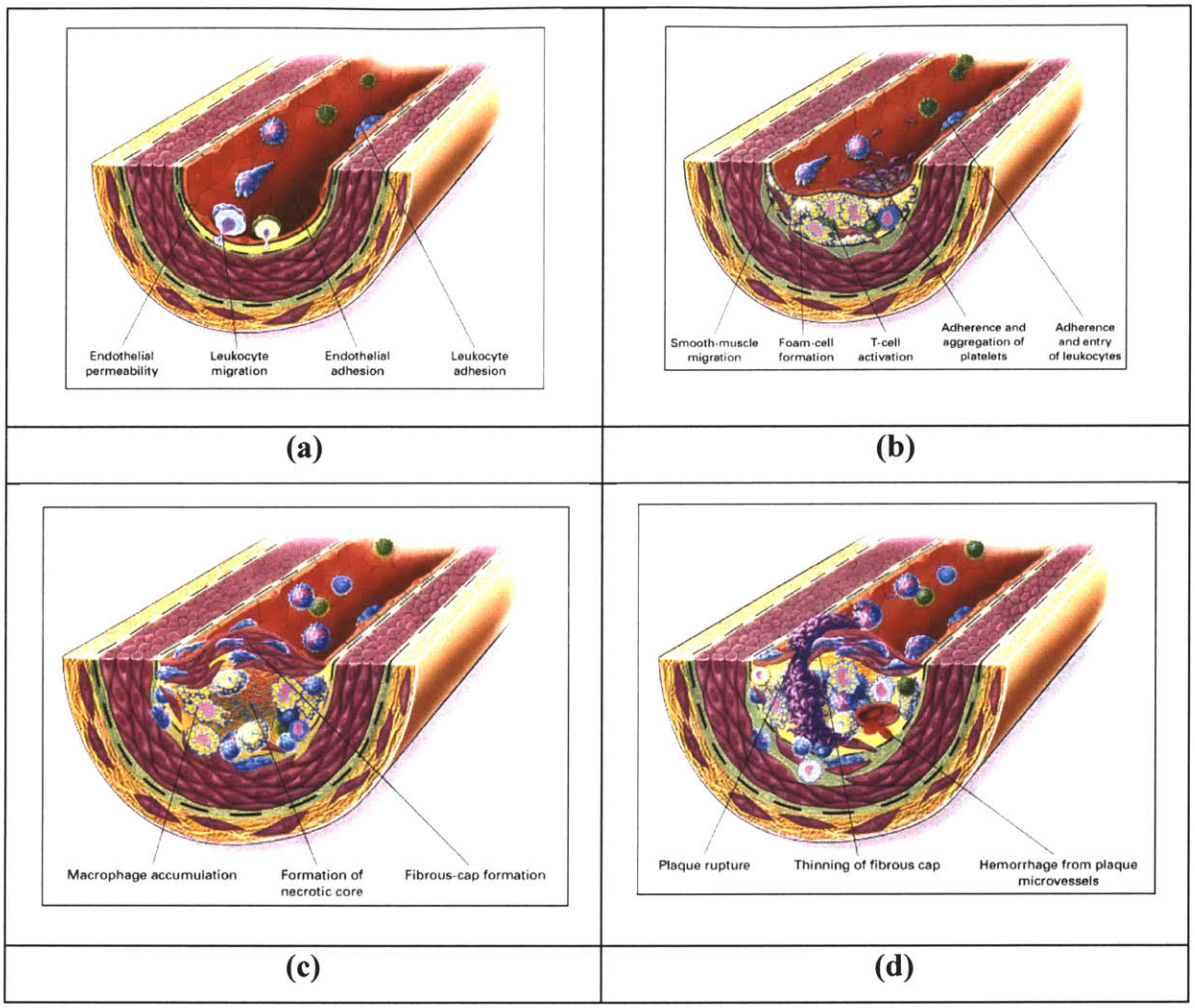
Endothelial permeability
Leukocyte migration
Endothelial adhesion
Leukocyte adhesion
(a)
Smooth-muscle migration
Foam-cell formation
T-cell activation
Adherence and aggregation of platelets
Adherence and entry of leukocytes
(b)
Macrophage accumulation
Formation of necrotic core
Fibrous-cap formation
(c)
Plaque rupture
Thinning of fibrous cap
Hemorrhage from plaque microvessels
(d)

Figure 2

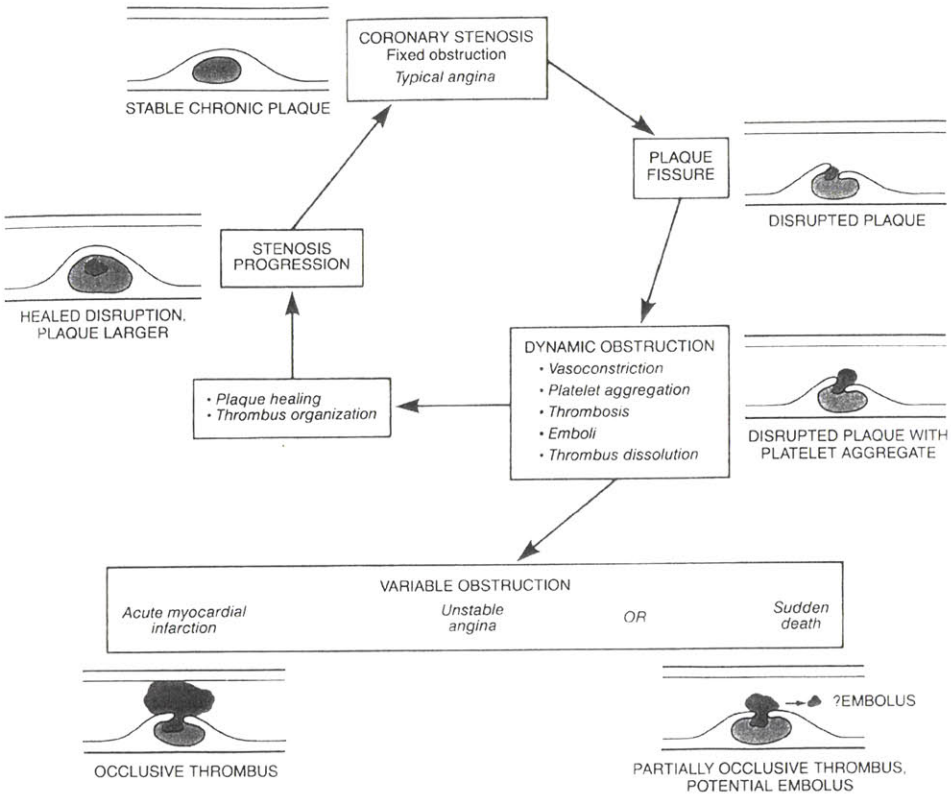

Figure 3

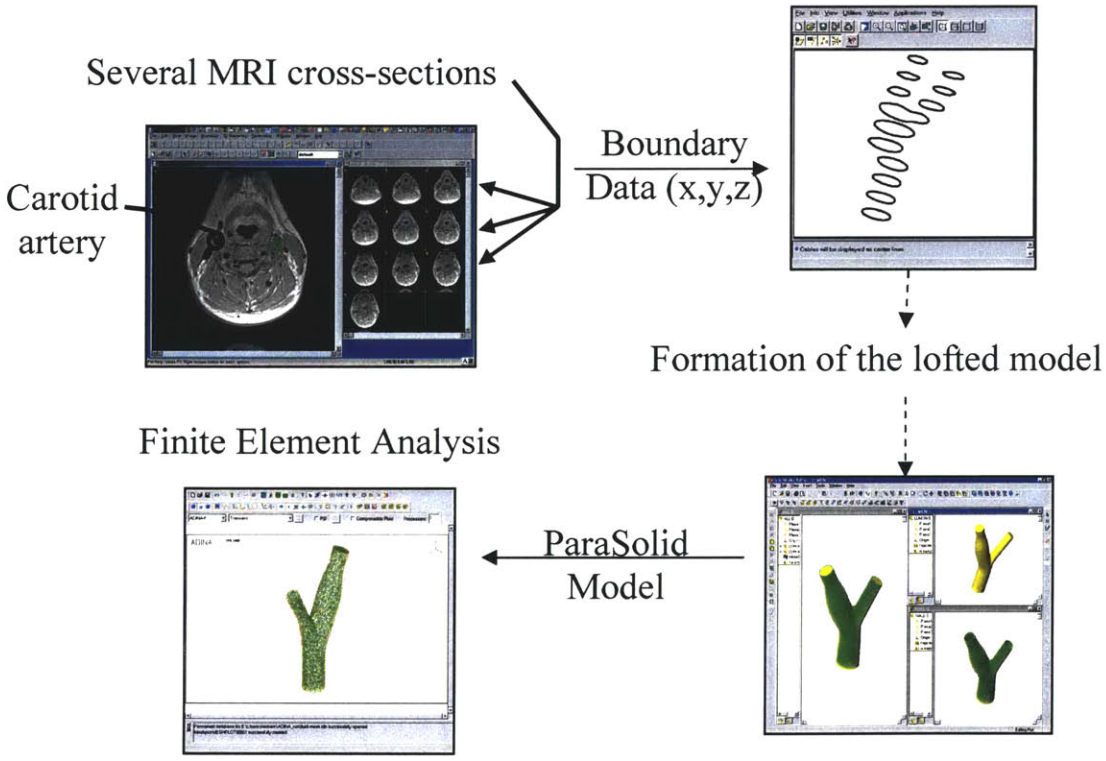

Figure 4

II. Challenges in Developing an Accurate Model for Carotid Bifurcation Blood Flow and Wall Mechanics

II.1. Abstract

Atherosclerosis is known to be associated with the stresses that act on or within the arterial wall. It has been established that various systemic risk factors predispose certain individuals to develop disease more readily than others, but these systemic factors fail to explain the uneven distribution of atherosclerotic lesions within the arterial tree. It has been proposed that these distributional differences can be explained by the presence in certain locations of low or oscillatory fluid shear stress, which has been shown to correlate well with areas of disease. Arterial disease is multi-factorial, however, and it is likely that mechanical stresses and/or strains also play a central role in disease progression. Because of resolution difficulties with many of the currently available imaging techniques, investigators have frequently resorted to numerical techniques to estimate the mechanical variables involved in disease progression. Here we present our recent work on the use of finite element models to analyze arterial wall deformation and discuss future numeric and modeling hurdles that need to be overcome in order to produce more realistic simulations.

Keywords: Atherosclerosis, Finite element analysis, Blood flow, Arterial wall stress, Low/oscillatory shear stress, Arterial mechanics, Carotid bifurcation.

II.2. Introduction

Cardiovascular disease claims more lives each year than the next seven leading causes of death combined [1]. Atherosclerosis, a major cause of cardiovascular disease, is an inflammatory process characterized by an initial thickening of the intimal layer of large arteries and subsequent plaque build up. In the later stages of disease, this plaque obstructs the flow of blood through the artery leading to ischemia and loss of function. Stresses generated in the wall of the artery can also lead to rupture and subsequently cause a blood clot or thrombus to form that can either partially or totally occlude the diseased artery [2].

Observations that atherosclerotic disease is focal, typically occurring at sites of complex hemodynamics, such as arterial bifurcations, junctions and/or regions of high curvature led to the hypothesis that low or oscillatory fluid dynamic shear stress correlates with atherosclerotic disease [3, 4]. These observations are supported by numerous studies demonstrating that changes in shear stress can alter the biologic function of endothelial cells in a variety of ways. Factors attributed to wall mechanics have also been identified in several studies. It has been proposed that regions of stress concentration could injure the artery and make it susceptible to atherosclerosis [5]. Cyclic strain amplitude has also been shown to affect endothelial cell morphology and enhance proliferation [6], increase monocyte adhesion [7, 8] and potentially be a contributing factor in atherogenesis [9, 10].

In this study, we use numerical methods to aid in understanding the biomechanical factors that promote early inflammation in the arterial wall with emphasis on the carotid bifurcation, a commonly diseased site of the cerebral circulation.

II.3. Methods

These simulations employ a finite element analysis (ADINA, version 7.3, Automatic Dynamic Incremental Nonlinear Analysis, Watertown, MA) and incorporate a non-linear, isotropic, hyperelastic model for the arterial wall. Blood is treated as an incompressible,

Newtonian fluid (an assumption that has repeatedly been shown to hold well for large arteries [4, 11], where shear rates generally exceed 100 s^{-1}) and the flow assumed laminar.

The arterial solid response is modeled using the standard Lagrangian formulation for large displacements and large strains [12]. An isotropic form of the strain energy density function for the (nearly) incompressible artery wall is specified [13]:

$$W = \frac{a}{b}\left(e^{\frac{b}{2}(I_1-3)} - 1 \right) \tag{1}$$

where a and b are elastic constants that reflect the elastic properties and tissue composition; I_1 is the first invariant of the strain tensor. In the Taylor series expansion, a has the significance of the elastic modulus. This exponential form is appropriate for arterial mechanics since it portrays the well-known strain-stiffening behavior of collagen. Continuity and the full Navier-Stokes equations are solved for the fluid.

Even though ADINA is capable of performing fully coupled, three dimensional, non-linear Fluid-Structure Interaction (FSI) analyses, the solutions presented here are of the uncoupled solid and fluid domains. Fluid-structure interaction analysis is important when large scale motions of the arteries are present and impact the flow field considerably, as in studies of arterial collapse when largely obstructive stenoses are present [14, 15] or where physiologic movement of blood vessels (e.g. coronary arteries) during the cardiac cycle affects blood flow patterns significantly [16]. Several studies [17-19] have investigated the effect of arterial compliance on fluid dynamic parameters under typical conditions in the carotid artery [20] and found it to be of minimal significance.

II.4. Model Description

A realistic 3D solid model of the carotid bifurcation (extending 3 cm distal to 3 cm proximal to the bifurcation) based on the work of Bharadvaj et. al. [21, 22] and Delfino

et. al. [13] was created in SolidWorks (SolidWorks Corporation, Concord, MA) and imported into the finite element code for meshing and analysis. Only half of the geometry was modeled and symmetry boundary conditions were exploited. The model used and boundary conditions imposed are illustrated in Figure 1.

The arterial wall was freely meshed (Figure 2) with 43,334 eleven-node 3D tetrahedral solid elements, producing 118,229 nodes and 351,176 equations. Doubling the number of elements changed the stress values by at most 8% in areas of stress concentration and no more than 3% elsewhere. An axial stretch of 10% was applied to the solid domain as measured *in situ* by Delfino [23]. Since the viscoelasticity of the arterial wall was not considered, a static inflation of the artery wall was performed to gain insight into the stress levels experienced by the bifurcation. The computation was performed using a SGI Origin 2000 computer equipped with 4 processors and 6 GB of RAM (only 1.2 GB were needed by this computation).

The fluid domain was solved in two stages, using time-dependent velocity boundary conditions similar to those specified by Perktold et. al. [11]. In the first stage, a Womersley type flow corresponding to the flow rate profile in the common carotid artery [24] was imposed node-by-node on the common carotid and a plug flow specified at the exit of the internal carotid. Flow profiles at the output of the external carotid artery at the end of stage one were used as an input boundary condition to the second computational stage. Flow rates and the flow rate division ratios between internal and external carotids were specified as measured by Ku [25] using non-invasive Doppler ultrasound velocimetry. The fluid domain was freely meshed using 56,209 four node tetrahedral elements (Figure 2), resulting in 11,597 nodes and 46,388 equations. So as to achieve a periodic solution, the transient flow computation was allowed to run over two heart cycles. This model was run on a 500 MHz PC equipped with 768 MB of RAM.

II.5. Results

Figure 3 illustrates the axial flow profiles during the decelerative phase of systole (cardiac ejection). The results compare favorably with those of Perktold et. al. [11]. Regions of flow separation (and low fluid shear stress) are observed at the outer wall of the internal-common junction (the carotid bulb), as would be expected due to the abrupt change in curvature and the associated adverse pressure gradient there. Also contributing to the tendency for separation is the increase in cross-sectional area, and consequent increase in pressure, just distal to the bifurcation.

Figure 4 displays a band plot of the maximum principal stresses (averaged) experienced by the carotid bifurcation under a static loading of 16 kPa; peak arterial pressure in a healthy adult. Computed stress values compare favorably with those of Delfino [23], with stress values generally varying between 120-160 kPa on the inner wall and 40-80 kPa on the outer wall. Deviations from this range are observed along the internal carotid where stress values fall in the ranges 180-200 kPa and 80-100 kPa on the inner, and outer walls, respectively. The carotid apex is seen to be a region of stress concentration, where stress values at the inner wall exceed 500 kPa.

II.6. Discussion

Flow and vessel deformation in the carotid bifurcation was simulated using finite element methods and a model of a "typical" vessel. The results obtained are consistent with those of previous investigators for the flow [11] and arterial wall stress [13, 23], thereby providing a degree of validation of the method. As shown previously, the carotid bulb is a region of low and/or oscillatory shear stress, correlating with a region predisposed to disease. Analysis of the wall stresses show that the flow divider, a region of early lesion development, experiences large stresses, possibly contributing to endothelial damage or apoptosis, and enhanced wall permeability. Studies of this type are instrumental in the interpretation of histological studies of arterial disease and the factors that cause it.

The arterial wall is a non-linear (materially and geometrically) viscoelastic, poroelastic, orthotropic and heterogeneous material whose modeling can be simplified when certain conditions are met. Fung [26] was the first to identify the arterial wall as being "pseudoelastic", a modeling assumption that exploits the observation that arteries display an almost replicable cyclic behavior after being "preconditioned" [27] by several stress cycles, thus eliminating the need for a viscoelastic analysis.

There exists much experimental evidence that the arterial wall can be treated as an incompressible rather than poroelastic material [28-30]. This assumption is valid when considering macroscopic fluid motion across the thickness, L, of a typical artery (on the order of *1 mm*) with fluctuations in loading on the time scale of a heart beat. Nevertheless, the fact that the wall is poroelastic may still be important in atherogenesis since mass transport across the endothelium, with a length scale on the order of microns, may be a critical factor in the early accumulation of lipids within the arterial wall [27].

The model used here incorporates the material and geometric non-linear behaviors of the arterial wall, but is limited to isotropic and homogeneous materials. Heterogeneity of the arterial wall can be important, both in terms of an artery with advanced, localized regions of disease, and in terms of differences between the media and the adventitia. These latter effects can be readily addressed by incorporating a separate layer of elements with different material properties in the outer artery wall, representing the adventitia.

Two remaining challenges are the incorporation of orthotropy and residual stresses. Arteries are orthotropic [31] and remain stressed even when unloaded [32, 33]. Both of these attributes can have a significant effect on the stress (and strain) distribution in an artery. Perhaps of a higher priority, however, is the need to gather more experimental data on the material properties of plaques and residual stress in an atherosclerotic vessel both of which will ultimately help us better understand the biomechanics of diseased arteries.

II.7. Conclusion

In summary, today's FEM models of arterial mechanics and blood flow are no longer limited by computing power. There exists a need, however, to continue to improve our models of arteries, diseased and healthy, to produce more accurate analyses.

II.8. References

1. AHA (1997) 1998 Heart and Stroke Statistical Update. American Heart Association, Dallas, TX.
2. Schoen, F.J. (1994) The Heart. In *Robbins Pathologic Basis of Disease* (R. S. Cotran, V. Kumar and S. L. Robbins, eds), Saunders, Philadelphia 517-582.
3. Ku, D. (1997) Blood Flow in Arteries. *Annual Review of Fluid Mechanics* **32**, 346-384.
4. Berger, S.A., Jou, L.D. (2000) Flows in Stenotic Vessels. *Annual Review of Fluid Mechanics* **32**, 347-384.
5. Salzar, R.S., Thubrikar, M.J., Eppink, R.T. (1995) Pressure-induced mechanical stress in the carotid artery bifurcation: a possible correlation to atherosclerosis. *J Biomech* **28**, 1333-40.
6. Li, G., Mills, I., Sumpio, B. (1994) Cyclic Strain Stimulates Endothelial Cell Proliferation: Characterization of Strain Requirements. *Endothelium* **2**, 177-81.
7. Wung, B.S., Cheng, J.J., Chao, Y.J., Lin, J., Shyy, Y.J., Wang, D.L. (1996) Cyclical strain increases monocyte chemotactic protein-1 secretion in human endothelial cells. *Am J Physiol* **270**, H1462-8.
8. Wang, D.L., Wung, B.S., Shyy, Y.J., Lin, C.F., Chao, Y.J., Usami, S., Chien, S. (1995) Mechanical strain induces monocyte chemotactic protein-1 gene expression in endothelial cells. Effects of mechanical strain on monocyte adhesion to endothelial cells. *Circ Res* **77**, 294-302.
9. Tropea, B.I., Schwarzacher, S.P., Chang, A., Asvar, C., Huie, P., Sibley, R.K., Zarins, C.K. (2000) Reduction of aortic wall motion inhibits hypertension-mediated experimental atherosclerosis. *Arterioscler Thromb Vasc Biol* **20**, 2127-33.
10. Younis, H., Chung, C., Kamm, R. (2000) Cyclic strain amplitude in the carotid bifurcation and its potential correlation to atherogenesis. *in progress* .
11. Perktold, K., Resch, M., Florian, H. (1991) Pulsatile non-Newtonian flow characteristics in a three-dimensional human carotid bifurcation model. *J Biomech Eng* **113**, 464-75.
12. Bathe, K.J. (1996) *Finite element procedures*. Prentice Hall, Englewood Cliffs, N.J.
13. Delfino, A., Stergiopulos, N., Moore, J.E., Jr., Meister, J.J. (1997) Residual strain effects on the stress field in a thick wall finite element model of the human carotid bifurcation. *J Biomech* **30**, 777-86.

14. Downing, J.M., Ku, D.N. (1997) Effects of frictional losses and pulsatile flow on the collapse of stenotic arteries. *J Biomech Eng* **119**, 317-24.
15. Bathe, M., Kamm, R.D. (1999) A fluid-structure interaction finite element analysis of pulsatile blood flow through a compliant stenotic artery. *J Biomech Eng* **121**, 361-9.
16. Moore, J.E., Jr., Guggenheim, N., Delfino, A., Doriot, P.A., Dorsaz, P.A., Rutishauser, W., Meister, J.J. (1994) Preliminary analysis of the effects of blood vessel movement on blood flow patterns in the coronary arteries. *J Biomech Eng* **116**, 302-6.
17. Perktold, K., Rappitsch, G. (1995) Computer simulation of local blood flow and vessel mechanics in a compliant carotid artery bifurcation model. *J Biomech* **28**, 845-56.
18. Steinman, D.A., Ethier, C.R. (1994) The effect of wall distensibility on flow in a two-dimensional end-to- side anastomosis. *J Biomech Eng* **116**, 294-301.
19. Friedman, M.H., Bargeron, C.B., Duncan, D.D., Hutchins, G.M., Mark, F.F. (1992) Effects of arterial compliance and non-Newtonian rheology on correlations between intimal thickness and wall shear. *J Biomech Eng* **114**, 317-20.
20. Ku, D.N., Giddens, D.P., Zarins, C.K., Glagov, S. (1985) Pulsatile flow and atherosclerosis in the human carotid bifurcation. Positive correlation between plaque location and low oscillating shear stress. *Arteriosclerosis* **5**, 293-302.
21. Bharadvaj, B.K., Mabon, R.F., Giddens, D.P. (1982) Steady flow in a model of the human carotid bifurcation. Part II--laser- Doppler anemometer measurements. *J Biomech* **15**, 363-78.
22. Bharadvaj, B.K., Mabon, R.F., Giddens, D.P. (1982) Steady flow in a model of the human carotid bifurcation. Part I--flow visualization. *J Biomech* **15**, 349-62.
23. Delfino, A. (1996) Analysis of Stress Field in a Model of the Human Carotid Bifurcation. In *Department of Physics*Ecole Polytechnique Federale de Lausanne, Lausanne, Switzerland.
24. He, X., Ku, D.N., Moore, J.E., Jr. (1993) Simple calculation of the velocity profiles for pulsatile flow in a blood vessel using Mathematica [published erratum appears in Ann Biomed Eng 1993 Sep-Oct;21(5):557-8]. *Ann Biomed Eng* **21**, 45-9.
25. Ku, D. (1983) Hemodynamics and Atherogenesis at the Human Carotid Bifurcation [Dissertation]. In *Department of Mechanical Engineering*Georgia Institute of Technology, Atlanta, GA.
26. Fung, Y.C., Fronek, K., Patitucci, P. (1979) Pseudoelasticity of arteries and the choice of its mathematical expression. *Am J Physiol* **237**, H620-31.
27. Humphrey, J.D. (1995) Mechanics of the arterial wall: review and directions. *Crit Rev Biomed Eng* **23**, 1-162.
28. Dobrin, P.B., Rovick, A.A. (1969) Influence of vascular smooth muscle on contractile mechanics and elasticity of arteries. *Am J Physiol* **217**, 1644-51.
29. Chuong, C.J., Fung, Y.C. (1984) Compressibility and constitutive equation of arterial wall in radial compression experiments. *J Biomech* **17**, 35-40.
30. Carew, T.E., Vaishnav, R.N., Patel, D.J. (1968) Compressibility of the arterial wall. *Circ Res* **23**, 61-8.

31. Humphrey, J.D. (1999) An evaluation of pseudoelastic descriptors used in arterial mechanics. *J Biomech Eng* **121**, 259-62.
32. Chuong, C.J., Fung, Y.C. (1986) On residual stresses in arteries [published erratum appears in J Biomech Eng 1990 Aug;112(3):249]. *J Biomech Eng* **108**, 189-92.
33. Fung, Y.C. (1991) What are the residual stresses doing in our blood vessels? *Ann Biomed Eng* **19**, 237-49.

II.9. Figures

II.9.1 Figure Captions

Fig. 1 Solid model used for the arterial wall. "P" represents the inner surfaces, where the pressure boundary condition was applied. The solid arrows represent an applied axial strain of 10%.

Fig. 2 Computational meshes used in simulations (a. solid mesh, b. fluid mesh)

Fig. 3 Velocity vectors (m/s) during the decelerative phase of systole. The region of flow separation is greatest at this time, when the fluid undergoes the largest reversal of momentum.

Fig. 4 Bandplot (Pa) of smoothed maximum principal stress at 16 kPa applied internal pressure.

II.9.2. Figures

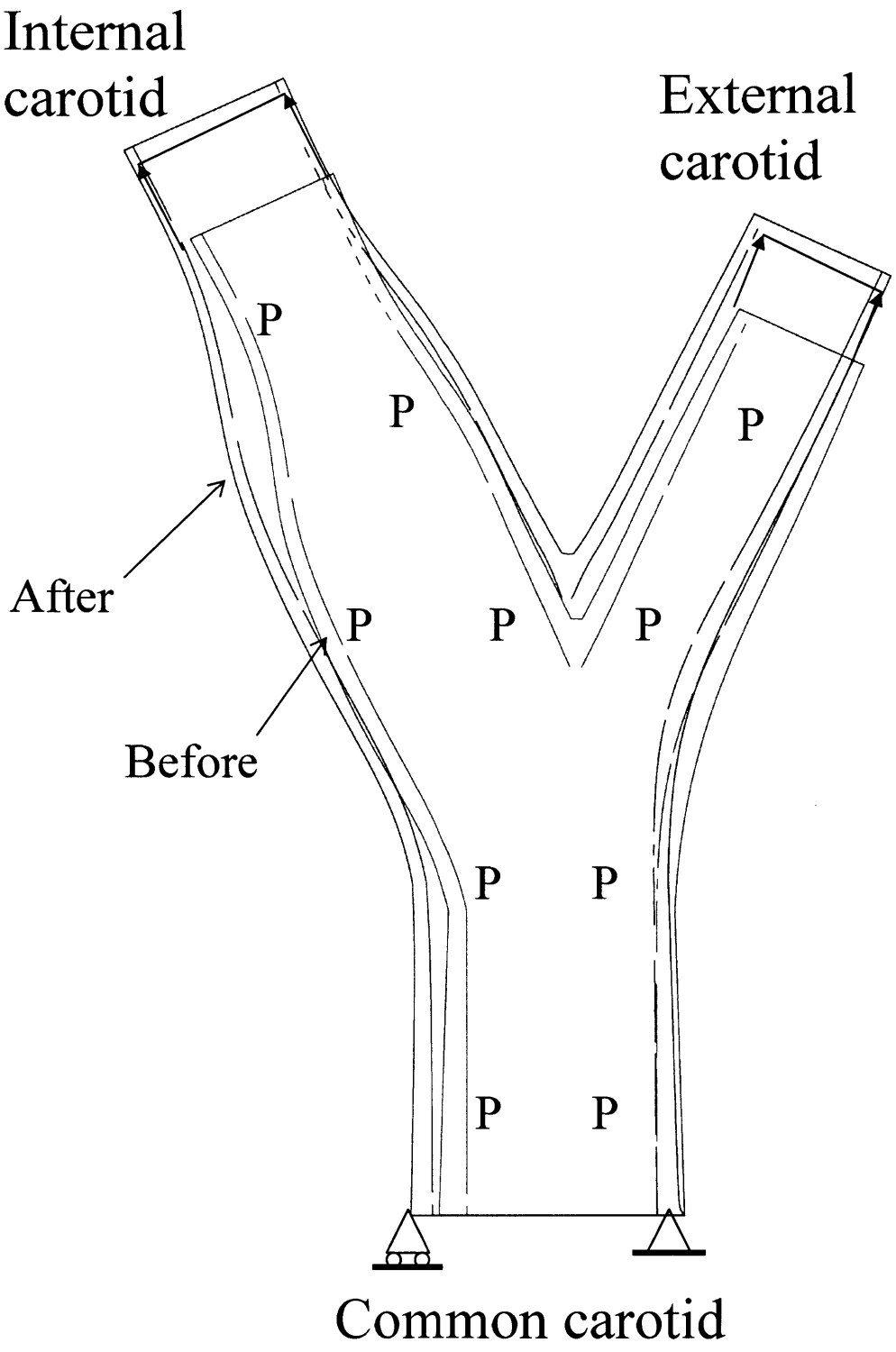

Figure 1

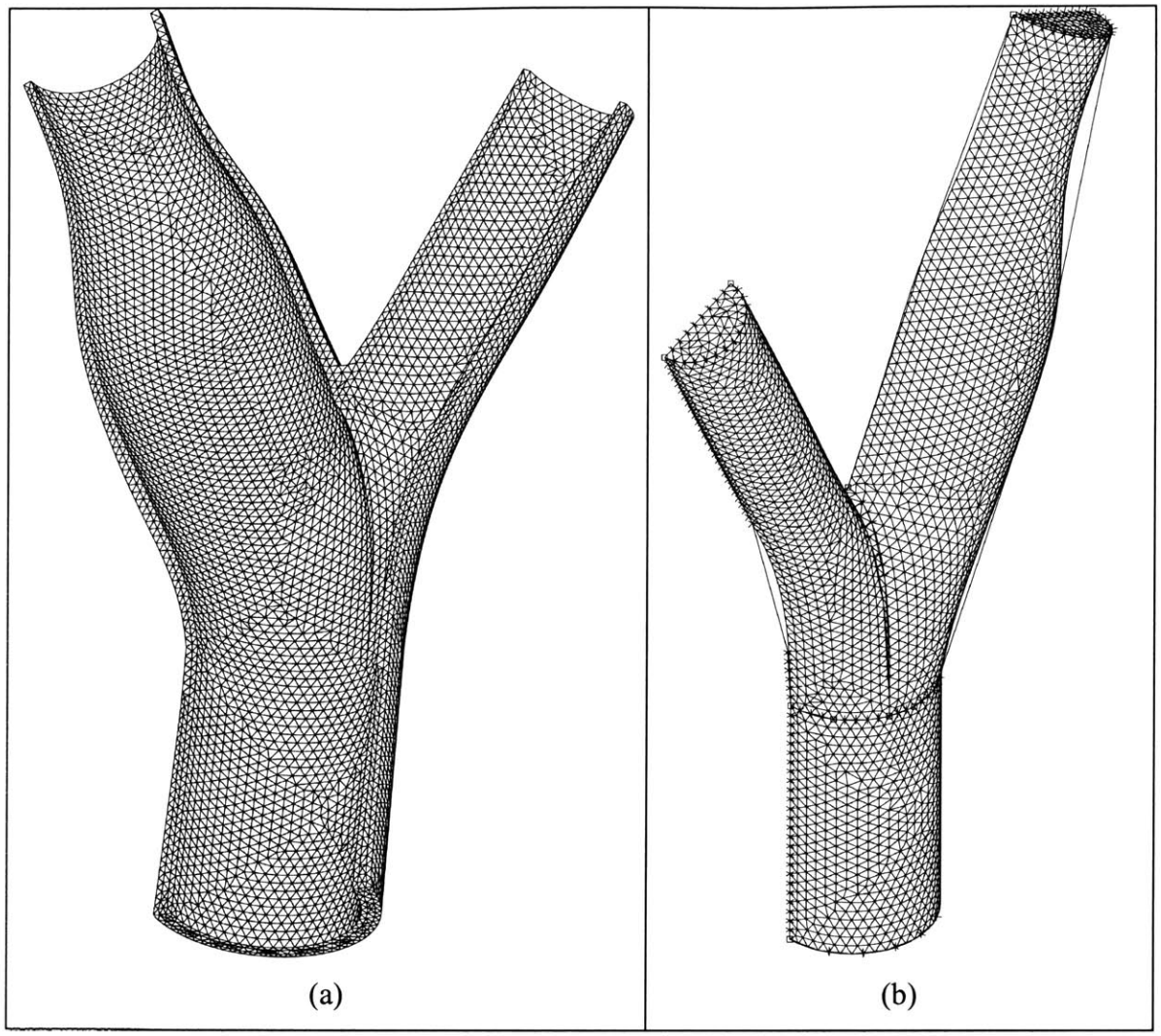

Figure 2

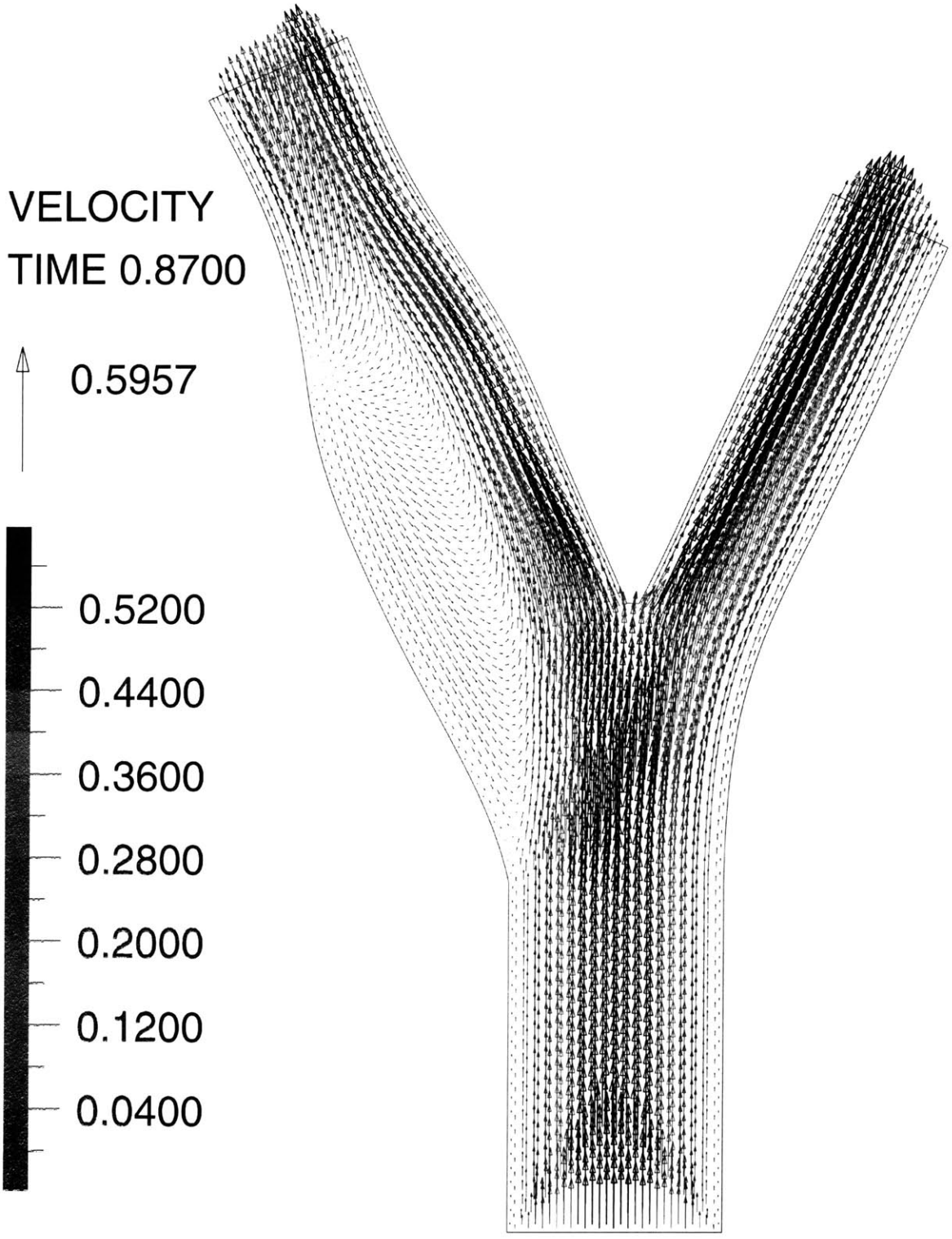
VELOCITY
TIME 0.8700
0.5957
0.5200
0.4400
0.3600
0.2800
0.2000
0.1200
0.0400

Figure 3

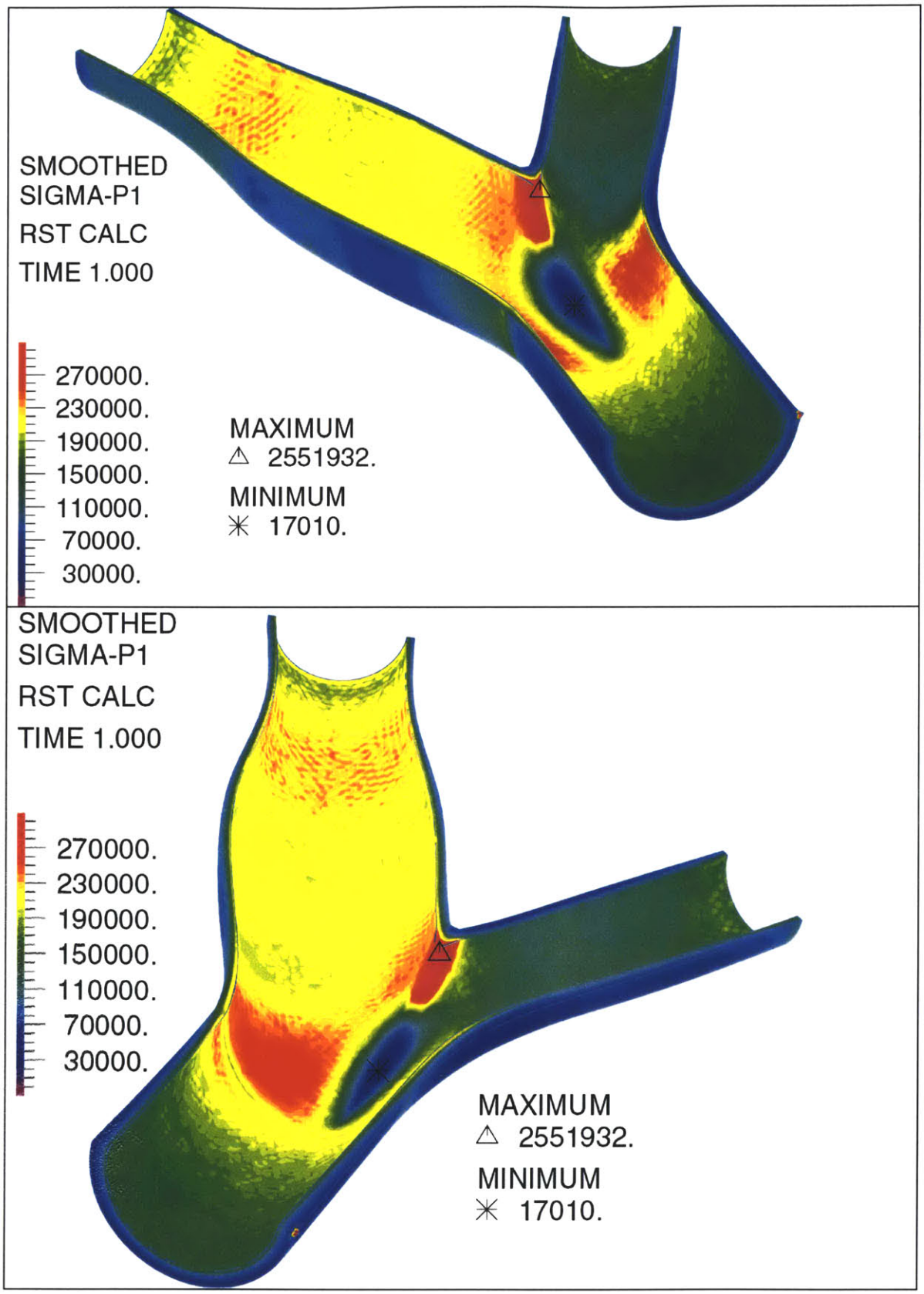
SMOOTHED
SIGMA-P1
RST CALC
TIME 1.000
270000.
230000.
190000.
150000.
110000.
70000.
30000.
MAXIMUM
2551932.
MINIMUM
17010.
SMOOTHED
SIGMA-P1
RST CALC
TIME 1.000
270000.
230000.
190000.
150000.
110000.
70000.
30000.
MAXIMUM
2551932.
MINIMUM
17010.

Figure 4

III. Cyclic Strain Amplitude in the Carotid Bifurcation and its Potential Correlation to Atherogenesis

III.1. Abstract

Various mechanical and fluid dynamic phenomena are thought to contribute to the pathogenesis of atherosclerosis. Most finite element analyses of the arterial wall to date have focused on the quantification of mechanical wall stresses, despite an abundance of experimental evidence suggesting that endothelial and smooth muscle cells readily respond to cyclic strain. Previous studies have shown that mechanical strain controls the release of fibroblast growth factor-2 (FGF-2), an agent implicated in early smooth muscle cell migration and proliferation), monocyte chemoattractant protein 1 (MCP-1), a chemokine involved in monocyte recruitment into the arterial wall and atherosclerotic lesions, as well as induce endothelial cell proliferation, morphologic change and migration. In this study, we calculate the physiologic cyclic strains in the carotid bifurcation, a common site of disease. A realistic three dimensional geometry is constructed and used for finite element analysis. The arterial wall is treated as homogenous, isotropic, and undergoing large strain, large displacement deformations. Our results show that the highest variations in cyclic strain are found at the adjoining wall of the external-common carotid and at the carotid apex, both frequent sites of early inflammation as well as immediately distal to the carotid bulb, a site of late stage disease, suggesting that cyclic strain may play a role in inflammation in that region as well.

Keywords: Atherosclerosis, cyclic strain, finite element analysis, endothelial cell proliferation, leaky junctions.

III.2. Introduction

Considerable evidence points to the potential role of cyclic strain in regulating the function of endothelial (ECs) and vascular smooth muscle cells (SMCs). Monocyte chemoattractant protein-1 (MCP-1), significant for its involvement in monocyte recruitment into the arterial wall and atherosclerotic lesions [1] is synthesized by both ECs and vascular SMCs subjected to mechanical deformation. MCP-1 mRNA expression in rat aortic SMCs has been shown to increase *in vitro* in response to mechanical deformation as well as *in vivo* in hypertensive rats [2, 3]. ECs have also been shown to exhibit similar gene expression patterns in response to cyclic strain [4-6].

Cyclic strain has also been shown to have numerous other effects on endothelial and smooth muscle cells. It stimulates vascular SMCs to release fibroblast growth factor-2 (FGF-2) in culture [7] which plays a role in early SMC migratory and proliferative responses following arterial injury [8] and has mitogenic effects on ECs and SMCs [9-11]. Additionally, Lee et. al., [12] have shown that versican, a vascular SMC proteoglycan that accumulates during atherosclerosis [13] and binds low-density lipoprotein cholesterol (LDLs) is induced by 4% cyclic strain. Cyclic strain has also been shown to increase EC proliferation as demonstrated by Li et. al. [14], who established that there exists an optimal cyclic strain range for EC proliferation (<6.4%), which if exceeded dampens the proliferative response.

EC mitosis has frequently been implicated as a mechanism for increasing the permeability of the arterial wall. Weinbaum et. al. [15] were the first to propose the "leaky cell junction hypothesis" in which transient pores resulting from "leaky" junctions in cell turnover provide the primary transendothelial pathway for LDLs. Experimentally, it has been shown that aortic ECs in mitosis indeed exhibit enhanced macromolecular permeability [16-18]. Since cyclic strain plays a role in EC mitosis, it is possible that there exists a correlation between high cyclic strain levels and enhanced macromolecular permeability, in turn leading to atherosclerotic inflammation. This is further supported by the work of Tropea et al. [19], who have shown that reduction of aortic wall motion

(using an external, stiff wrap) in the rabbit inhibits experimentally induced atherosclerosis.

It has already been demonstrated that low/oscillatory fluid shear stress correlates well with some commonly diseased sites in the arterial tree, such as the carotid bulb [20], but the low shear stress hypothesis has failed to explain the prevalence of atherosclerotic inflammation/intimal thickening as observed by several researchers in other sites, such as the inner wall of the external carotid artery [21] and flow dividers [22], a high shear stress region.

Despite the growing body of evidence that cyclic strain may be a critical factor in early disease, most previous numerical studies using Finite Element analyses (FEA) of the arterial wall have focused on the quantification of mechanical wall stresses rather than strains [23, 24]. In this study, we use FEA methods to aid in understanding the biomechanical factors that promote early inflammation in the arterial wall with emphasis on cyclic strain in the carotid bifurcation, a commonly diseased site of the cerebral circulation.

III.3. Methods and Model Description

The simulations herein employ a finite element analysis (ADINA, version 7.4, Automatic Dynamic Incremental Nonlinear Analysis, Watertown, MA) to simulate the wall deformation and internal stresses accompanying typical pressure variations found in a healthy carotid bifurcation. The arterial solid response is modeled using the standard Lagrangian formulation for large displacements and large strains [25] artery and incorporates a non-linear, isotropic, hyperelastic model for the arterial wall. An isotropic form of the strain energy density function for the (nearly) incompressible artery wall is specified [23] :

$$W = \frac{a}{b}\left(e^{\frac{b}{2}(I_1-3)} - 1 \right) \qquad (1)$$

where a and b are elastic constants that reflect the elastic properties and tissue composition; I_1 is the first invariant of the strain tensor. In the Taylor series expansion, a has the significance of the elastic modulus. This exponential form has been found to be appropriate for arterial mechanics since it portrays the well-known strain-stiffening behavior of collagen.

An idealized but realistic 3D solid model of the healthy carotid bifurcation (extending 3 cm distal to 3 cm proximal to the bifurcation) based on the work of Bharadvaj et. al. [26, 27] was created in SolidWorks (SolidWorks Corporation, Concord, MA) and imported into the finite element code for meshing and analysis. Only half of the geometry was modeled and symmetry boundary conditions were exploited. The model used and boundary conditions and loads imposed are illustrated in Figure 1.

The arterial wall was freely meshed (Figure 2) with 43,334 eleven-node quadratic 3D tetrahedral solid elements, producing 118,229 nodes and 351,176 equations. An axial stretch of 10% was applied to the solid domain as measured *in situ* by Delfino [28].The initial internal pressure was ramped incrementally from 0 mmHg to 80 mmHg (diastole) to 120 mmHg (systole). All calculations were performed using a SGI Origin 2000 computer equipped with 4 processors and 6 GB of RAM (1.2 GB were needed for this computation).

Since the arterial wall has been shown to behave in a *pseudoelastic* manner [29], viscoelasticity of the arterial wall was not considered and only a static inflation of the artery was performed to gain insight into the strain levels experienced as a function of location in the bifurcation. The output was stored at systole (120 mmHg) and diastole (80 mmHg) and the Von Mises (VM) cyclic strain computed as the difference between these two states:

$$\varepsilon_{VM,cyclic} = \varepsilon_{VM,systolic} - \varepsilon_{VM,diastolic} \qquad (2)$$

where the Von Mises strain is a strain invariant defined by:

$$\varepsilon_{VM} = \left[\frac{(\varepsilon_I - \varepsilon_{II})^2 + (\varepsilon_{II} - \varepsilon_{III})^2 + (\varepsilon_I - \varepsilon_{III})^2}{2} \right]^{1/2} \quad (3)$$

and ε_I, ε_{II} and ε_{III} are the principal strains.

It should emphasized that the cyclic strain components, rather than absolute strain are what are believed to play a role in biological modeling. It has already been shown that bio-modeling and remodeling can both be governed by strain perturbations [30].

III.4. Results

Figure 3 shows a bandplot of the Von Mises cyclic strain amplitude plotted along the inner wall of the carotid bifurcation. Since we are interested in the EC response (SMC biological response to cyclic strain is similar—see Introduction), cyclic strain values at the inner wall are of greatest concern. The cyclic strain amplitudes vary in a nearly linear fashion from 2-3% on the outer wall (not shown) up to 5-7% on the inner wall. Strain amplitudes are slightly smaller downstream of the carotid sinus, but the differences are rather small.

Only in the vicinity of the bifurcation do we see significant variations in strain amplitude. The wall opposite to the flow divider of the external carotid (the common-external adjoining wall) and the carotid apex, both common sites of early inflammation, as well as immediately distal to the carotid bulb, a site of late stage inflammation are seen to experience the highest cyclic strain of 6-7% (vs. 4-5% elsewhere on the inner wall of the bifurcation).

Doubling the number of elements changed the cyclic strain values by at most 5% in areas of stress concentration and no more than 3% elsewhere.

III.5. Discussion

The cyclic strain levels recorded herein, compare favorably with distensibility levels detected clinically. Non-invasive measurements by Van Merode et. al. [31] reveal distensibility values of ~ 5% in older volunteers (ages 50-60) and ~ 11% in younger volunteers (ages 20-30) in the common carotid. The values detected herein are of ~ 5 % and circumferentially uniform over the inner wall of the common carotid. In other simulations based on MR images of normal human subjects [32], we record higher values of cyclic strain, in the range of 5% to 8% in the common carotid. Due to the geometric complexity of the carotid bifurcation, it is not surprising that at areas of curvature and sharp intersections (e.g. the apex), the strain field is non-uniform. This is expected due to stress (and subsequently strain) concentrations arising there [24].

Schwenke and Carew [33] inspected the permeability of arterial branch sites in the normal rabbit aorta and showed that such sites have a permeability that is on the order of four times higher than that of non-branching regions. Friedman et. al. also [22] note the increase in intimal permeability in regions of high wall shear stress and hypothesize that since albumin uptake is enhanced by shear, it is possible that other chemical reactions be mediated by high shear, but do not attempt to link this to intimal thickening. It is more likely, given the substantial amount of experimental evidence that links cyclic strain to EC proliferation, that the enhanced permeability occurs from "leaky cell junctions" [15] during EC mitosis enhanced by high cyclic strain as is suggested by our results.

Whereas the earlier results of Friedman et. al. [22] attribute the increased permeability to high shear stress, our results within suggest an alternative explanation, linking high cyclic strain to enhanced permeability via "leaky cell junctions." This is apparent at the carotid apex, which is a branch site with higher permeability [33] and experiences cyclic strain levels of ~7%, approximately 40% higher than elsewhere in the bifurcation. With levels of cyclic strain as high as 6% also in the adjoining wall of the external-common carotid, both these results support the possible role of cyclic strain in early stage inflammation, since these two locations were also observed as regions of early atherosclerotic inflammation [21, 22]. This is further supported by the results of Li et. al. [14] who

showed that cyclic strain increases EC proliferation and established that there exists an optimal cyclic strain range for EC proliferation (<6.4% – vs. 6-7% observed here), which if exceeded dampens the proliferative response.

On the other hand, we were struck by the high degree of uniformity in strain amplitude over much of the wall. By not revealing dramatic differences in cyclic strain amplitudes, the results are suggestive but not conclusive of a positive correlation between inflammation and elevated cyclic strain level. Limitations of this study include the nature of the geometry used, based on an average carotid geometry as in Bharadvaj et. al. [27] and the use of one set of material properties even though it is based on excised arterial segments from human cadavers [28]. Given today's Magnetic Resonance Imaging (MRI) capabilities, arterial geometries can readily be reconstructed and this hypothesis be further verified with a more substantial segment of the population. It should be noted, however, that even early disease, accompanied by moderate plaque formation and arterial stiffening could alter these findings.

A potentially more important concern is residual stresses since previous researchers [23, 34, 35] have shown that residual stresses can exert a significant effect on the stress field in an artery. When cut, an excised arterial segment typically springs open (eventually to a steady state opening angle), suggesting that in the closed configuration, the artery is not in the stress free state when the transmural pressure is zero [35]. However, it is the dynamic component of strain that has been found to elicit a cellular response and is of interest. Even though the absolute magnitude of the stresses (and strains) in an artery is changed by the inclusion of residual stresses, the strain amplitude remains unchanged in the case of a cylindrical artery (see figure 4). Delfino et. al. [23] proposed incorporating residual stresses by using a bending moment to "re-close" the opening angle of a similar 3D finite element model of the carotid bifurcation, but still obtained a region in the carotid bulb with large stress gradients across the wall. The results of the cylinder presented in figure 4, in combination with a lack of an unambiguous means to introduce residual stress, led us to ignore its effect (on cyclic strain) in the case of a bifurcation considered herein.

If high cyclic strain is an important factor in initiating disease, the presence of plaques in the carotid bulb [20], a region of low/oscillatory fluid shear stress, appears to be a region of moderate cyclic strain amplitude of approximately 5% and is thus not explained by our hypothesis. An area of elevated cyclic strain amplitude (6-7%) is detected immediately distal to the bulb, however, suggesting that cyclic strain may play a role in that region. This adds to the notion that arterial disease is multi-factorial and cannot be attributed to one single mechanical (or biochemical) factor.

III.6. Summary

There are many experimental results, both *in vivo* and *in vitro* that are in favor a correlation between cyclic strain and atherogenesis, based on observations that implicate high cyclic strain to the stimulation of endothelial and smooth muscle cells. A 3D idealized, but realistic model of the carotid bifurcation was analyzed herein using finite element methods to identify high cyclic strain regions. The adjoining wall of the external-common carotid and the carotid apex, both frequent sites of early inflammation were seen to experience high cyclic strains, in the range of 6-7%. An area of elevated cyclic strain amplitude is also detected immediately distal to the bulb, suggesting that cyclic strain may play a role in that region as well.

These correlations are, however, not strong, with cyclic strain values being at 5% in most areas, and 6-7% in susceptible areas. Nevertheless, the finite element techniques employed herein are of value in assessing the stress and strain fields in arteries. Similar methods to those employed here can be used to evaluate the importance of cyclic strain in advanced lesions.

III.7. References

1. Reape, T.J., Groot, P.H. (1999) Chemokines and atherosclerosis. *Atherosclerosis* **147**, 213-25.

2. Capers, Q., Alexander, R.W., Lou, P., De Leon, H., Wilcox, J.N., Ishizaka, N., Howard, A.B., Taylor, W.R. (1997) Monocyte chemoattractant protein-1 expression in aortic tissues of hypertensive rats. *Hypertension* **30**, 1397-402.
3. Jiang, M.J., Yu, Y.J., Chen, Y.L., Lee, Y.M., Hung, L.S. (1999) Cyclic strain stimulates monocyte chemotactic protein-1 mRNA expression in smooth muscle cells. *J Cell Biochem* **76**, 303-10.
4. Wang, D.L., Wung, B.S., Shyy, Y.J., Lin, C.F., Chao, Y.J., Usami, S., Chien, S. (1995) Mechanical strain induces monocyte chemotactic protein-1 gene expression in endothelial cells. Effects of mechanical strain on monocyte adhesion to endothelial cells. *Circ Res* **77**, 294-302.
5. Wung, B.S., Cheng, J.J., Chao, Y.J., Lin, J., Shyy, Y.J., Wang, D.L. (1996) Cyclical strain increases monocyte chemotactic protein-1 secretion in human endothelial cells. *Am J Physiol* **270**, H1462-8.
6. Wung, B.S., Cheng, J.J., Hsieh, H.J., Shyy, Y.J., Wang, D.L. (1997) Cyclic strain-induced monocyte chemotactic protein-1 gene expression in endothelial cells involves reactive oxygen species activation of activator protein 1. *Circ Res* **81**, 1-7.
7. Cheng, G.C., Briggs, W.H., Gerson, D.S., Libby, P., Grodzinsky, A.J., Gray, M.L., Lee, R.T. (1997) Mechanical strain tightly controls fibroblast growth factor-2 release from cultured human vascular smooth muscle cells. *Circ Res* **80**, 28-36.
8. Clowes, A.W., Reidy, M.A., Clowes, M.M. (1983) Mechanisms of stenosis after arterial injury. *Lab Invest* **49**, 208-15.
9. Jackson, C.L., Reidy, M.A. (1993) Basic fibroblast growth factor: its role in the control of smooth muscle cell migration. *Am J Pathol* **143**, 1024-31.
10. Lindner, V., Reidy, M.A. (1993) Expression of basic fibroblast growth factor and its receptor by smooth muscle cells and endothelium in injured rat arteries. An en face study. *Circ Res* **73**, 589-95.
11. Mason, I.J. (1994) The ins and outs of fibroblast growth factors. *Cell* **78**, 547-52.
12. Richard T. Lee, C.Y., Yajun Feng, Susan Potter-Perigo, William H. Briggs, Katherine T. Landschulz, Thomas G. Turi, John F. Thompson, Peter Libby, and Thomas N. Wight (2001) Mechanical Strain Induces Specific Changes in the Synthesis and Organization of Proteoglycans by Vascular Smooth Muscle Cells. *Journal of Biological Chemistry* .
13. Lemire, J.M., Braun, K.R., Maurel, P., Kaplan, E.D., Schwartz, S.M., Wight, T.N. (1999) Versican/PG-M isoforms in vascular smooth muscle cells. *Arterioscler Thromb Vasc Biol* **19**, 1630-9.
14. Li, G., Mills, I., Sumpio, B. (1994) Cyclic Strain Stimulates Endothelial Cell Proliferation: Characterization of Strain Requirements. *Endothelium* **2**, 177-81.
15. Weinbaum, S., Tzeghai, G., Ganatos, P., Pfeffer, R., Chien, S. (1985) Effect of cell turnover and leaky junctions on arterial macromolecular transport. *Am J Physiol* **248**, H945-60.
16. Lin, S.J., Jan, K.M., Schuessler, G., Weinbaum, S., Chien, S. (1988) Enhanced macromolecular permeability of aortic endothelial cells in association with mitosis [published erratum appears in Atherosclerosis 1989 Jul;78(1):87]. *Atherosclerosis* **73**, 223-32.

17. Lin, S.J., Jan, K.M., Weinbaum, S., Chien, S. (1989) Transendothelial transport of low density lipoprotein in association with cell mitosis in rat aorta. *Arteriosclerosis* **9**, 230-6.
18. Chien, S., Lin, S.J., Weinbaum, S., Lee, M.M., Jan, K.M. (1988) The role of arterial endothelial cell mitosis in macromolecular permeability. *Adv Exp Med Biol* **242**, 59-73.
19. Tropea, B.I., Schwarzacher, S.P., Chang, A., Asvar, C., Huie, P., Sibley, R.K., Zarins, C.K. (2000) Reduction of aortic wall motion inhibits hypertension-mediated experimental atherosclerosis. *Arterioscler Thromb Vasc Biol* **20**, 2127-33.
20. Ku, D.N., Giddens, D.P., Zarins, C.K., Glagov, S. (1985) Pulsatile flow and atherosclerosis in the human carotid bifurcation. Positive correlation between plaque location and low oscillating shear stress. *Arteriosclerosis* **5**, 293-302.
21. Masawa, N., Glagov, S., Zarins, C.K. (1994) Quantitative morphologic study of intimal thickening at the human carotid bifurcation: I. Axial and circumferential distribution of maximum intimal thickening in asymptomatic, uncomplicated plaques. *Atherosclerosis* **107**, 137-46.
22. Friedman, M.H., Deters, O.J., Bargeron, C.B., Hutchins, G.M., Mark, F.F. (1986) Shear-dependent thickening of the human arterial intima. *Atherosclerosis* **60**, 161-71.
23. Delfino, A., Stergiopulos, N., Moore, J.E., Jr., Meister, J.J. (1997) Residual strain effects on the stress field in a thick wall finite element model of the human carotid bifurcation. *J Biomech* **30**, 777-86.
24. Salzar, R.S., Thubrikar, M.J., Eppink, R.T. (1995) Pressure-induced mechanical stress in the carotid artery bifurcation: a possible correlation to atherosclerosis. *J Biomech* **28**, 1333-40.
25. Bathe, K.J. (1996) *Finite element procedures*. Prentice Hall, Englewood Cliffs, N.J.
26. Bharadvaj, B.K., Mabon, R.F., Giddens, D.P. (1982) Steady flow in a model of the human carotid bifurcation. Part II--laser- Doppler anemometer measurements. *J Biomech* **15**, 363-78.
27. Bharadvaj, B.K., Mabon, R.F., Giddens, D.P. (1982) Steady flow in a model of the human carotid bifurcation. Part I--flow visualization. *J Biomech* **15**, 349-62.
28. Delfino, A. (1996) Analysis of Stress Field in a Model of the Human Carotid Bifurcation. In *Department of Physics*Ecole Polytechnique Federale de Lausanne, Lausanne, Switzerland.
29. Fung, Y.C., Fronek, K., Patitucci, P. (1979) Pseudoelasticity of arteries and the choice of its mathematical expression. *Am J Physiol* **237**, H620-31.
30. Huiskes, R., Ruimerman, R., van Lenthe, G.H., Janssen, J.D. (2000) Effects of mechanical forces on maintenance and adaptation of form in trabecular bone. *Nature* **405**, 704-6.
31. Van Merode, T., Brands, P.J., Hoeks, A.P., Reneman, R.S. (1996) Different effects of ageing on elastic and muscular arterial bifurcations in men. *J Vasc Res* **33**, 47-52.
32. Younis, H.F., Kaazempur-Mofrad, M.R., Chan, R.C., Chau, A.H., Hinton, D.P., Isasi, A.G., Kim, L.A., Kamm, R.D. (2001) A Numerical Study of Carotid Artery

Wall and Fluid Mechanics based on in vivo Magnetic Resonance Images of Healthy Volunteers. *in progress* .
33. Schwenke, D.C., Carew, T.E. (1989) Initiation of atherosclerotic lesions in cholesterol-fed rabbits. II. Selective retention of LDL vs. selective increases in LDL permeability in susceptible sites of arteries. *Arteriosclerosis* **9**, 908-18.
34. Chuong, C.J., Fung, Y.C. (1986) On residual stresses in arteries [published erratum appears in J Biomech Eng 1990 Aug;112(3):249]. *J Biomech Eng* **108**, 189-92.
35. Fung, Y.C. (1991) What are the residual stresses doing in our blood vessels? *Ann Biomed Eng* **19**, 237-49.

III.9. Figures

III.9.1. Figure Captions

Fig. 1 Solid model used for the arterial wall. "P" represents the inner surfaces, where the pressure boundary condition was applied. The solid arrows represent an applied axial strain of 10%. The pressure was ramped from 0 mmHg through 80 mmHg (diastole) to 120 mmHg (systole) and the results saved at diastole and systole.

Fig. 2 Computational mesh used in simulations. Half the bifurcation was modeled by making use of symmetry.

Fig. 3 Bandplot of Von Mises cyclic strain. Note the areas of elevated (~6-7%) strain, namely the external carotid wall opposite the flow divider, the flow divider itself and immediately distal to the carotid bulb.

Fig. 4 The effect of residual stresses on the strain field across the thickness of an axisymmetric cylindrical artery. The x-axis is plotted as a function of normalized thickness, with "0" being along the inner wall surface. The top graph illustrates the strain at systole and diastole without the inclusion of residual stresses, the lower graph with. Note that even though the strain field is altered (more uniform when residual stresses are included), the magnitude of the cyclic strain (obtained as the difference between the solid and dashed lines) is identical in both cases.

III.9.1. Figures

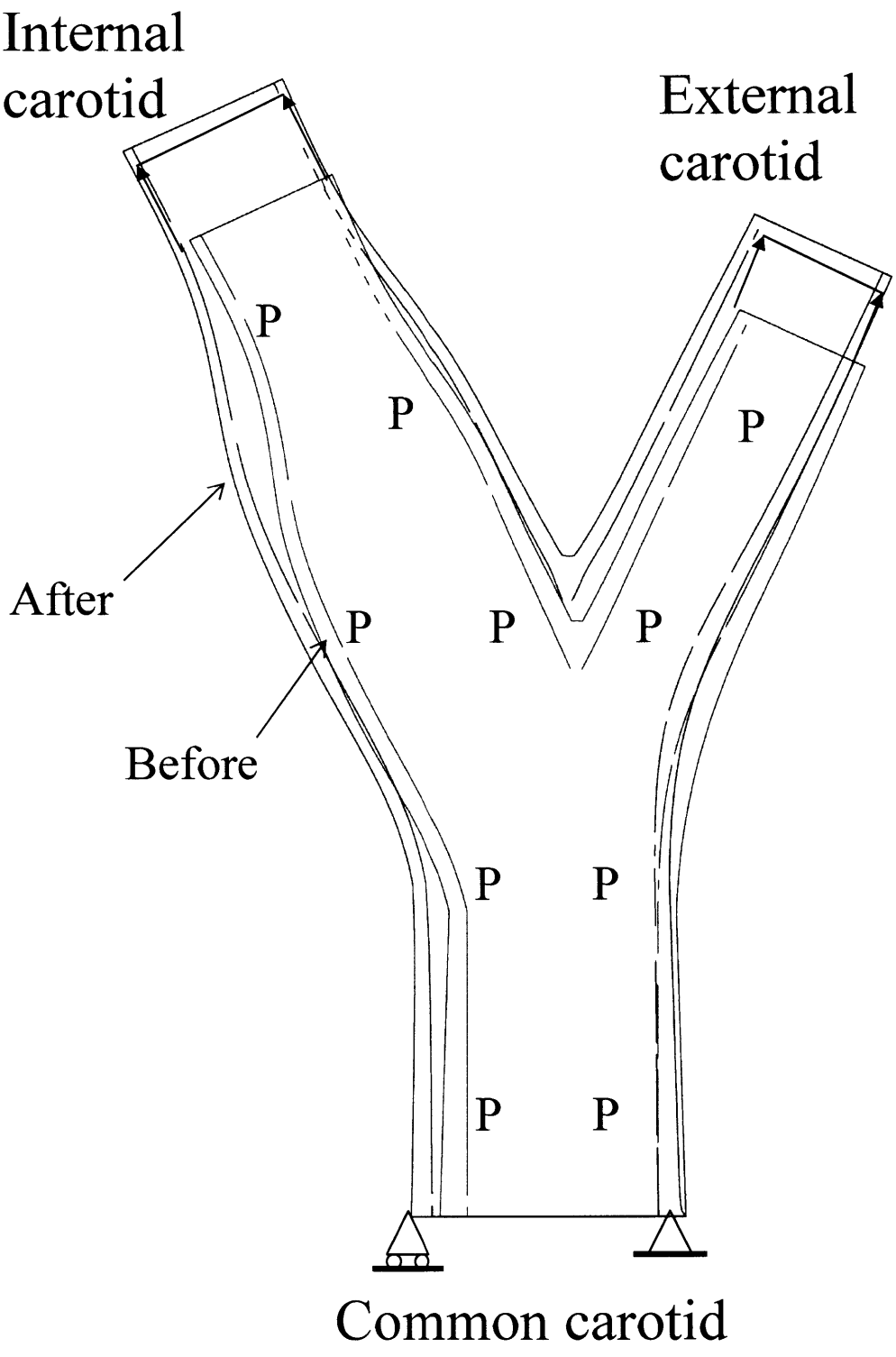

Figure 1

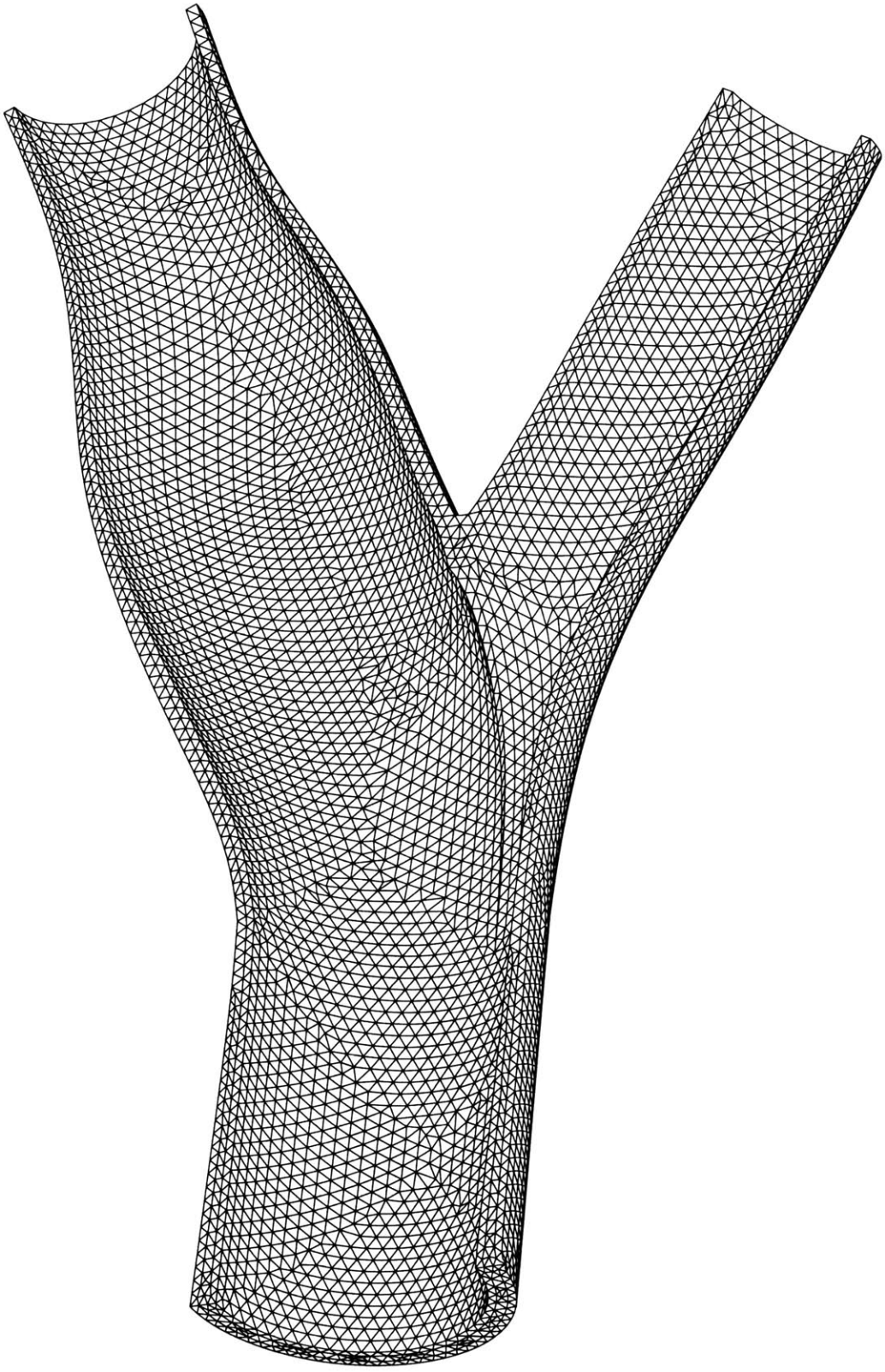

Figure 2

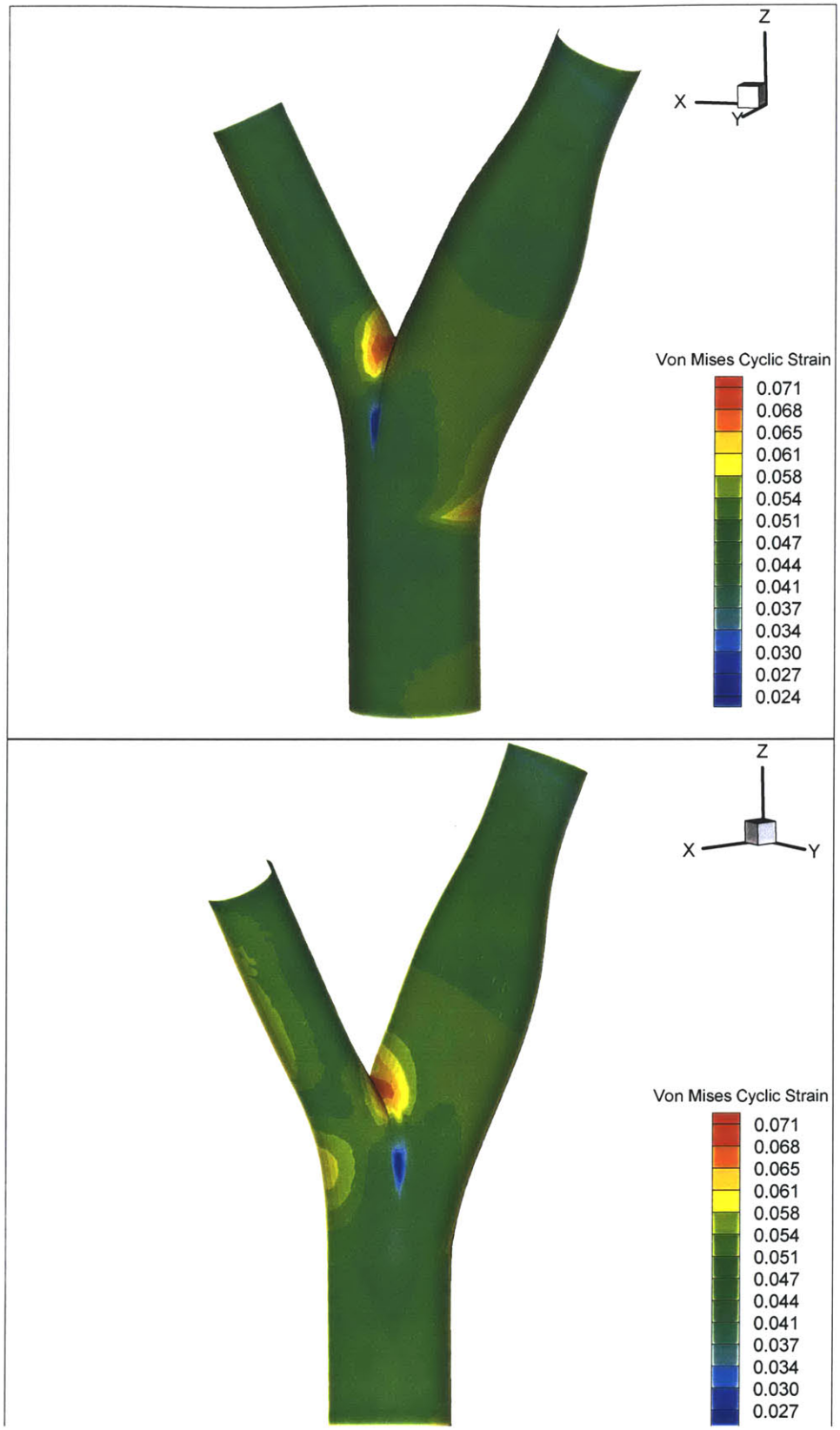
Z
X
Y
Von Mises Cyclic Strain
0.071
0.068
0.065
0.061
0.058
0.054
0.051
0.047
0.044
0.041
0.037
0.034
0.030
0.027
0.024
Z
X
Y
Von Mises Cyclic Strain
0.071
0.068
0.065
0.061
0.058
0.054
0.051
0.047
0.044
0.041
0.037
0.034
0.030
0.027

Figure 3

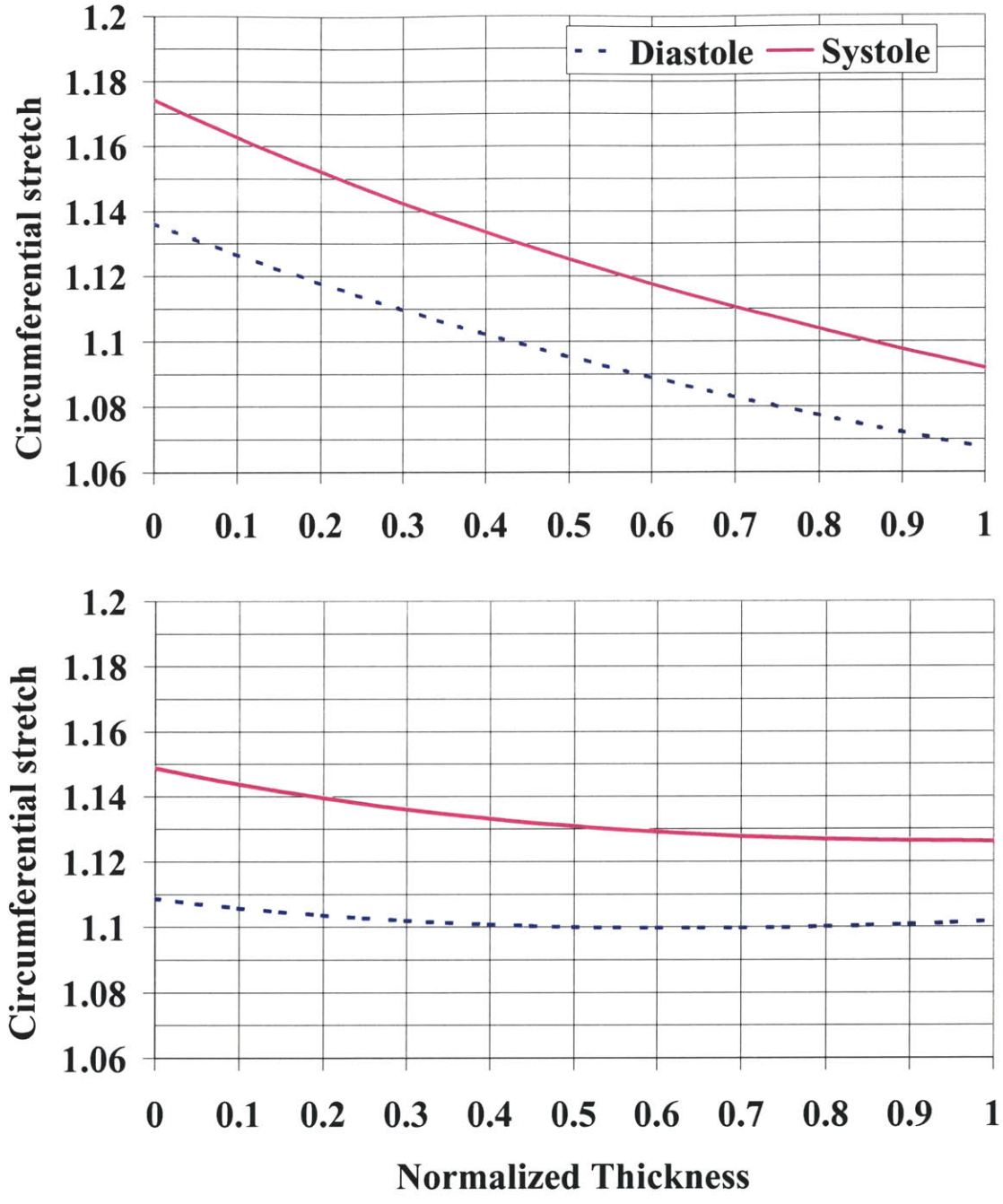
Diastole
Systole
Circumferential stretch
1.2
1.18
1.16
1.14
1.12
1.1
1.08
1.06
0
0.1
0.2
0.3
0.4
0.5
0.6
0.7
0.8
0.9
1
Normalized Thickness

Figure 4

IV. Fluid-Structure Interaction Finite Element Analysis to Investigate the Effect of Exercise on Fluid Mechanical Variables in the Carotid Bifurcation

IV.1. Abstract

The important influence of hemodynamic factors in the initiation and progression of arterial disease is well-documented and has led to numerous studies to numerically simulate blood flow at sites of disease and examine potential correlative factors. In these simulations, an attempt has been made to include all potentially important effects. Among these are the non-Newtonian properties of blood, the two phase nature of blood, arterial wall compliance and realistic geometries. Although these studies provide considerable insight, each typically considers only a single set of flow conditions. It is well-known, however, that heart rate, blood pressure and flow or pressure waveforms at a given location can vary considerably during the course of normal, daily activity. This study considers these variations and examines the differences in hemodynamics produced by varying heart rate in a fully coupled fluid-structure 3D finite element model of a carotid bifurcation. Results show that even for a 50% increase in heart rate, as would occur during a vigorous walk, significant differences in the fluid mechanical parameters of interest occur. The lowest values of wall shear stress (WSS) occur at the carotid bulb, and are almost doubled by the 50% increase in heart rate associated with moderate exercise. Values for the maximum wall shear stress temporal gradient (WSSTG), another potentially relevant parameter in atherogenesis, also double at the carotid bulb.

Keywords: Exercise, finite element analysis, carotid bifurcation, blood flow, wall shear stress.

IV.2. Introduction

Due to the strong correlations known to exist between sites of atherosclerosis and variations in local hemodynamics, a vast amount of research has been performed to date on arterial blood flow in bifurcations, junctions and grafts. These studies include numerical simulations since those provide vast amount of information on detailed flow and shear stress patterns in regions of interest. In a continuing attempt to increase the realism of these simulations, new factors have been introduced including non-Newtonian blood properties, arterial wall compliance and at times treating the blood as a two phase medium. Each added factor represents another step toward a realistic prediction of wall shear stress (and other related parameters), so that these might be correlated with measures of disease or the various biological factors known to cause it.

For example, a study by Gijsen et. al. [1] on the influence of non-Newtonian properties of steady blood flow in the carotid bifurcation demonstrated that notable differences exist between Newtonian and non-Newtonian models. The axial velocity field of the non-Newtonian fluid was flattened, and it had higher velocity gradients at the non-divider wall and lower gradients at the divider wall than the Newtonian model. On the other hand, Perktold et. al. [2] found that in the case of pulsatile flow, the general flow characteristics between Newtonian and non-Newtonian models were largely unchanged in the carotid bifurcation. An experimental investigation by Friedman et. al. [3] supported this conclusion by noting that the effect of fluid rheology in the aortic bifurcation is minimal in quantifying the correlation between intimal thickening and shear rate.

Another aspect of arterial blood flow that has been much investigated is the effect of arterial wall compliance on the flow characteristics. Friedman et. al. [3] demonstrated that the effect of compliance is also insignificant. Steinman and Ethier [4] have observed that only minor changes in overall wall shear stress patterns were observed when the effect of wall distensibility was included in an end-to-side anastomosis. In another simulation, Perktold and Rappitsch [5] demonstrated that flow separation and wall shear stress are reduced in a distensible wall model of the carotid bifurcation. Their work

shows that at the location of greatest interest; the outer wall of the carotid bulb, where it is generally believed that atherosclerosis initiates, the wall shear stress profiles between rigid and complaint models are almost identical. Significant differences in wall shear stress, of up to 25%, only appeared at the flow divider.

In view of the number of previous studies, it is surprising that the effect of normal, daily variations in local hemodynamic conditions. These could far exceed the small effects associated with non-Newtonian rheology or even wall compliance. Depending on the level of activity and the variations that a person experiences during the course of a day, blood flow rate changes resulting from heart rate fluctuations might cause more significant variations in the abovementioned parameters. These variations are not only due to intense exercise, but even be seen in mild exertion such as brisk walk causing elevation of the heart rate. In addition, due to the effect of pulse wave reflections on shaping the local pressure waveform, even the pattern of pressure and velocity variations could change.

IV.3. Methods

To investigate this effect, pulsatile blood flow in a model carotid bifurcation is simulated using fully coupled fluid-structure interaction finite element methods at two different heart rates: 72 bpm representing a person at rest and the other at 108 bpm (50% increase). A previously published model [6] is used to compute the flow and pressure waveforms at these two conditions, for a given, fixed, arterial network. For each case, wall shear stress values, relevant integrated parameters of wall shear stress over the cycle as well as temporal gradients of wall shear stress are compared to identify significant differences among them.

IV.3.1. Material Models and Solution Process

The simulations employ finite element analysis (ADINA, version 7.3, Automatic Dynamic Incremental Nonlinear Analysis, Watertown, MA) and incorporate a non-linear, isotropic, hyperelastic model for the arterial wall. Blood is treated as an incompressible,

Newtonian fluid (an assumption that has repeatedly been shown to hold well for large arteries [2, 7], where shear rates generally exceed 100 s^{-1}) and the flow assumed laminar.

The arterial solid response is modeled using the standard Lagrangian formulation for large displacements and large strains [8]. An isotropic form of the strain energy density function for the (nearly) incompressible artery wall is specified [9]:

$$W = \frac{a}{b}\left(e^{\frac{b}{2}(I_1-3)} - 1 \right) \tag{1}$$

where a and b (a = *44.25 kPa, b = 16.73*) are elastic constants that reflect the elastic properties and tissue composition; their values are obtained using a non-linear regression fit to pressure-diameter inflation tests of the carotid artery [9, 10]. I_1 is the first invariant of the strain tensor. In the Taylor series expansion, a has the significance of the elastic modulus. This exponential form is appropriate for arterial mechanics since it portrays the well-known strain-stiffening behavior of collagen.

Continuity and the full Navier-Stokes equations are solved for the fluid. For fluid domains with moving boundaries, it is necessary to utilize the Arbitrary Lagrangian Eulerian (ALE) formulation of the momentum equation [11]. Full coupling between the fluid and solid domains requires that displacement continuity and force equilibrium are satisfied at the fluid-structure interface at each step. In the ADINA system (version 7.3), this is done iteratively between the fluid and solvers at each time step until sufficient convergence had been reached. The fluid-structure interaction module of the code has been previously validated by Bathe et. al. [11] and used extensively in several previous studies, e.g. [12-14].

Fluid-structure interaction analysis is generally important when large scale motions of the arteries are present and impact the flow field considerably, as in studies of arterial collapse when largely obstructive stenoses are present [14, 15] or where physiologic movement of blood vessels (e.g. coronary arteries) during the cardiac cycle affects blood flow patterns significantly [16]. In the carotid bifurcation, even though the motions due to

arterial wall motion are relatively small, the effect of wall compliance can have a locally significant effect (up to 25% difference in wall shear stress) at the divider wall [5] and was thus included in the simulations herein. The results presented focus on the fluid domain; the solid mechanical strain distributions are presented elsewhere [17, 18].

IV.3.2. Model Description and Boundary Conditions

A idealized but realistic 3D solid model of the carotid bifurcation (extending 3 cm distal to 3 cm proximal to the bifurcation) based on the work of Bharadvaj et. al. [19, 20] and Delfino et. al. [9] was created in SolidWorks (SolidWorks Corporation, Concord, MA) and imported into the finite element code for meshing and analysis. Only half of the geometry was modeled and symmetry boundary conditions were exploited. The (solid) model used and boundary conditions imposed are illustrated in Figure 1. The arterial wall was freely meshed with 43,334 eleven-node 3D tetrahedral solid elements, producing 118,229 nodes and 351,176 equations.

The fluid-structure simulations where performed in 2 stages: An "inflation" stage (from 0 to 1 *s*) in which the fluid velocity vectors where ramped up from zero to diastolic values and within which simultaneously an axial stretch of 10% (as measured *in situ* by Delfino [10]) was applied incrementally to the solid domain (and subsequently stretched the fluid domain). This was followed by the "transient" stage, in which the result files from the "inflation" stage were used as initial conditions; the arterial wall stretch remained fixed at 10% and the fluid velocity pulsatile boundary conditions were applied. To achieve a periodic solution, the "transient" stage flow computation was allowed to run over two heart cycles, saving only the second one. The boundary conditions (flow rate and blood pressure profiles – see figure 2) to the "transient stage" were obtained using the using the one dimensional arterial model of Ozawa et. al. [6]. This is a network model of an entire arterial network with 32 arterial segments. In this model, the heart rate was increased, while reducing the systemic vascular resistance (SVR) to keep the mean arterial pressure (MAP) nearly constant (13 kPa in the 72bpm vs. 12 kPa in the 108 bpm case), thus causing the cardiac output to increase. The mean flow rates increased by 31% from 12.5 ml/s (72 bpm) to 16.4 ml/s (108 bpm).

The "transient" stage was subsequently solved in two more steps, similar to that first introduced by Perktold et. al. [2]. The pressure profiles shown in Figure 2 were added to the computed pressure drop using the "pressure datum" function in ADINA; they where therefore transmitted to the solid domain to achieve arterial pulsatility. In the first step, a Womersley type flow corresponding to the flow rate profile in the common carotid artery [21] was imposed node-by-node at the inlet to the common carotid and a plug flow specified at the exit of the internal carotid, while the external carotid was specified as having zero normal traction. Flow profiles at the output of the external carotid artery at the end of this step were then used as a boundary condition to the second computational step of this "transient" stage, while retaining the Womersley flow at the common carotid and imposing a traction-free boundary condition at the internal carotid. This second step was then considered the final computed solution [2]. The entire procedure was repeated twice; first for 72 bpm and then 108 bpm.

Wall shear stress, oscillatory shear index and maximum wall shear stress temporal gradients are then computed for comparison between the two cases. "Size" of the recirculation region, *Ls*, is defined as the normalized length along the common-internal carotid adjoining wall (line 1 of figure 1) which exhibits reversed shear stress. It is normalized to the entire length of the common-internal carotid adjoining wall as simulated in the model, with the carotid bulb spanning the non-dimensional length s = 0.40 to 0.73, where s is the non-dimensional distance along line 1.

The fluid domain was freely meshed using 56,209 four node tetrahedral elements, resulting in 11,597 nodes and 46,388 equations. The meshes used for the fluid and solid domains are shown in Figure 3. The computation was performed using a SGI Origin 2000 computer equipped with 4 processors and 6 GB of RAM.

IV.4. Results

IV.4.1. Wall Shear Stress (WSS)

The fluid parameter that appears to be of greatest relevance to atherogenesis is the magnitude of the wall shear stress vector [22]. This is presented in the form of bandplots of the WSS averaged over the cycle (WSSavg) for the 72 and 108 bpm solutions (figure 4). WSSavg differs by up to 50% for the two heart rates simulated (depending on location), with the substantially lower WSS values occurring at the lower heart rate as expected. Also of note is that the area of low WSS ($< 1.0\ Pa$) shrunk considerably with increasing heart rate (108 bpm vs. 72 bpm). Overall, the average WSS levels in the common carotid are uniform as expected in a perfectly cylindrical geometry and the increase in WSS from the 108 bpm over the 72 bpm case (~2.3 *Pa* vs. 1.8 *Pa* respectively) reflects the subsequent 30 % increase in average flow rate.

It is of particular interest to consider the outer wall of the carotid bifurcation from the common to internal carotid (line 1 on Figure 1), which spans the carotid bulb, a commonly diseased site. The chosen time points for comparison are at peak acceleration (A), peak flow (B) and peak deceleration (C) as well as the time of lowest flow rate (D), which occurs at the decelerative trough of the second peak in both cases and coincides with the largest negative velocity gradient throughout the cycle. Time point (D) is also the time at which there exists the largest recirculation zone for both flow rates. Flow separation was observed to start immediately after time (B). Times (A) and (C) were chosen so that they correspond to approximately the same flow rate. WSS along line 1 at these relevant time steps are shown in Figure 5. Table 1 summarizes the wall shear stress values and non-dimensional lengths of the recirculation regions along this line.

	72 bpm		108 bpm	
Time point in cardiac cycle	Max WSS in carotid bulb (Pa)	Normalized length of the recirculation region, *Ls*	Max WSS in carotid bulb (Pa)	Normalized length of the recirculation region, *Ls*
A	1.9	None	1.9	None
B	2.9	0.09 (0.4 to 0.49)	3.0	0.12 (0.38 to 0.52)
C	1.6 (-ve)	0.46 (0.32 to 0.78)	2.0 (-ve)	0.45 (0.32 to 0.77)
D	0.8 (-ve)	0.45 (0.32 to 0.77)	2.9 (-ve)	0.87 (0 to 0.87)

Table 1 Maximum wall shear stress in the carotid bulb and size of the re-circulation region at different intervals in time during the cardiac cycle: peak acceleration (A), peak flow (B) and peak deceleration (C) as well as the time of lowest flow rate (D) for the case of a person at rest (72 bpm) and a person exercising moderately (108 bpm). (-ve) signifies that the wall shear stress vector reversed direction. Length of the recirculation region, *Ls*, is defined as the normalized length along the common-internal carotid adjoining wall (line 1 of figure 1) with reversed shear stress. It is normalized to the entire length of the common-internal carotid adjoining wall as simulated in the model, with the carotid bulb spanning the non-dimensional length $s = 0.40$ to 0.73, where s is the distance along line 1. The values in parentheses represent the non-dimensional coordinate *s* over which flow reversal occurs. At time point D of the 108 bpm run, the flow enters the common carotid artery separated due to the fully developed Womersley flow boundary condition associated with the sharp deceleration there.

The highest values of WSS along the carotid bulb do not occur during the accelerative phase of systole as one might expect. In the 72 bpm case, the maximum WSS in the bulb over the cycle occurs during the decelerative phase of systole at time point (C) and is 1.6 Pa, whereas in the 108 bpm case, this occurs at the point of lowest flow rate (D) and is 2.9 Pa. Both these values are in reverse flow since they lie within the re-circulation region in the carotid bulb. This illustrates that a moderate increase in heart rate of 50 % can almost double the maximum level of WSS in the carotid bulb. Comparing the values at similar points in the cycle between the two heart rates, we see little or no difference in WSS (1.9 Pa) during the accelerative phase of systole (A) nor at peak systole(B) (2.9 vs. 3.0 Pa). During the decelerative phase of systole (C) a 25 % increase in WSS is observed as heart rate is increased and at the point of lowest flow rate (D) the WSS increases by 262 % to 2.9 Pa.

Also of interest is the size of the re-circulation zone in the carotid bulb. Even though the overall size of the recirculation region over the entire cycle seemed relatively unaffected by heart rate (see *OSI* below), there were some variations along the cardiac cycle. In

general, increasing the heart rate seemed to increase the length, *Ls*, of the recirculation zone (see Table 1). At time point D of the 108 bpm run, the flow enters the common carotid artery already separated due to the fully developed Womersley flow boundary condition associated with the sharp deceleration there.

In contrast, no flow separation was seen along the outside wall of the external carotid. Comparison of the maximum wall shear stress values in that region (at peak systole) reveals an increase in peak WSS levels from 16 to 20 Pa with the increase in heart rate. The same comparison at the carotid apex reveals an increase from 17.5 to 26 Pa.

IV.4.2. OSI and WSS Maximum Temporal Gradient

Two other parameters that have been investigated are the oscillatory shear index (OSI) (Figure 6) as defined by Ku et. al. [22] and the maximum WSS temporal gradient (Figure 7) over the cycle. The OSI is a non-dimensional measure that quantifies the fractional time a particular wall region in the cycle experiences cross or reverse flow. The mean flow direction is defined by the temporal mean of the shear stress vector. For purely oscillatory flow, the OSI approaches 0.5. Note that the OSI does not take into account the magnitude of the shear stress vectors, only the directions. There are no notable differences difference between the two cases.

Maximum WSS temporal gradient (Max WSSTG) is defined as the maximum value of the gradient in WSS calculated between every two consecutive time points during the cycle. The magnitudes are notably higher in the 108 bpm case but the differences cannot be explained by the higher flow rates alone. In the common carotid, Max WSSTG averages 140 Pa/s (72 bpm) and increases to 215 Pa/s (108 bpm). In the carotid bulb, Max WSSTG doubles in value from 35 to 70 Pa/s with the increase in heart rate. In contrast, Max WSSTG at the region of curvature in the wall adjoining the common-external carotid reaches 285 Pa/s (72 bpm) and 430 Pa/s (108 bpm). At the carotid apex, the Max WSSTG is an order of magnitude greater than at the bulb and reaches values of 600 Pa/s (72 bpm) and 800 Pa/s (108 bpm). Within the external carotid, further down

from the region of curvature, the max. WSSTG is seen to vary between 350-500 Pa/s (72 bpm) and 550-700 (108 bpm).

IV.4.3. Pressure Drop

The final parameter of interest is the pressure drop along the carotid bifurcation. Pressure drops were compared at point (C) during the decelerative phase of systole in both cases; this time step experiences some of the largest adverse pressure gradients throughout the cycle (results not shown). In both runs, a pressure drop (due to fluid Bernoulli affects) of 700 Pa was recorded at this time step, which is only 4 % of the applied systolic pressure.

IV.5. Discussion

The most important fluid mechanic parameter in relation to atherogenesis is the WSS. It is widely accepted now [22-24] that low WSS regions are more prone to atherosclerosis. WSS levels greater than 1.5 *Pa* are generally believed to induce endothelial quiescence and an atheroprotective gene expression profile, whereas low shear stress levels (less than 1.0 *Pa*) stimulate an atherogenic phenotype and are generally observed at atherosclerosis-prone sites [25]. This is evident in the average WSS results. With the increase in heart rate, the low WSS region in the carotid bulb reduces in size, and WSS values elsewhere are generally higher, up to 50% higher in some locations. This conclusion supports the notion that exercise promotes an atheroprotective phenotype.

WSSTG has been related to the expression of atherogenesis-related genes in endothelial cells (ECs). Bao et.al. [26] have found that the temporal gradient in shear but not steady shear stimulates the expression of monocyte chemoattractant protein-1 (MCP-1), a potent chemotactic agent for monocytes, and platelet-derived growth factor A (PDGF-A), a potent mitogen and chemotactic agent for smooth muscle cells. The higher values of max WSSTG experienced during the 108 bpm simulation suggest, therefore, that exercise may lead to another pathway that works to *increase* rather than decrease the atherogenicity of ECs.

These solutions also provide insight into the importance of performing a coupled fluid and structure interaction (FSI) solution. Since many codes lack this capability, it is important to assess the need for this additional complexity. The maximum pressure drop along the carotid bifurcation is (due to inertial affects) is ~ 4% of the systolic pressure. This small change in the wall pressure distribution supports the notion that FSI analyses may not be necessary in assessing the wall mechanical strains when examining arteries with non-severe stenoses. With respect to the fluid mechanical parameters, Perktold and Rappitsch [5] show that the significant differences in wall shear stress, of up to 25%, only appeared at the divider wall between the distensible and non-distensible models. They observed no difference in WSS between the two models at the primary region of atherogenic interest, the carotid bulb. Thus, in numerical studies aimed at understanding atherogenesis in the carotid bulb, FSI analyses may not be necessary. This may not be the case, however, in cases of severe disease (90% stenoses and above). In such cases, the blood pressures will be much larger, and so will the pressure drop across the stenosis, resulting in large scale wall motion, even with the presence of a stiffer diseased arterial wall [14].

IV. 6. Summary

A numerical study was carried out to observe the effect of moderate exercise on fluid mechanical parameters in the carotid bifurcation, a commonly diseased site of the cerebral circulation. It was observed that the lowest values of WSS occurred at the carotid bulb, and were almost doubled by the 50% increase in heart rate associated with moderate exercise, suggesting that exercise promotes an atheroprotective phenotype. The values of maximum WSSTG, which is associated with inducing an atherogenic phenotype, also doubled along the carotid bulb, however, leaving no clear conclusion to the overall effect of exercise on atherogenesis. What remains clear, nonetheless, is the need to incorporate the effect of heart rate variability in future numerical studies of blood flow in arteries in order to identify the range of conditions to which the endothelial surface is subjected.

IV.7. References

1. Gijsen, F.J., van de Vosse, F.N., Janssen, J.D. (1999) The influence of the non-Newtonian properties of blood on the flow in large arteries: steady flow in a carotid bifurcation model. *J Biomech* **32**, 601-8.
2. Perktold, K., Resch, M., Florian, H. (1991) Pulsatile non-Newtonian flow characteristics in a three-dimensional human carotid bifurcation model. *J Biomech Eng* **113**, 464-75.
3. Friedman, M.H., Bargeron, C.B., Duncan, D.D., Hutchins, G.M., Mark, F.F. (1992) Effects of arterial compliance and non-Newtonian rheology on correlations between intimal thickness and wall shear. *J Biomech Eng* **114**, 317-20.
4. Steinman, D.A., Ethier, C.R. (1994) The effect of wall distensibility on flow in a two-dimensional end-to- side anastomosis. *J Biomech Eng* **116**, 294-301.
5. Perktold, K., Rappitsch, G. (1995) Computer simulation of local blood flow and vessel mechanics in a compliant carotid artery bifurcation model. *J Biomech* **28**, 845-56.
6. Ozawa, E.T., Bottom, K.E., Xiao, X., Kamm, R.D. (2001) Numerical simulation of enhanced external counterpulsation. *Ann Biomed Eng* **29**, 284-97.
7. Berger, S.A., Jou, L.D. (2000) Flows in Stenotic Vessels. *Annual Review of Fluid Mechanics* **32**, 347-384.
8. Bathe, K.J. (1996) *Finite element procedures*. Prentice Hall, Englewood Cliffs, N.J.
9. Delfino, A., Stergiopulos, N., Moore, J.E., Jr., Meister, J.J. (1997) Residual strain effects on the stress field in a thick wall finite element model of the human carotid bifurcation. *J Biomech* **30**, 777-86.
10. Delfino, A. (1996) Analysis of Stress Field in a Model of the Human Carotid Bifurcation. In *Department of Physics*Ecole Polytechnique Federale de Lausanne, Lausanne, Switzerland.
11. Bathe, K.J., Zhang, H., Ji, S. (1999) Finite element analysis of fluid flows fully coupled with structural interactions. *Computers and Structures* **72**, 1-16.
12. Chu, T.M., Reddy, N.P., Padovan, J. (1995) Three-dimensional finite element stress analysis of the polypropylene, ankle-foot orthosis: static analysis. *Med Eng Phys* **17**, 372-9.
13. Tang, D., Yang, J., Yang, C., Ku, D.N. (1999) A nonlinear axisymmetric model with fluid-wall interactions for steady viscous flow in stenotic elastic tubes. *J Biomech Eng* **121**, 494-501.
14. Bathe, M., Kamm, R.D. (1999) A fluid-structure interaction finite element analysis of pulsatile blood flow through a compliant stenotic artery. *J Biomech Eng* **121**, 361-9.
15. Downing, J.M., Ku, D.N. (1997) Effects of frictional losses and pulsatile flow on the collapse of stenotic arteries. *J Biomech Eng* **119**, 317-24.
16. Moore, J.E., Jr., Guggenheim, N., Delfino, A., Doriot, P.A., Dorsaz, P.A., Rutishauser, W., Meister, J.J. (1994) Preliminary analysis of the effects of blood vessel movement on blood flow patterns in the coronary arteries. *J Biomech Eng* **116**, 302-6.

17. Younis, H.F., Chung, C.I., Kamm, R.D. (2001) Challenges in developing an accurate model for carotid bifurcation blood flow and wall mechanics in First MIT Conference on Computational Fluid and Solid Mechanics, Cambridge, MA.
18. Younis, H., Chung, C., Lee, R., Kamm, R. (2001) Cyclic strain amplitude in the carotid bifurcation and its potential correlation to atherogenesis. *in progress* .
19. Bharadvaj, B.K., Mabon, R.F., Giddens, D.P. (1982) Steady flow in a model of the human carotid bifurcation. Part II--laser- Doppler anemometer measurements. *J Biomech* **15**, 363-78.
20. Bharadvaj, B.K., Mabon, R.F., Giddens, D.P. (1982) Steady flow in a model of the human carotid bifurcation. Part I--flow visualization. *J Biomech* **15**, 349-62.
21. He, X., Ku, D.N., Moore, J.E., Jr. (1993) Simple calculation of the velocity profiles for pulsatile flow in a blood vessel using Mathematica [published erratum appears in Ann Biomed Eng 1993 Sep-Oct;21(5):557-8]. *Ann Biomed Eng* **21**, 45-9.
22. Ku, D.N., Giddens, D.P., Zarins, C.K., Glagov, S. (1985) Pulsatile flow and atherosclerosis in the human carotid bifurcation. Positive correlation between plaque location and low oscillating shear stress. *Arteriosclerosis* **5**, 293-302.
23. Ross, R. (1999) Atherosclerosis--an inflammatory disease. *N Engl J Med* **340**, 115-26.
24. Ku, D. (1997) Blood Flow in Arteries. *Annual Review of Fluid Mechanics* **32**, 346-384.
25. Malek, A.M., Alper, S.L., Izumo, S. (1999) Hemodynamic shear stress and its role in atherosclerosis. *Jama* **282**, 2035-42.
26. Bao, X., Lu, C., Frangos, J.A. (1999) Temporal gradient in shear but not steady shear stress induces PDGF-A and MCP-1 expression in endothelial cells: role of NO, NF kappa B, and egr-1. *Arterioscler Thromb Vasc Biol* **19**, 996-1003.

IV.8. Figures

IV.8.1. Figure Captions

Fig 1. Ideal model of the carotid bifurcation used for fluid-structure interaction simulations showing boundary conditions imposed on arterial wall (see text for description of fluid boundary conditions). Due to symmetry, a half model of the carotid bifurcation was utilized. "P" represents the inner surfaces, where the FSI (fluid-structure interaction) boundary condition was applied. The solid arrows represent an applied axial strain of 10%. Comparisons in wall shear stress are conducted along 'line 1' labeled above which spans the entire length (along the normalized coordinate variable *s*) of the common-internal wall, including the carotid bulb.

Fig 2. Pressure (top panel) and flow rate boundary conditions on the fluid domain representing two states: 72 bpm (middle panel) and 108 bpm (lower panel) as obtained from the 1D arterial tree lumped parameter model of Ozawa et. al.(2001). Labeled points

for comparison are: accelerative (A), peak flow (B) and decelerative (C) phase of systole as well as the point of lowest flow rate (D).

Fig 3. Finite element meshes used for the solid (a) and fluid (b) domains.

Fig 4. Wall shear stress (WSS) plots averaged over the entire cardiac cycle: 72 bpm (above); 108 bpm (below).

Fig 5. Wall shear stress (WSS) along the wall of the common-internal carotid (along line 1 of Figure 1) at different time points (A,B,C, and D as identified in Figure 2). Top panel 72 bpm; bottom panel 108 bpm.

Fig 6. Oscillatory shear index (OSI) plots: 72 bpm (above); 108 bpm (below).

Fig 7. Maximum wall shear stress temporal gradient (WSSTG): 72 bpm (above) 108 bpm (below). 'dt' refers to the time step with which the simulation was run and 'sf' refers to the saving frequency.

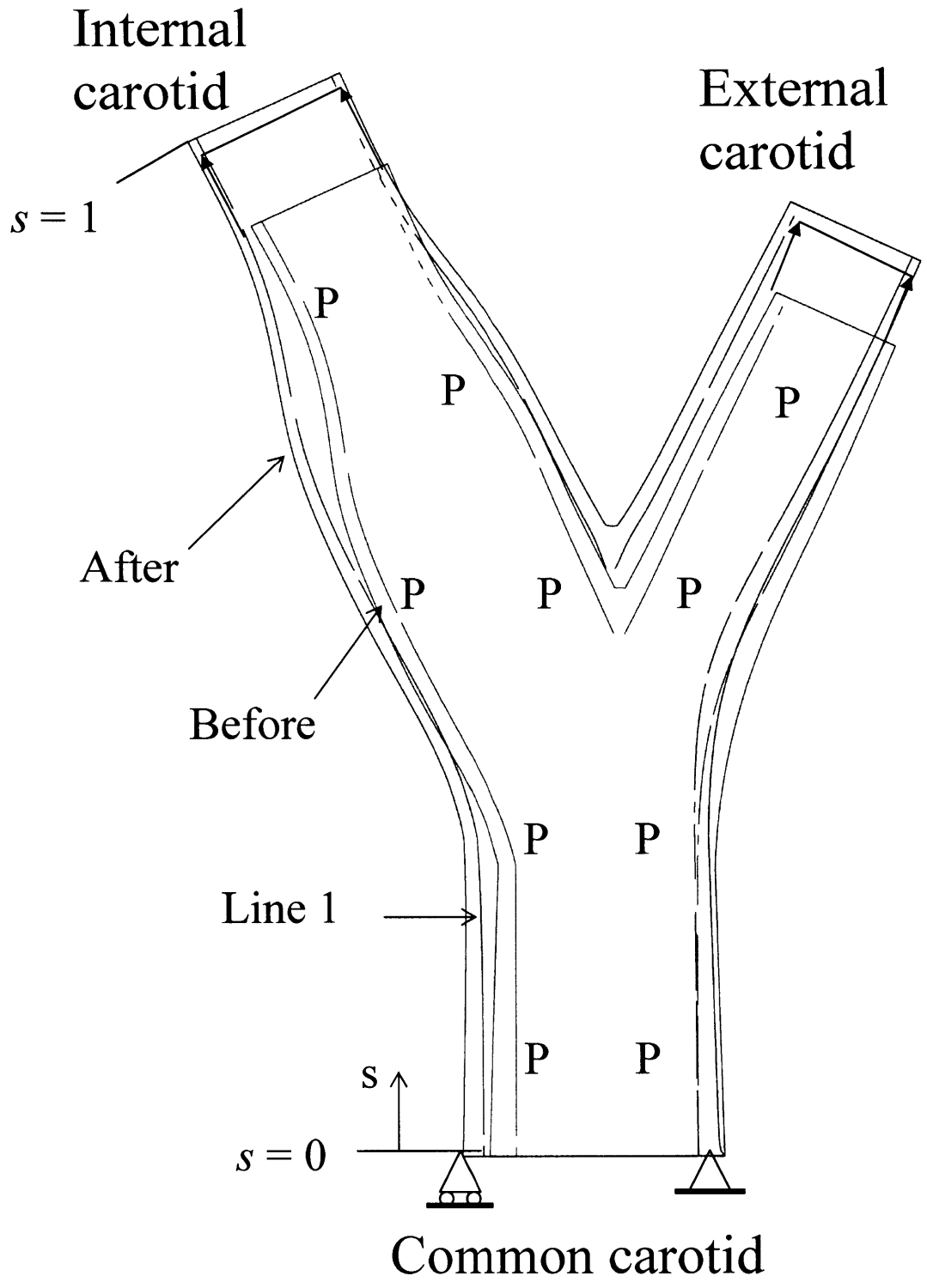
Internal carotid
External carotid
s = 1
P
P
P
After
P
P
P
Before
P
P
Line 1
P
P
s
s = 0
Common carotid

Figure 1

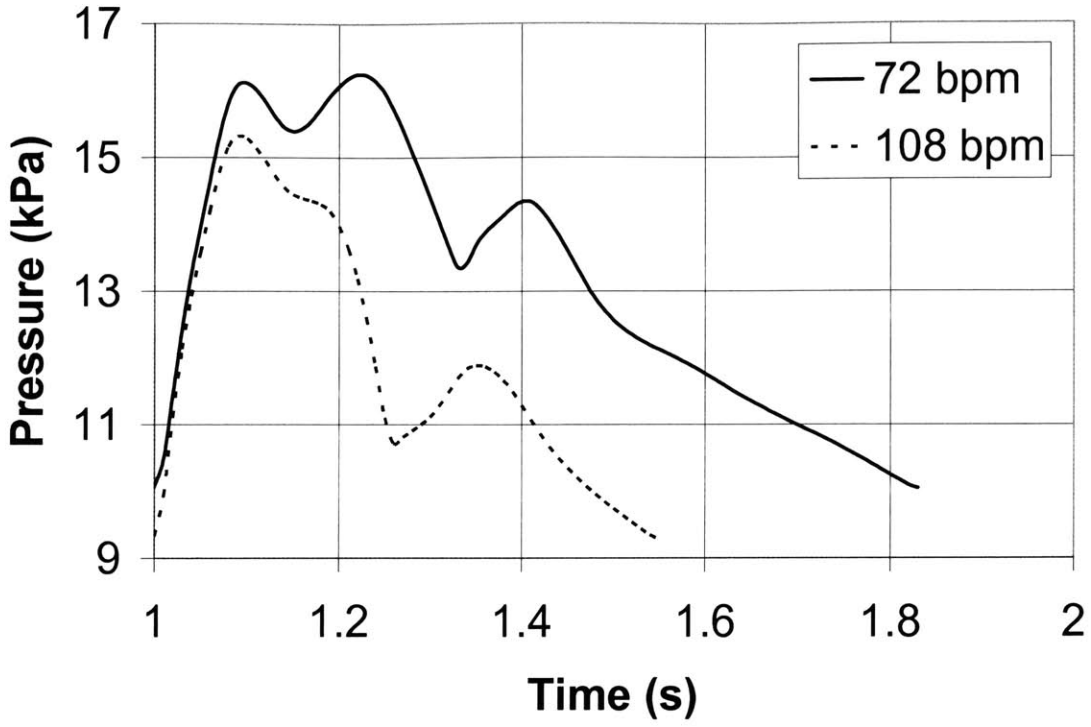

Figure 2 Top Panel

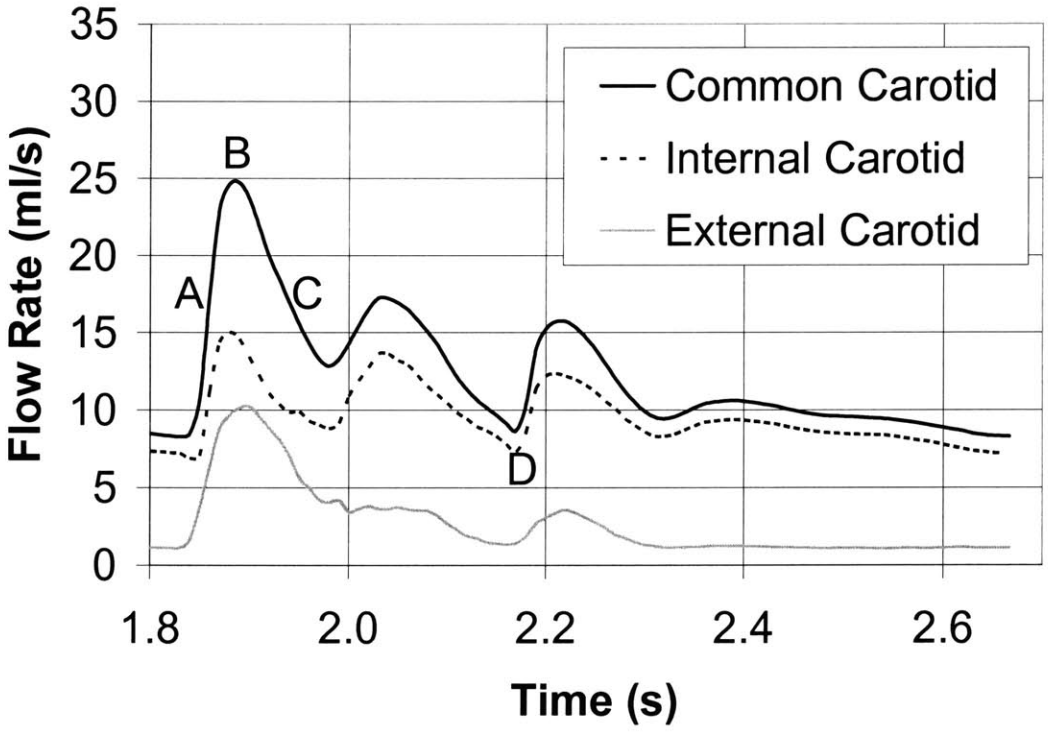

Figure 2 Middle Panel

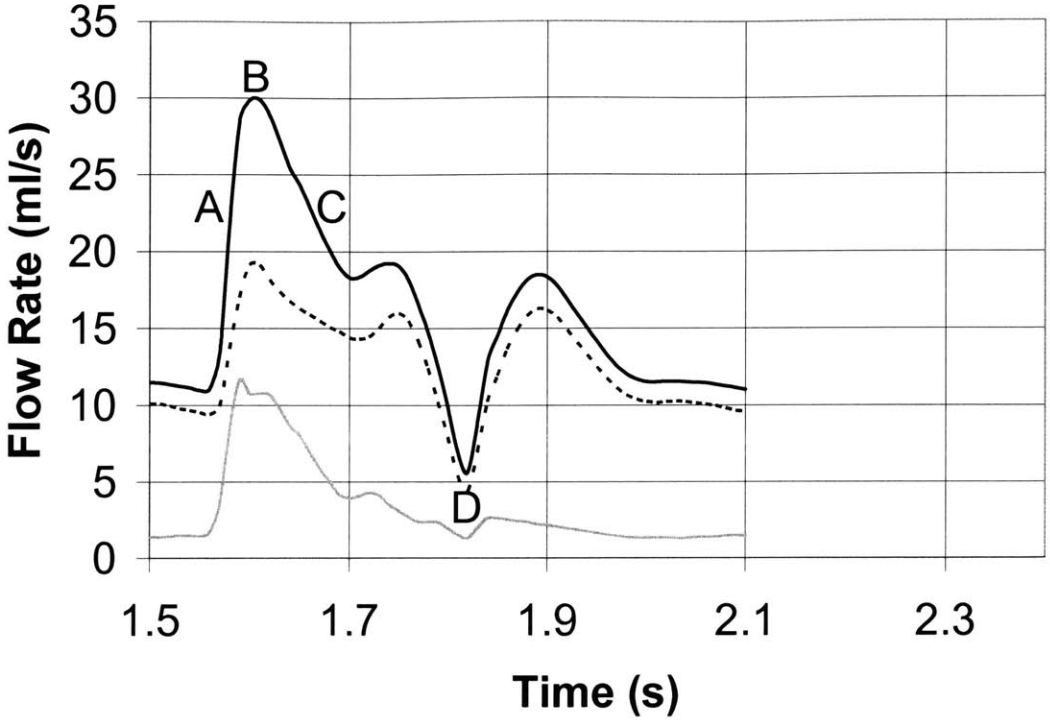

Figure 2 Lower Panel

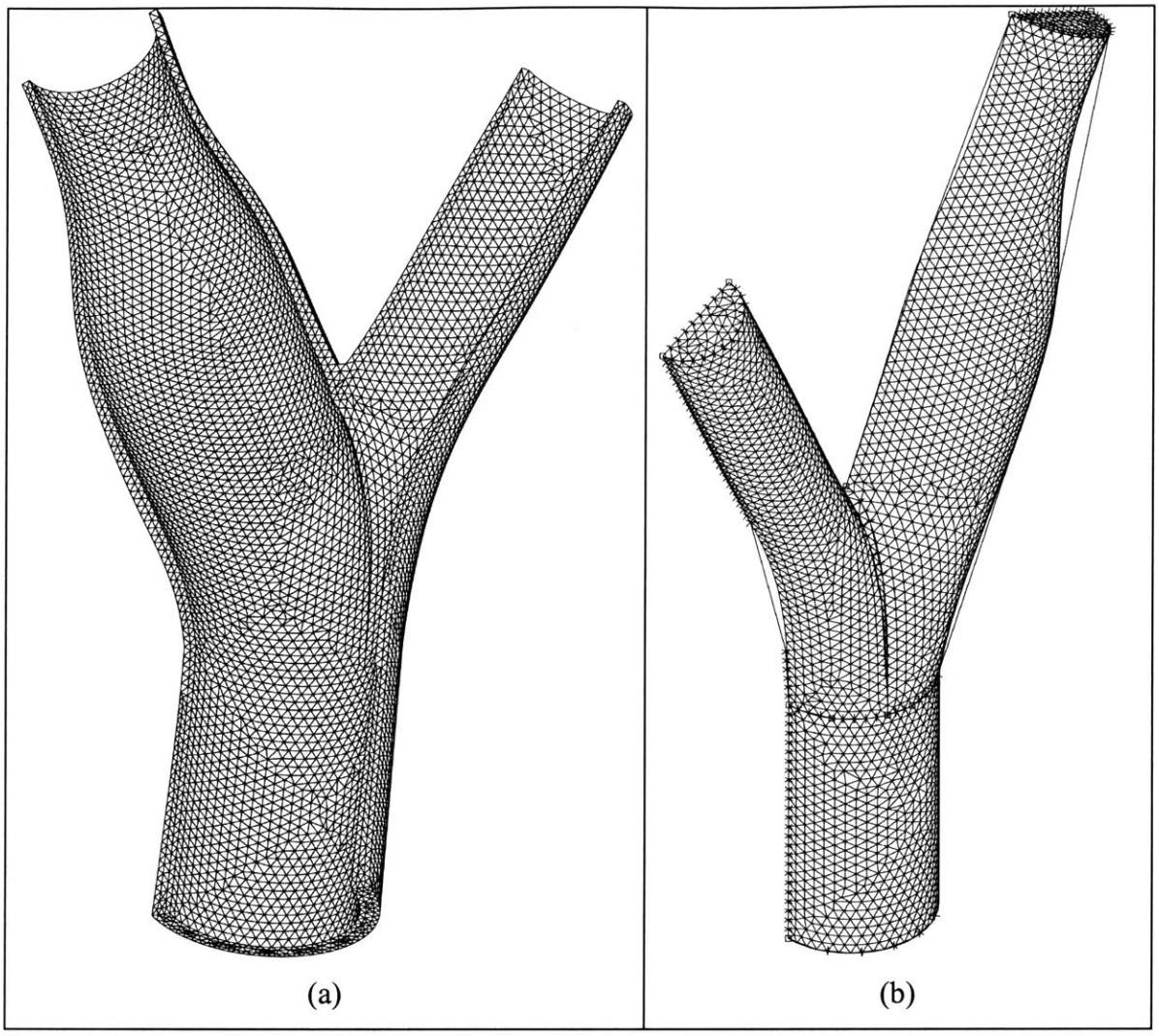

Figure 3

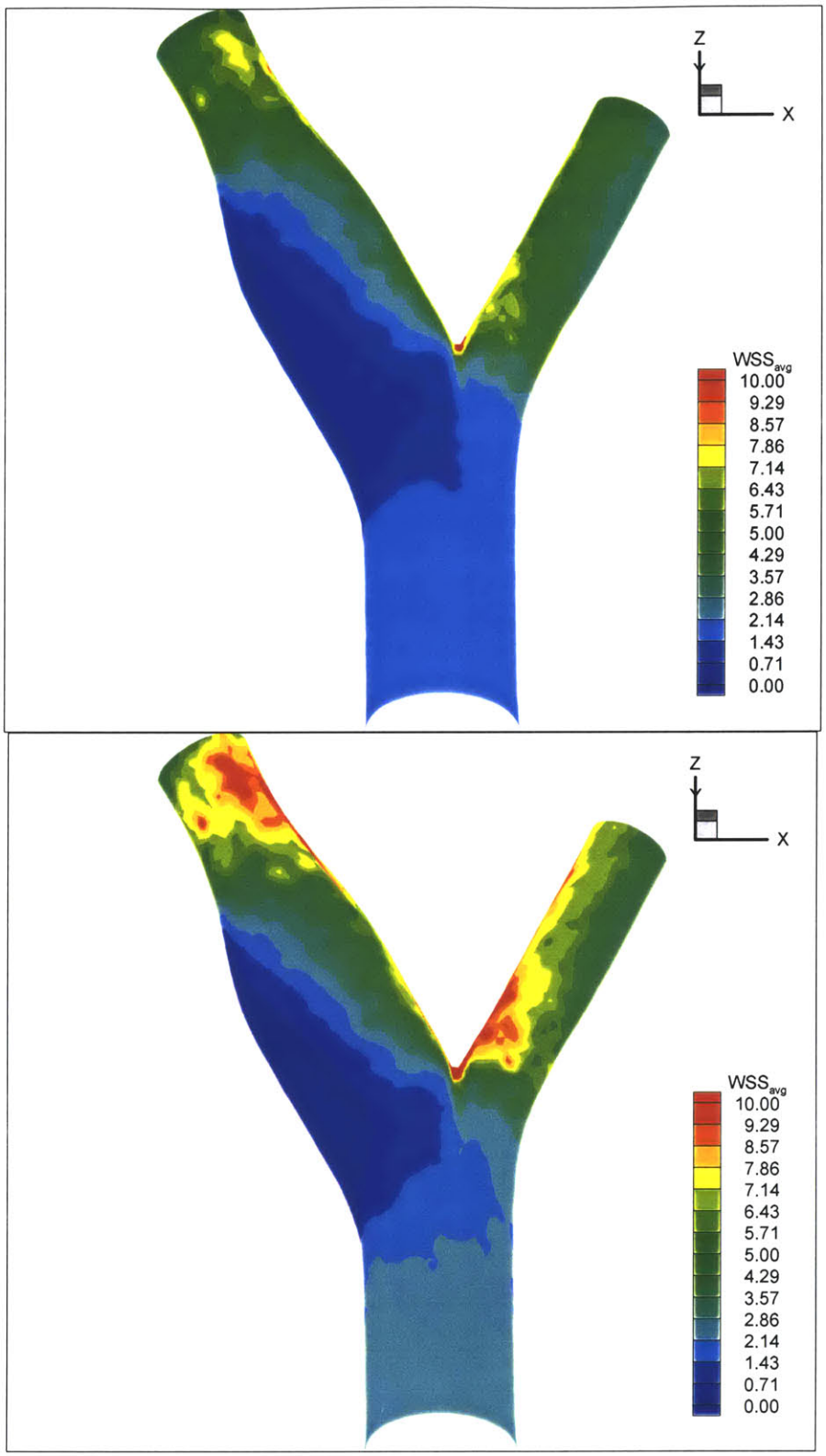
Z
X
WSS$_{avg}$
10.00
9.29
8.57
7.86
7.14
6.43
5.71
5.00
4.29
3.57
2.86
2.14
1.43
0.71
0.00
Z
X
WSS$_{avg}$
10.00
9.29
8.57
7.86
7.14
6.43
5.71
5.00
4.29
3.57
2.86
2.14
1.43
0.71
0.00

Figure 4

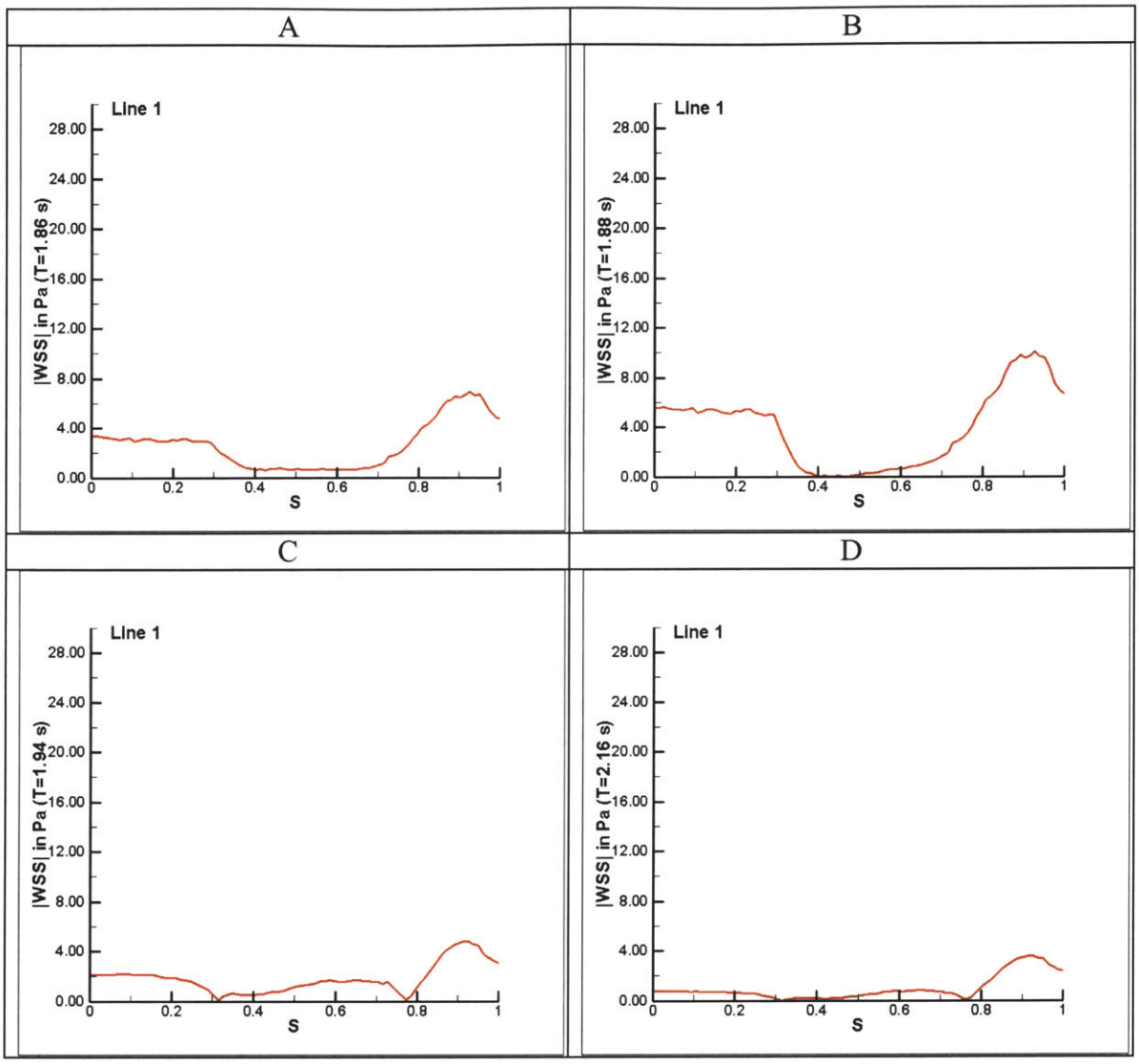

Figure 5 Top Panel

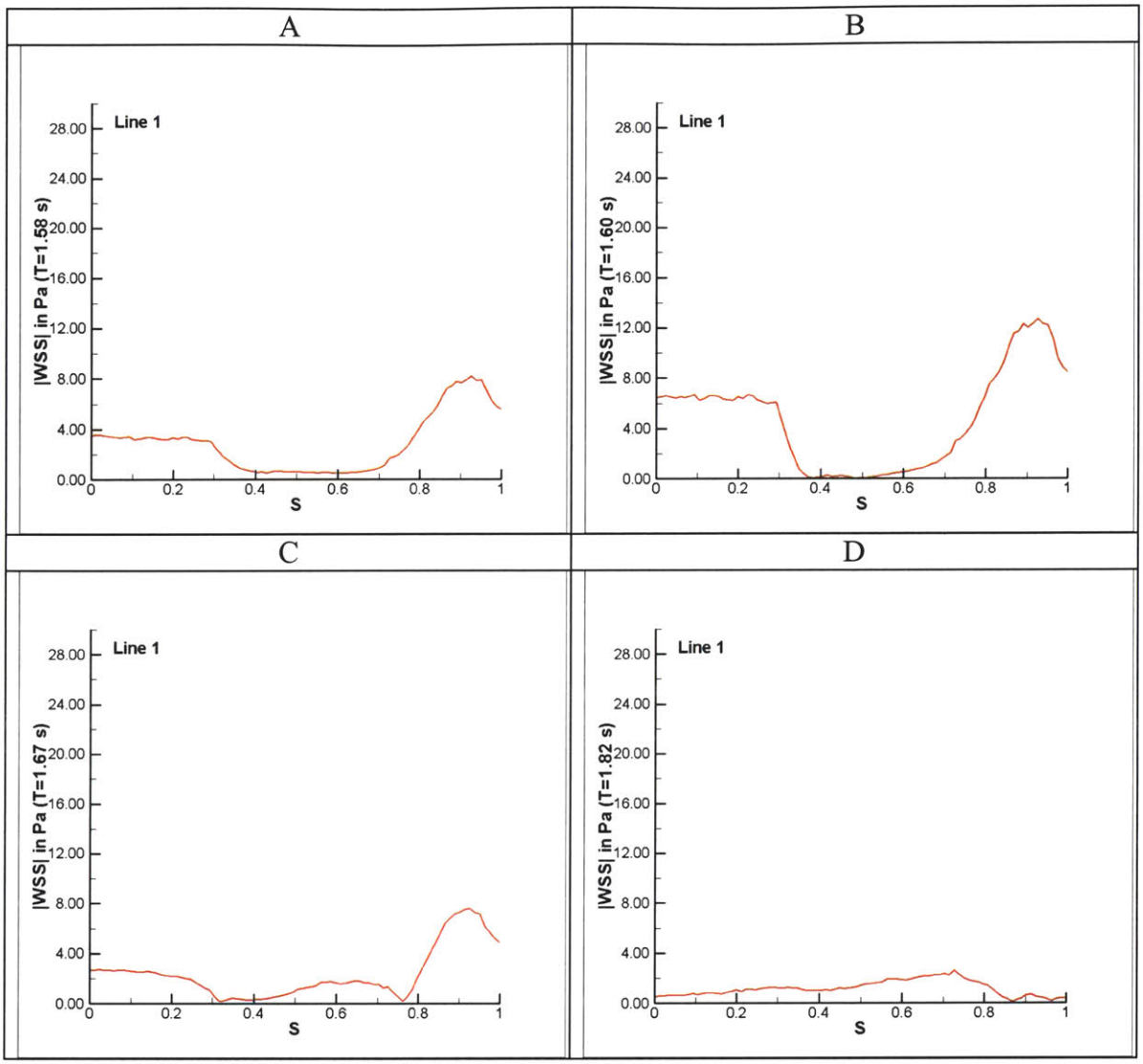

Figure 5 Bottom Panel

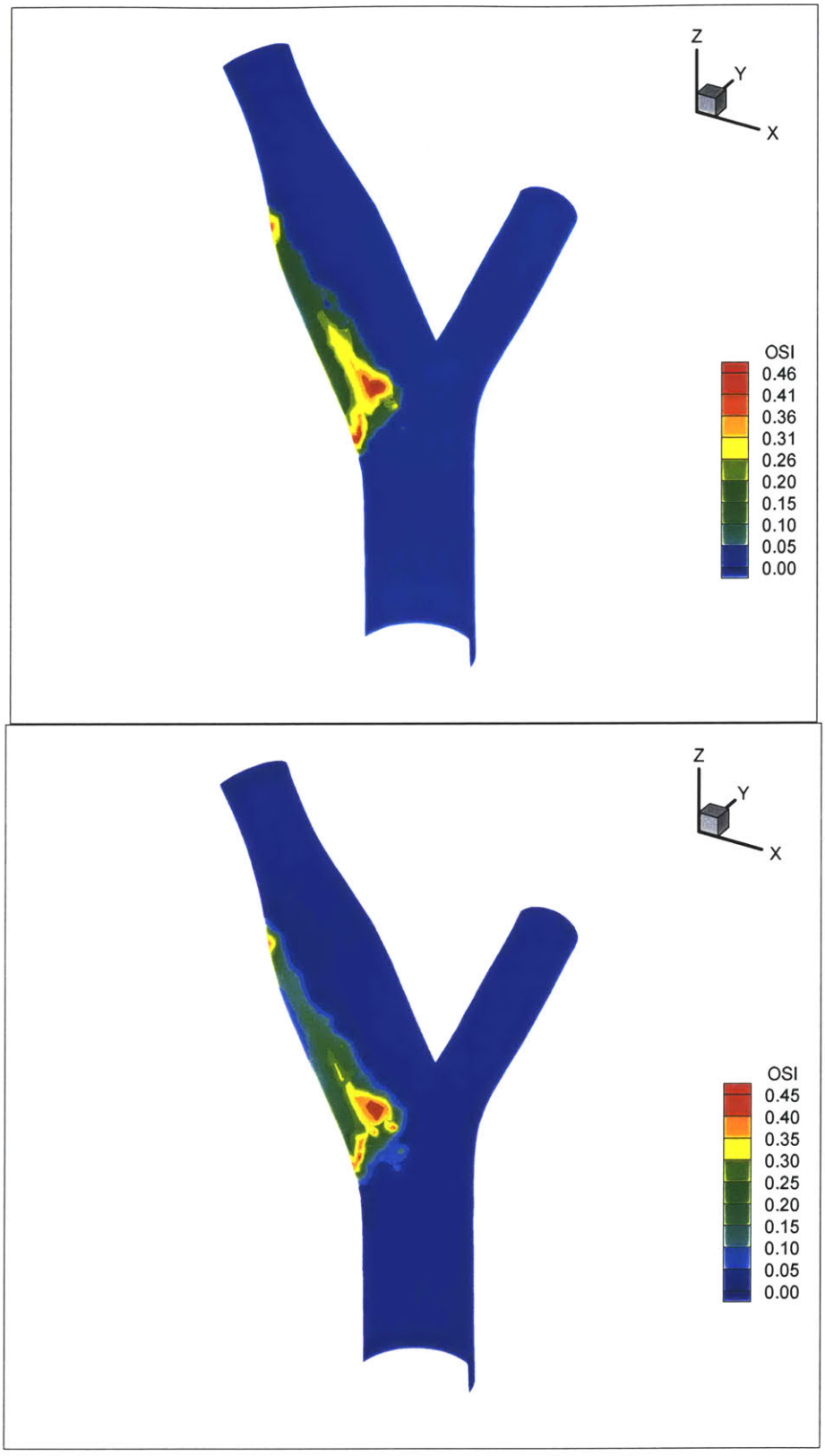
Z
Y
X
OSI
0.46
0.41
0.36
0.31
0.26
0.20
0.15
0.10
0.05
0.00
Z
Y
X
OSI
0.45
0.40
0.35
0.30
0.25
0.20
0.15
0.10
0.05
0.00

Figure 6

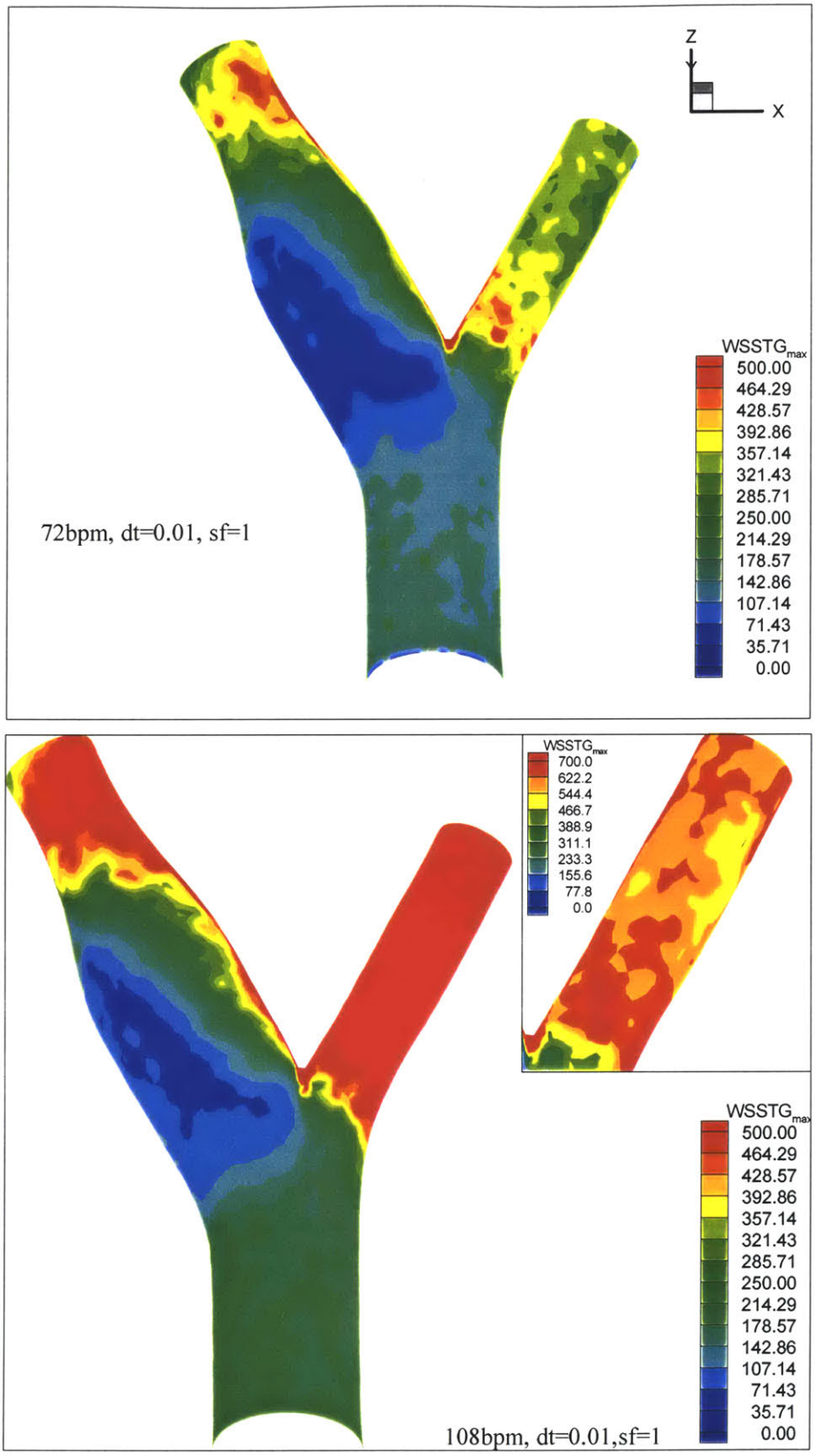
Z
X
WSSTG$_{max}$
500.00
464.29
428.57
392.86
357.14
321.43
285.71
250.00
214.29
178.57
142.86
107.14
71.43
35.71
0.00
72bpm, dt=0.01, sf=1
WSSTG$_{max}$
700.0
622.2
544.4
466.7
388.9
311.1
233.3
155.6
77.8
0.0
WSSTG$_{max}$
500.00
464.29
428.57
392.86
357.14
321.43
285.71
250.00
214.29
178.57
142.86
107.14
71.43
35.71
0.00
108bpm, dt=0.01,sf=1

Figure 7

V. A Numerical Study of Carotid Artery Wall and Fluid Mechanics based on *in vivo* Magnetic Resonance Images of Healthy Volunteers

V.1. Abstract

Computational finite element models (FEM) of the fluid/solid mechanics and interactions are performed based on *in vivo* MRI measurements of structural anatomy and ultrasound measurements of flow boundary conditions in healthy human carotid bifurcations using a commercial FEM package (ADINA, Watertown, MA). Localized separated flow regions are observed, especially near the outer wall of the internal carotid (the carotid bulb), in response to the localized abrupt changes in the curvature and cross-sectional area of the artery wall. The oscillation and low mean value of wall shear stress in these regions has been widely correlated to atherogenesis and late stage atherosclerotic inflammation. Localized high cyclic strains (which have been implicated in the stimulation of endothelial and smooth muscle cells) and high maximum wall shear stress temporal gradients (which are related to the expression of atherogenesis-related genes in endothelial cells) are observed at the flow divider and along the outside wall of the external carotid, both common sites of early inflammation. These observations provide yet further evidence that arterial atherosclerosis cannot be attributed to a single mechanical factor.

A comparison in fluid mechanic parameters of interest is made for one normal volunteer with and without fluid-structure interaction analysis, confirming that the incorporation of distensible walls on the fluid mechanic parameters of interest, with the exception of oscillatory shear index, is negligible everywhere other than at the flow divider.

Keywords: Atherosclerosis, cyclic strain, finite element analysis, wall shear stress, carotid bifurcation.

V.2. Introduction

There is a long standing hypothesis that correlates fluid dynamic forces and atherosclerotic disease. Many analytical, numerical and experimental studies have been conducted. Much of what inspired these studies is the observation that atherosclerotic disease is focal, typically occurring at sites of complex hemodynamics. These include arterial bifurcations, junctions and/or regions of high curvature.

Fry [1, 2] was the first to postulate that high wall shear stresses (WSS) would cause damage to the arterial wall; endothelial disruption or denudation could lead to atherosclerosis. Since then, however, it has become widely accepted that low or oscillatory shear stress rather than high contribute to atherogenesis [3-5]. Previous studies have shown that regions of low or oscillatory shear stress cause monocyte adhesion to the endothelial wall, an early stage in atherogenesis of the disease. Low shear stress leads to the expression of VCAM-1, a monocyte adhesion molecule [6], increased and prolonged NF-kappa B activity, a regulator of some endothelial cell adhesion molecules [7] and a reduction in NO release (augmented levels inhibit monocyte adhesion) [8, 9].

Wall shear stress temporal gradient (WSSTG) has also been related to the expression of atherogenesis-related genes in endothelial cells (ECs). Bao et.al. [10] have found that the temporal gradient in shear but not steady shear stimulates the expression of monocyte chemoattractant protein-1 (MCP-1), a potent chemotactic agent for monocytes, and platelet-derived growth factor A (PDGF-A), a potent mitogen and chemotactic agent for smooth muscle cells. Higher values of WSSTG are thus likely to increase the atherogenicity of ECs.

In addition to fluid shear stress, mechanical cyclic strain may play a role in atherosclerosis. Accumulating evidence demonstrates that cyclic strain affects endothelial (ECs) and vascular smooth muscle cells (SMCs). Monocyte chemoattractant protein-1 (MCP-1), significant for its involvement in monocyte recruitment into the arterial wall and atherosclerotic lesions [11] is synthesized by both ECs and vascular SMCs subjected

to mechanical deformation. MCP-1 mRNA expression in rat aortic SMCs has been shown to increase *in vitro* in response to mechanical deformation as well as *in vivo* in hypertensive rats [12, 13]. ECs have also been shown to exhibit similar gene expression patterns in response to cyclic strain [14-16].

Cyclic strain has also been shown to have numerous other effects on endothelial and smooth muscle cells. It stimulates vascular SMCs to release fibroblast growth factor-2 (FGF-2) in culture [17] which plays a role in early SMC migratory and proliferative responses following arterial injury [18] and has mitogenic effects on ECs and SMCs [19-21]. Additionally, Lee et. al., [22] have shown that versican, a vascular SMC proteoglycan that accumulates during atherosclerosis [23] and binds low-density lipoprotein cholesterol (LDLs) is induced by cyclic strain. Cyclic strain has also been shown to increase EC proliferation as demonstrated by Li et. al. [24]. EC mitosis has frequently been implicated in increasing the permeability of the arterial wall. Weinbaum et. al. [25] were the first to propose the "leaky cell junction hypothesis" in which transient pores resulting from "leaky" junctions in cell turnover provide the primary transendothelial pathway for LDLs. Experimentally, it has been shown that aortic ECs in mitosis indeed exhibit enhanced macromolecular permeability [26-28]. Since cyclic strain plays a role in EC mitosis, it is possible that there exists a correlation between high cyclic strain levels and enhanced macromolecular permeability, in turn leading to atherosclerotic inflammation. This is further supported by the work of Tropea et al. [29], who have shown that reduction of aortic wall motion (using a wrap) in the rabbit inhibits experimentally induced atherosclerosis.

A major goal of this present study is thus to validate the hypothesis that low or oscillatory shear and high cyclic strain correlates with known inflammation sites in the carotid bifurcation. This is done using solid and fluid (and coupled solid-fluid) 3D computational finite element (FEM) analyses based on realistic flow profiles obtained with the aid of ultrasound measurements and geometries by input of actual data gathered from *in vivo* magnetic resonance images.

V.3. Techniques Employed

Three healthy volunteers, referred to as NV1, NV2 and NV4 (ages 24-30) were chosen for this study (a fourth volunteer, NV3, was not available for ultrasound flow measurements and was thus omitted). The procedure for the processing of each normal volunteer's data is composed of several stages: MR (magnetic resonance) imaging, edge detection, lofting, flow profile generation and finally, finite element analysis. Acquisition of MR geometry is achieved using a surface coil that matches the jawline just above the carotid bifurcation. The edge detection protocol reads the geometry MR data to generate a series of 2D slices. The 3D vascular structure is reconstructed using a solid modeling software, by lofting across the 2D cross-sectional structures of each level of the carotid bifurcation. The geometry, velocity at the inlet (common carotid), and velocity at the outlet (internal carotid) files (from ultrasound measurements) are then imported into the FEM software to simulate the fluid dynamics and wall mechanics of *in vivo* data. An overall schematic of this process is illustrated in figure 1. Each step is described in more detail below.

V.3.1. Magentic Resonance Imaging

The 2D MR images are obtained using a Siemens Sonata 1.5 Tesla system at the Massachusetts General Hospital NMR Center. The surface coil, attached at the jaw where the carotid bifurcation is located, yields an in-plane resolution (lateral voxel dimension) of approximately 0.39 mm. The slice thickness (voxel height) is set to 2mm. 20 slices (2 cm below to 2 cm above the carotid bifurcation) are acquired using a spin-echo sequence over the course of 20 cardiac cycles. Image acquisition is gated to the cardiac cycle using the ECG. The surface area of the images is 256 by 256 pixels. The resulting vessel diameter for healthy subjects is 20 - 30 pixels at the common carotid level and the wall thickness is 2 - 3 pixels.

V.3.2. Extraction of Inner and Outer Wall curves

This is a two step process, developed originally for edge detection of ultrasound images throughout the carotid bifurcation [30]. Step 1 consists of a variational functional

minimization which jointly estimates the desired vessel edge field and smoothes the frame in an anisotropic, directionally sensitive manner. The resulting edge field and smoothed field estimates greatly enhance arterial structure visualization. Step 2 consists of vessel contour extraction from the edge field estimate by using standard active contours, or *snakes* [31].

V.3.3 Lofting to create 3D geometries

The curves resulting from the method described above are transferred to Solidworks (SolidWorks Corporation, Concord, MA), a solid modeling software, where a base loft function interpolates across the 2D cross-sectional structures of each level of carotid bifurcation in order to yield 3D structures. The solid that results from interpolating across the outer contours produces the external 3D solid body, while the 3D structure that results from interpolating across the inner contours produces the 3D fluid volume. Next, the fluid volume is subtracted from the external volume, hollowing out the 3D outer wall solid body and yielding the arterial wall 3D solid structure. Figure 2 depicts the entire set of fluid and wall geometries for each volunteer.

V.3.4. Flow Profile Generation

Next, the obtained geometric model is imported into the FEM software, where a mesh is constructed that matches the vessel geometry, and the nodes on the inlet plane to the carotid bifurcation (common carotid), and those of one of the outlet planes to the carotid bifurcation (internal carotid), are extracted. The coordinates of these nodes are entered as arguments into a function [32] that generates a fully developed Womersley-type flow based on the ultrasound centerline velocity measurements. The resulting flow rate waveforms are illustrated in figure 3 for the rigid-walled simulations. Flow rates in the external carotid artery are computed by subtracting the internal carotid flow rates from the common carotid flow rate to ensure mass conservation. Measured flow rates in the external carotid artery were not used since, distal to the bifurcation where the domain of the MR generated image ends and the velocity boundary conditions need to be applied, several smaller vessels that are difficult to image have branched off from the external carotid [33]. Note that this procedure overestimates the flow in the external carotid artery.

This has been previously shown [34], however, to have a minimal effect on hemodynamics in the carotid bulb, the region of most relevance to atherogenesis, but could influence the details elsewhere, particularly in the external carotid.

V.3.5. Finite Element Analysis

The simulations employ a finite element analysis (ADINA, version 7.4, Automatic Dynamic Incremental Nonlinear Analysis, Watertown, MA) and incorporate a non-linear, isotropic, hyperelastic model for the arterial wall. Blood is treated as an incompressible, Newtonian fluid (an assumption that has repeatedly been shown to hold well for large arteries [35, 36], where shear rates generally exceed $100\ s^{-1}$) and the flow assumed laminar.

The arterial solid response is modeled using the standard Lagrangian formulation for large displacements and large strains [37]. An isotropic form of the strain energy density function for the (nearly) incompressible artery wall is specified as [38]:

$$W = \frac{a}{b}\left(e^{\frac{b}{2}(I_1-3)} - 1 \right) \tag{4}$$

where a and b are elastic constants that reflect the elastic properties and tissue composition; I_1 is the first invariant of the strain tensor. In the Taylor series expansion, a has the significance of the elastic modulus. This exponential form is appropriate for arterial mechanics since it portrays the well-known strain-stiffening behavior of collagen. Continuity and the full Navier-Stokes equations are solved for the fluid. No-slip boundary conditions are imposed at the walls.

Even though ADINA is capable of performing fully coupled, three dimensional, non-linear Fluid-Structure Interaction (FSI) analyses, most of the solutions presented here are of the uncoupled solid and fluid domains. Fluid-structure interaction analysis is clearly important when large scale motions of the arteries are present that significantly impact the flow field, as in studies of arterial collapse when largely obstructive stenoses are

present [39, 40] or where physiologic movement of blood vessels (e.g. coronary arteries) during the cardiac cycle affects blood flow patterns significantly [41]. In the carotid bifurcation, even though the motions due to arterial wall motion are relatively small, the effect of wall compliance has been found to have a locally significant effect (up to 25% difference in wall shear stress) at the divider wall [42]. In order to investigate this effect using an *in vivo* geometry, we include a comparison for a single volunteer (NV2) with and without distensible walls.

For fluid domains with moving boundaries, it is necessary to utilize the Arbitrary Lagrangian Eulerian (ALE) formulation of the momentum equation [43]. Full coupling between the fluid and solid domains requires that displacement continuity and force equilibrium are satisfied at the fluid-structure interface. In ADINA, this was done iteratively between the fluid and solid solvers at each time step until sufficient convergence had been reached.

The maximum pressure drop along a healthy carotid bifurcation (primarily due to inertial effects) is on the order of 700 *Pa*, or no more than ~ 5% of the systolic pressure [44]. This, in addition to the fact that the arterial wall behaves in a *pseudoelastic* manner [45] (i.e. viscoelasticity of the arterial wall does not need to be considered), enabled us to perform static inflation of the arterial walls analyzed to gain insight into the strain levels within the bifurcation. An axial stretch of 10% was applied to the solid domain (the MRI reconstructed models were first shrunk uniformly by 10% to simulate the ex-vivo load-free state; this compensated for the distensibility due to blood pressure as well as the axial pre-stretch) as measured *in situ* by Delfino [46]. The pressure was ramped incrementally from zero *Pa* to diastole to systole. The output was stored only at systole and diastole and the Von Mises [47] cyclic strain computed as the difference between these two states.

The rigid-walled fluid simulations were solved separately in two steps, using the fully developed Womersley-type flow velocity boundary conditions described earlier. In the first step, a Womersley-type flow corresponding to the centerline fluid velocity in the

common carotid and internal carotid arteries was imposed on the respective arteries, while the external carotid left at zero traction. Flow profiles at the output of the external carotid artery at the end of this step were then used as an input boundary condition to the second computational step, while retaining the Womersley flow at the common carotid and imposing a traction-free boundary condition at the internal carotid. This second step was then considered the final computed solution as in Perktold et. al. [35]. To achieve a periodic solution, the flow computation was allowed to run over two heart cycles, saving only the second one.

Free meshing was performed due to the complexity of the geometries involved (figure 4). The element size used for the solid and fluid elements was 0.4 mm (NV1 and NV4 solid simulations used a 0.45 mm mesh), which provided 2-3 solid elements across the wall and 15-20 elements across the common carotid. 11 node quadratic elements were used for the wall domain, while 4 node linear elements were used for the fluid domain. The mesh sizes used for every volunteer in each domain, artery dimensions as well as the applied systolic and diastolic pressures are summarized in table 1.

All computations were performed using a SGI Origin 2000 computer equipped with 4 processors and 6 GB of RAM. Solution times varied between 12 and 24 hours.

Volunteer Number	Pressure Syst/Dias (*mmHg*)	Solid Elements; Nodes	Fluid Elements; Nodes	CCA Diameter (*mm*)	ICA Diameter (*mm*)	ECA Diameter (*mm*)
1	112/58	75076; 199049	123525; 24010	7.2	6.0	4.5
2	100/58	124992; 326610	83939; 17267	5.9	4.5	3.9
4	105/80	74275; 197258	116006; 23022	7.0	5.9	4.6

Table 1 Finite element mesh details and artery dimensions of each of the normal volunteers investigated in this study. See figure 4 for the finite element meshes. CCA, ICA and ECA represent common carotid artery, internal carotid artery and external carotid artery, respectively.

V.4. Results

V.4.1. Wall Shear Stress (WSS)

To quantify the magnitude of the wall shear stress vector [4], average WSS bandplots over the cycle are presented in figure 5 for each normal volunteer. To emphasize the regions of low wall shear stress, the plots are made using a logarithmic scale, with the shades of blue representing the entire range of WSS below 0.5 Pa. This is the level of WSS below which it is believed that an atherogenic phenotype is stimulated [48]. One striking similarity prevails between all three normal volunteer models: the largest continuous region of low WSS seems to exist in the carotid bulb, where late atherosclerotic inflammation develops [4]. A common feature between models NV2 and NV4 is the 'spot' of low WSS distal to the bifurcation at the inner wall of the external carotid artery (ECA), although they seem to result from different phenomena in each case. In NV4, the spot is part of a longer stripe that reaches all the way to the exit of the ECA and is a result of both the increase in area immediately downstream of the initial constriction in the ECA as well as the adverse pressure gradient associated with the boundary condition of flow reversal in the ECA. In NV2, the ECA hardly experiences any flow reversal and the decelerative gradient is substantially smaller than in NV4; the low WSS spot is a recirculation zone due to the sudden change in curvature.

An interesting feature is observed in NV1 and NV2. The low WSS patches in the common carotid are continuous with the low WSS region of the carotid bulb. The regions of low WSS coil around the common carotid. This pattern is absent in NV4.

The high WSS patterns are similar at the apex in all three cases: NV1, NV2 and NV4. In all three cases, the apex experiences WSS values between 6-10 Pa and there exists a very

small localized region of WSS above 10 Pa, which seems to be closer to the inner wall of the external carotid in all three cases. Values of WSS above 1.5 Pa induce endothelial quiescence and an atheroprotective gene expression profile [48].

V.4.2. OSI and WSS Maximum Temporal Gradient

Two other parameters that have been investigated for each Normal Volunteer are the oscillatory shear index (OSI) (figure 6) as defined by Ku et. al. [4] and the maximum WSS temporal gradient (figure 7) over the cycle. The OSI is a dimensionless measure that quantifies the time a particular wall region in the cycle experiences cross or reverse flow. The mean flow direction is defined as the temporal mean of the shear stress vector. For purely oscillatory flow, the OSI equals 0.5. The OSI does not take into account the magnitude of the shear stress vectors, merely the directions. Maximum WSS temporal gradient (Max WSSTG) is the maximum value of the time-derivative in WSS calculated between every two consecutive time points during the cycle.

A common feature among all geometries is that the areas of high OSI lie within the areas of low WSS; this confirms that these are also areas of flow reversal. In NV1, flow is reversal is observed mainly along the external wall of the internal-common carotid adjoining wall. High OSI values of up to 0.45 are found immediately proximal to the carotid bulb. In NV2 a helical pattern of high OSI wrapping around the CCA appears with high OSI values occurring right at the center of the carotid bulb. The regions of high OSI, on the other hand occur mostly away from the ICA and the carotid bulb in NV4; the entire ECA experiences levels of OSI above 0.1. In contrast with NV1 and NV2, the external adjoining wall of the ECA and CCA in NV4 experiences some of the highest levels of OSI in the model.

The models predict levels of maximum WSSTG below approximately 250 Pa/s in all areas but the ECA. In NV1 and NV4, levels in the ECA readily exceed 500 Pa/s. The highest levels of maximum WSSTG occur at the flow divider in all cases, reaching as high as 1000 Pa/s. The adjoining wall of the ECA and CCA all display WSSTG of 300 Pa/s and above, and as high as 700 Pa/s in NV4.

V.4.3. Pressure Drop

Pressure drops across the carotid bifurcation are compared during the decelerative phase of systole in each case. This time period experiences some of the largest adverse pressure gradients throughout the cycle (results not shown). Pressure drop (primarily due to inertial effects) of 500-700 Pa were recorded at this time step, which are < 5 % of the applied systolic pressure. These results support our approach of computing the arterial wall stresses and deformation separately in a quasi-static inflation.

V.4.4. Comparison to the case with distensible walls

As mentioned in the methods section, fluid-structure interaction simulations were not performed for all the simulations but were only carried out for one model (NV2) to verify that the effects of distensible walls indeed do not significantly impact the fluid mechanical parameters of interest. Examination of the average WSS plots of NV2 and NV2 with distensible walls (figure 5) reveals that the patterns of low WSS, as depicted by the location of islands of low WSS and their magnitudes are similar, even when plotted on a logarithmic scale that exaggerates the differences substantially. Major differences (of up to 25%) are only seen at the carotid apex, consistent with the observations of Perktold and Rappitsch [42]. Only minor differences appear in the WSSTG plots as well, again with the greatest change in the immediate vicinity of the carotid apex.

Incorporating wall distensibility does, however, have a significant effect on the OSI (see figure 6). Even though the overall patterns are unchanged, several differences can be noted. With the incorporation of distensible walls, the OSI in the common carotid doubles at most locations. In the carotid bulb, even though the patterns are similar, the region of high oscillating flow is now separated into two islands of high OSI instead of one continuous region in the case with rigid walls. In the external carotid artery (internal and external walls), the regions of high OSI reduce in size.

V.4.5. Cyclic Strain

Figure 8 shows the cyclic strain bandplots at the interior face of the bifurcation (corresponding to strain experienced by the endothelium) for each NV studied. A common feature to all of them is that the levels of cyclic strain are highest at the apex (NV1: 14 %; NV2: 11 %; NV4: 6 %). A second area of high cyclic strain in all the geometries, although of smaller magnitude, is at the external-common adjoining wall (NV1: 11%, NV2: 9%, NV4: 5%). A region of elevated cyclic strain (12%) unique to NV1 appears between the ICA bulb and the apex. Another region of elevated cyclic strain (5%) is visible immediately proximal to the carotid bulb in NV4. NV4 also shows several patches of high cyclic strain in the common carotid artery which are absent in NV1 and NV2. In all the geometries (except the ECA of NV1), there are localized regions of high cyclic strain at the ending of the internal and external carotid arteries immediately proximal to where the 10% axial stretch boundary conditions are applied; these are likely artifacts resulting from the proximity of the applied loads.

V.5. Discussion

The carotid bulb is one of the first sites in the carotid bifurcation to develop late stage atherosclerotic inflammation [4, 46, 48, 49]. Our results in several individual geometries are consistent with those of previous investigators that show this to be a region of low WSS [4, 33]. We found the regions of flow separation (and low fluid shear stress) to be mostly observed at the outer wall of the internal-common junction (the carotid bulb). These regions (as well as late stage inflammation for the most part) are absent from the outer wall of the external-common junction in all the simulated volunteer models.

Flow separation at the carotid bulb is expected due to the abrupt change in curvature and the associated adverse pressure gradient along the outer wall. Also contributing to the tendency for separation is the increase in cross-sectional area, and the consequent increase in pressure, just distal to the bifurcation. High momentum fluid is incapable of instantaneously changing direction to accommodate the curvature. This region of separation is greatest during the decelerative phase of systole, when the fluid undergoes the largest reversal of momentum.

The coiling of the regions of low WSS around the common carotid and their joining pattern to the region of low WSS in the bulb as seen in NV1 and NV2 is remarkably similar to what is observed by Milner et. al. [33], who also investigated flow in models of geometries reconstructed from MRI. As in their study, this is likely caused by helical flow in the ICA, due to asymmetry and twist in the vessels, but it should be kept in mind that (at least in the case of NV1) the proximity of the boundary conditions to the lower part of the CCA may also contribute.

A low WSS area unique to NV4 and absent from similar carotid fluid mechanic simulations to date, both realistic and idealized, is found on the inner (divider) wall of the internal carotid artery, immediately distal to the bifurcation. This has traditionally been thought to be an area of elevated shear stress [4, 33, 35], but even in comparison with NV1 and NV2 herein, this region exhibits much lower WSS values (< 0.5 Pa vs. ~ 3 Pa). This is due to the expansion at that location on NV4 that is absent from the other two models.

Although these variations in flow pattern and magnitude of WSS seem to be primarily geometry dependent [33], flow conditions can also have a significant impact on the magnitudes of WSS and other integrated parameters over the cycle. We have previously shown [44] that changes of up to 100 % in WSS and WSSTG can occur due to modest changes in heart rate that can occur during the day.

The results also show that the carotid apex and adjoining wall of the external-common carotid exhibit two common features: high maximum WSSTG and high cyclic strain. These regions have been identified previously to be sites of early atherosclerotic inflammation [5, 49, 50]. High values of WSSTG have been related to the expression of atherogenesis-related genes in endothelial cells (ECs) [10] and high cyclic strain has been implicated in stimulation of endothelial and smooth muscle cells (SMC biological response to cyclic strain is similar to endothelial response – see Introduction). This suggests that more than one mechanical factor, rather than WSS alone, plays a role in

atherogenesis, confirming the theory that atherosclerosis is a multi-factorial disease. In interpreting these results, it should be recognized that the simulated values of WSSTG are overestimates of the in vivo case. Flow rates in the external carotid are overestimated due to neglecting the flow out of smaller, adjacent vessels that could not be imaged (see methods section), resulting in higher than realistic WSS (and subsequently WSSTG) in that branch.

Another point of concern with regard to the accuracy of our wall simulations is residual stress. Previous researchers [38, 51, 52] have shown that residual stresses can have significant effects on the stress (and strain) field in an artery. When cut, an excised arterial segment opens, suggesting that in the closed configuration, the artery is not at a stress free state. However, it is most likely the dynamic component of strain that elicits cellular response since resident cells will eventually accommodate to the mean strain level of the wall locally. It has already been shown that bio-modeling and remodeling can both be governed by strain perturbations [53], rather than absolute strain levels. Furthermore, endothelial cells do not support any of the load on the arterial wall [54], and likely adapt to the mean strain level, responding only to changes in the dynamic strain levels. Even though the absolute magnitude of the stresses (and strains) in an artery is changed by the inclusion of residual stresses, the strain amplitude remains unchanged in the case of a cylindrical artery (see figure 9). We extrapolate this result to the case of the bifurcations considered herein.

V. 6. Summary

Computational finite element models (FEM) of the fluid/solid mechanics and interactions were performed based on *in vivo* MRI measurements of structural anatomy and ultrasound measurements of flow boundary conditions in three healthy human carotid bifurcations in order to investigate the effect of mechanical variables on atherogenesis. Low wall shear stress and high oscillatory shear index correlated to a frequently observed site of late atherosclerotic inflammation, the carotid bulb. Other parameters, such as maximum wall shear stress temporal gradient and cyclic strain were also found to be

elevated at the carotid apex and the adjoining wall of the external-common carotid, both sites of early stage atherosclerosis. This adds to the notion that atherosclerosis is multi-factorial and should not be attributed to a single mechanical factor.

A comparison in fluid mechanic parameters of interest, made for one normal volunteer with and without fluid-structure interaction analysis, confirmed that the inclusion of distensible walls on the wall shear stress and maximum wall shear stress temporal gradient values is negligible everywhere except at the flow divider. Oscillatory shear index, a non-dimensional measure that quantifies the time a particular wall region in the cycle experiences cross or reverse flow, was strongly affected, however, by the inclusion of wall distensibility.

V.7. References

1. Fry, D.L. (1968) Acute vascular endothelial changes associated with increased blood velocity gradients. *Circ Res* **22**, 165-97.
2. Fry, D.L. (1969) Certain histological and chemical responses of the vascular interface to acutely induced mechanical stress in the aorta of the dog. *Circ Res* **24**, 93-108.
3. Caro, C.G., Fitz-Gerald, J.M., Schroter, R.C. (1971) Atheroma and arterial wall shear. Observation, correlation and proposal of a shear dependent mass transfer mechanism for atherogenesis. *Proc R Soc Lond B Biol Sci* **177**, 109-59.
4. Ku, D.N., Giddens, D.P., Zarins, C.K., Glagov, S. (1985) Pulsatile flow and atherosclerosis in the human carotid bifurcation. Positive correlation between plaque location and low oscillating shear stress. *Arteriosclerosis* **5**, 293-302.
5. Friedman, M.H., Hutchins, G.M., Bargeron, C.B., Deters, O.J., Mark, F.F. (1981) Correlation of human arterial morphology with hemodynamic measurements in arterial casts. *J Biomech Eng* **103**, 204-7.
6. Gonzales, R.S., Wick, T.M. (1996) Hemodynamic modulation of monocytic cell adherence to vascular endothelium. *Ann Biomed Eng* **24**, 382-93.
7. Mohan, S., Mohan, N., Sprague, E.A. (1997) Differential activation of NF-kappa B in human aortic endothelial cells conditioned to specific flow environments. *Am J Physiol* **273**, C572-8.
8. Tsao, P.S., Lewis, N.P., Alpert, S., Cooke, J.P. (1995) Exposure to shear stress alters endothelial adhesiveness. Role of nitric oxide. *Circulation* **92**, 3513-9.
9. Tsao, P.S., Buitrago, R., Chan, J.R., Cooke, J.P. (1996) Fluid flow inhibits endothelial adhesiveness. Nitric oxide and transcriptional regulation of VCAM-1. *Circulation* **94**, 1682-9.

10. Bao, X., Lu, C., Frangos, J.A. (1999) Temporal gradient in shear but not steady shear stress induces PDGF-A and MCP-1 expression in endothelial cells: role of NO, NF kappa B, and egr-1. *Arterioscler Thromb Vasc Biol* **19**, 996-1003.
11. Reape, T.J., Groot, P.H. (1999) Chemokines and atherosclerosis. *Atherosclerosis* **147**, 213-25.
12. Capers, Q., Alexander, R.W., Lou, P., De Leon, H., Wilcox, J.N., Ishizaka, N., Howard, A.B., Taylor, W.R. (1997) Monocyte chemoattractant protein-1 expression in aortic tissues of hypertensive rats. *Hypertension* **30**, 1397-402.
13. Jiang, M.J., Yu, Y.J., Chen, Y.L., Lee, Y.M., Hung, L.S. (1999) Cyclic strain stimulates monocyte chemotactic protein-1 mRNA expression in smooth muscle cells. *J Cell Biochem* **76**, 303-10.
14. Wang, D.L., Wung, B.S., Shyy, Y.J., Lin, C.F., Chao, Y.J., Usami, S., Chien, S. (1995) Mechanical strain induces monocyte chemotactic protein-1 gene expression in endothelial cells. Effects of mechanical strain on monocyte adhesion to endothelial cells. *Circ Res* **77**, 294-302.
15. Wung, B.S., Cheng, J.J., Chao, Y.J., Lin, J., Shyy, Y.J., Wang, D.L. (1996) Cyclical strain increases monocyte chemotactic protein-1 secretion in human endothelial cells. *Am J Physiol* **270**, H1462-8.
16. Wung, B.S., Cheng, J.J., Hsieh, H.J., Shyy, Y.J., Wang, D.L. (1997) Cyclic strain-induced monocyte chemotactic protein-1 gene expression in endothelial cells involves reactive oxygen species activation of activator protein 1. *Circ Res* **81**, 1-7.
17. Cheng, G.C., Briggs, W.H., Gerson, D.S., Libby, P., Grodzinsky, A.J., Gray, M.L., Lee, R.T. (1997) Mechanical strain tightly controls fibroblast growth factor-2 release from cultured human vascular smooth muscle cells. *Circ Res* **80**, 28-36.
18. Clowes, A.W., Reidy, M.A., Clowes, M.M. (1983) Mechanisms of stenosis after arterial injury. *Lab Invest* **49**, 208-15.
19. Jackson, C.L., Reidy, M.A. (1993) Basic fibroblast growth factor: its role in the control of smooth muscle cell migration. *Am J Pathol* **143**, 1024-31.
20. Lindner, V., Reidy, M.A. (1993) Expression of basic fibroblast growth factor and its receptor by smooth muscle cells and endothelium in injured rat arteries. An en face study. *Circ Res* **73**, 589-95.
21. Mason, I.J. (1994) The ins and outs of fibroblast growth factors. *Cell* **78**, 547-52.
22. Richard T. Lee, C.Y., Yajun Feng, Susan Potter-Perigo, William H. Briggs, Katherine T. Landschulz, Thomas G. Turi, John F. Thompson, Peter Libby, and Thomas N. Wight (2001) Mechanical Strain Induces Specific Changes in the Synthesis and Organization of Proteoglycans by Vascular Smooth Muscle Cells. *Journal of Biological Chemistry* .
23. Lemire, J.M., Braun, K.R., Maurel, P., Kaplan, E.D., Schwartz, S.M., Wight, T.N. (1999) Versican/PG-M isoforms in vascular smooth muscle cells. *Arterioscler Thromb Vasc Biol* **19**, 1630-9.
24. Li, G., Mills, I., Sumpio, B. (1994) Cyclic Strain Stimulates Endothelial Cell Proliferation: Characterization of Strain Requirements. *Endothelium* **2**, 177-81.
25. Weinbaum, S., Tzeghai, G., Ganatos, P., Pfeffer, R., Chien, S. (1985) Effect of cell turnover and leaky junctions on arterial macromolecular transport. *Am J Physiol* **248**, H945-60.

26. Lin, S.J., Jan, K.M., Schuessler, G., Weinbaum, S., Chien, S. (1988) Enhanced macromolecular permeability of aortic endothelial cells in association with mitosis [published erratum appears in Atherosclerosis 1989 Jul;78(1):87]. *Atherosclerosis* **73**, 223-32.
27. Lin, S.J., Jan, K.M., Weinbaum, S., Chien, S. (1989) Transendothelial transport of low density lipoprotein in association with cell mitosis in rat aorta. *Arteriosclerosis* **9**, 230-6.
28. Chien, S., Lin, S.J., Weinbaum, S., Lee, M.M., Jan, K.M. (1988) The role of arterial endothelial cell mitosis in macromolecular permeability. *Adv Exp Med Biol* **242**, 59-73.
29. Tropea, B.I., Schwarzacher, S.P., Chang, A., Asvar, C., Huie, P., Sibley, R.K., Zarins, C.K. (2000) Reduction of aortic wall motion inhibits hypertension-mediated experimental atherosclerosis. *Arterioscler Thromb Vasc Biol* **20**, 2127-33.
30. Chan, R. (2001) Non-invasive ultrasound monitoring of regional carotid wall structure and deformation in atherosclerosis. In *Health Sciences and Technology*MIT, Cambridge, MA.
31. Shah, J. (1996) A common framework for curve evolution, segmentation and anisotropic diffusion in IEEE Computer Society Conference on Computer Vision and Pattern Recognition, San Francisco, CA.
32. He, X., Ku, D.N., Moore, J.E., Jr. (1993) Simple calculation of the velocity profiles for pulsatile flow in a blood vessel using Mathematica [published erratum appears in Ann Biomed Eng 1993 Sep-Oct;21(5):557-8]. *Ann Biomed Eng* **21**, 45-9.
33. Milner, J.S., Moore, J.A., Rutt, B.K., Steinman, D.A. (1998) Hemodynamics of human carotid artery bifurcations: computational studies with models reconstructed from magnetic resonance imaging of normal subjects. *J Vasc Surg* **28**, 143-56.
34. Zhao, S.Z., Xu, X.Y., Collins, M.W., Stanton, A.V., Hughes, A.D., Thom, S.A. (1999) Flow in carotid bifurcations: effect of the superior thyroid artery. *Med Eng Phys* **21**, 207-14.
35. Perktold, K., Resch, M., Florian, H. (1991) Pulsatile non-Newtonian flow characteristics in a three-dimensional human carotid bifurcation model. *J Biomech Eng* **113**, 464-75.
36. Berger, S.A., Jou, L.D. (2000) Flows in Stenotic Vessels. *Annual Review of Fluid Mechanics* **32**, 347-384.
37. Bathe, K.J. (1996) *Finite element procedures*. Prentice Hall, Englewood Cliffs, N.J.
38. Delfino, A., Stergiopulos, N., Moore, J.E., Jr., Meister, J.J. (1997) Residual strain effects on the stress field in a thick wall finite element model of the human carotid bifurcation. *J Biomech* **30**, 777-86.
39. Downing, J.M., Ku, D.N. (1997) Effects of frictional losses and pulsatile flow on the collapse of stenotic arteries. *J Biomech Eng* **119**, 317-24.
40. Bathe, M., Kamm, R.D. (1999) A fluid-structure interaction finite element analysis of pulsatile blood flow through a compliant stenotic artery. *J Biomech Eng* **121**, 361-9.

41. Moore, J.E., Jr., Guggenheim, N., Delfino, A., Doriot, P.A., Dorsaz, P.A., Rutishauser, W., Meister, J.J. (1994) Preliminary analysis of the effects of blood vessel movement on blood flow patterns in the coronary arteries. *J Biomech Eng* **116**, 302-6.
42. Perktold, K., Rappitsch, G. (1995) Computer simulation of local blood flow and vessel mechanics in a compliant carotid artery bifurcation model. *J Biomech* **28**, 845-56.
43. Bathe, K.J., Zhang, H., Ji, S. (1999) Finite element analysis of fluid flows fully coupled with structural interactions. *Computers and Structures* **72**, 1-16.
44. Younis, H.F., M. R. Kaazempur-Mofrad, M.R., Chung, C., Kamm, R.D. (2001) Fluid-Structure Interaction Finite Element Analysis to Investigate the Effect of Exercise on Fluid Mechanical Variables in the Carotid Bifurcation. *in progress* .
45. Fung, Y.C., Fronek, K., Patitucci, P. (1979) Pseudoelasticity of arteries and the choice of its mathematical expression. *Am J Physiol* **237**, H620-31.
46. Delfino, A. (1996) Analysis of Stress Field in a Model of the Human Carotid Bifurcation. In *Department of Physics*Ecole Polytechnique Federale de Lausanne, Lausanne, Switzerland.
47. Shigley, J.E., Mischke, C.R. (1989) *Mechanical Engineering Design*. McGraw-Hill, New York.
48. Malek, A.M., Alper, S.L., Izumo, S. (1999) Hemodynamic shear stress and its role in atherosclerosis. *Jama* **282**, 2035-42.
49. Masawa, N., Glagov, S., Zarins, C.K. (1994) Quantitative morphologic study of intimal thickening at the human carotid bifurcation: I. Axial and circumferential distribution of maximum intimal thickening in asymptomatic, uncomplicated plaques. *Atherosclerosis* **107**, 137-46.
50. Salzar, R.S., Thubrikar, M.J., Eppink, R.T. (1995) Pressure-induced mechanical stress in the carotid artery bifurcation: a possible correlation to atherosclerosis. *J Biomech* **28**, 1333-40.
51. Chuong, C.J., Fung, Y.C. (1986) On residual stresses in arteries [published erratum appears in J Biomech Eng 1990 Aug;112(3):249]. *J Biomech Eng* **108**, 189-92.
52. Fung, Y.C. (1991) What are the residual stresses doing in our blood vessels? *Ann Biomed Eng* **19**, 237-49.
53. Huiskes, R., Ruimerman, R., van Lenthe, G.H., Janssen, J.D. (2000) Effects of mechanical forces on maintenance and adaptation of form in trabecular bone. *Nature* **405**, 704-6.
54. Humphrey, J.D. (1995) Mechanics of the arterial wall: review and directions. *Crit Rev Biomed Eng* **23**, 1-162.

V.8. Figures

V.8.1. Figure Captions

Fig 1. Procedure to be used to import MRI image data from source into finite element package. Note that both fluid and solid domains are generated.

Fig 2. Lofted wall and fluid geometries based on MR data. These are later imported into the finite element package for analysis. NV1 (top), NV2 (middle) and NV4 (bottom).

Fig 3. Fully developed Womersley-type flow rates for the rigid-walled simulations based on ultrasound centerline velocity measurements. In these plots, the flow rates in the external carotid artery were computed by subtracting the internal carotid flow rates from the common carotid to ensure mass conservation. Measured flow rates in the external carotid artery based on the ultrasound measurements were not used (see text). NV1 (top), NV2 (middle) and NV4 (bottom).

Fig 4. Meshes used for finite element analysis. The element size used for the solid and fluid elements was 0.4 mm (NV1 and NV4 solid simulations used a 0.45 mm mesh), which provided 2-3 solid elements across the wall and 15-20 elements across the common carotid. 11 node quadratic elements were used for the wall domain, while 4 node linear elements were used for the fluid domain. NV1 (top), NV2 (middle) and NV4 (bottom).

Fig 5. Average wall shear stress (WSS) plots [*Pa*] over the cycle for each NV. Logarithmic scales are used to emphasize low ($< 0.5\ Pa$) wall shear stress below which an atherosclerotic gene expression profile is expected. NV1 (a), NV2 (b), NV2 with distensible walls (c), NV4 (d).

Fig 6. Oscillatory shear index (OSI) for each NV. The maximum value, 0.5, represents purely oscillatory flow. NV1 (a), NV2 (b), NV2 with distensible walls (c), NV4 (d).

Fig 7. Maximum wall shear temporal gradient (WSSTG) [*Pa/s*] for each NV. This is obtained by calculating the gradient in WSS between every two consecutive time points along the cycle and taking the maximum of these values along the entire cycle. NV1 (a), NV2 (b), NV2 with distensible walls (c), NV4 (d).

Fig 8. Von Mises cyclic strain for each NV. Cyclic strain is computed as the difference between systolic and diastolic strain. NV1 (a), NV2 (b), NV4 (c).

Fig 9. The effect of residual stresses on the strain field across the thickness of an axisymmetric cylindrical artery. The x-axis is plotted as a function of normalized thickness, with "0" being along the inner wall surface. The top graph illustrates the strain at systole and diastole without the inclusion of residual stresses, the lower graph with. Note that even though the strain field is altered (more uniform when residual stresses are included), the magnitude of the cyclic strain (obtained as the difference between the solid and dashed lines) is identical in both cases. Applied systolic pressure here: 120 *mmHg*; diastolic pressure: 80 *mmHg*.

V.8.2. Figures

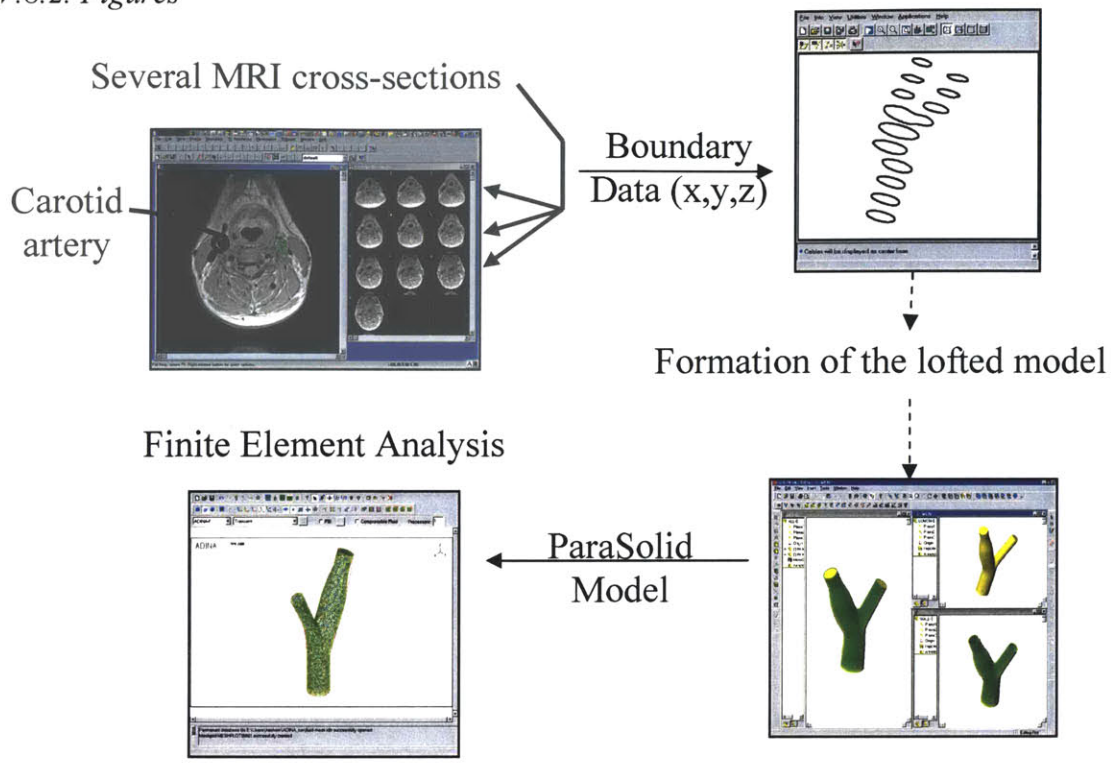

Figure 1

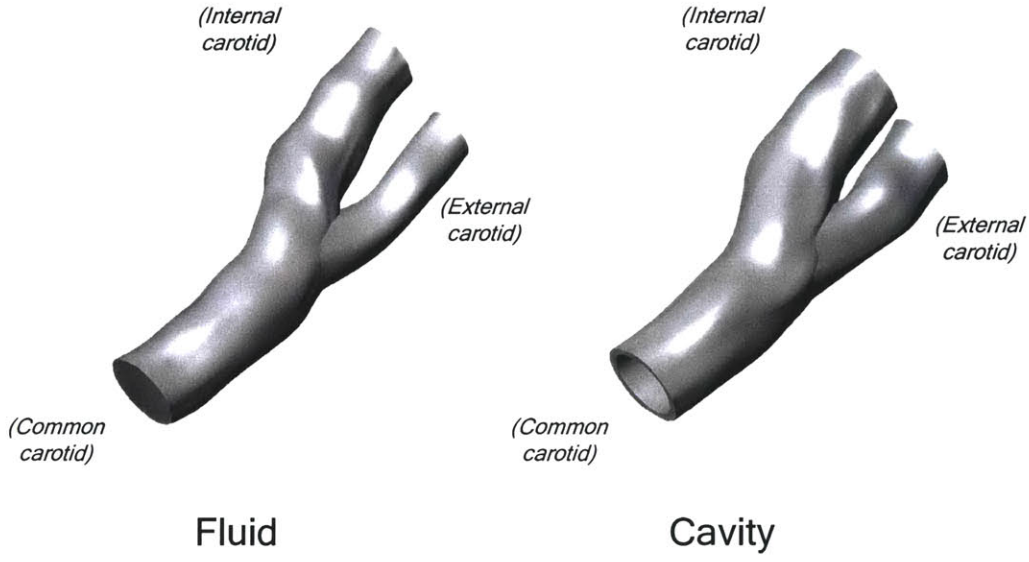

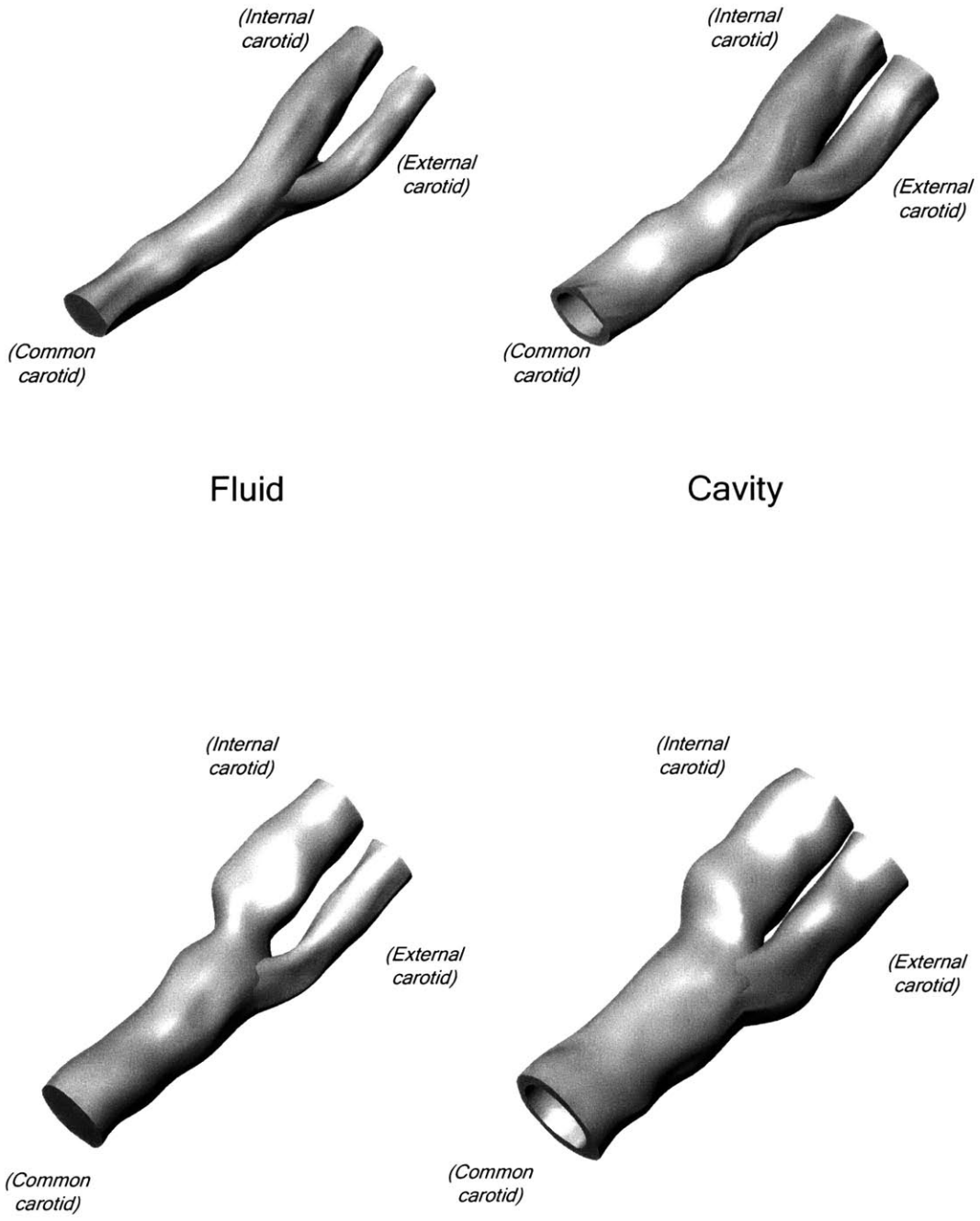
(Internal carotid)
(External carotid)
(Common carotid)
Fluid
(Internal carotid)
(External carotid)
(Common carotid)
Cavity
(Internal carotid)
(External carotid)
(Common carotid)
Fluid
(Internal carotid)
(External carotid)
(Common carotid)
Cavity

Figure 2

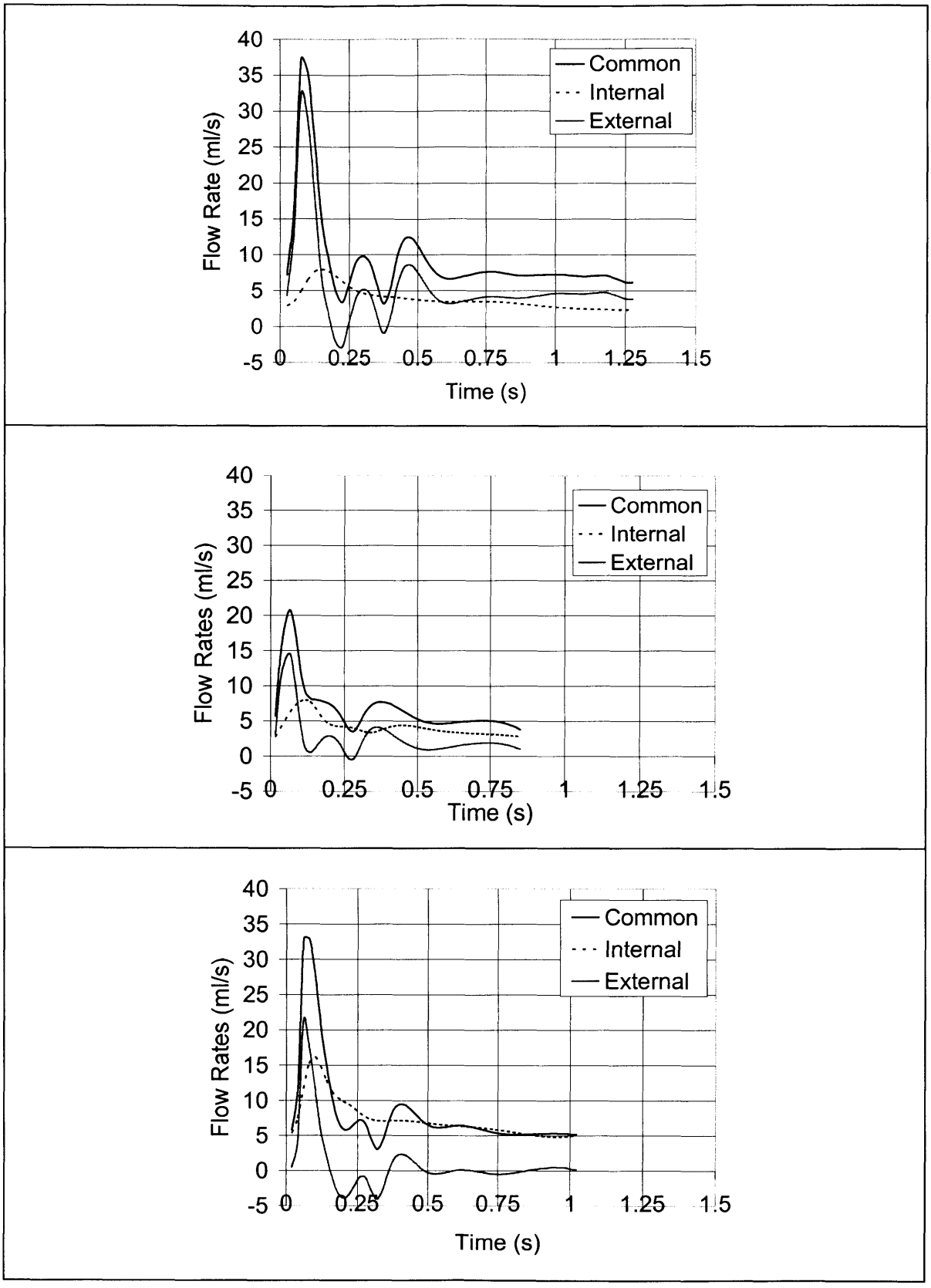
Flow Rate (ml/s)
Time (s)
Common
Internal
External
Flow Rates (ml/s)
Time (s)
Common
Internal
External
Flow Rates (ml/s)
Time (s)
Common
Internal
External

Figure 3

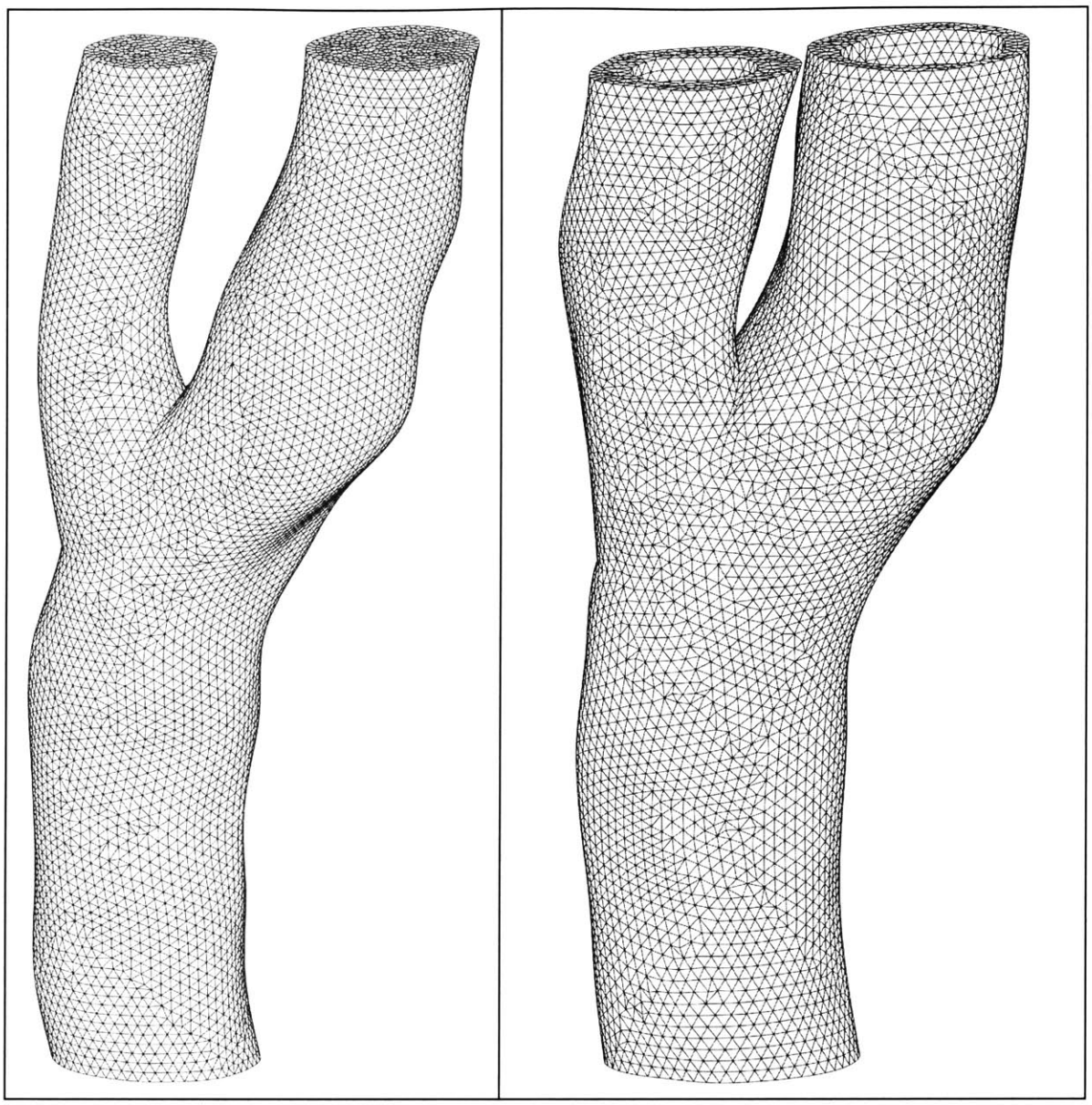

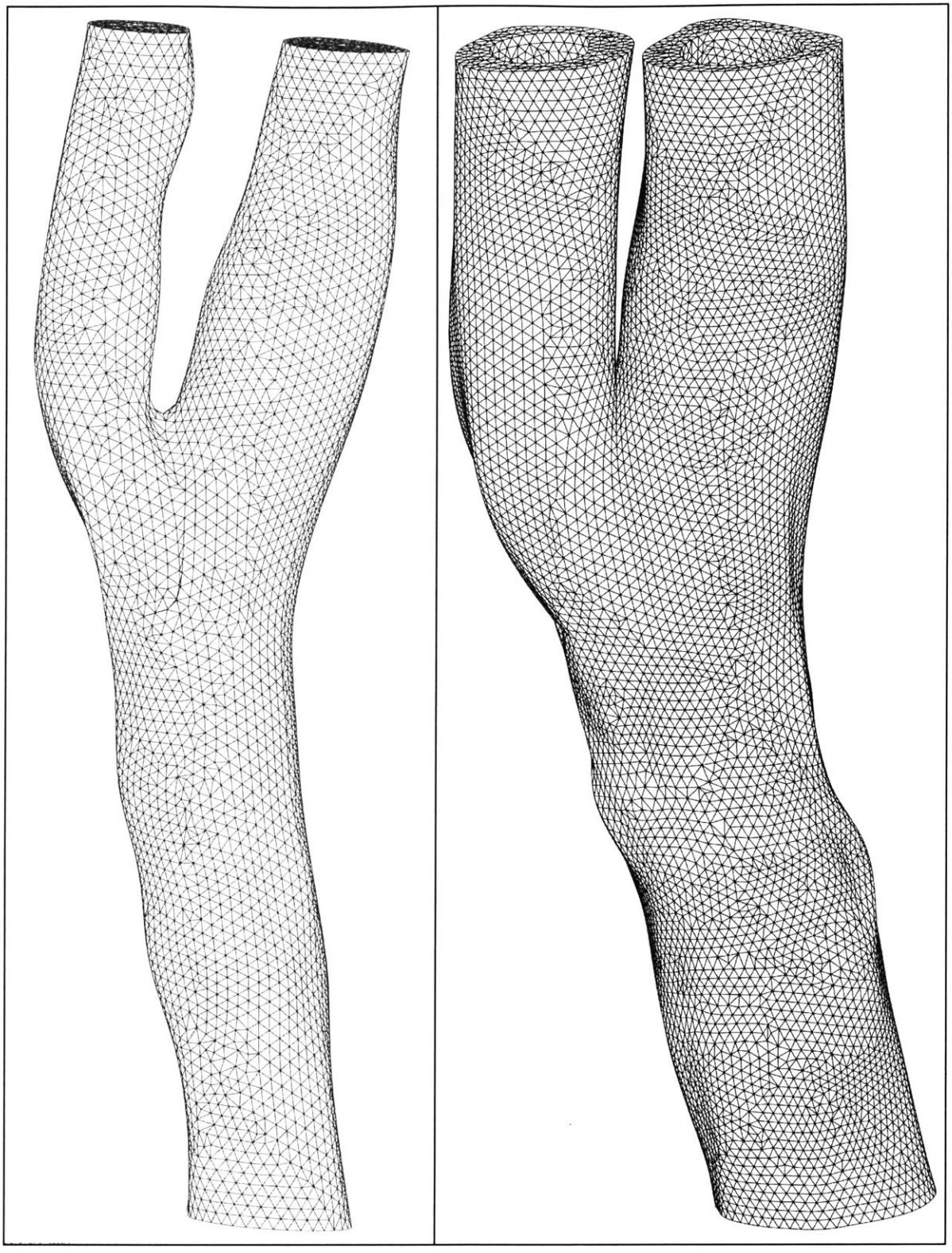

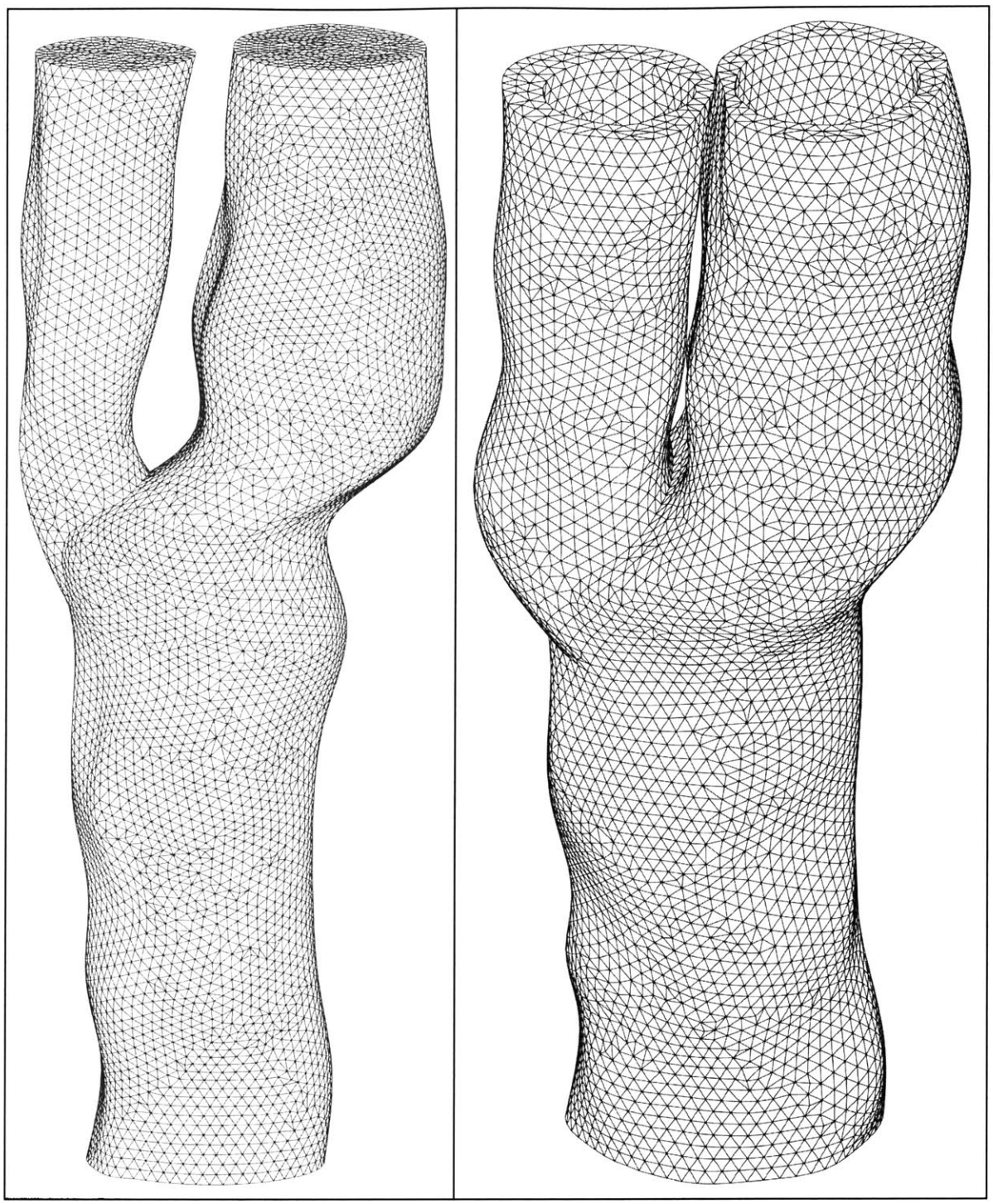

Figure 4

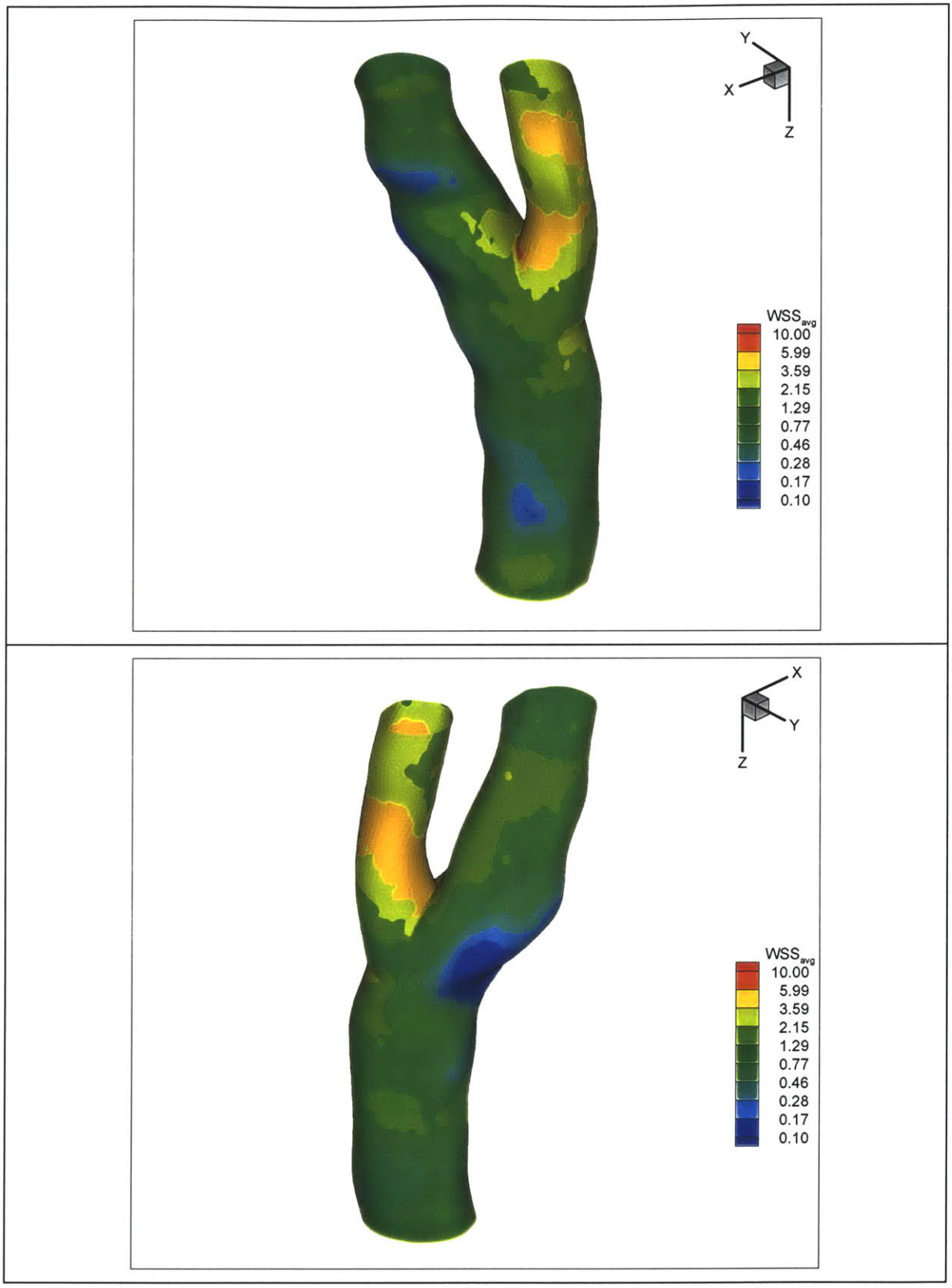
Y
X
Z
WSS$_{avg}$
10.00
5.99
3.59
2.15
1.29
0.77
0.46
0.28
0.17
0.10
X
Y
Z
WSS$_{avg}$
10.00
5.99
3.59
2.15
1.29
0.77
0.46
0.28
0.17
0.10

(a)

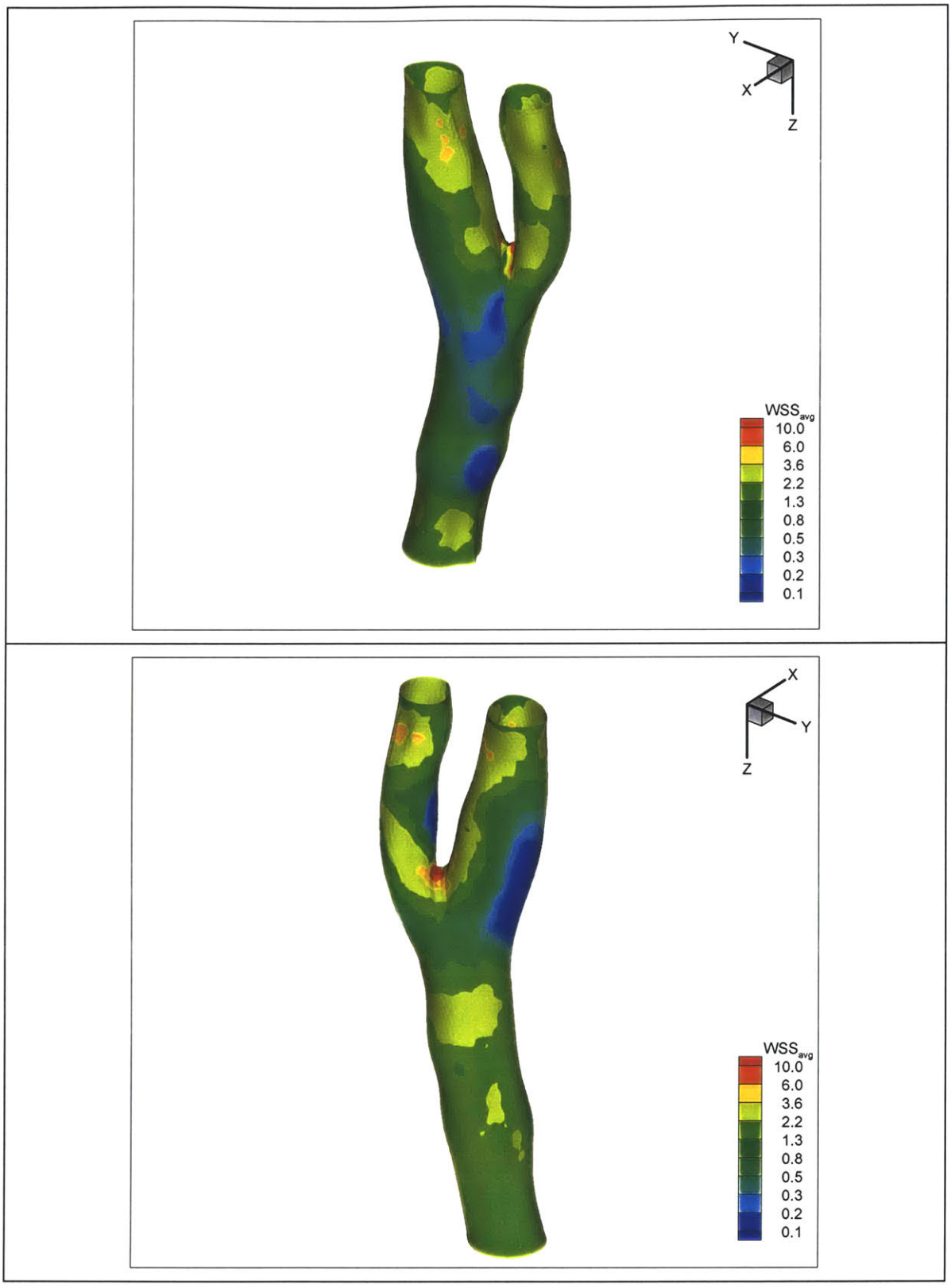
Y
X
Z
WSS$_{avg}$
10.0
6.0
3.6
2.2
1.3
0.8
0.5
0.3
0.2
0.1
X
Y
Z
WSS$_{avg}$
10.0
6.0
3.6
2.2
1.3
0.8
0.5
0.3
0.2
0.1

(b)

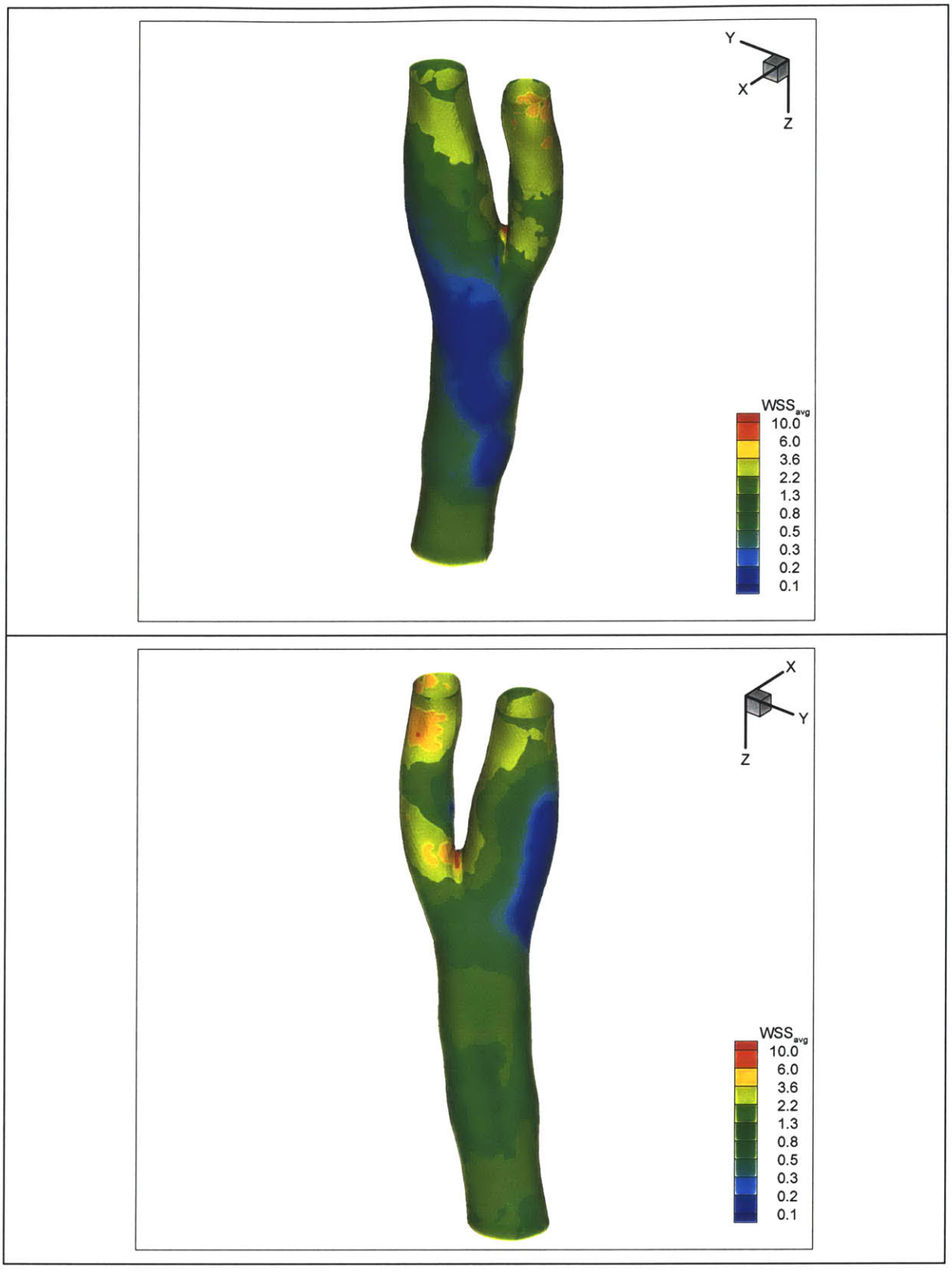
Y
X
Z
WSS$_{avg}$
10.0
6.0
3.6
2.2
1.3
0.8
0.5
0.3
0.2
0.1
X
Y
Z
WSS$_{avg}$
10.0
6.0
3.6
2.2
1.3
0.8
0.5
0.3
0.2
0.1

(c)

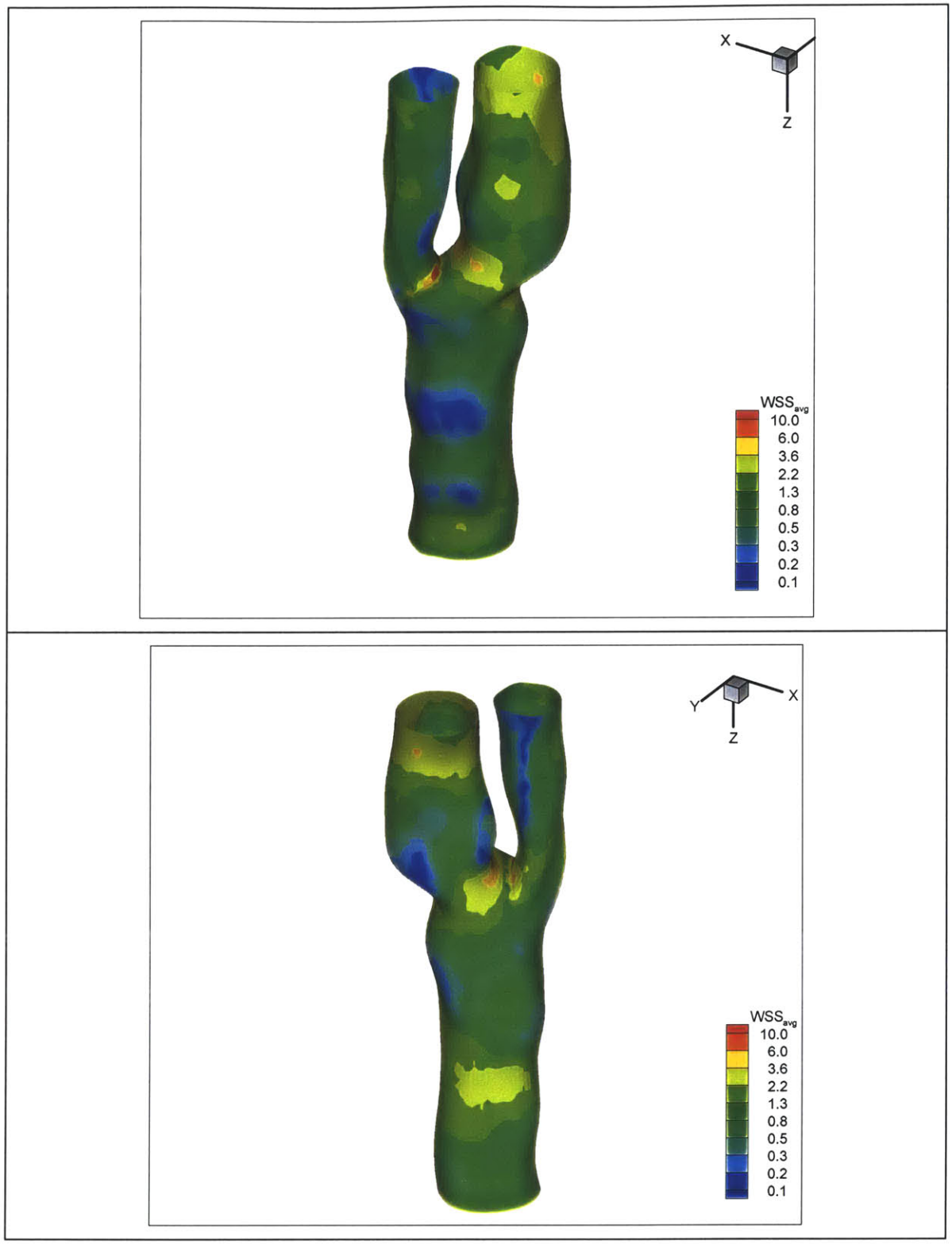
X
Z
WSS$_{avg}$
10.0
6.0
3.6
2.2
1.3
0.8
0.5
0.3
0.2
0.1
Y
X
Z
WSS$_{avg}$
10.0
6.0
3.6
2.2
1.3
0.8
0.5
0.3
0.2
0.1

(d)

Figure 5

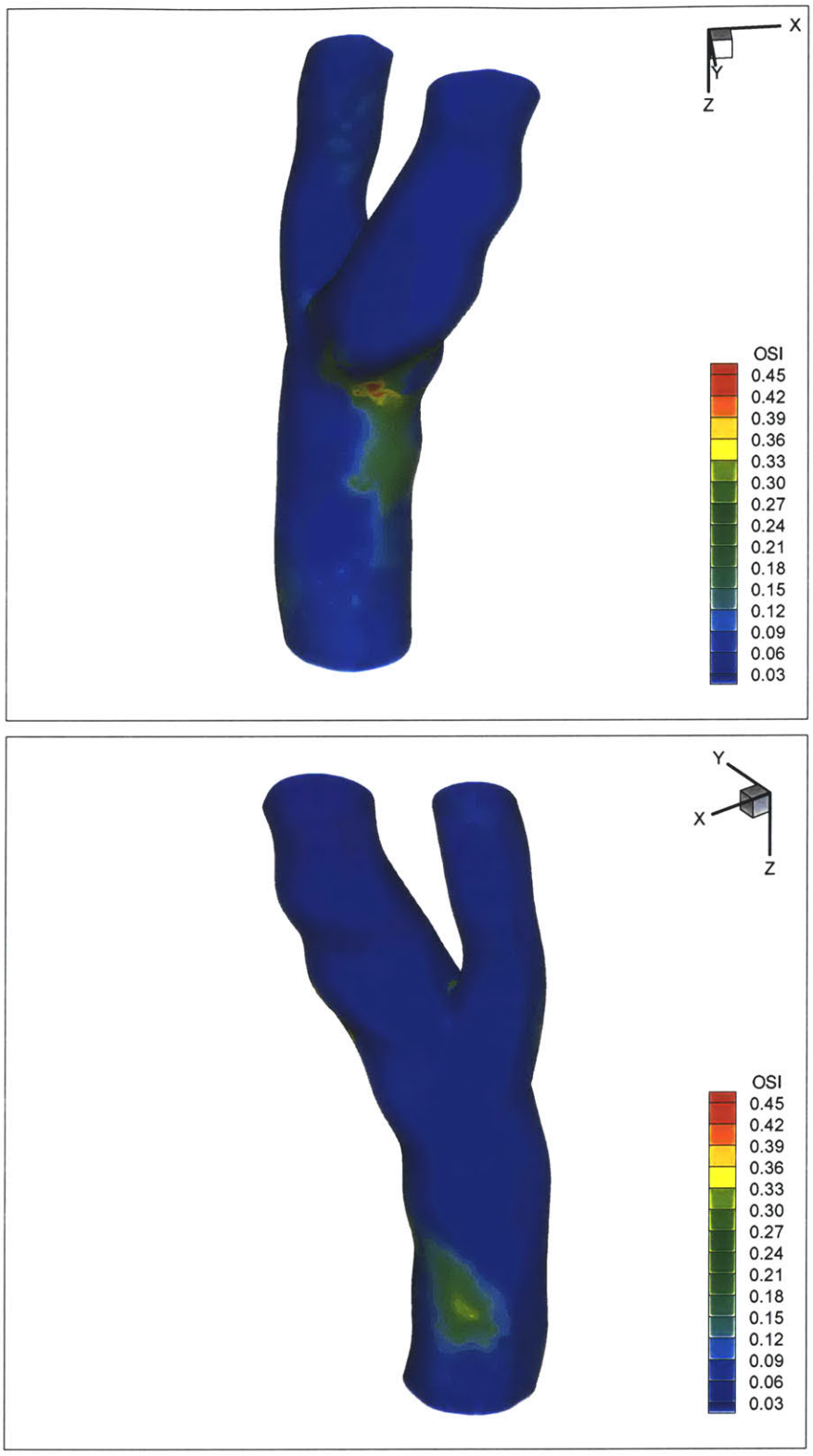
X
Y
Z
OSI
0.45
0.42
0.39
0.36
0.33
0.30
0.27
0.24
0.21
0.18
0.15
0.12
0.09
0.06
0.03
Y
X
Z
OSI
0.45
0.42
0.39
0.36
0.33
0.30
0.27
0.24
0.21
0.18
0.15
0.12
0.09
0.06
0.03

(a)

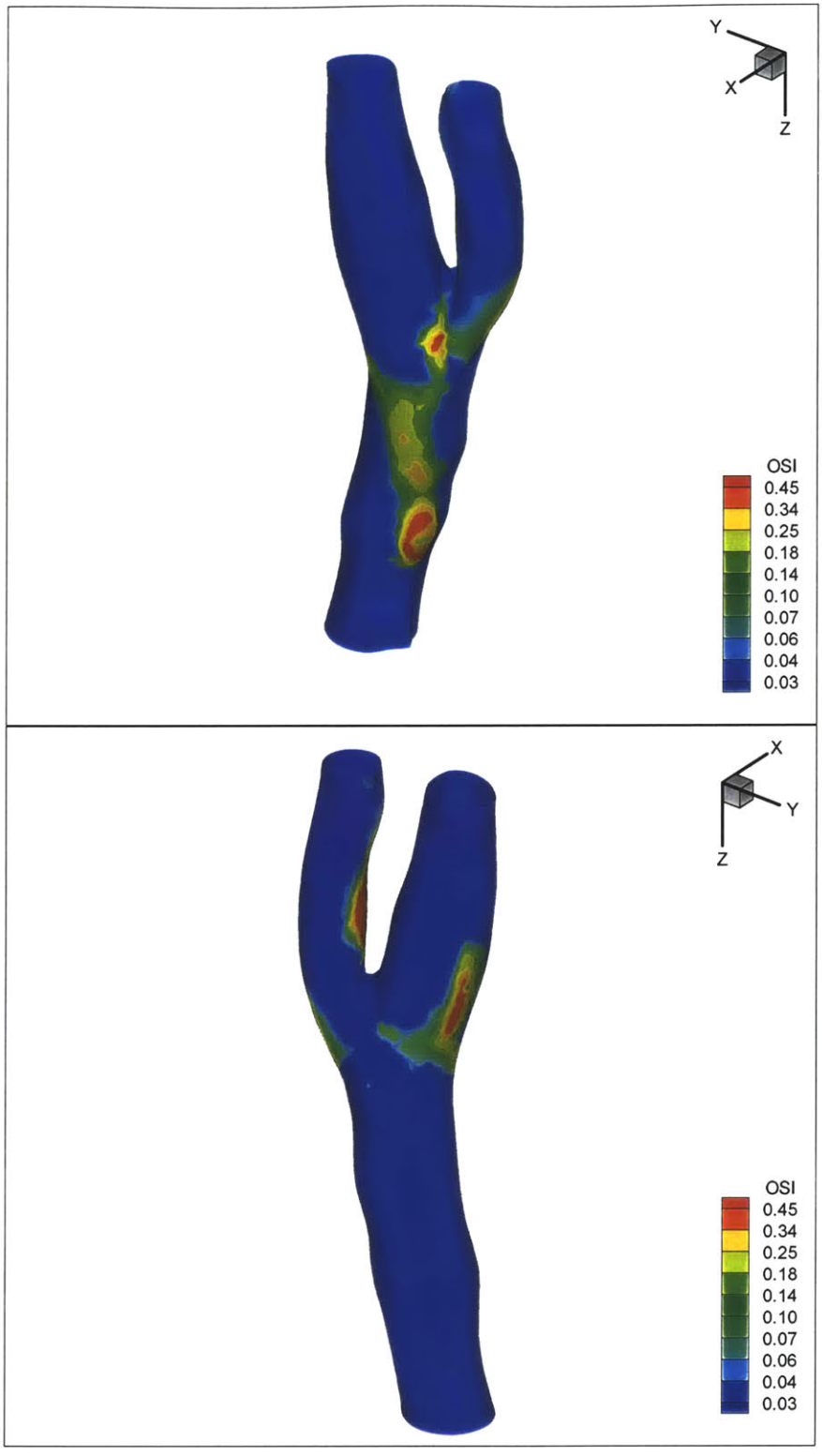
Y
X
Z
OSI
0.45
0.34
0.25
0.18
0.14
0.10
0.07
0.06
0.04
0.03
X
Y
Z
OSI
0.45
0.34
0.25
0.18
0.14
0.10
0.07
0.06
0.04
0.03

(b)

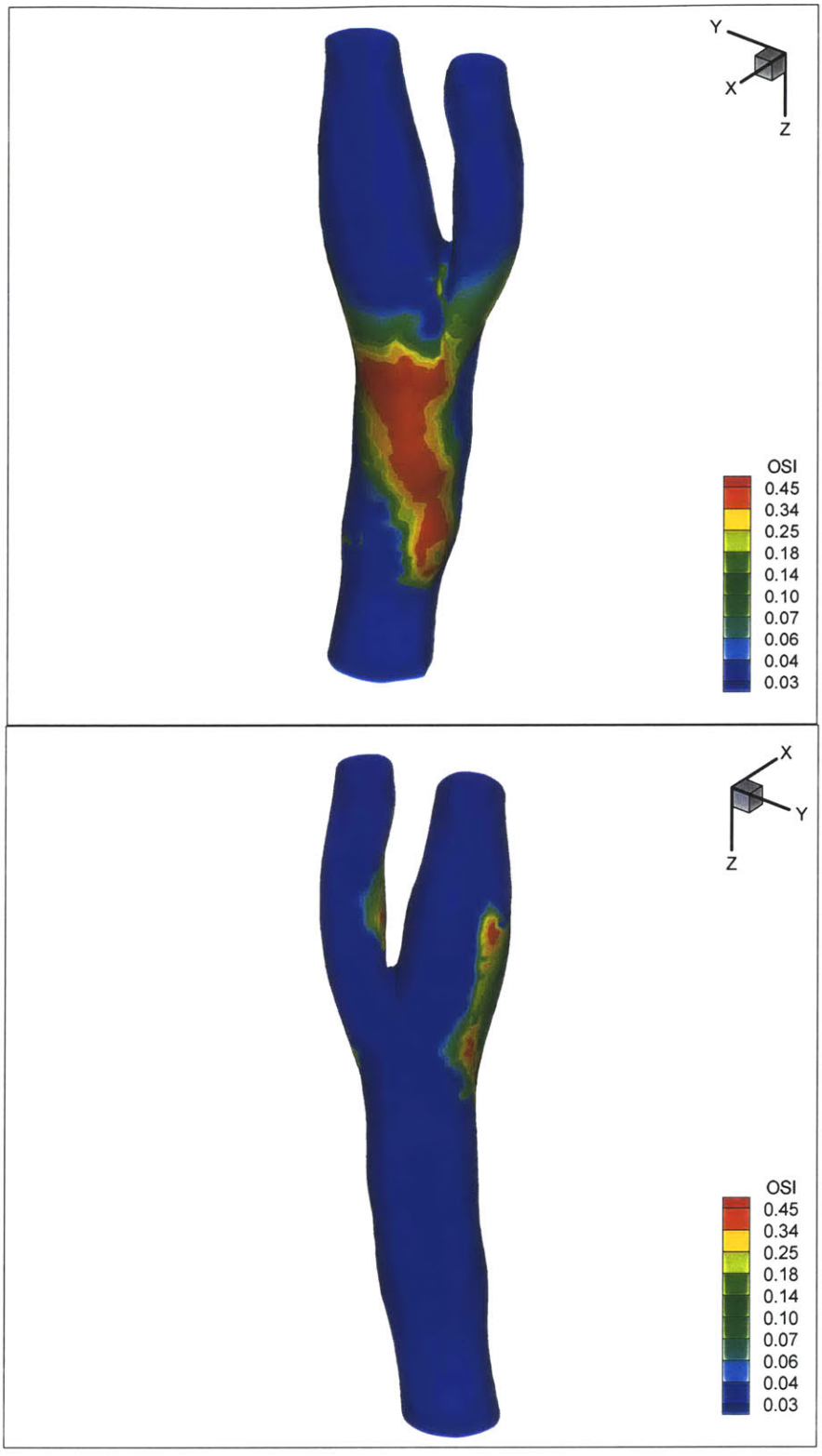
Y
X
Z
OSI
0.45
0.34
0.25
0.18
0.14
0.10
0.07
0.06
0.04
0.03
X
Y
Z
OSI
0.45
0.34
0.25
0.18
0.14
0.10
0.07
0.06
0.04
0.03

(c)

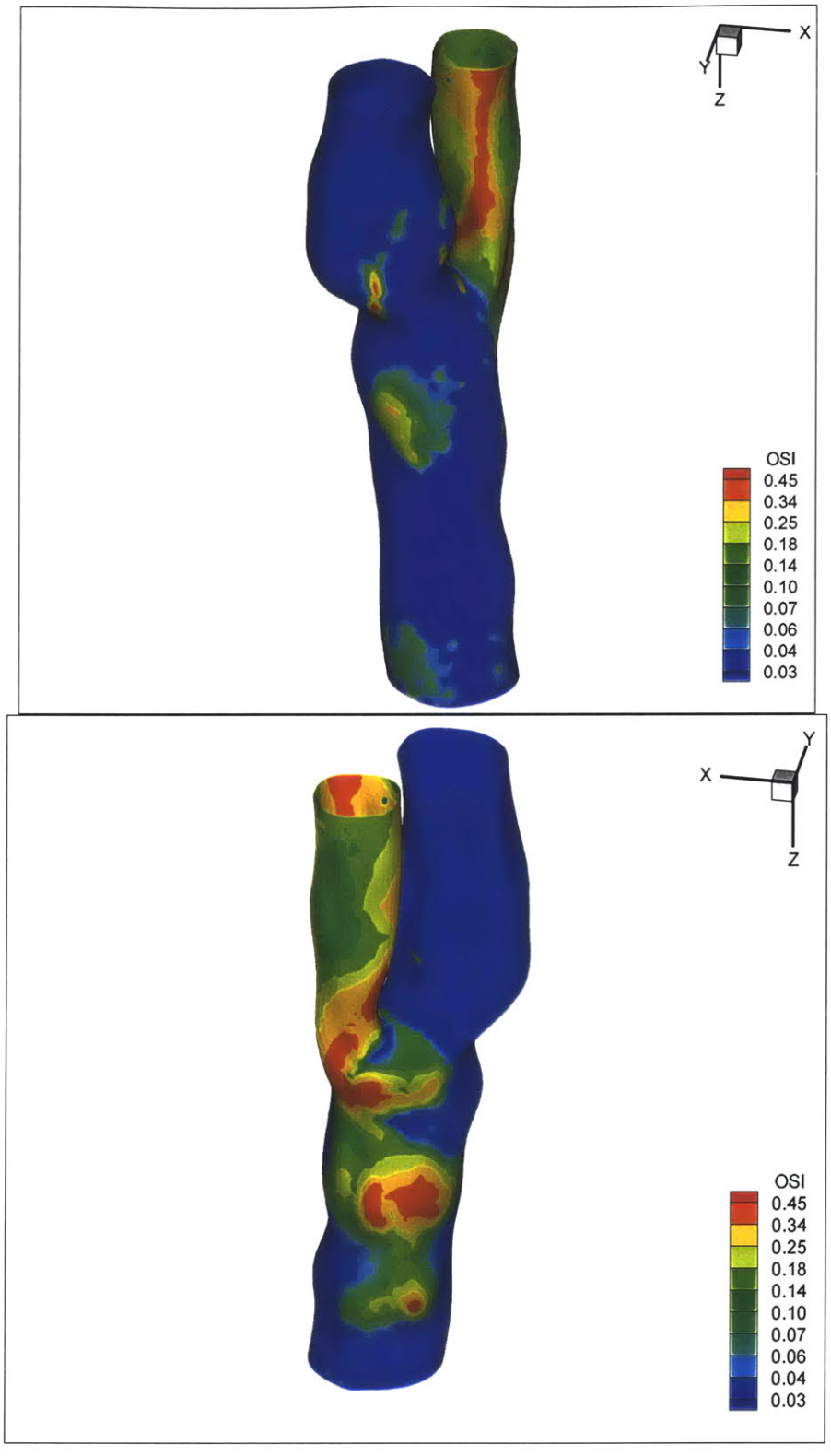
X
Y
Z
OSI
0.45
0.34
0.25
0.18
0.14
0.10
0.07
0.06
0.04
0.03
Y
X
Z
OSI
0.45
0.34
0.25
0.18
0.14
0.10
0.07
0.06
0.04
0.03

(d)

Figure 6

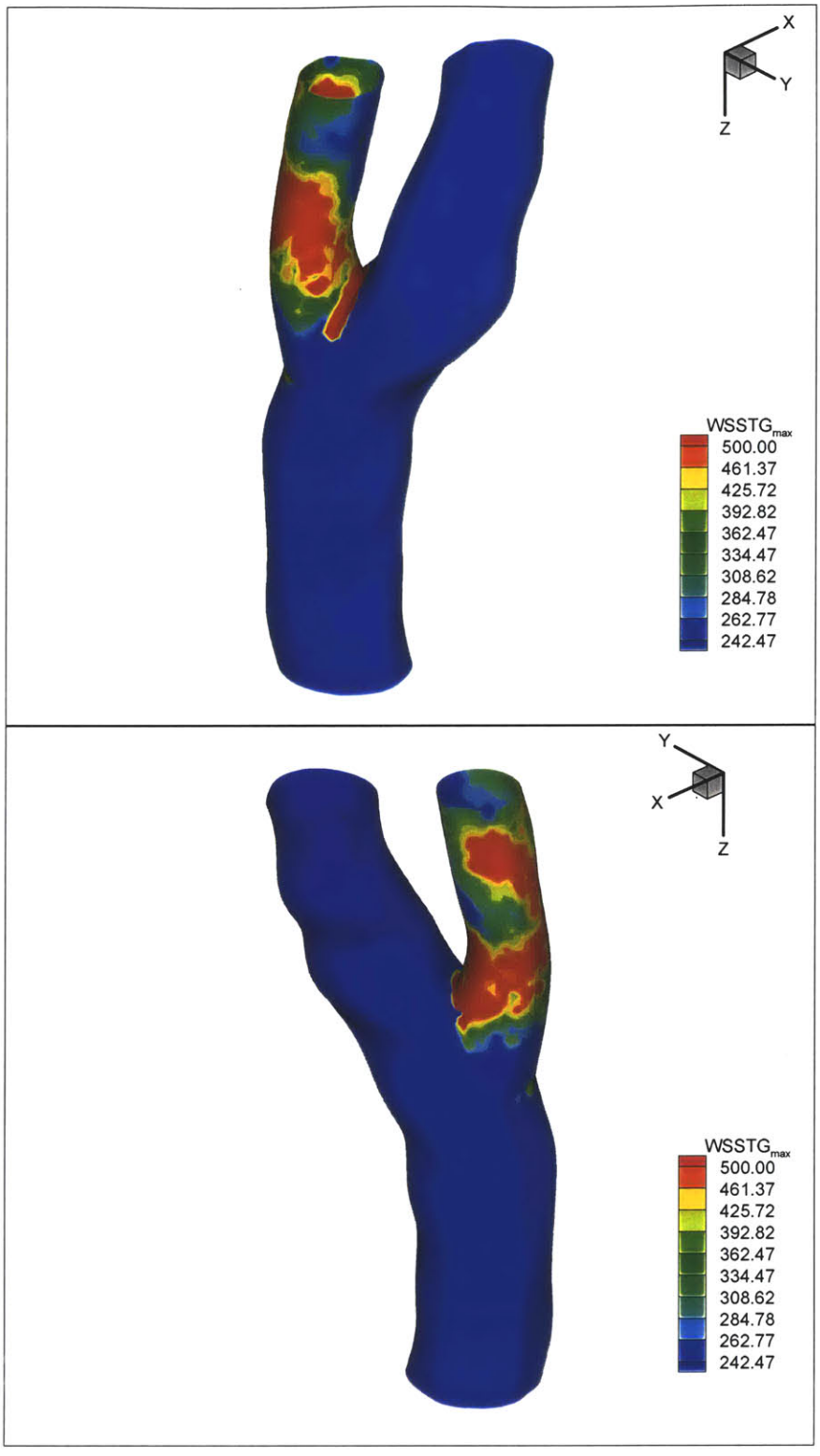
X
Y
Z
WSSTG$_{max}$
500.00
461.37
425.72
392.82
362.47
334.47
308.62
284.78
262.77
242.47
Y
X
Z
WSSTG$_{max}$
500.00
461.37
425.72
392.82
362.47
334.47
308.62
284.78
262.77
242.47

(a)

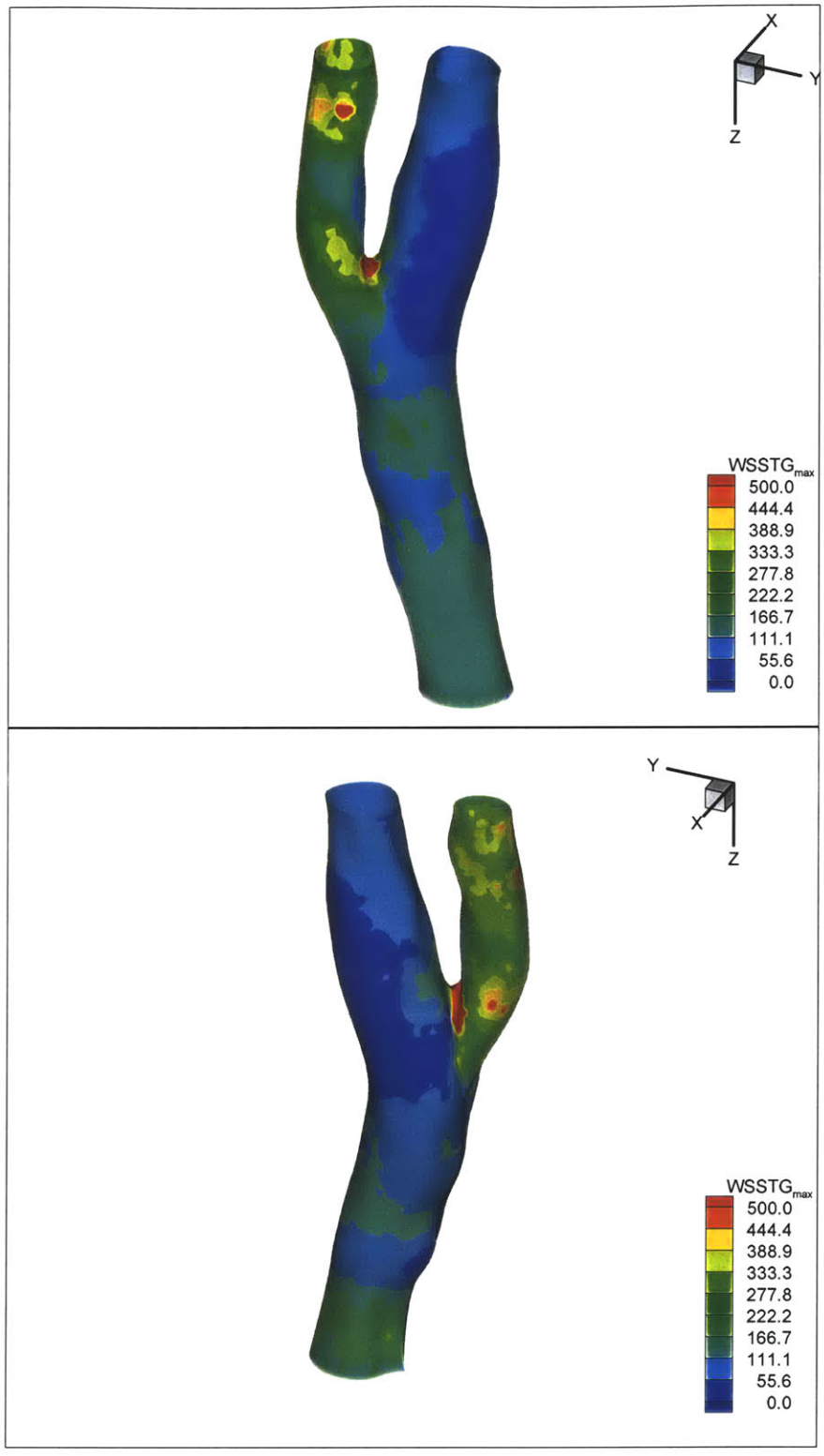
X
Y
Z
WSSTG$_{max}$
500.0
444.4
388.9
333.3
277.8
222.2
166.7
111.1
55.6
0.0
Y
X
Z
WSSTG$_{max}$
500.0
444.4
388.9
333.3
277.8
222.2
166.7
111.1
55.6
0.0

(b)

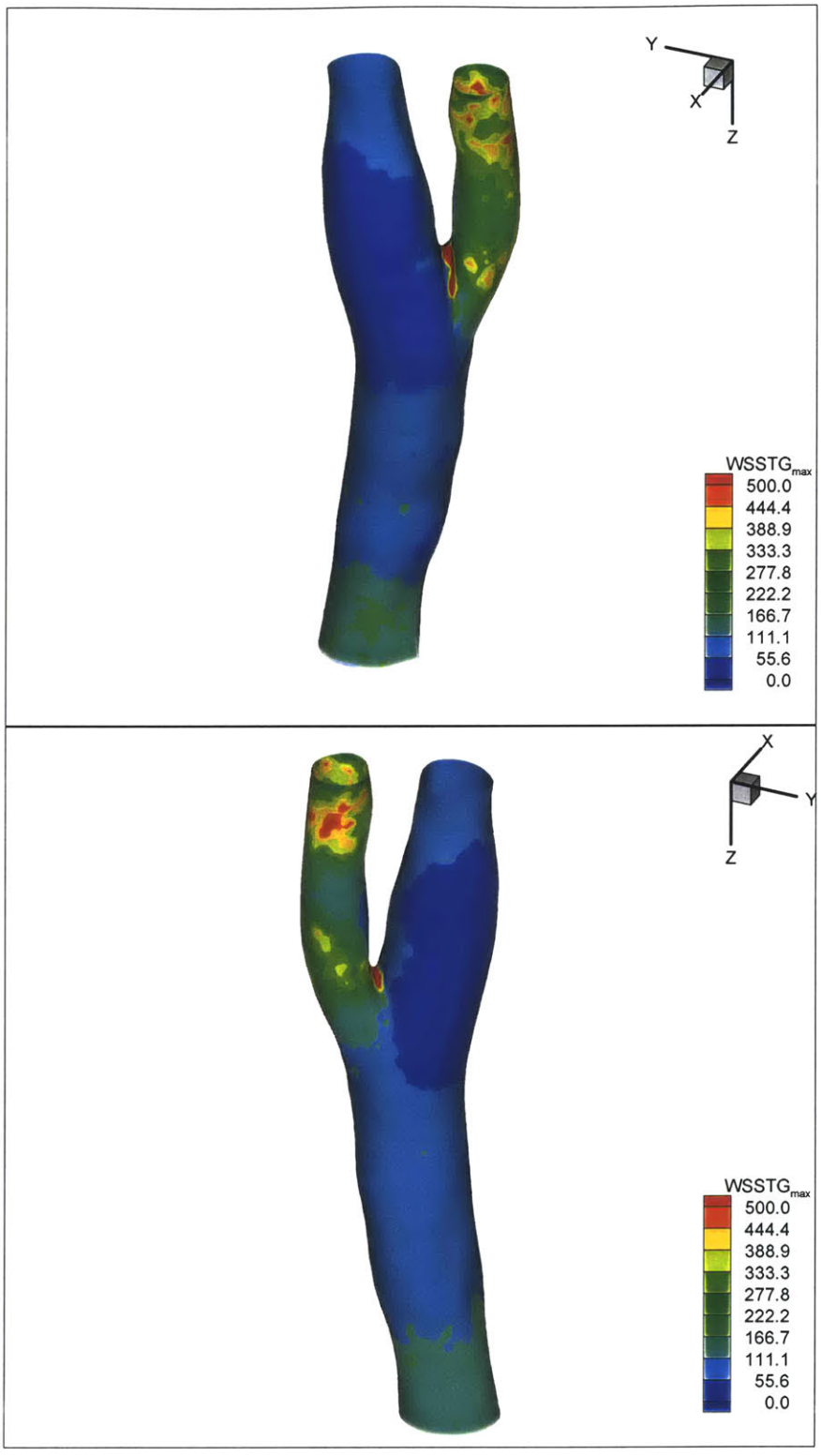
Y
X
Z
WSSTG$_{max}$
500.0
444.4
388.9
333.3
277.8
222.2
166.7
111.1
55.6
0.0
X
Y
Z
WSSTG$_{max}$
500.0
444.4
388.9
333.3
277.8
222.2
166.7
111.1
55.6
0.0

(c)

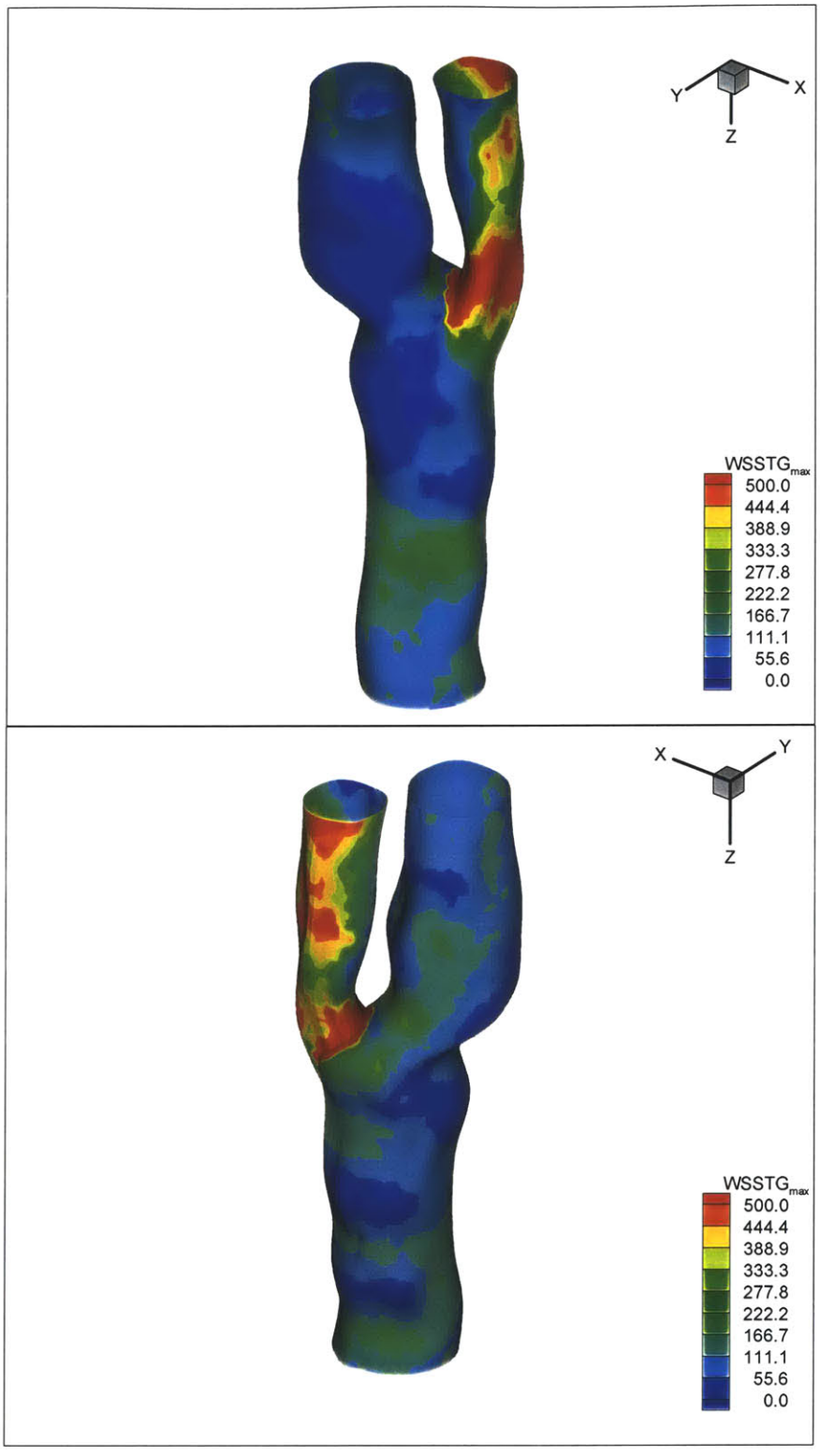
Y
X
Z
WSSTG$_{max}$
500.0
444.4
388.9
333.3
277.8
222.2
166.7
111.1
55.6
0.0
X
Y
Z
WSSTG$_{max}$
500.0
444.4
388.9
333.3
277.8
222.2
166.7
111.1
55.6
0.0

(d)

Figure 7

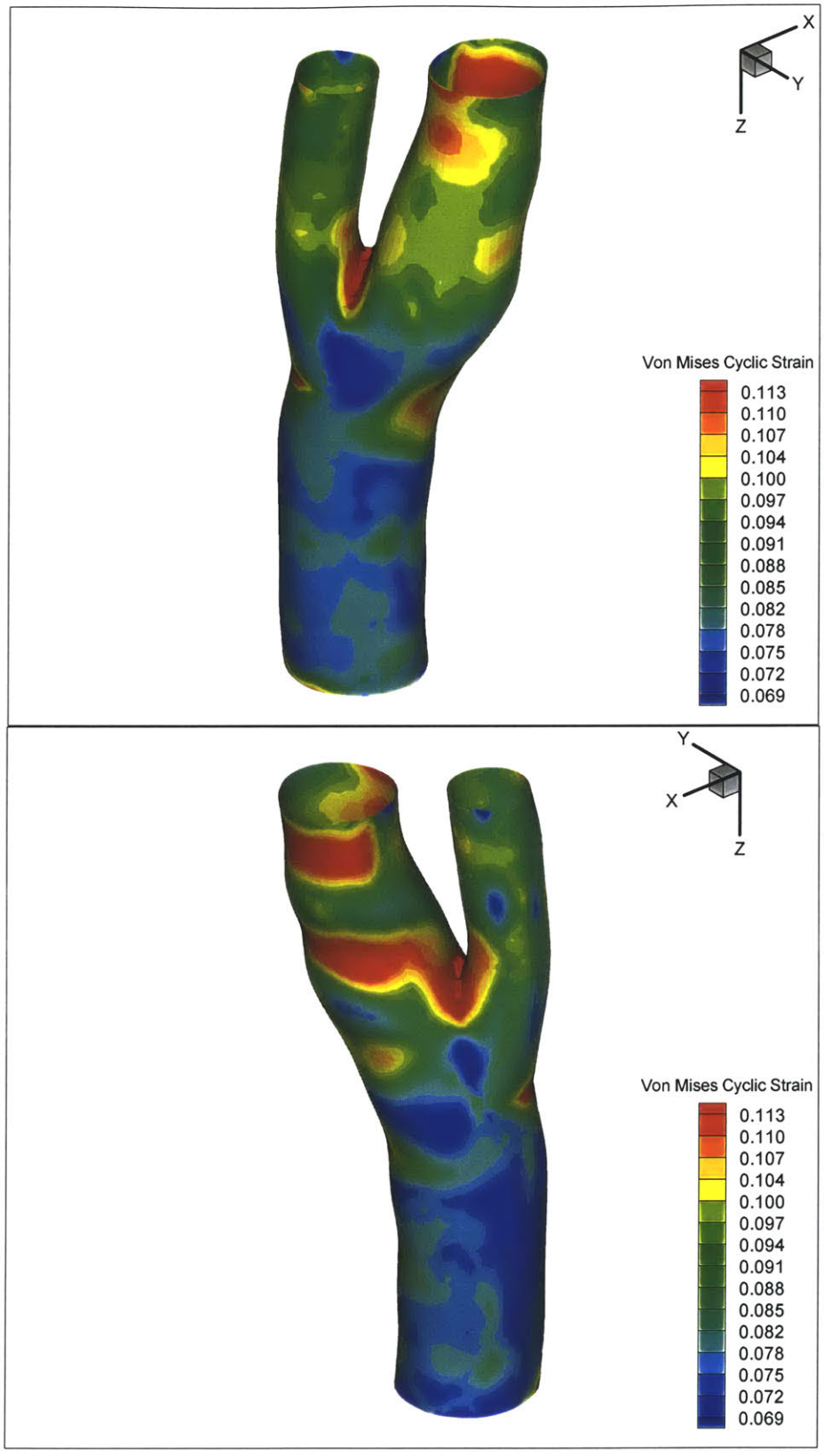
X
Y
Z
Von Mises Cyclic Strain
0.113
0.110
0.107
0.104
0.100
0.097
0.094
0.091
0.088
0.085
0.082
0.078
0.075
0.072
0.069
Y
X
Z
Von Mises Cyclic Strain
0.113
0.110
0.107
0.104
0.100
0.097
0.094
0.091
0.088
0.085
0.082
0.078
0.075
0.072
0.069

(a)

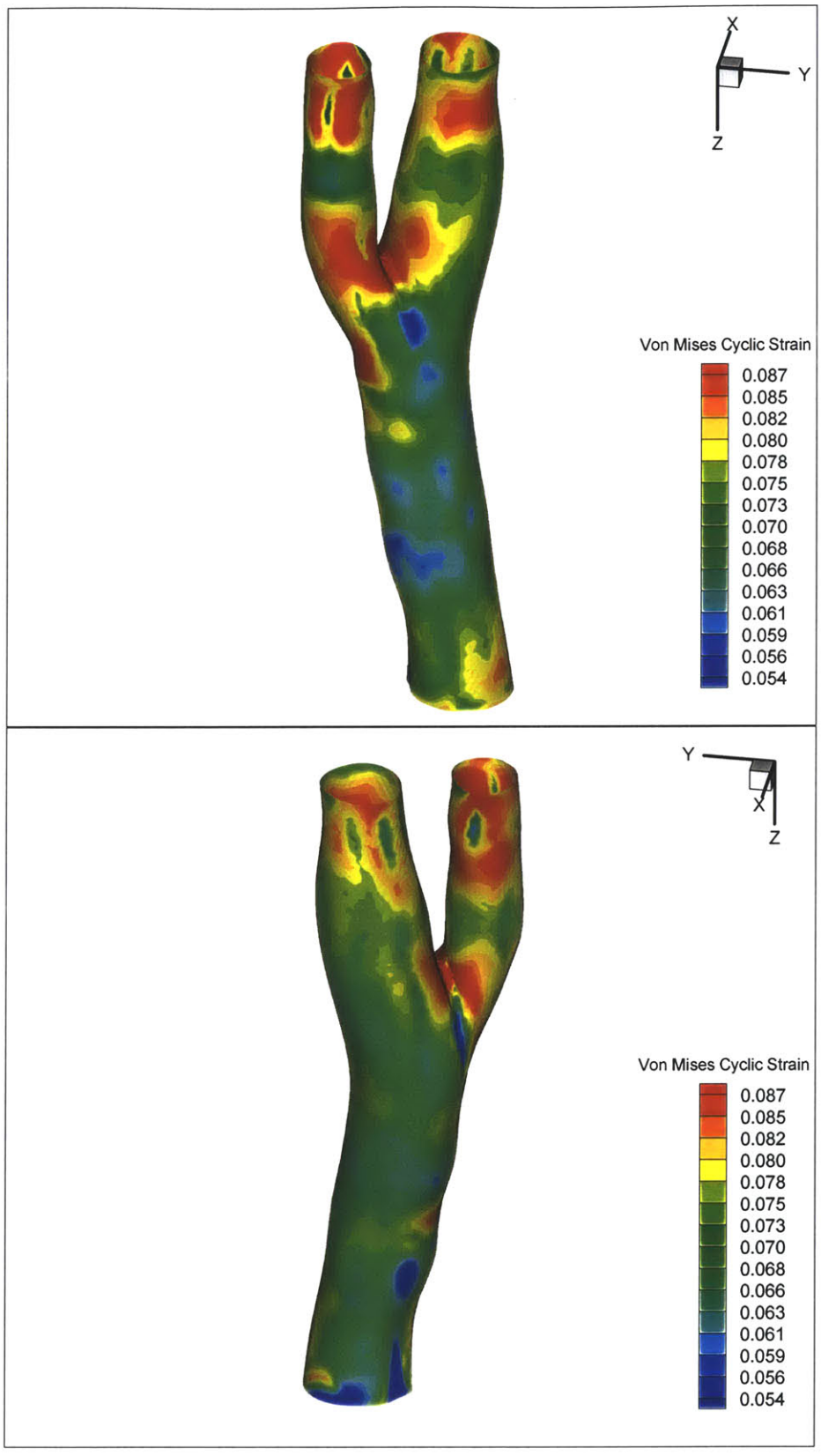
X
Y
Z
Von Mises Cyclic Strain
0.087
0.085
0.082
0.080
0.078
0.075
0.073
0.070
0.068
0.066
0.063
0.061
0.059
0.056
0.054
Y
X
Z
Von Mises Cyclic Strain
0.087
0.085
0.082
0.080
0.078
0.075
0.073
0.070
0.068
0.066
0.063
0.061
0.059
0.056
0.054

(b)

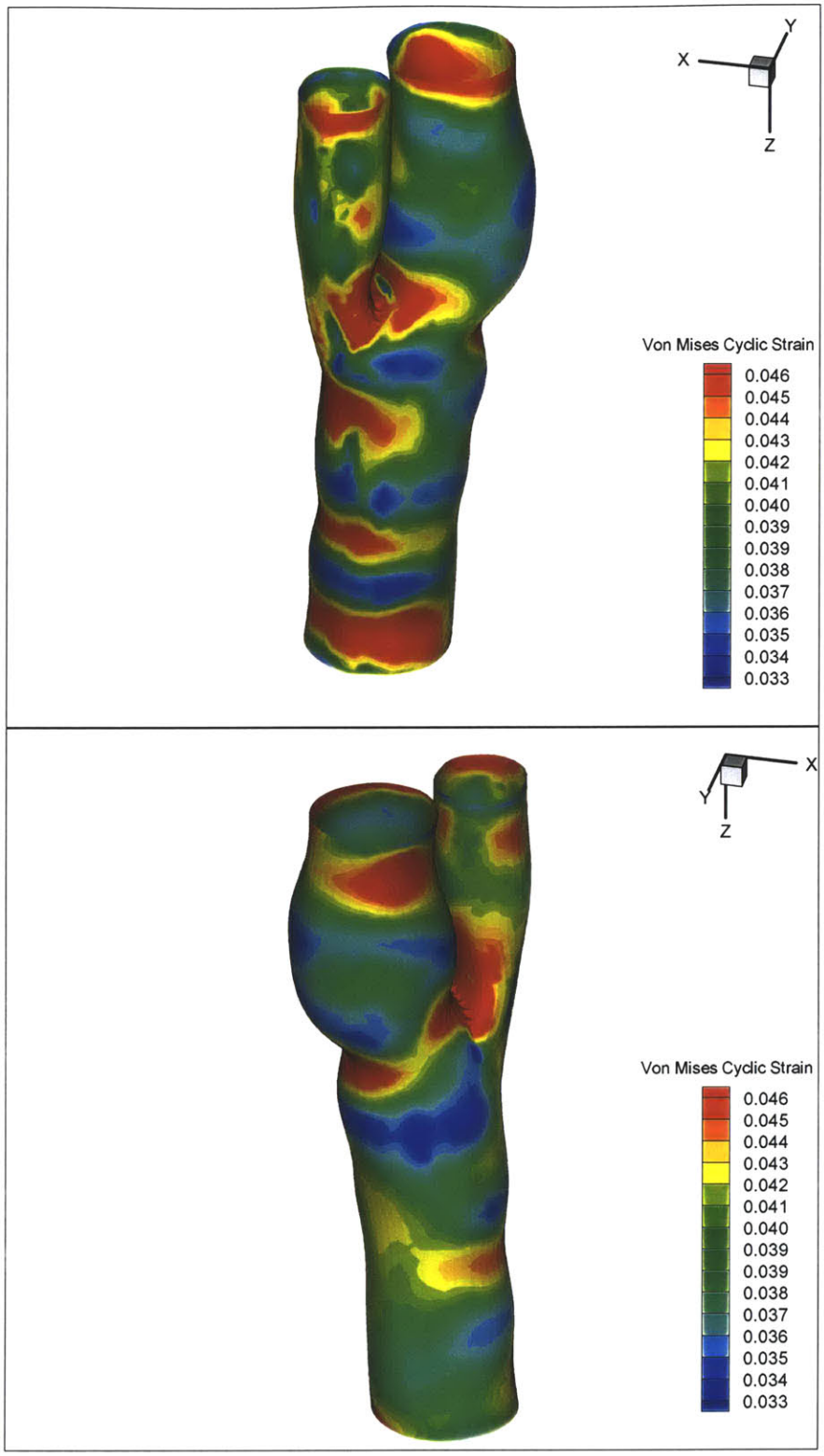
Y
X
Z
Von Mises Cyclic Strain
0.046
0.045
0.044
0.043
0.042
0.041
0.040
0.039
0.039
0.038
0.037
0.036
0.035
0.034
0.033
X
Y
Z
Von Mises Cyclic Strain
0.046
0.045
0.044
0.043
0.042
0.041
0.040
0.039
0.039
0.038
0.037
0.036
0.035
0.034
0.033

(c)

Figure 8

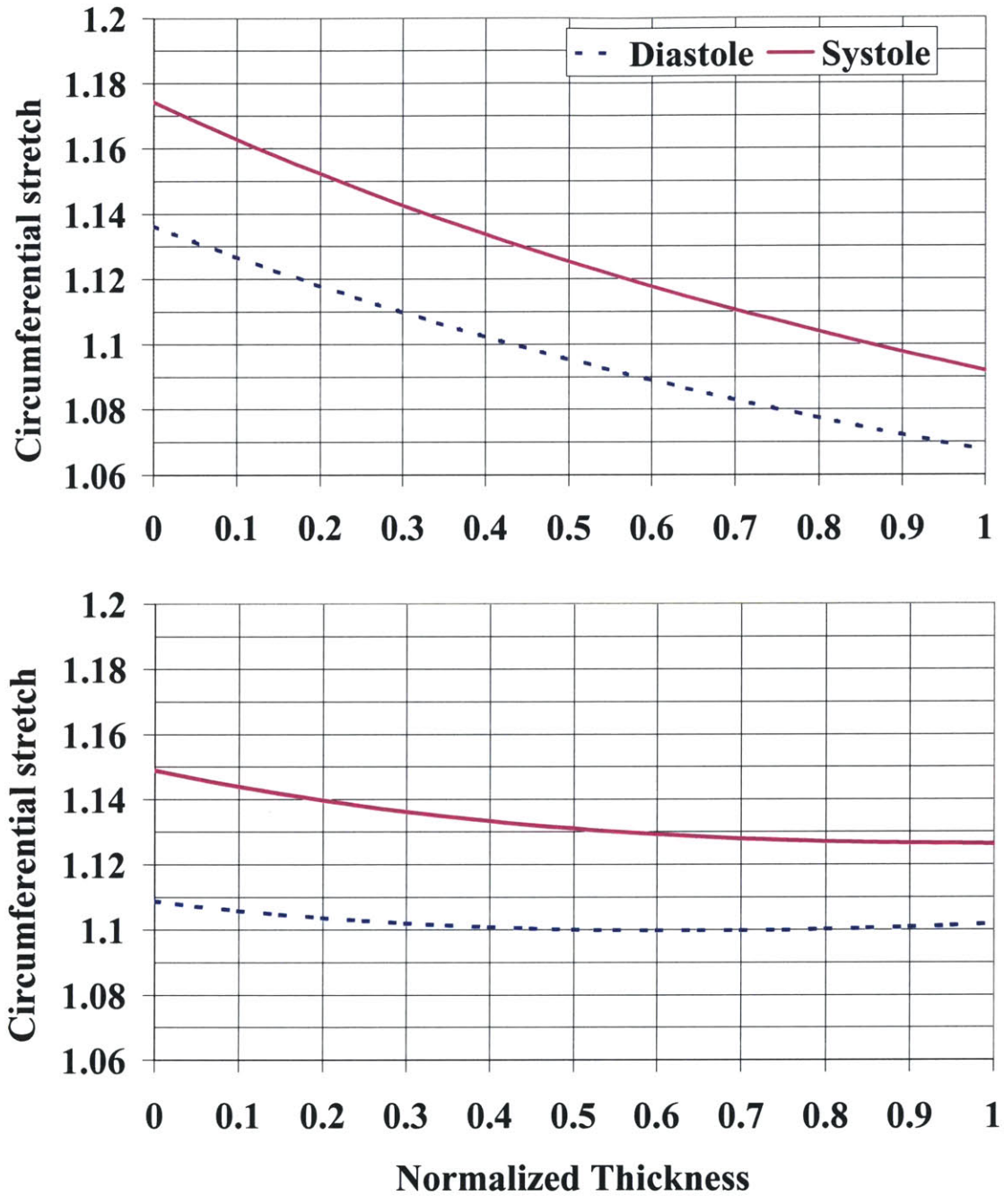
Diastole
Systole
Circumferential stretch
1.2
1.18
1.16
1.14
1.12
1.1
1.08
1.06
0
0.1
0.2
0.3
0.4
0.5
0.6
0.7
0.8
0.9
1
Normalized Thickness

Figure 9

VI. A Numerical Study of Diseased Carotid Bifurcation Fluid Mechanics based on *in vivo* Magnetic Resonance Images: Histological Correlations to the Inflammatory Response.

VI.1. Abstract

Atherosclerosis is an inflammatory disease characterized by endothelial dysfunction, monocyte infiltration and differentiation, smooth muscle proliferation, lipid deposition and arterial wall remodeling. Even though systemic factors pre-dispose one individual over another to develop atherosclerosis, it remains to be explained why the disease is focal, appearing mainly at sites of complex hemodynamics, e.g. bifurcations, arterial junctions and branches. One widely held theory in the literature attributes the uneven distribution of atherosclerotic lesions to variations in wall shear stress in the arterial tree, particularly the carotid bifurcation. Even though this theory is widely accepted today, it has never, to our knowledge, been verified rigorously by correlating histology to wall shear distributions based on *in vivo* measurements. A major goal of this present study is thus to validate the hypothesis that low or oscillatory shear stress correlates with the progression of atherosclerosis using 3D computational finite element fluid mechanic analyses based on realistic geometries and flow profiles by input of actual data gathered from *in vivo* magnetic resonance imaging of the carotid bifurcations four diseased patients. Histology specimens (advanced plaques) from diseased arteries harvested from the same patients after carotid endarterectomy provide a conclusive method to correlate regions of monocyte deposition/macrophage accumulation, smooth muscle proliferation, lipid deposition and collagen production, all characteristics of the inflammatory/remodeling process, to regions of low and oscillating fluid wall shear stress, measured by the average wall shear stress over the cycle (WSS) and the oscillatory shear index (OSI).

The results indicate that strong correlations exist in the vicinity of the carotid bulb, immediately downstream of observed stenoses, although the sign of the correlation coefficient seems to depend on the severity of the stenosis. The results in the two patients

(P1 and P2) with non-constricting (< *50%*) stenoses, show that the WSS (OSI) in P1 at that location generally exhibits strong negative (positive) correlations with SMC, lipid and collagen presence, but no significant correlation with macrophage presence. A different patient (P2), interestingly, exhibits the opposite tendency, showing strong correlations with macrophage presence but no significant correlation with the other parameters. This is evidence that the inflammatory process, although at different stages in each case, is continuing downstream of the stenosis. In a third patient (P3) with an *80%* stenosis, the WSS at that location correlates *positively* with SMC, lipids, macrophages and collagen. The difference is believed to be due to the extensive re-modeling and the advanced stenosis present. No statistically significant correlations were found in the case of P4.

Keywords: Atherosclerosis, vulnerable plaque, low wall shear stress, stenosis, macrophages.

VI.2. Introduction

Atherosclerosis is believed to be initiated by endothelial dysfunction from a variety of causes including elevated and modified LDL cholesterol (low-density lipoprotein), free radicals caused by cigarette smoking, hypertension and possibly infectious microorganisms. Endothelial dysfunction leads to compensatory responses that change the normal homeostatic properties of the endothelium leading to increased permeability and adhesiveness of the endothelium to leukocytes and platelets [1] that contribute to the inflammatory response observed in the early stages of the disease. If the offending agents are not removed or neutralized, the inflammatory response continues. Fatty streaks appear in the lesion [2] consisting of lipid-laden monocytes and macrophages (foam cells) and T lymphocytes. Monocytes that migrate through the artery wall differentiate and become macrophages. Inflammation can also stimulate smooth-muscle migration. The resulting mass of cells forms an intermediate lesion. Up to a point, the lumen area remains unchanged; the arterial wall can still expand its outer diameter to accommodate the thickening.

As macrophage and smooth muscle cell accumulation by migration and proliferation continues, the lesion grows. Eventually, the artery can no longer expand to accommodate the changes and the now advanced lesion progresses into the lumen. As it does, a fibrous cap forms that walls it off from the blood. The enclosed mass contains a mixture of leukocytes, lipids, and debris, which may form a necrotic core. The lesion may continue to grow through leukocyte adhesion and infiltration at the shoulders of the cap [1].

Several studies have shown that macrophages may stimulate metalloproteinase (MMP) production in the lesions [3-5]. MMPs such as collagenases, elastases, and stromelysins may cause degradation of the collagenous fibrous cap. Depending on the local stresses, typically highest at the shoulders of the lesion due to stress concentrations there [6-8], an event referred to as plaque rupture may occur, followed by platelet aggregation and thrombosis.

There is a long standing hypothesis that correlates fluid dynamic forces and atherosclerotic disease. Many analytical, numerical and experimental studies have been conducted, inspired by the observation that atherosclerotic disease is focal, typically occurring at sites of complex hemodynamics. These include arterial bifurcations, junctions and/or regions of high curvature.

Fry [9, 10] was the first to postulate that high wall shear stresses would cause damage to the arterial wall; endothelial disruption or denudation could lead to atherosclerosis. Since then, however, it has become widely accepted that low or oscillatory shear stress rather than high contribute to atherogenesis [11-13].

Previous studies (for an up to date review, see [14]) have shown that regions of low or oscillatory shear stress cause monocyte adhesion to the endothelial wall, the first stage in progression of the disease. Low shear stress leads to the expression of VCAM-1, a monocyte adhesion molecule [15], increased and prolonged NF-kappa B activity, a

regulator of some endothelial cell adhesion molecules [16] and a reduction in NO release (augmented levels inhibit monocyte adhesion), [17, 18].

Extensive numerical work has gone into identifying such regions of low shear stress for stenosed arteries, healthy and diseased bifurcations. With many such studies conducted, it is somewhat surprising that none of them (to the authors' knowledge) have rigorously tested the validity of the low shear stress hypothesis by using *in vivo* data and correlating the resulting distributions to histology, although each of these two aspects has been studied separately and extensively. On the first topic, Berger and Jou [19] provide a comprehensive summary of all the work conducted to date on fluid mechanic modeling of steady and unsteady three dimensional flows in stenotic vessels. Despite this, very few researchers, (e.g.[20] have used realistic geometries to represent the diseased arterial wall. On the second topic, a recent article by Dirksen et. al. [21] showed that the distribution of smooth muscle cells and macrophages relate to the *direction* of flow, but they came short of calculating detailed wall shear stress (WSS) distributions.

A major goal of this present study is thus to test the hypothesis that low or oscillatory shear correlates to the progression of atherosclerosis using 3D computational finite element fluid mechanic analyses based on realistic geometries and flow profiles by input of actual data gathered from *in vivo* imaging of diseased patients. Histology specimen (advanced plaques) from diseased arteries harvested from the same patients after carotid endarterectomy provide a conclusive method to correlate regions of monocyte deposition/macrophage accumulation, smooth muscle proliferation, lipid deposition and collagen production, all characteristics of the inflammatory/remodeling process, to regions of low and oscillating fluid wall shear stress. The carotid bifurcation was chosen for this study for its size and ease of imaging on the one hand and because carotid endarterectomy is still the most common treatment for advanced carotid lesions, providing a ready source of specimens for study.

VI.3. Techniques Employed

Four patients, referred to as P1, P2, P3 and P4 (ages 61-73) were chosen for this study. The procedure for the processing of each patient's data set from magnetic resonance imaging and geometry reconstruction to finite element analysis has been discussed in detail previously [22] and will consequently only be summarized here. This procedure consists of several stages: MR (magnetic resonance) imaging, edge detection, lofting, flow profile generation and finite element analysis. The final steps, histological staining and processing, and the correlation to finite element results is used to process the patient specimens obtained at the time of surgery. These final steps are discussed in detail below. A schematic of the entire process is summarized in figure 1.

VI.3.1. From Magnetic Resonance Imaging to Finite Element Analysis

Acquisition of MR geometry by a Siemens Sonata 1.5 Tesla machine is achieved using a surface coil that fits to the jawline beneath which the carotid bifurcation is located and achieves 0.39mm in-plane resolution over 2mm thick slices. An edge detection protocol then reads the geometry MR data to generate a series of 2D slices. Estimation of regional vessel structure is based on variational energy minimization and curve evolution [23]. Lofting across these 2D cross-sectional structures at each level of the carotid bifurcation is carried out using a solid modeling software (SolidWorks Corporation, Concord, MA). Interpolation across the outer contours of these slices produces the external 3D solid body, while the 3D structure that results from interpolating across the inner contours produces the 3D fluid volume. Subtraction of these two entities yields the 3D vascular structure (not used in the simulations, but used later in matching the histological slice location to the histology specimen). Figure 2 shows the solid models for each patient. The 3D fluid geometry, velocity at the inlet (common carotid), and velocity at the outlet (internal carotid) files (based on fully developed Womersley profiles with centerline velocities from ultrasound measurements – see figure 3) are then imported into the finite element software (ADINA, version 7.4, Automatic Dynamic Incremental Nonlinear Analysis, Watertown, MA) to simulate the fluid dynamics in a 2 step process. The output velocity profile at the external carotid from the first step is used as an input to the second step, which is considered the final solution, following the procedure of Perktold et. al. [24]. Blood is treated as an incompressible, Newtonian fluid (an assumption that has

repeatedly been shown to hold well for large arteries [19, 24], where shear rates generally exceed 100 s^{-1}) and the flow assumed laminar, an assumption that holds well for smooth, non-severe stenoses [25], as encountered herein. The more severe constrictions could certainly cause turbulence, but the turbulence intensity is likely to be small. The simulations performed are rigid-walled; arterial wall motion is neglected in lieu of the fact that the presence of plaque in diseased arteries significantly reduces strain levels [26]. Free meshing using linear elements was used with an element edge size of 0.4 mm. The finite element meshes used are presented in figure 4 and model details are summarized in table 1. All computations were performed using a SGI Origin 2000 equipped with 4 processors and 6 GB of RAM. Solution times varied between 12 and 24 hours..

VI.3.2. Plaque Specimen Cutting, Histological Staining and Processing

As mentioned in earlier, it was chosen to correlate regions of macrophage accumulation, smooth muscle presence, lipid deposition and collagen production, all characteristics of the inflammatory/remodeling process to the fluid mechanical parameters of interest. Macrophages have been chosen because of their key role in disease progression. Increased macrophage concentration is a direct consequence of increased monocyte migration into the arterial wall where they differentiate to become macrophages and is, in that sense, a gauge of endothelial 'adhesiveness' (through the presence of vascular adhesion molecules on the endothelium, e.g. VCAM-1 and monocyte chemoattractants, e.g. MCP-1). Macrophages take up modified LDL (low density lipoprotein) and become foam cells. Modified LDL, trapped in foam cells, is chemotactic for other monocytes and can thus help expand the inflammatory response by stimulating the migration of more monocyte-derived macrophages. Smooth muscle cell proliferation and arterial remodeling, associated with increased collagen I, III, and IV production in the extracellular matrix, are also features of atherosclerotic inflammation [1]. Lipids, on the other hand were chosen for their prominent role in plaque instability. A recent study [27] demonstrated that the presence of lipid pools in atherosclerotic plaques dramatically increases mechanical stresses in the lesion, thus decreasing the mechanical stability of the atheroma.

Specimens are extracted from patients a few days after magnetic resonance imaging. Plaque angular orientation is tracked by observing the location of the surgical incision, which is asigned a reference value of zero degrees, and runs down the centerline of the carotid bulb-common carotid interface. Due to the absence of the incision in the external carotid artery, its angular orientation is unknown; all correlations with fluid dynamic parameters herein are therefore solely of the common and internal carotid arteries.

The specimen is then stored in a cold saline solution and is transported to a vascular histopathology lab where it is cut, at chosen vertical positions (see figure 5), and later stained. Four thin sections (2-3 microns thick) are obtained at each vertical position for individual staining. Collagen is stained by sirius red (0.1% solution of Sirius Red F3BA in saturated aqueous piciric acid), lipids by oil red O (0.5% oil red O solution in 100% propylene glycol), macrophages by CD68 (monoclonal antibody anti-surface antigen) and smooth muscle cells by HHF-35 (monoclonal antibody anti-alfa-actin). Sample staining for each is illustrated in figure 6.

Once stained, each specimen is photographed, digitized and then imported into a commercial image processing software, OPTIMAS (Media Cybernetics) for quantitative analysis. Each slice is divided into sixteen equiangular segments over which the area of each histological variable (SMC, lipids, macrophages or collagen) being examined is recognized in yellow (see figure 7 for an example) and recorded. Each yellow area is then normalized to the largest histologic area of a segment within each patient.

VI.3.3. Regression analysis

The dimensionless areas for each histological variable (SMC, lipids, macrophages or collagen) are then used to correlate against wall shear stress (WSS averaged over the entire cycle) and oscillatory shear index (OSI as defined by Ku et. al. [12]) averaged per 22.5° segments (and 1 mm thickness; 0.5 mm above and 0.5 mm below the selected slice or cutting plane) obtained from the finite element simulations.

It was necessary to assign a finite thickness to the section to permit extraction of finite element data, since the models were meshed using free meshes and the nodal points do not lie on the same plane. A 2 mm slice (1 mm above and 1 mm below the selected cutting plane) was also used to verify that slice width was not a source of significant error; the values were within 2% of one another (using a 1mm vs a 2 mm slice thickness) and the profile shapes (ie. shape of the wall shear stress vs. angle curve) virtually identical.

Maximum wall shear stress temporal gradient (WSSTG) was also calculated and correlated to histology. It is obtained by computing the gradient in WSS between every two consecutive time points during the cycle and taking the maximum of these values. Each of the correlations are performed slice-by-slice.

All correlations are based on linear least squares regression unless otherwise indicated. N (number of data points) = 16 per slice. Zero values throughout a section are indicated if that is the reason that no correlation was found there. Stringent criteria ($p < 0.1\%$) [12, 28] are used to name a correlation highly statistically significant. Correlations with $p > 5\%$ were not recorded.

VI.4. Results

VI.4.1. Wall Shear Stress and Oscillatory Shear Index Patterns

The average WSS profiles and OSI bandplots are plotted in figures 8 and 9, respectively. WSS is plotted on a logarithmic scale to exaggerate the regions of low WSS. We define 'low WSS' as pools of WSS less than 0.5 Pa, the range for which an atherosclerotic gene expression profile is expected [14].

Several regions of pathologically high wall shear stress exist. P1 has two stenoses present, with the more severe one in the external carotid. Both P1 and P3 have severely stenosed external carotid arteries. P1, however, has a much less severe stenosis in the internal carotid artery than P3. The wall shear stresses throughout P1's external carotid

stenosis exceed 10 Pa in most of the branch, since the stenosis is severe and long. In P3, shear stress in both throats of the internal and external carotids at the stenosis exceed 10 Pa, but do not extend throughout the length of the artery, due to the dilating of the arteries immediately distal to the bifurcation. Shear stress levels this high are not seen in P2 and P4, not even at the throat of the stenoses in the internal carotid of P2 (values between 3-6 Pa) except right at the flow divider, which are typical for that region [24, 29]. Levels of shear stress increase again, however, at the outlet of the external carotid of P2.

Pronounced areas of low wall shear stresses (and flow recirculation) can be found downstream of each of the stenoses in each of the patients. This also coincides with areas of high OSI in *some* (see Discussion) of the patients. Another prominent region of low WSS is just at the carotid bulb of P4, which was not subjected to excessive remodeling in this particular patient, and looks remarkably similar to observed WSS patterns in the carotid bulb of healthy volunteers [22, 29].

The WSS levels in the common carotid are quite uniform and hover around 1 Pa in all patients, except P4, in which a significant portion of the common carotid was not imaged.

VI.4.2. Regression Analysis

The result of the regression analyses is shown in tables 2 (a) through (d). Highly statistically significant correlations [12, 28] are indicated in bold typeface. P4 has regression coefficients with absolute magnitudes as high as 0.67, but none are statistically significant. Correlations within P1, P2 and P3 exhibit several common features. First, all but one of the statistically significant correlations in these patients correspond to the same location: the proximal internal carotid just upstream of the carotid bulb (slice 5 in P1, slice 4 in P2 and slice 4 in P3), downstream of a stenosis. Furthermore, the values of WSS at these locations with statistically significant correlations span both the ranges of low ($< 0.4\ Pa$) and high ($> 1.5\ Pa$) WSS.

Correlations with WSSTG were found to follow the same trend as the WSS and were subsequently omitted from table 2 for the lack of displaying any interesting (or different) trends.

VI.5. Discussion

VI.5.1. Explanation of observed flow profiles

Downstream of a stenosis, pressure recovery and the wall curvature associated with the increase in flow cross-sectional area gives rise to flow separation. Even though this is the case, pools of high OSI are observed in some, and not all, the regions of patients 1-4 where low shear stress reversing flow exists. This relates to the definition of the OSI as a non-dimensional measure that quantifies the time a particular wall region experiences cross or reverse flow. The mean flow direction is defined as the temporal mean of the shear stress vector. For purely oscillatory flow, the OSI approaches 0.5. Note that the OSI does not take into account the magnitude of the shear stress vectors, solely the directions [12]. This means that regions with uninterrupted re-circulating flow will not be identified by the OSI, since the temporal mean direction of flow will be reversed. Regions that exhibit this behavior include: immediately downstream of the stenosis in the internal carotid artery of P3, on the side of the flow divider, where a re-circulating pool of blood is trapped between slices 2 and 3 (see figure 4 for slice locations), as well as immediately distal to the stenosis at slice 6 of P4, where recirculation lies in the WSS zone at the end of the fluid domain. Areas as such are more susceptible to thrombus formation [25].

VI.5.2. The presence and absence of correlations

The values 0.4 and 1.5 *Pa* have important biological significance. WSS levels above 1.5 *Pa* are believed to induce endothelial quiescence and an atheroprotective gene expression profile, whereas WSSs below 0.4 *Pa* stimulate an atherogenic phenotype [14]. It is possible that the statistically significant correlations are detected mostly (there are a few exceptions where statistically insignificant correlations or no correlations at all are also detected) at these sites where both low and high WSS are exhibited (the proximal internal carotid just upstream of the carotid bulb – slice 5 in P1, slice 4 in P2 and slice 4 in P3,

downstream of a stenosis) solely because of this bi-modal behavior; and significant correlations are absent elsewhere because of the absence of wall shear stresses that span both these limits within the same slice, thus no different cellular response is elicited and hence, a correlation is absent. It should not be surprising then, that the occurrence of significant correlations is the exception, rather than the norm within the results.

With the absence of these correlations, it can be argued that WSS or fluid dynamics in general, plays a relatively minor role in disease progression. It should be noted, however, that the significant correlations are almost all (with the notable exception of a correlation between WSS and smooth muscle cells in the CCA of P3; see slice 1) encountered in the vicinity of the carotid bulb (immediately distal) which has been recognized as one of the first sights of plaque formation and low WSS [14, 19, 25]. This being the case, it is possible that the earliest plaques are initiated as a result of the functional regulation of the endothelium by local wall shear stress [14] mobilizing the biochemical sequence that follows, which expands the disease to surrounding areas (e.g. through chemoattractants).

The carotid sinus itself (see slices at mid-bulb level: P1-slice 4, P2-slice 3, P3-slice 2) is already stenosed in all the patients studied (except in P4). It is conceivable that the correlations at midpoint carotid sinus disappeared due to the fact that the stenosis is *already* present—that the lipids, macrophages, smooth muscle cell proliferation and collagen production has already occurred and transformed the WSS from a low/high distribution along the circumference to high ($> \sim 1.5\ Pa$) at the throat of the stenoses all around the circumference. This is supported by the observation that in P4, which is the only patient that does not have a stenosis at the IC bulb, some weak correlations exist there (see P4-slice 2 in table 2d): WSS correlates negatively and OSI positively with macrophage and lipid presence, suggesting that the monocyte/lipid deposition and the monocyte differentiation into macrophages processes are still ongoing and that this particular correlation is not concealed by the presence of the stenoses.

In P1-slice 5 and P2-slice 4, the regression coefficients correlate negatively with the WSS and positively with the OSI, as is expected immediately downstream of the stenosis

which precedes these sections. Regions of flow separation (and low fluid shear stress) are observed at the outer wall, as would be expected due to the abrupt change in curvature and the associated adverse pressure gradient there. Also contributing to the tendency for separation is the increase in cross-sectional area, and consequent increase in pressure, just distal to the stenosis. The WSS (OSI) in P1 generally observes strong negative (positive) correlations with SMC, lipid and collagen presence, but no correlation to macrophage presence and vice versa in P2, which experiences solely strong correlations with macrophage presence. This is evidence that the inflammatory process, although possibly at different stages in each case, is continuing downstream of the stenosis.

In P3-slice 4, the WSS correlates *positively* with SMC, lipids, macrophages and collagen. The difference here is believed to be due to the extensive re-modeling and the advanced stenosis (80% stenosis) present. As can be seen in figure 3, the carotid bulb is severely narrowed. Blood is forced to flow as a high velocity jet through the stenosis away from the divider wall towards the outer wall (velocity profiles not shown here). This causes elevated levels of wall shear stress along the outer wall of the internal carotid and a recirculation zone (of low shear stress) along the inner wall (between slice 3 and 4). Before the existence of the stenosis, the wall shear stress patterns might well have been opposite, with high wall shear stress levels at the divider wall and low wall shear stress throughout the bulb. With time, the inflammatory process deposited lipids and promoted monocyte migration into the arterial wall as well as promoted smooth muscle cell proliferation and collagen production at these *initial* regions of low WSS. Through continued inflammation and remodeling, the originally low regions of low WSS transformed to form constricted regions of high WSS, explaining why the observed correlations are positive. This 'stress-induced adaptation' illustrates a vessel remodeling process in which the vessel attempts to bring the WSS up, and subsequently succeeds, though exaggeratingly, forcing the vessel further and further into the closure direction. This behavior is currently absent in P1, P2 and P4 that have less severe stenoses; the low wall shear stress localities remain on the outer wall of the internal carotid (in P1 and P2; albeit shifted further downstream from the bulb with respect to the healthy case – due to the stenoses there).

Correlations with the OSI in P3-slice 4 are absent due to the reasons mentioned earlier about the definition of OSI. Even though there is a region of flow separation on the inner divider wall between slice 3 and 4, this region is a trapped pool of blood were no flow reversal occurs. One might consider two possible hypotheses: the first is that since the blood is trapped, no exchange of monocytes, lipids, etc... is present and indeed the separated flow region does not contribute to atherogenesis and that the value of OSI equals zero is appropriate. On the other hand, it is possible that some monocytes and lipids enter this separated flow pool (almost certainly in an unsteady flow like this) of blood right at the shear layer interface between the high velocity jet exiting the stenoses and the low WSS pool, so that a more indicative manner of detecting separating flow (rather than just oscillating flow) needs to be devised. This question needs to be answered by using mass transfer tools and treating lipids and monocytes as different phases in the blood solution. What is clear, however, is that one should always have access to the unprocessed data (namely the predicted velocity distributions) when making conclusions of this sort.

VI.6. Summary

3D finite element analyses of the diseased carotid bifurcation using reconstructed geometries based on *in vivo* geometries and ultrasound velocity measurements were conducted and the resulting wall shear stress (WSS) and oscillatory shear index (OSI) distributions correlated to histological parameters involved in atherogenesis.

The results indicate that strong correlations exist in the vicinity of the carotid bulb, immediately downstream of observed stenoses, although the sign of the correlation coefficient seems to depend on the severity of the stenosis. The results in the two patients (P1 and P2) with non-constricting ($< 50\%$) stenoses, show that the WSS (OSI) in P1 at that location generally observes strong negative (positive) correlations with SMC, lipid and collagen presence, but no correlation to macrophage presence and vice versa in P2, which experiences solely strong correlations with macrophage presence. This is evidence

that the inflammatory process, although eliciting a different response in each case, is continuing downstream of the stenosis. In P3 (*80%* stenosis), the WSS at that location correlates *positively* with SMC, lipids, macrophages and collagen. The difference is believed to be due to the extensive re-modeling and the advanced stenosis present. No statistically significant correlations were found in the case of P4.

VI.7. References

1. Ross, R. (1999) Atherosclerosis--an inflammatory disease. *N Engl J Med* **340**, 115-26.
2. Napoli, C., D'Armiento, F.P., Mancini, F.P., Postiglione, A., Witztum, J.L., Palumbo, G., Palinski, W. (1997) Fatty streak formation occurs in human fetal aortas and is greatly enhanced by maternal hypercholesterolemia. Intimal accumulation of low density lipoprotein and its oxidation precede monocyte recruitment into early atherosclerotic lesions. *J Clin Invest* **100**, 2680-90.
3. Shah, P.K., Falk, E., Badimon, J.J., Fernandez-Ortiz, A., Mailhac, A., Villareal-Levy, G., Fallon, J.T., Regnstrom, J., Fuster, V. (1995) Human monocyte-derived macrophages induce collagen breakdown in fibrous caps of atherosclerotic plaques. Potential role of matrix-degrading metalloproteinases and implications for plaque rupture. *Circulation* **92**, 1565-9.
4. Galis, Z.S., Sukhova, G.K., Lark, M.W., Libby, P. (1994) Increased expression of matrix metalloproteinases and matrix degrading activity in vulnerable regions of human atherosclerotic plaques. *J Clin Invest* **94**, 2493-503.
5. Schonbeck, U., Mach, F., Sukhova, G.K., Murphy, C., Bonnefoy, J.Y., Fabunmi, R.P., Libby, P. (1997) Regulation of matrix metalloproteinase expression in human vascular smooth muscle cells by T lymphocytes: a role for CD40 signaling in plaque rupture? *Circ Res* **81**, 448-54.
6. Richardson, P.D., Davies, M.J., Born, G.V. (1989) Influence of plaque configuration and stress distribution on fissuring of coronary atherosclerotic plaques. *Lancet* **2**, 941-4.
7. Loree, H.M., Kamm, R.D., Stringfellow, R.G., Lee, R.T. (1992) Effects of fibrous cap thickness on peak circumferential stress in model atherosclerotic vessels. *Circ Res* **71**, 850-8.
8. Cheng, G.C., Loree, H.M., Kamm, R.D., Fishbein, M.C., Lee, R.T. (1993) Distribution of circumferential stress in ruptured and stable atherosclerotic lesions. A structural analysis with histopathological correlation. *Circulation* **87**, 1179-87.
9. Fry, D.L. (1968) Acute vascular endothelial changes associated with increased blood velocity gradients. *Circ Res* **22**, 165-97.
10. Fry, D.L. (1969) Certain histological and chemical responses of the vascular interface to acutely induced mechanical stress in the aorta of the dog. *Circ Res* **24**, 93-108.

11. Caro, C.G., Fitz-Gerald, J.M., Schroter, R.C. (1971) Atheroma and arterial wall shear. Observation, correlation and proposal of a shear dependent mass transfer mechanism for atherogenesis. *Proc R Soc Lond B Biol Sci* **177**, 109-59.
12. Ku, D.N., Giddens, D.P., Zarins, C.K., Glagov, S. (1985) Pulsatile flow and atherosclerosis in the human carotid bifurcation. Positive correlation between plaque location and low oscillating shear stress. *Arteriosclerosis* **5**, 293-302.
13. Friedman, M.H., Hutchins, G.M., Bargeron, C.B., Deters, O.J., Mark, F.F. (1981) Correlation of human arterial morphology with hemodynamic measurements in arterial casts. *J Biomech Eng* **103**, 204-7.
14. Malek, A.M., Alper, S.L., Izumo, S. (1999) Hemodynamic shear stress and its role in atherosclerosis. *Jama* **282**, 2035-42.
15. Gonzales, R.S., Wick, T.M. (1996) Hemodynamic modulation of monocytic cell adherence to vascular endothelium. *Ann Biomed Eng* **24**, 382-93.
16. Mohan, S., Mohan, N., Sprague, E.A. (1997) Differential activation of NF-kappa B in human aortic endothelial cells conditioned to specific flow environments. *Am J Physiol* **273**, C572-8.
17. Tsao, P.S., Lewis, N.P., Alpert, S., Cooke, J.P. (1995) Exposure to shear stress alters endothelial adhesiveness. Role of nitric oxide. *Circulation* **92**, 3513-9.
18. Tsao, P.S., Buitrago, R., Chan, J.R., Cooke, J.P. (1996) Fluid flow inhibits endothelial adhesiveness. Nitric oxide and transcriptional regulation of VCAM-1. *Circulation* **94**, 1682-9.
19. Berger, S.A., Jou, L.D. (2000) Flows in Stenotic Vessels. *Annual Review of Fluid Mechanics* **32**, 347-384.
20. Stroud, J.S. (2000) Numerical simulations of blood flow in stenotic vessels. University of California at Berkeley, Berkeley.
21. Dirksen, M.T., van der Wal, A.C., van den Berg, F.M., van der Loos, C.M., Becker, A.E. (1998) Distribution of inflammatory cells in atherosclerotic plaques relates to the direction of flow. *Circulation* **98**, 2000-3.
22. Younis, H.F., Kaazempur-Mofrad, M.R., Chan, R.C., Chau, A.H., Hinton, D.P., Isasi, A.G., Kim, L.A., Kamm, R.D. (2001) A Numerical Study of Carotid Artery Wall and Fluid Mechanics based on in vivo Magnetic Resonance Images of Healthy Volunteers. *in progress* .
23. Chan, R. (2001) Non-invasive ultrasound monitoring of regional carotid wall structure and deformation in atherosclerosis. In *Health Sciences and Technology*MIT, Cambridge, MA.
24. Perktold, K., Resch, M., Florian, H. (1991) Pulsatile non-Newtonian flow characteristics in a three-dimensional human carotid bifurcation model. *J Biomech Eng* **113**, 464-75.
25. Ku, D. (1997) Blood Flow in Arteries. *Annual Review of Fluid Mechanics* **32**, 346-384.
26. Williamson, S.D., Lam, Y., Younis, H.F., Huang, H., Kamm, R.D. (2001) On the Sensitivity of Wall Stresses in Diseased Arteries to Variable Material Properties. *submitted to the Journal of Biomechanical Engineering* .
27. Huang, H., Virmani, R., Younis, H., Burke, A.P., Kamm, R.D., Lee, R.T. (2001) The impact of calcification on the biomechanical stability of atherosclerotic plaques. *Circulation* **103**, 1051-6.

28. Taylor, J.R. (1997) *An Introduction to Error Analysis*. University Science Books, Sausalito, California.
29. Milner, J.S., Moore, J.A., Rutt, B.K., Steinman, D.A. (1998) Hemodynamics of human carotid artery bifurcations: computational studies with models reconstructed from magnetic resonance imaging of normal subjects. *J Vasc Surg* **28**, 143-56.

VI.8. Figures and Tables

VI.8.1. Table Captions

Table 1. Finite element mesh details for each patient.

Table 2. Correlations between hemodynamic variables and normalized area (normalized to the largest histological area of 22.5° section of each patient– see methods section) of smooth muscle cells (SMCs), lipids (Lip), macrophages (Mac) and collagen (Col); X indicates any single histological variable. WSS (Pa) is the average wall shear stress over the cycle and OSI the oscillatory shear index. CC: common carotid; IC: internal carotid; FD: flow divider. A graphical representation of the slice location is shown in figure 3. All correlations are based on linear least squares regression unless otherwise indicated. N (number of data points) = 16 per slice. Zero values throughout a section are indicated if that is the reason that no correlation was found there. Highly statistically significant correlations ($p < 0.1\%$) are indicated in bold. Correlations with $p > 5\%$ were not recorded.

VI.8.2. Tables

Patient	Number of elements	Number of nodes	Number of equations
P1	72014	14524	58096
P2	103570	21013	84052
P3	56225	11412	45648
P4	211869	41547	166188

Table 1

(a) Patient 1 Slice Number and Location	Correlating Variables	Range of Hemodynamic Variable (WSS: *Pa*; OSI: no units)	Range of Normalized Area of Histological Variable (%)	*r* Correlation Coefficient	*p* Probability (%)
1 – Proximal CC	WSS-Lip	0.6 – 1.6	0	-	-
	WSS-Mac	0.6 – 1.6	0	-	-
	OSI-X	0	-	-	-
2 – Mid CC	WSS-Lip	0.4 – 2.2	0	-	-
	OSI-X	0	-	-	-
3 – Distal CC	WSS-SMC	1.2 – 1.9	1 – 15	+ 0.72	< 0.2
	OSI-X	0	-	-	-
4 – IC Bulb and FD	WSS-SMC	1.5 – 21	0 – 10	+ 0.62	< 1
	WSS-Mac	1.5 – 21	0 – 4.5	- 0.53*	< 3.5
	OSI-Mac	0 – 0.05	0 – 4.5	+ 0.71	< 0.22
5 – Distal IC Bulb / Proximal IC	WSS-SMC	0 – 3.3	2 – 23	**- 0.80**	< 0.05
	WSS-Lip	0 – 3.3	0 – 15	**- 0.81***	< 0.05
	WSS-Mac	0 – 3.3	0	-	-
	WSS-Col	0 – 3.3	0 – 29	**- 0.95***	< 0.05
	OSI-SMC	0 – 0.38	2 – 23	+ 0.56	< 2.4
	OSI-Lip	0 – 0.38	0 – 15	**+ 0.76**	< 0.05
	OSI-Mac	0 – 0.38	0	-	-
	OSI – Col	0 – 0.38	0.6728 ??	**+ 0.82**	< 0.05
All Slices together (N=80)	WSS-SMC	0 – 21	0 – 32	**- 0.45***	< 0.05
	WSS-Lip	0 – 21	0 – 15	**- 0.45***	< 0.05
	OSI-Lip	0 – 0.38	0 – 15	**+ 0.68**	< 0.05
* Exponential regression that considerably improved curve fit used.					

(b) Patient 2 Slice Number and Location	Correlating Variables	Range of Hemodynamic Variable (WSS: *Pa*; OSI: no units)	Range of Normalized Area of Histological Variable (%)	*r* Correlation Coefficient	*p* Probability (%)
1 – Distal CC	WSS-SMC	0.6 – 2.9	0	-	-
	WSS-Col	0.6 – 2.9	1 – 30	- 0.63	< 0.9
	OSI-X	0	-	-	-
2 – Proximal IC bulb / FD	WSS-SMC	0.4 – 5.5	0	-	-
	OSI-SMC	0 – 0.09	0	-	-
3 – Mid IC Bulb and Distal to FD	OSI-X	0	-	-	-
4 – Proximal IC	WSS-Mac	0.1 – 3.3	0.2 – 11	**- 0.95***	< 0.05
	OSI-Mac	0 – 0.07	0.2 – 11	**+ 0.75**	< 0.1
5 – Mid IC	WSS-Lip	1.4 – 3.6	1.7 – 8.5	+ 0.52	< 3.9
	WSS-Col	1.4 – 3.6	2 – 16	+ 0.68	< 0.2
	OSI-X	0	-	-	-
6 – Distal IC	WSS-SMC	2.7 – 6.5	0 – 2	+ 0.50	< 4.9
	WSS-Lip	2.7 – 6.5	0.5 – 21	+ 0.51	< 4.4
	OSI-X	0	-	-	-
All Slices together (N=96)	WSS-Mac	0.1 – 6.5	0 – 11	**- 0.50***	< 0.05
	WSS-Col	0.1 – 6.5	0.6 – 44	**- 0.36***	< 0.08
	OSI-Mac	0 – 0.09	0 – 11	+ 0.28	< 0.7
* Exponential regression that considerably improved curve fit used.					

(c) Patient 3 Slice Number and Location	Correlating Variables	Range of Hemodynamic Variable (WSS: *Pa*; OSI: no units)	Range of Normalized Area of Histological Variable (%)	*r* Correlation Coefficient	*p* Probability (%)
1 – Mid CC	WSS-SMC	0.6 – 1.7	0 – 5	+ **0.76**	< 0.1
	WSS-Lip	0.6 – 1.7	0 – 2	- 0.51	< 4.4
	WSS-Mac	0.6 – 1.7	0 – 13	+ 0.59	< 1.6
	WSS-Col	0.6 – 1.7	4 – 11	+ 0.57	< 2.2
	OSI-X	0	-	-	-
2 – Distal CC/Proximal IC Bulb	WSS-Lip	2.5 – 4.7	1 – 13	- 0.50	< 4.9
	WSS-Col	2.5 – 4.7	5 – 24	+ 0.57	< 2.2
	OSI-X	0	-	-	-
3 – Distal IC Bulb / Proximal IC	WSS-Lip	1 – 13	0 – 6.5	- 0.51	< 4.4
	WSS-Col	1 – 13	1 – 9	- 0.53	< 3.5
	OSI-X	0 (except for one point = 0.1)		-	-
4 – Proximal IC	WSS-SMC	0.5 – 13	0 – 5	+ **0.79**	< 0.06
	WSS-Lip	0.5 – 13	0 – 4.3	+ **0.87**	< 0.05
	WSS-Mac	0.5 – 13	0 – 15	+ **0.84**	< 0.05
	WSS-Col	0.5 – 13	0 – 30	+ 0.72	< 0.2
	OSI-X	0	-	-	-
All Slices Together (N=64)	WSS-Col	0.5 – 13	0 – 29	+ 0.30	< 1.7

(d) Patient 4 Slice Number and Location	Correlating Variables	Range of Hemodynamic Variable (WSS: *Pa*; OSI: no units)	Range of Normalized Area of Histological Variable (%)	*r* Correlation Coefficient	*p* Probability (%)
1 – Distal CC	WSS-SMC	0 – 2.5	0	-	-
	OSI-SMC	0.04 – 0.35	0	-	-
	OSI-Col	0.04 – 0.35	0 – 3.5	+ 0.53	< 3.5
2 – IC Bulb and FD	WSS-SMC	0.1 – 1.6	0	-	-
	WSS-Lip	0.1 – 1.6	0 – 2.2	- 0.67*	< 0.5
	WSS-Mac	0.1 – 1.6	0 – 0.65	- 0.66*	< 0.6
	OSI-SMC	0 – 0.37	0	-	-
	OSI-Lip	0 – 0.37	0 – 2.2	+ 0.54	< 3.1
	OSI-Mac	0 – 0.37	0 – 0.65	+ 0.62	< 1.0
3 – Mid IC Bulb and Distal to FD	WSS-SMC	0.06 – 1.3	0	-	-
	WSS-Lip	0.06 – 1.3	0	-	-
	WSS-Mac	0.06 – 1.3	0	-	-
	OSI-SMC	0 – 0.25	0	-	-
	OSI-Lip	0 – 0.25	0	-	-
	OSI-Mac	0.06 – 1.3	0	-	-
4 – Proximal IC	WSS-SMC	0.6 – 1.5	0	-	-
	OSI-SMC	0	0	-	-
5 – Mid IC	None	-	-	-	-
6 – Distal IC	WSS-Col	3 – 5.3	0 – 34	- 0.53	< 3.5
	OSI-X	0	-	-	-
All Slices Together (N=96)	WSS-SMC	0 – 5.3	0 – 8	+ 0.23	< 2.9
	WSS-Lip	0 – 5.3	0 – 17.5	+ 0.32	< 0.2
* Exponential regression that considerably improved curve fit used.					

Table 2

VI.8.3. Figure Captions

Fig 1. Overall schematic of research protocol, from data collection to extraction of correlations.

Fig 2. Fluid models of patient geometries produced by reconstruction of MR data. The internal carotid artery is always on the left of each figure.

Fig 3. Womersley flow rate profiles based on ultrasound centerline velocity measurements.

Fig 4. Finite element meshes used in study.

Fig 5. Vertical positions at which cuts in the plaque were made for histological staining and analysis. These figures cut through the center of the 3D model segmented from the MR data. Note that the shaded area represents the arterial wall and the innermost curves represent the lumen. Slice 1 is the lowermost slice in the common carotid in each patient. Internal carotid artery is always on the left.

Fig 6. Sample staining of a slice from an extracted plaque specimen for smooth muscle cells (a), lipids (b), macrophages (c) and collagen (d). The stained areas are marked in red.

Fig 7. Subdivision of a stained specimen into sixteen equiangular segments and recognition (in yellow), using image processing software, the stained area per segment. These areas are then used to correlate with fluid dynamic variables. This particular slide is extracted from patient 1 (distal common carotid; immediately proximal to the bifurcation).

Fig 8. Computed average wall shear stress [Pa] profiles (WSS) over the cycle for each patient studied: P1 through P4.

Fig 9. Computed oscillatory shear index (OSI) bandplot over the cycle for each patient studied: P1 through P4.

VI.8.4. Figures

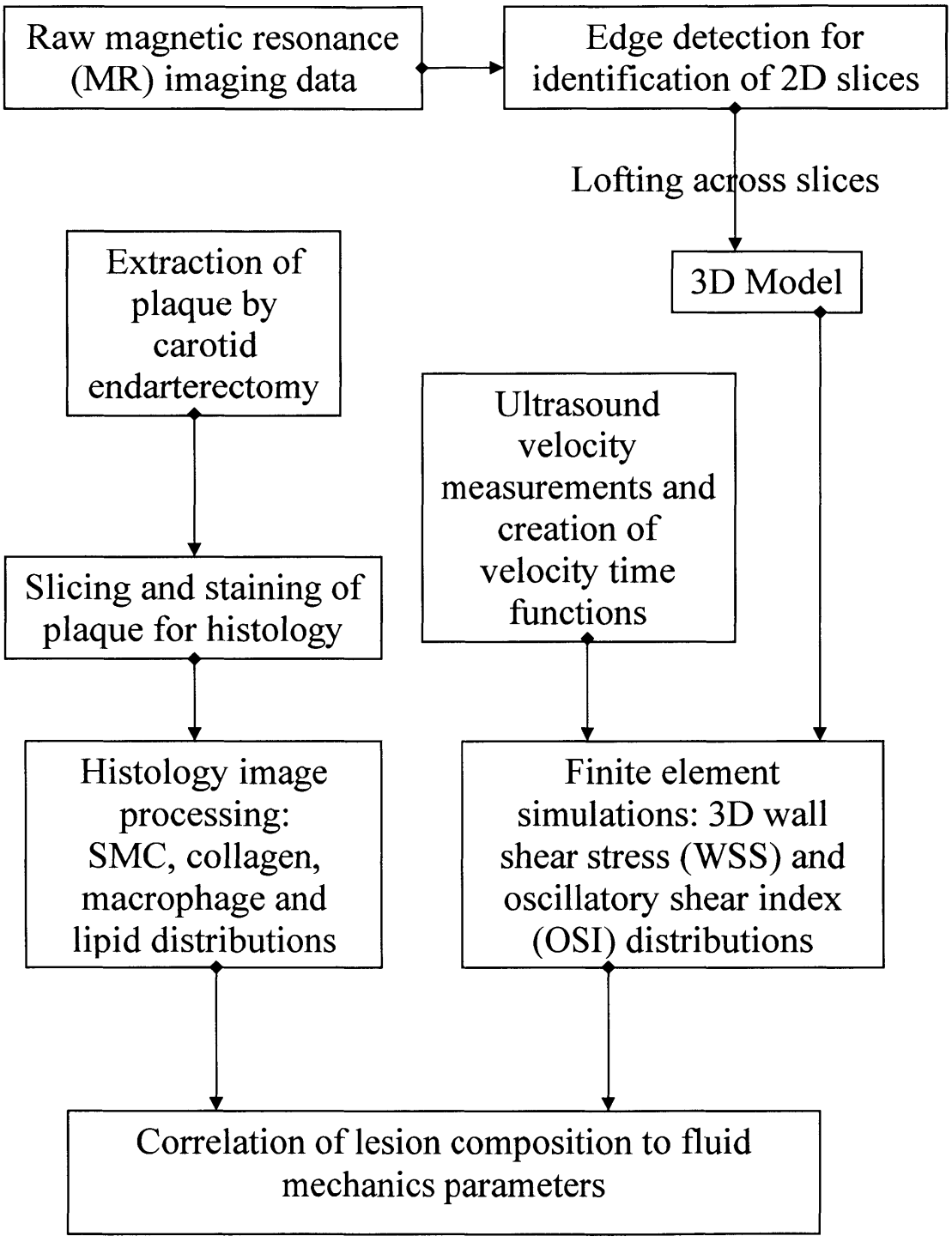

Figure 1

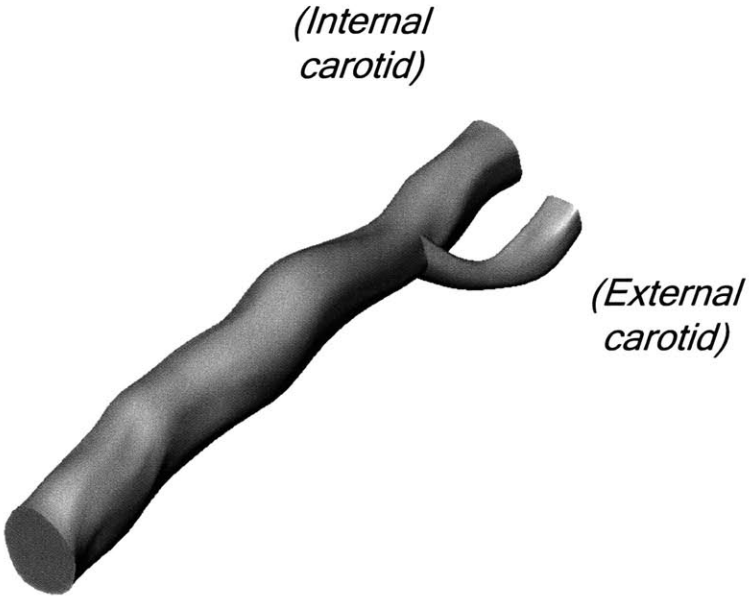

Patient 1

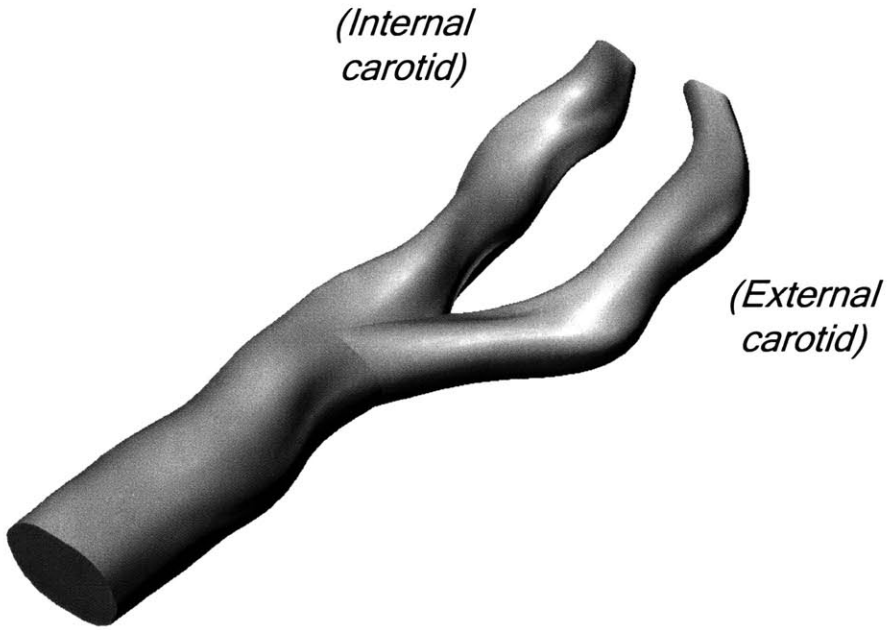

Patient 2

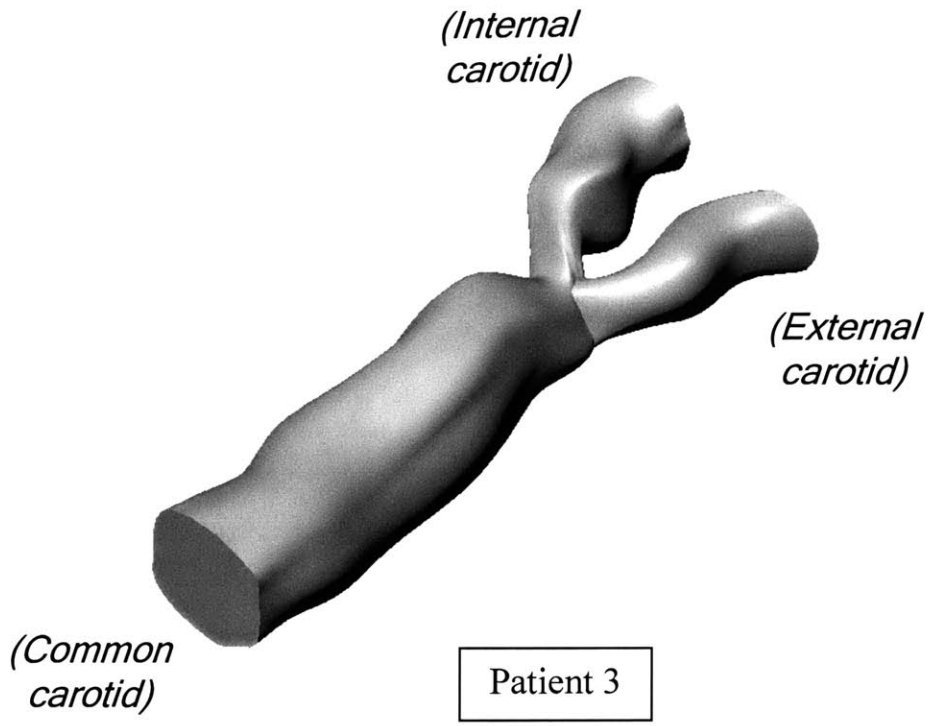
(Internal carotid)
(External carotid)
(Common carotid)
Patient 3
(Internal carotid)
(External carotid)
(Common carotid)
Patient 4

Figure 2

Patient 1

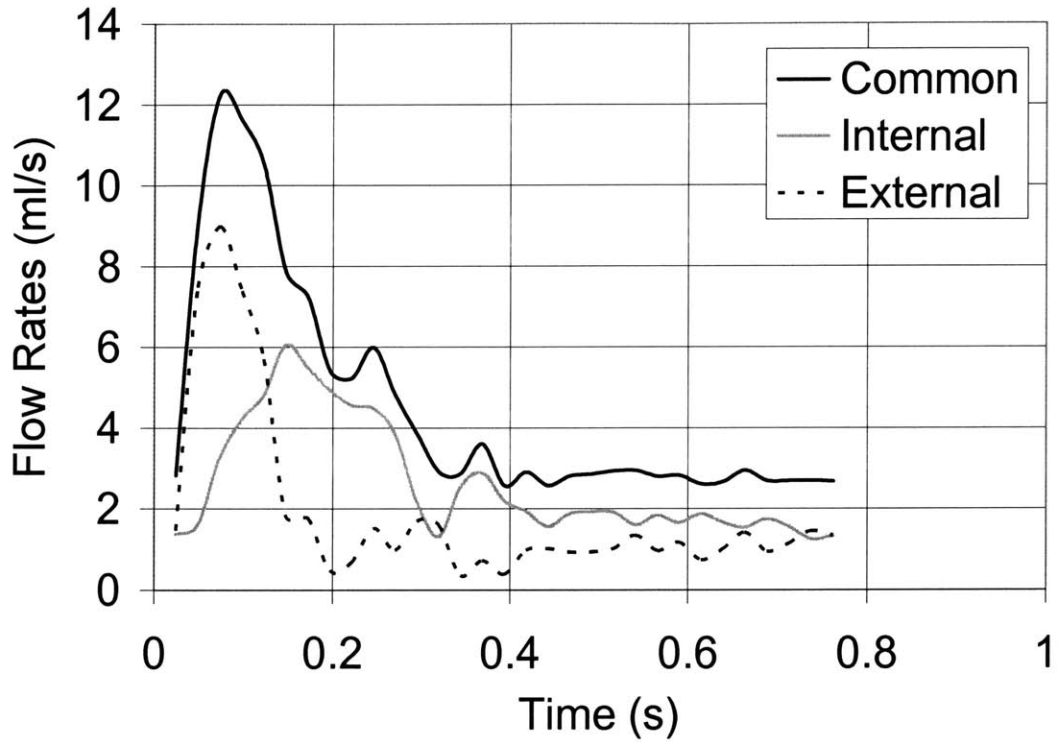

Patient 2

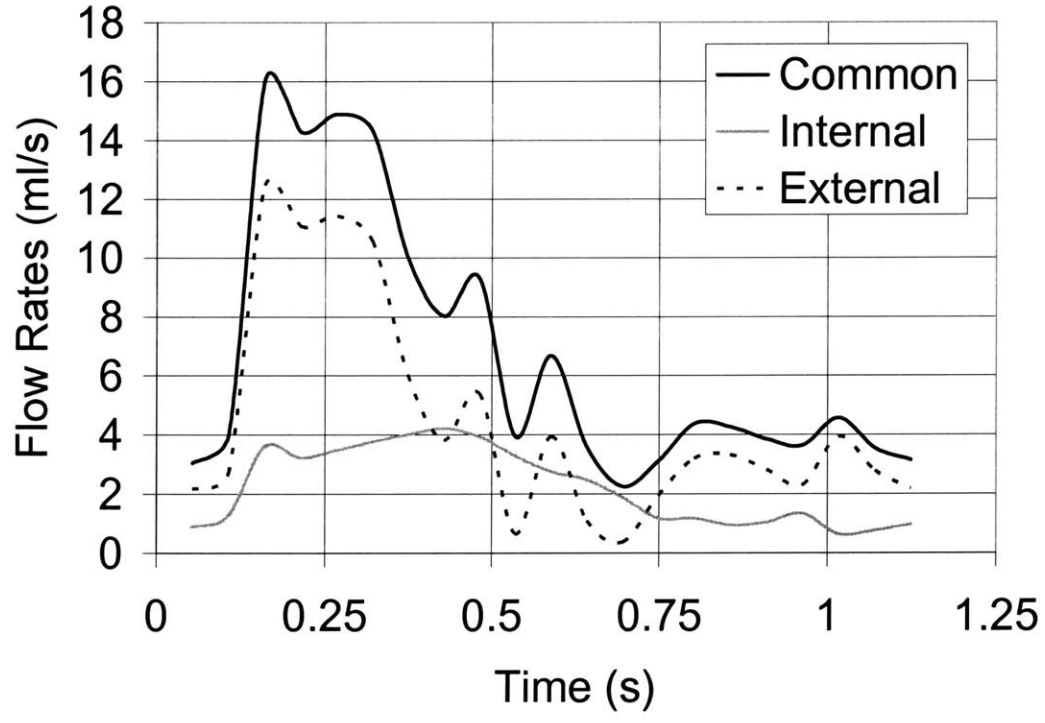

Patient 3

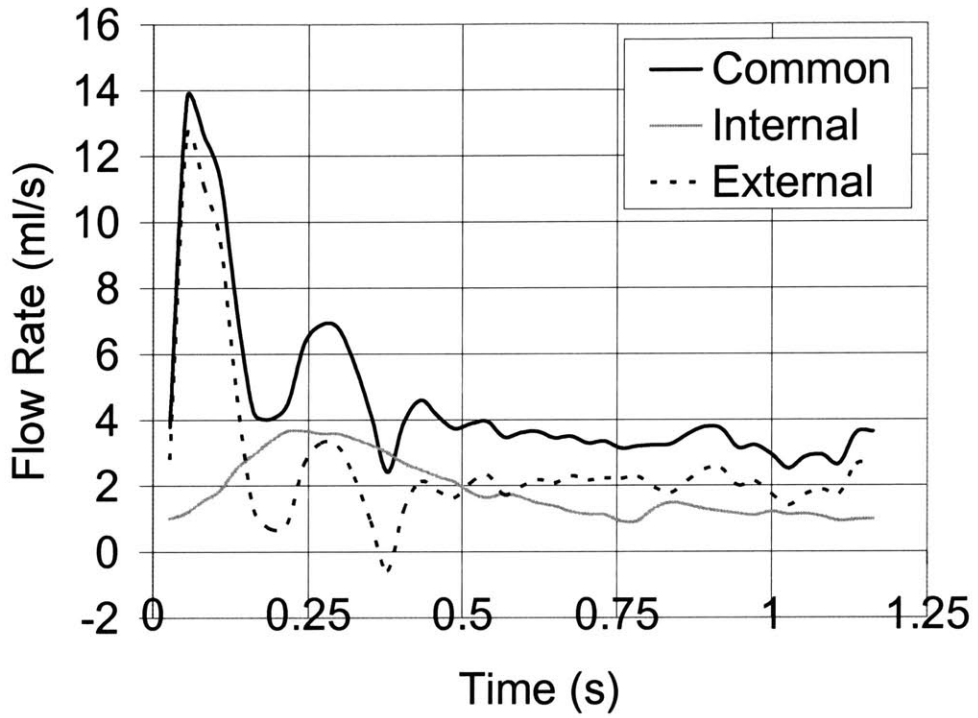

Patient 4

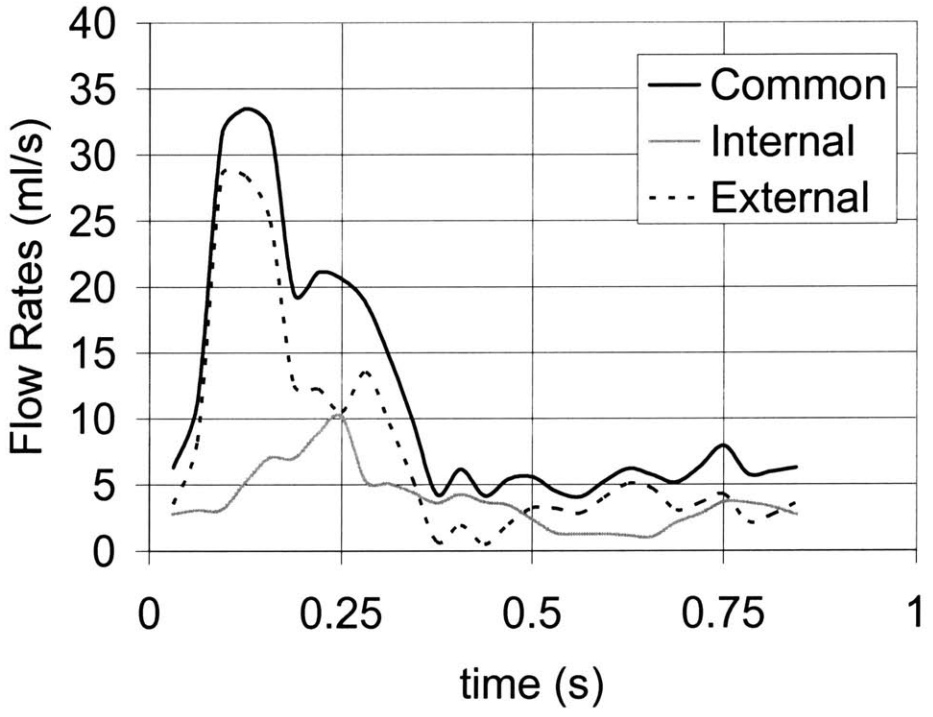

Figure 3

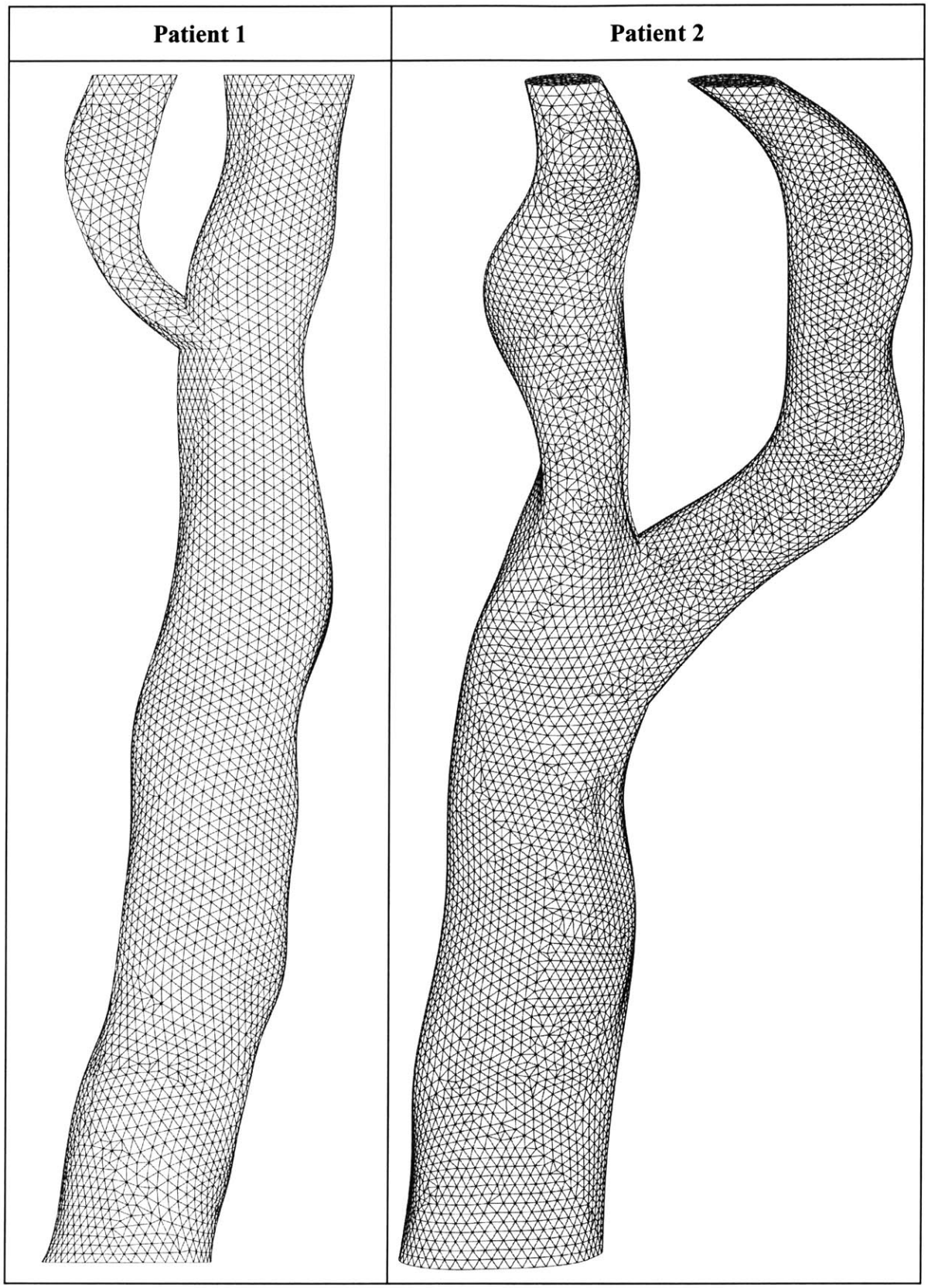
Patient 1
Patient 2

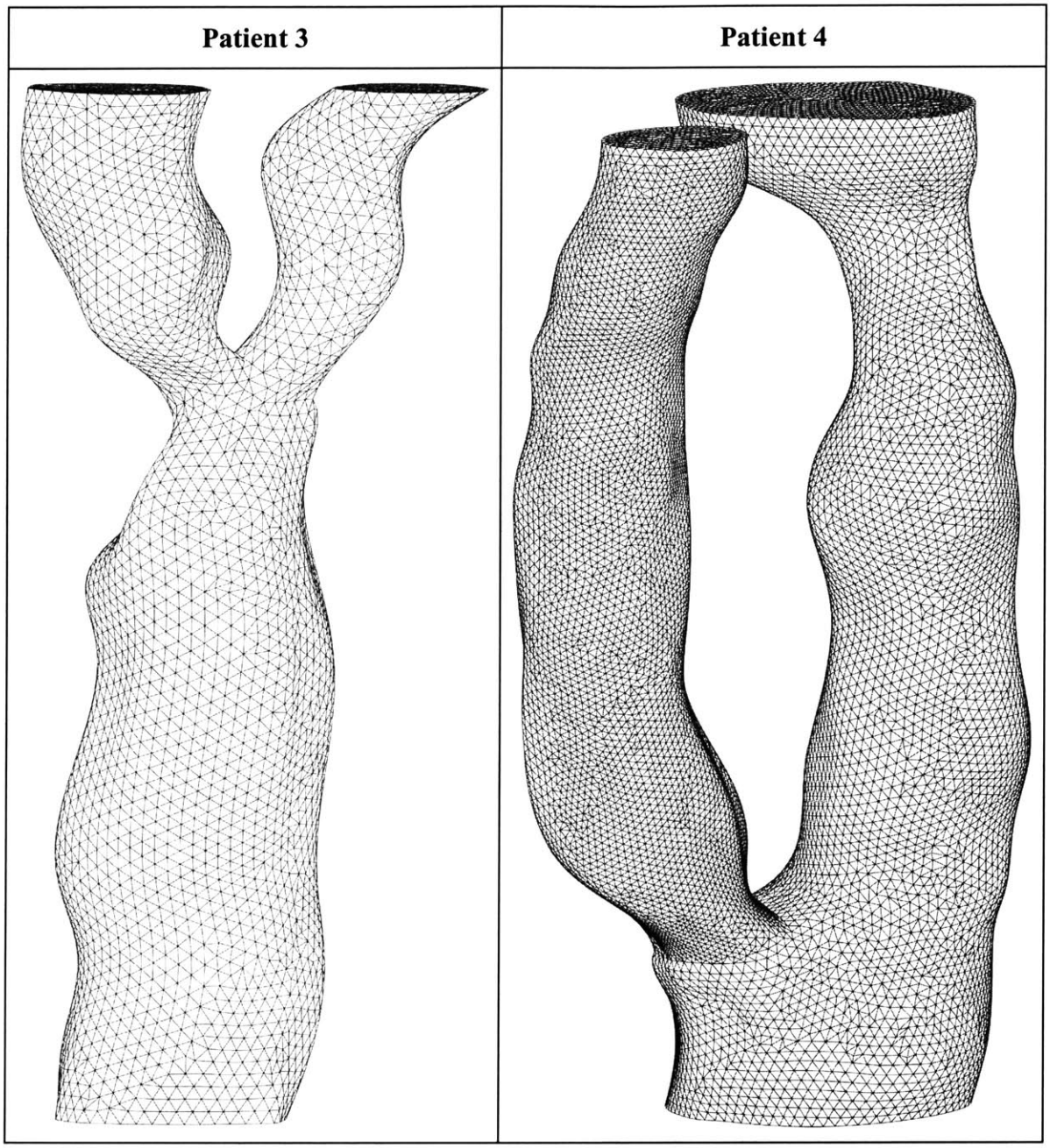

Figure 4

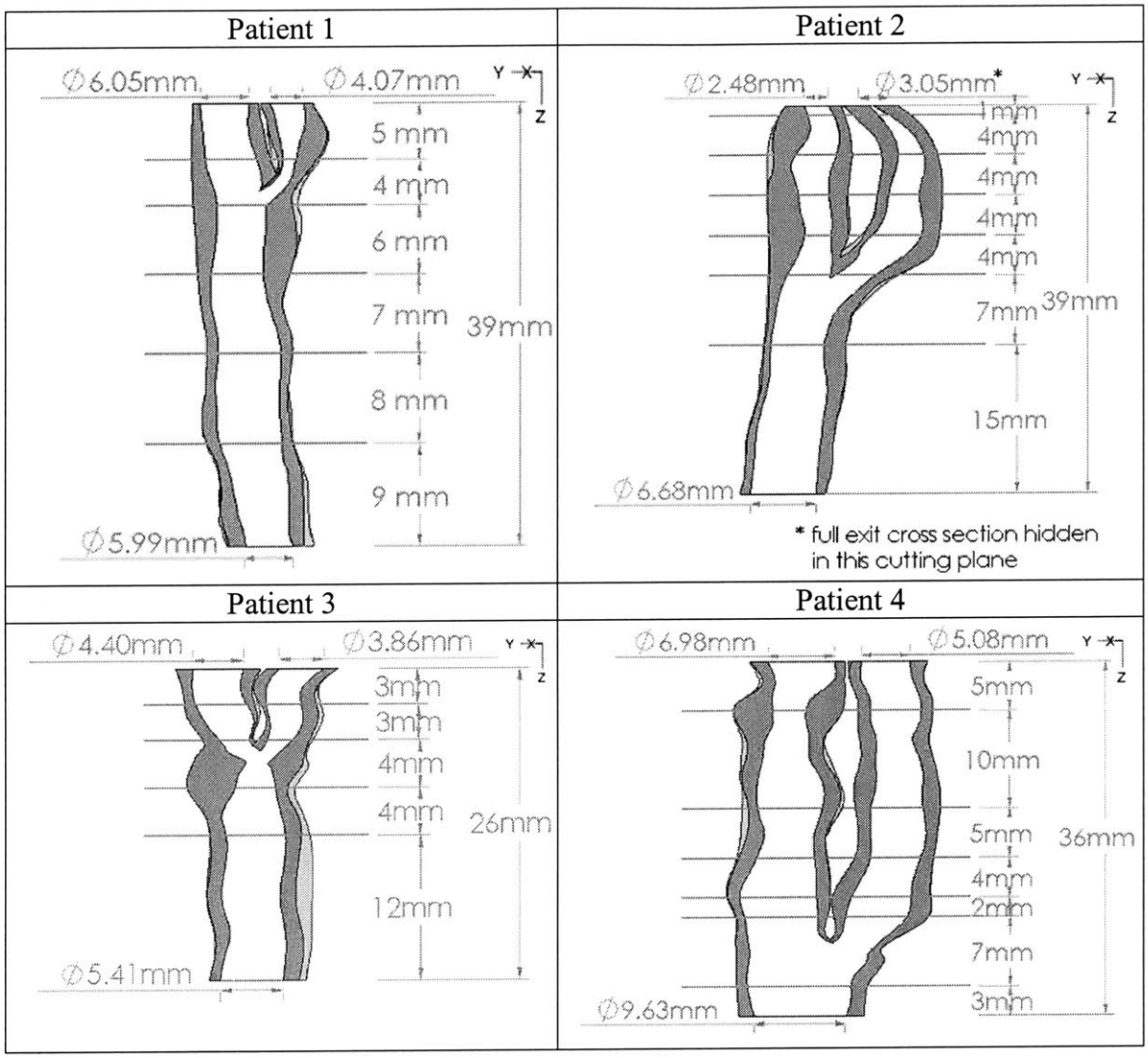
Patient 1
Ø6.05mm
Ø4.07mm
Y
Z
5 mm
4 mm
6 mm
7 mm
8 mm
9 mm
39mm
Ø5.99mm
Patient 2
Ø2.48mm
Ø3.05mm*
1mm
4mm
4mm
4mm
4mm
7mm
39mm
15mm
Ø6.68mm
* full exit cross section hidden in this cutting plane
Patient 3
Ø4.40mm
Ø3.86mm
3mm
3mm
4mm
4mm
26mm
12mm
Ø5.41mm
Patient 4
Ø6.98mm
Ø5.08mm
5mm
10mm
5mm
36mm
4mm
2mm
7mm
3mm
Ø9.63mm

Figure 5

(a) Smooth Muscle Cells	(b) Lipids
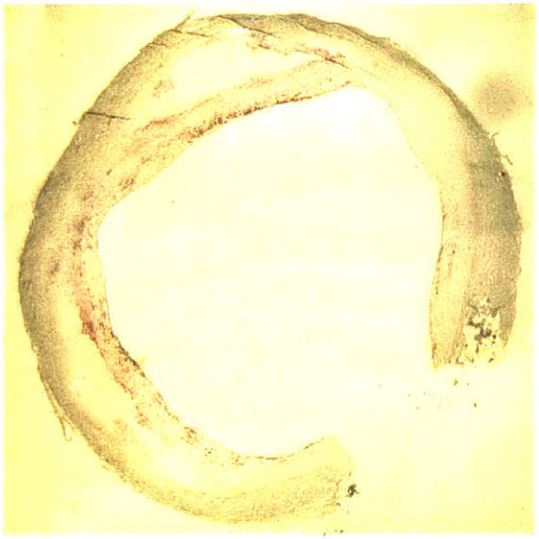	
(c) Macrophages	**(d) Collagen**
	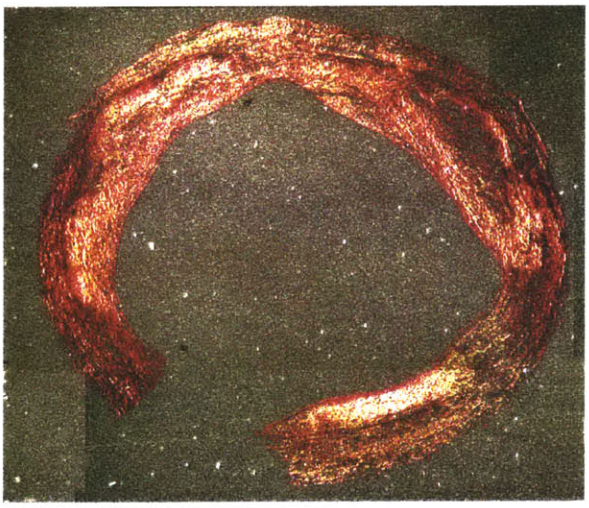

Figure 6

Before Image Processing	After Angular Division and Stain Quantification
	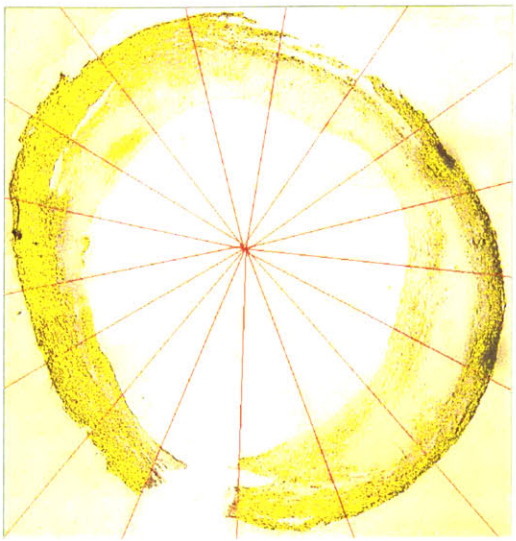

Figure 7

Patient 1 – Average WSS over the cardiac cycle (Pa)

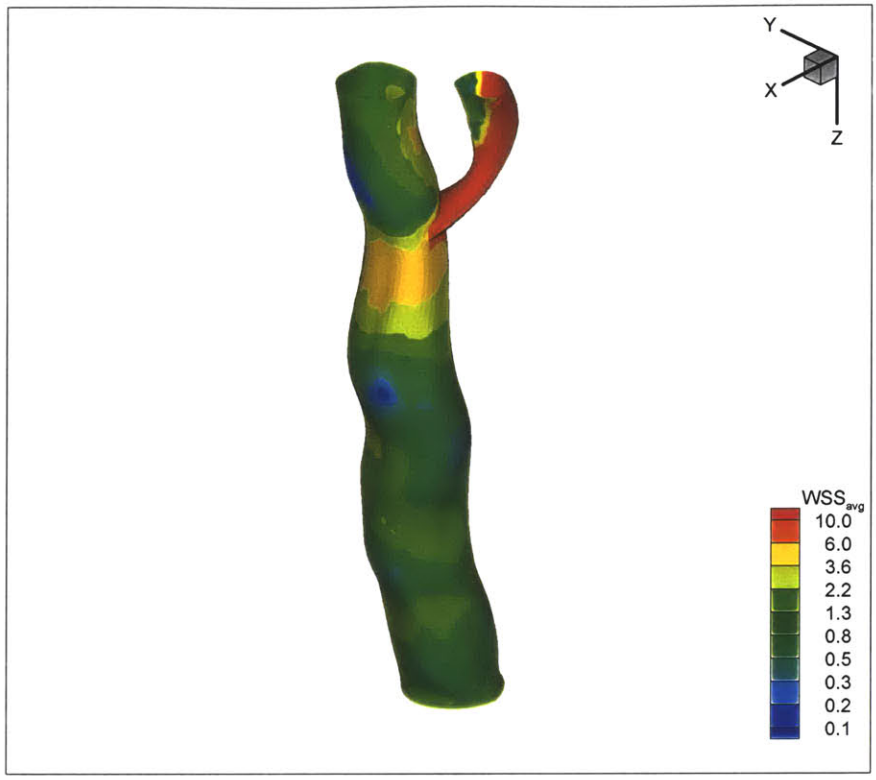

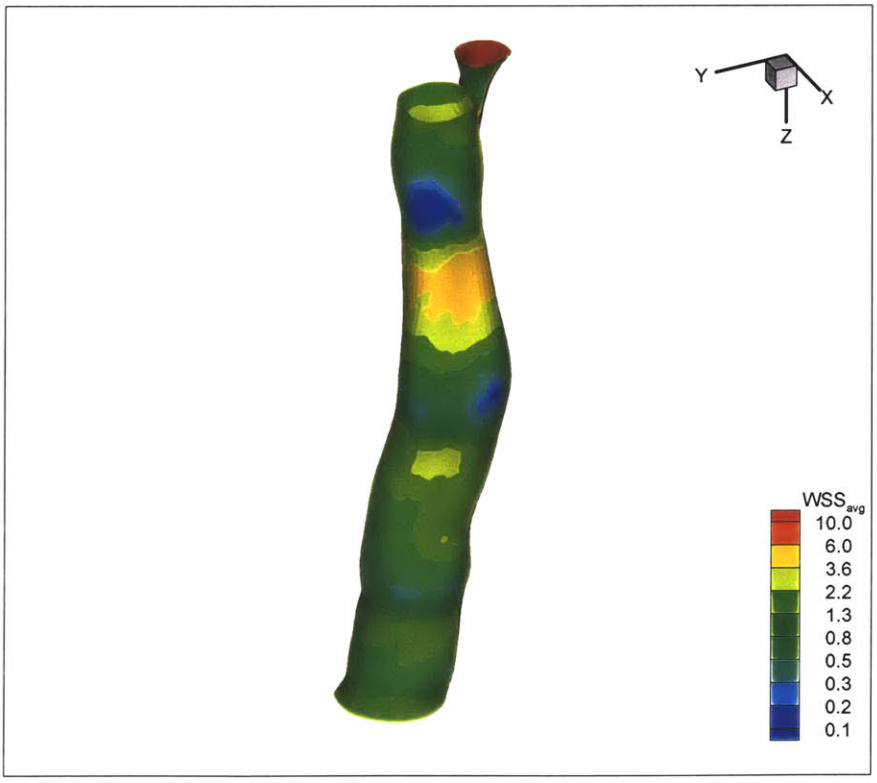

Patient 2 – Average WSS over the cardiac cycle (Pa)

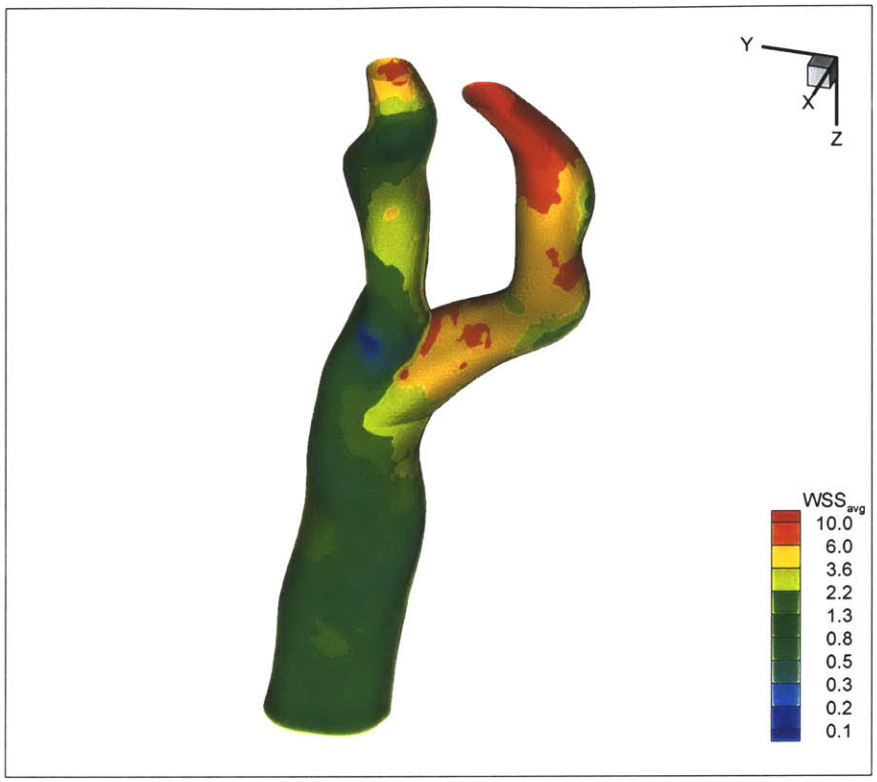

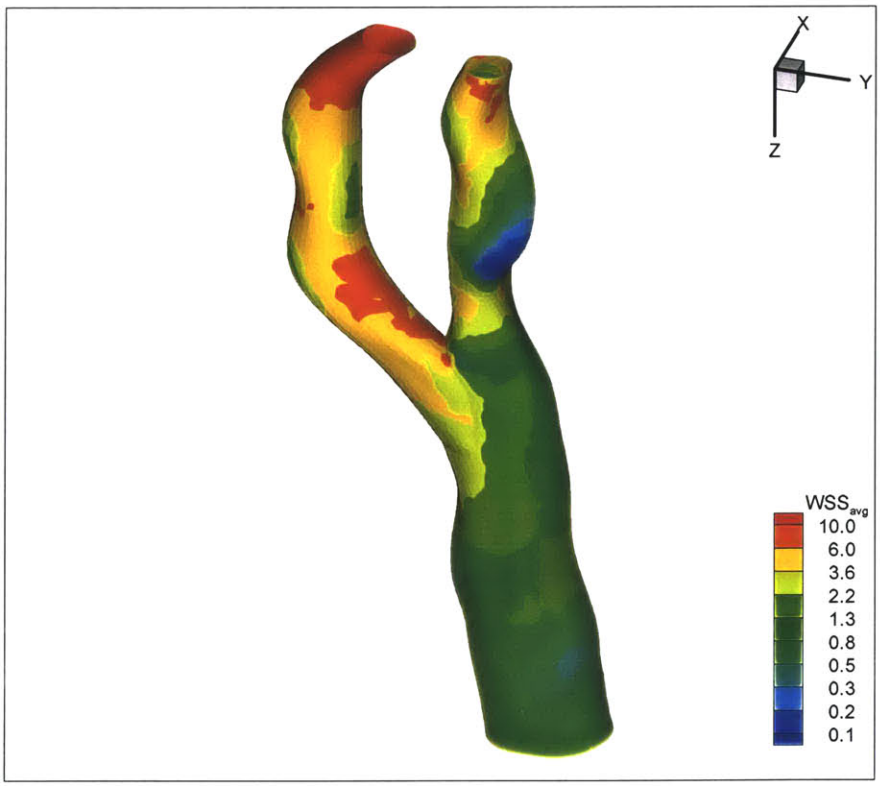

Patient 3 – Average WSS over the cardiac cycle (Pa)

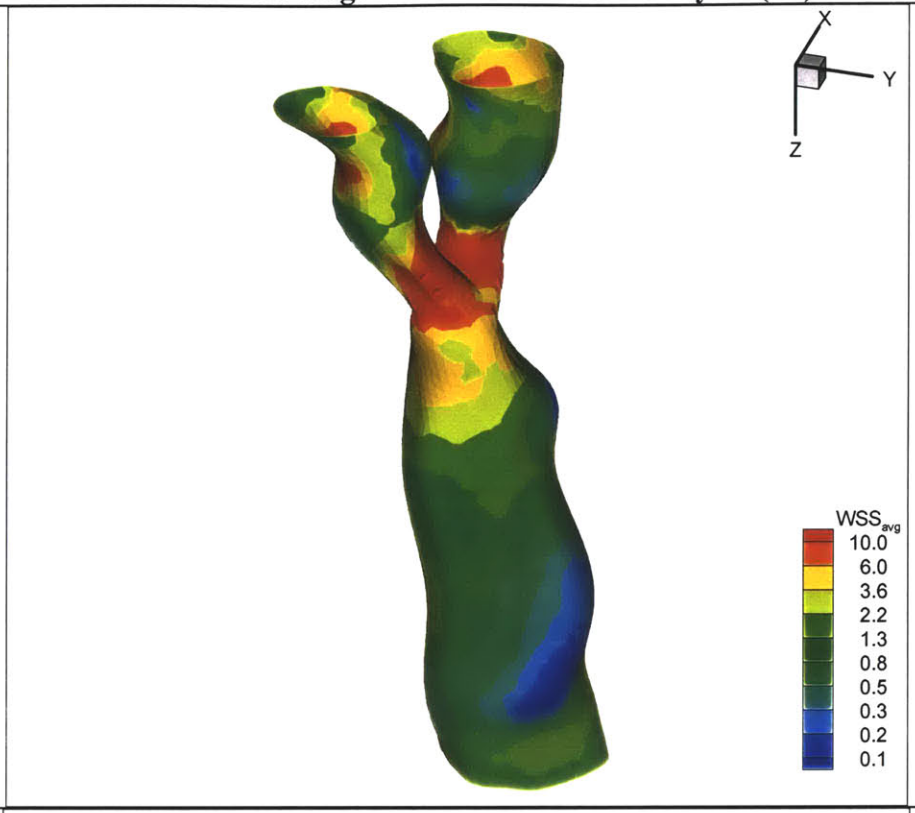

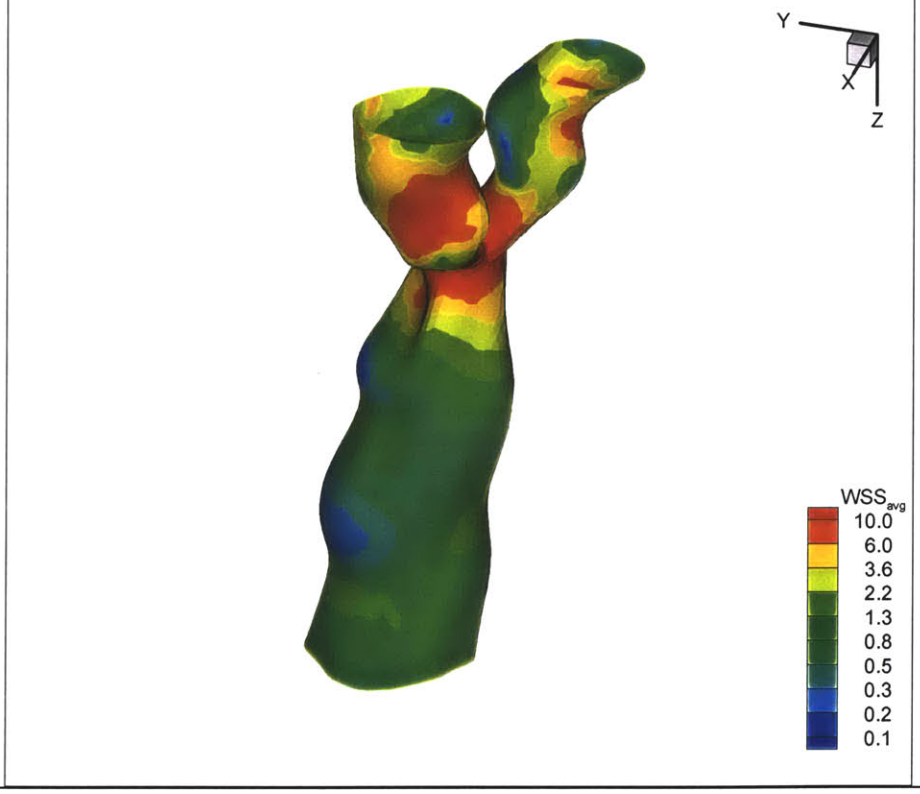

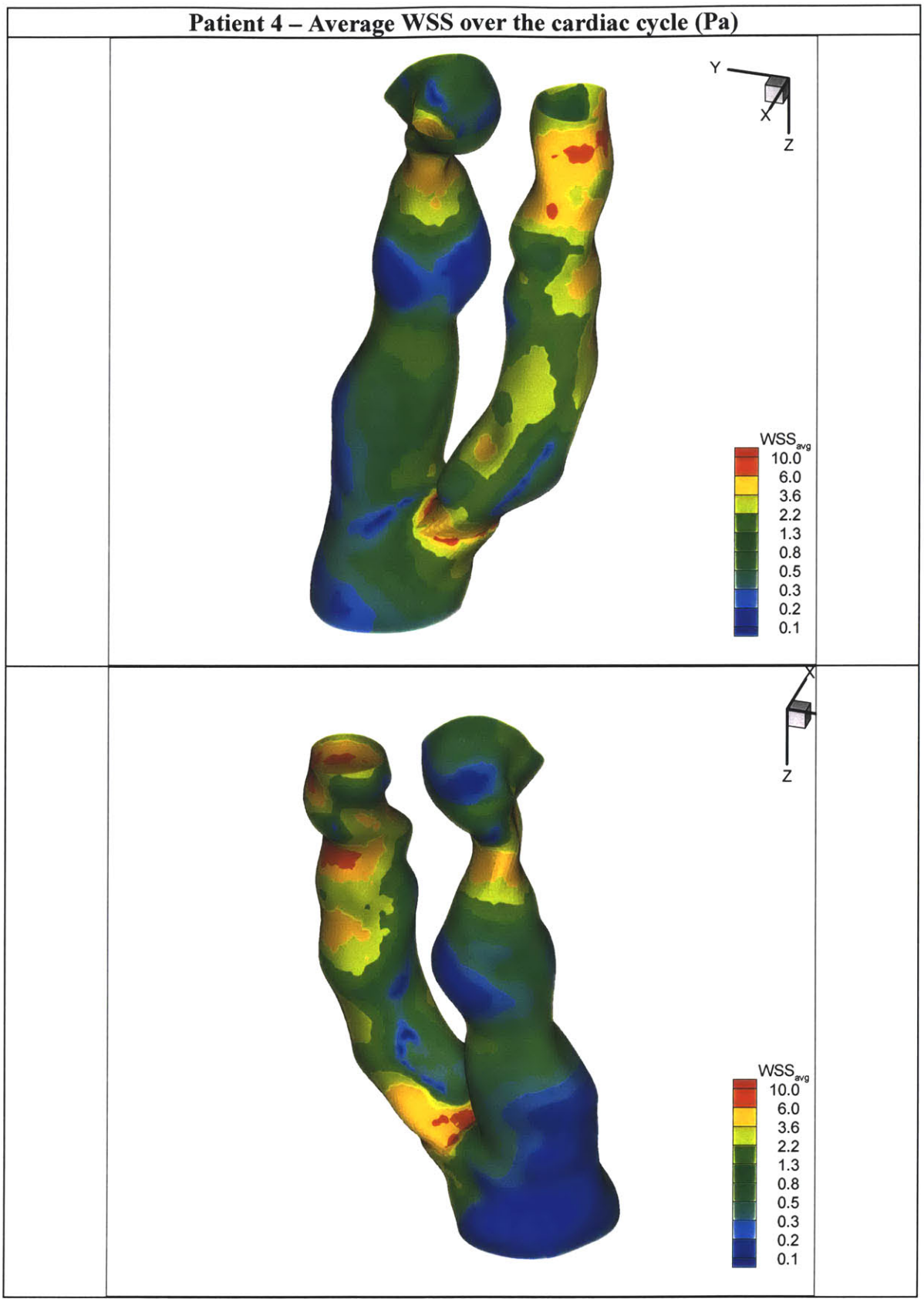
Patient 4 – Average WSS over the cardiac cycle (Pa)
Y
X
Z
WSS avg
10.0
6.0
3.6
2.2
1.3
0.8
0.5
0.3
0.2
0.1
X
Z
WSS avg
10.0
6.0
3.6
2.2
1.3
0.8
0.5
0.3
0.2
0.1

Figure 8

Patient 1 – Oscillatory Shear Index

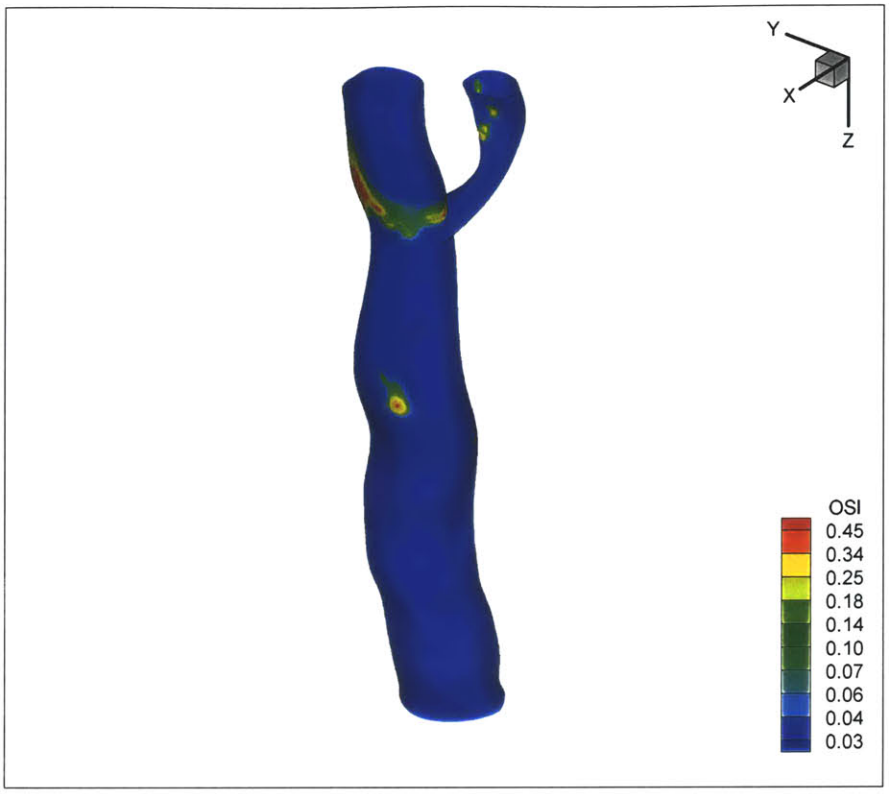

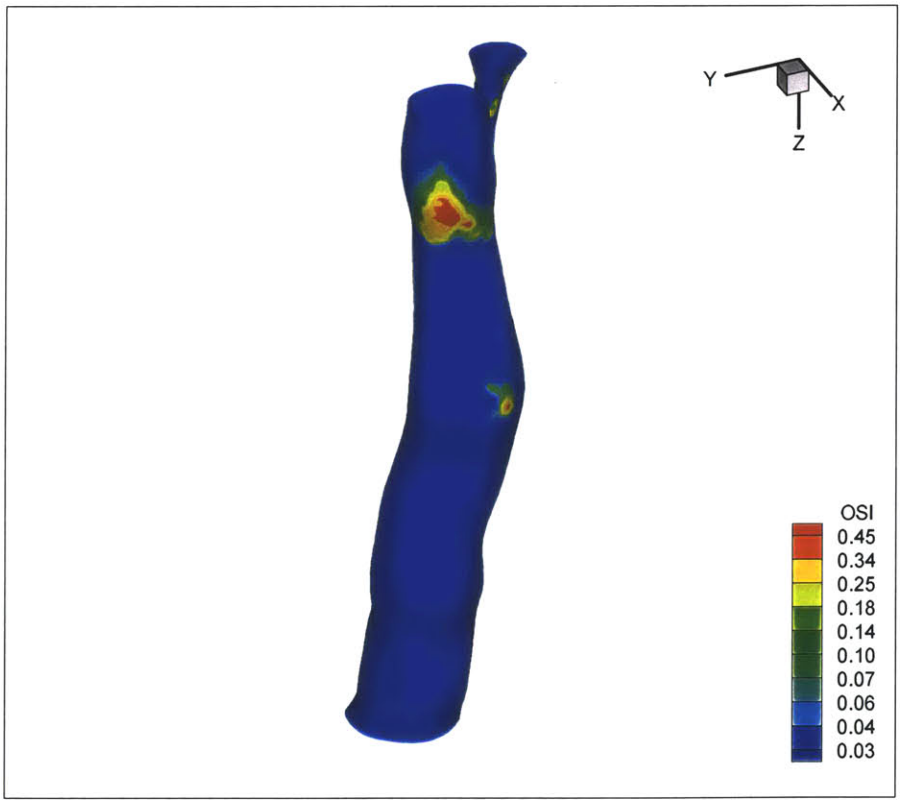

Patient 2 – Oscillatory Shear Index

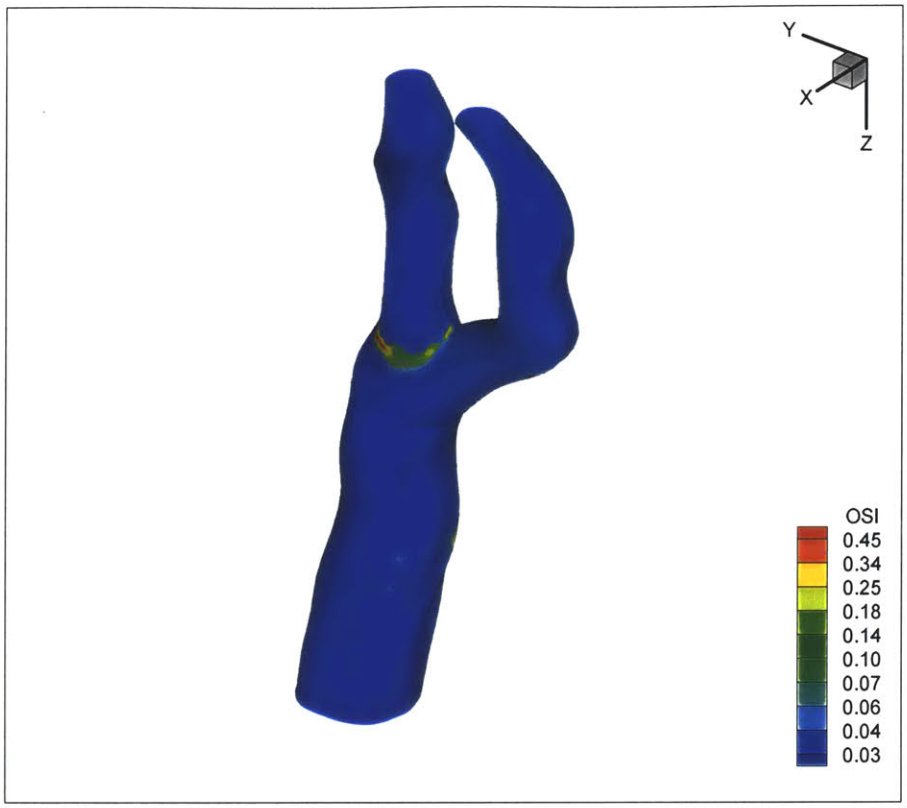

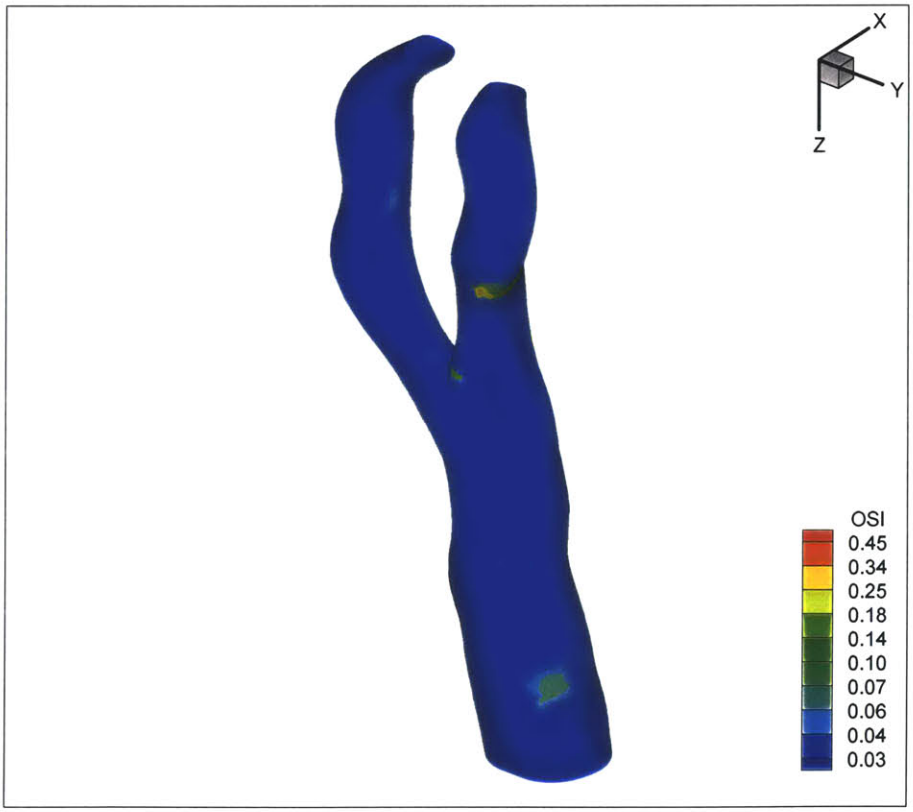

Patient 3 – Oscillatory Shear Index

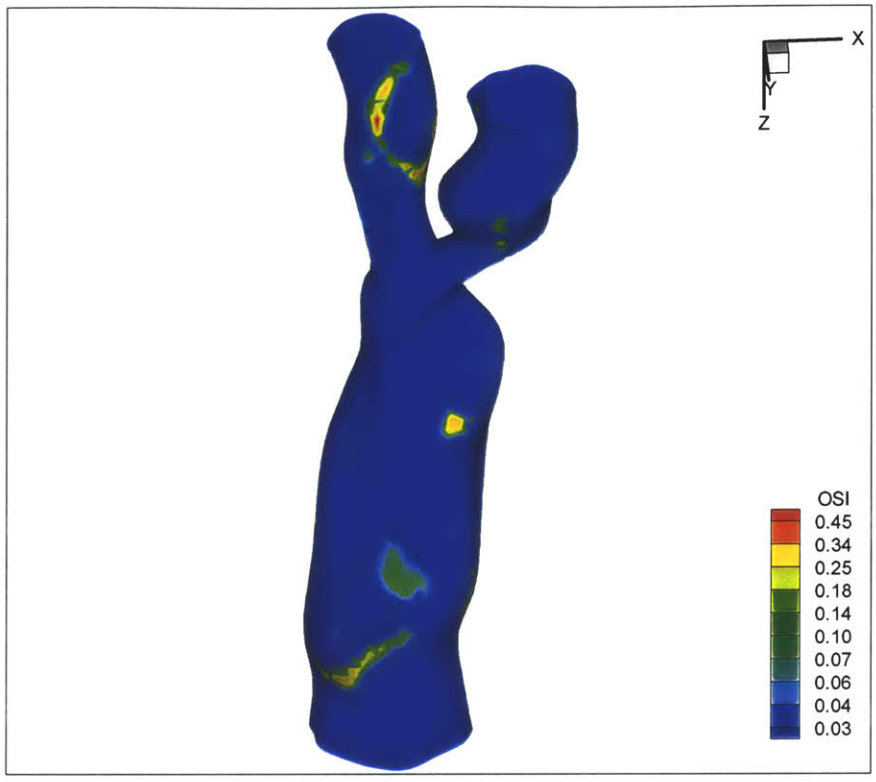

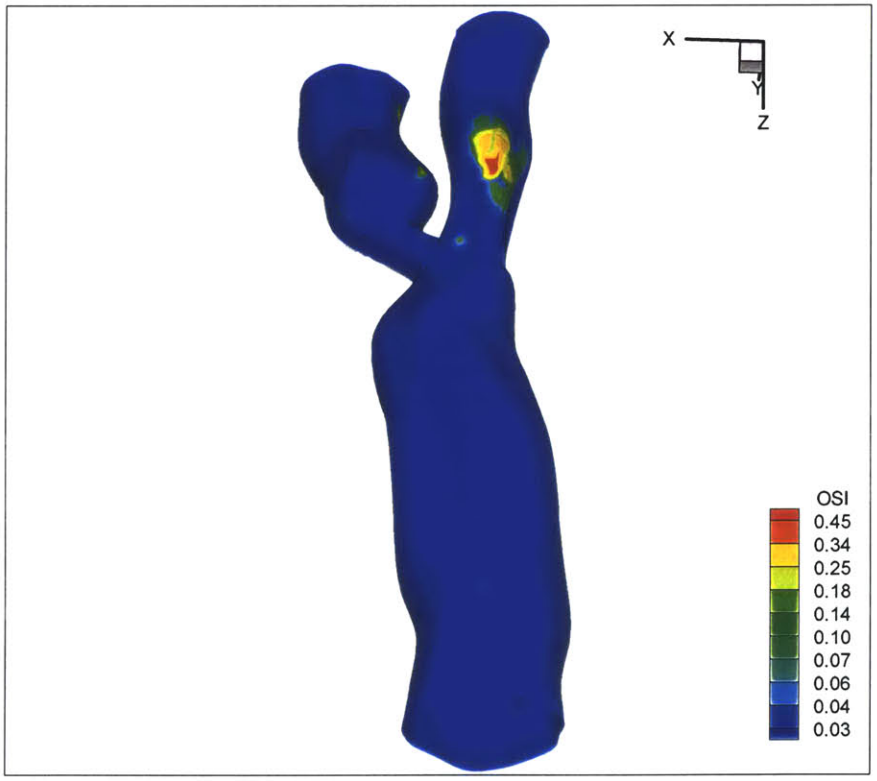

Patient 4 – Oscillatory Shear Index

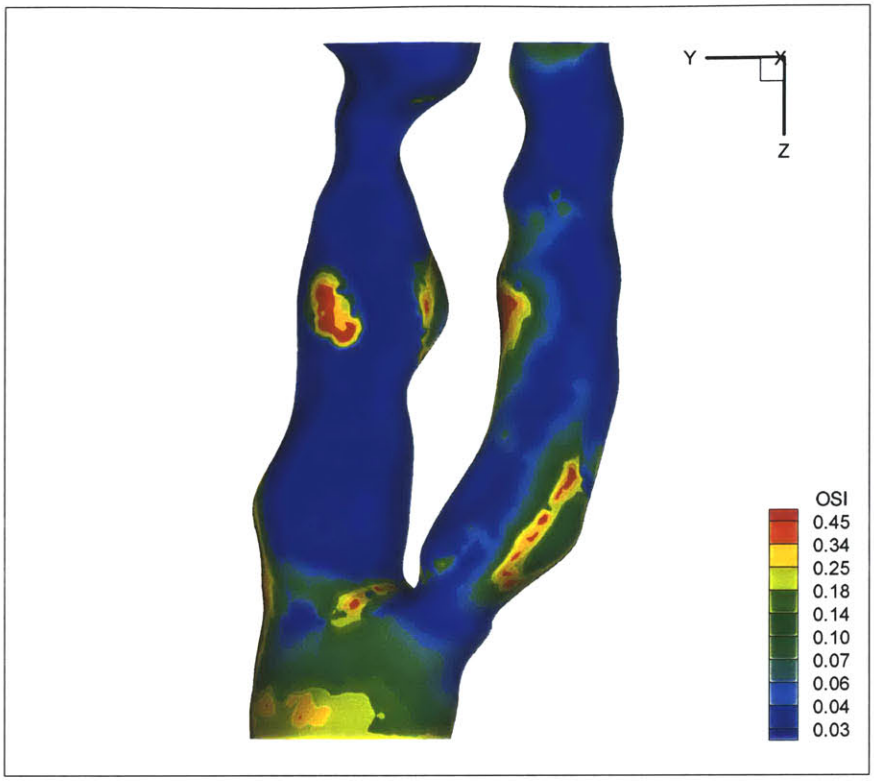

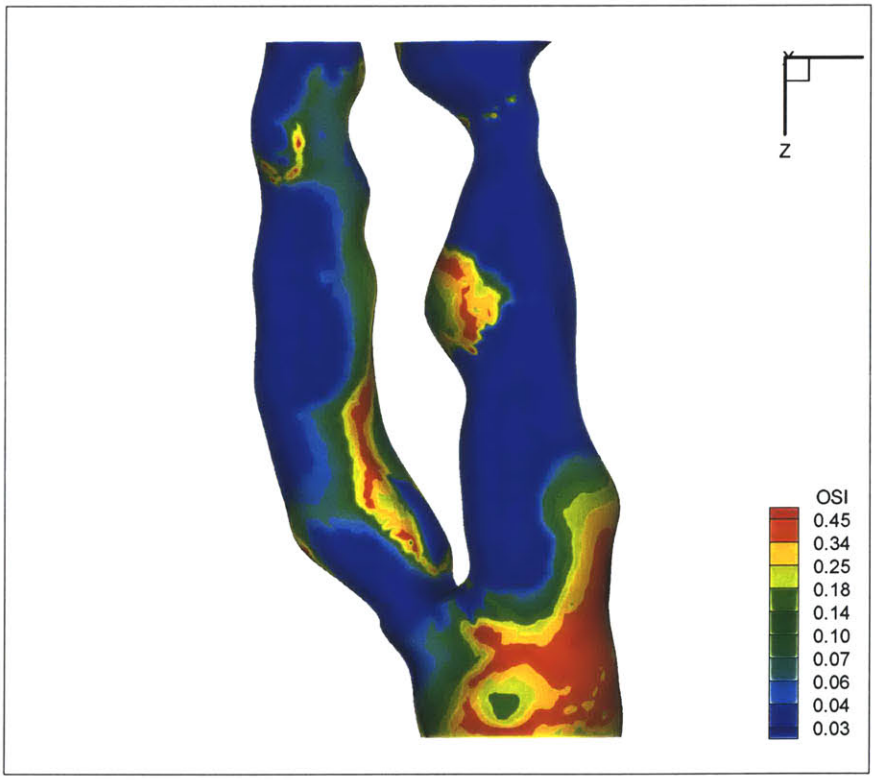

Figure 9

VII. On the Sensitivity of Wall Stresses in Diseased Arteries to Variable Material Properties

VII.1. Abstract

Accurate estimates of stress in an atherosclerotic lesion require knowledge of the material properties of its components (e.g., normal wall, fibrous plaque, calcified regions, lipid pools) that can only be approximated. This leads to considerable uncertainty in these computational predictions. The purpose of this study is to test the sensitivity of predicted levels of stress and strain to the parameter values of plaque via finite element analysis. The results show that the stresses within the arterial wall, fibrous plaque, calcified plaque, and lipid pool have low sensitivities for a $\pm$10% variation in Young's modulus, E. The sensitivity due to the variation in E is consistent between isotropic (linear and nonlinear), isotropic linear with residual strains, and transversely isotropic models. Therefore, stress analysis may be used with confidence that the material properties contribute relatively small errors in the prediction of stresses in the wall. Either isotropic or anisotropic models provide useful estimates, however the predictions in regions of stress concentration (e.g., the site of rupture) are somewhat more sensitive to the specific model used, increasing by up to 30% from the isotropic to orthotropic model in the present example and almost halving when residual stresses are included.

Keywords: Atherosclerosis, stress analysis, finite element analysis, plaque rupture

VII.2. Introduction

Although the precise mechanisms of plaque rupture are not yet fully understood, structural analyses of arteries suggest that it occurs in areas of high stress concentration [1,2]. In that the stress concentrations are critically dependent upon the geometry and mechanical properties of the lesion, the potential exists for using computational analysis of the stress distribution in conjunction with magnetic resonance or ultrasound imaging, as a diagnostic tool. Accurate estimates of stress, however, require knowledge of the material properties of the different regions within the wall (e.g., normal wall, fibrous plaque, calcified regions, lipid pools) that can only be approximated and have been shown to be widely variable [3,4,8]. Thus there is considerable potential uncertainty in these computational predictions.

The purpose of this study is to test the sensitivity of predicted levels of stress to these parameter values. Strains are also considered since wall deformation has been implicated in the stimulation of secretion, synthesis and gene expression in connection with a variety of factors implicated in the disease process. Models for analysis include isotropic (linear, nonlinear) and anisotropic. Residual strains were also incorporated into the isotropic linear model for further analysis.

VII.3. Methods

VII.3.1. Overview

Finite element analysis was applied to a typical two-dimensional cross-section of a diseased, ruptured artery excised post mortem. In order to generate the pre-ruptured geometry, we examined a post mortem specimen obtained from the coronary artery (figure 1). Regions of artery wall, fibrous plaque, lipid deposits, and calcified plaque were identified in a histological cross section of the specimen. The model was then generated using the commercial package OPTIMAS (Media Cybernetics) making all reasonable attempts at simulating the actual *in vivo* geometry. An investigator not involved in the current study reconstructed the pre-rupture geometry in an attempt to reproduce its original cross-sectional geometry. This geometry and its imposed boundary conditions were then used to create a finite element model.

VII.3.2 Parameters

Fibrous plaque, cellular plaque, and arterial wall are each initially modeled as linearly elastic, orthotropic materials due to the in-plane load carrying capability of their collagenous components. Their mechanical properties are described by E_r and E_θ (Young's moduli in the r and θ directions, respectively), $\nu_{r\theta}$ and $\nu_{\theta z}$ (Poisson's ratios in the r-θ and θ-z planes, respectively), and $G_{r\theta}$ (shear modulus in the r-θ plane) [1,6]. The properties in the θ-direction are taken to be the same as for the z-direction, constituting a transversely isotropic material.

In determining the anisotropic parameters, E_θ for the plaque and artery were taken from the most recent data known at the time of this study [4]. In the same reference, E_r was estimated to be 5% of E_θ. The value of $\nu_{\theta z}$ is based on previous data from canine aortas [5]. From these numbers, $\nu_{r\theta}$ was then calculated to satisfy the conditions for a positive-definitive stiffness matrix [6]. The value for $G_{r\theta}$ was calculated as the average of its upper and lower limits. The upper bound was taken as E_θ while the lower bound was calculated by modeling the materials as incompressible and isotropic, in which case, $G_{r\theta}=(E_r/3)$ [7]. Therefore, the resulting value of $G_{r\theta} = [E_\theta + (E_r/3)]/2$ was used.

Calcified plaque and lipid are assumed to be linearly elastic, (nearly) incompressible, isotropic materials. Their mechanical properties are described by E, the Young's modulus and ν, the Poisson's ratio. Values for E were taken from recent measurements [4,8], and for ν, a value of 0.45 was chosen, close to that for an incompressible material but slightly smaller to avoid complications in the solution procedure.

For the purpose of comparison, the specimen was also modeled with all of its tissues assumed to be linearly elastic, incompressible, and isotropic. Hence, fibrous plaque, cellular plaque, calcified plaque, lipid, and the normal arterial wall were each described by values for E and ν. In this case, for those tissues previously described as orthotropic, we assumed that $E = E_\theta$, and $\nu = 0.45$. The circumferential value for E was used since it is an order of magnitude higher than that in the radial direction and was therefore thought to be more important than the radial

modulus in determining the peak stresses and deformation. The resulting parameters are summarized in tables 1 and 2.

	ARTERY	FIBROUS	CALCIFIED	LIPID
E (kPa)	100.0	2312.0	1466.0	0.345
ν	0.45	0.45	0.45	0.45

Table 1 Isotropic linear material parameters.

	ARTERY	FIBROUS	CALCIFIED	LIPID
E_r (kPa)	10.0	115.6		
E_θ (kPa)	100.0	2312.0	1466	0.345
$\nu_{r\theta}$	1.00	1.35		
$\nu_{\theta z}$	0.27	0.27	0.45	0.45
$G_{r\theta}$ (kPa)	51.67	1175.27		

Table 2 Anisotropic linear material parameters.

In order to incorporate non-linear behavior, the specimen was also modeled using the standard Lagrangian formulation for large displacements and large strains [10]. An isotropic form of the strain energy density function (SEDF) for the (nearly) incompressible artery wall is specified [12]:

$$W = \frac{a}{b}\left(e^{\frac{b}{2}(I_1-3)} - 1 \right)$$

where a and b are elastic constants (see table 3) that reflect the elastic properties and tissue composition; I_1 is the first invariant of the strain tensor. In the Taylor series expansion, a has the significance of the elastic modulus; b is related to the strain-stiffening behavior of the material. The data of Loree et. al. [8] were again used to obtain the values a and b by matching to the average of the uniaxial stress-strain curves in the θ direction. This SEDF, despite being isotropic, has been shown to perform well when compared to other types of SEDFs in the literature [13]. Its predicted response is in good qualitative agreement with experimental measurements since it describes the well-known strain stiffening behavior of arteries.

Material	a (kPa)	b
Artery	33.333	16.73
Fibrous Plaque	770.667	40
Calcified Plaque	488.667	30
Lipid	0.345	0.115

Table 3 Isotropic non-linear material parameters.

VII.3.3. Finite Element Analysis

The finite element analysis was carried out using ADINA, version 7.3 for the isotropic linear and anisotropic cases, and version 7.4 for the isotropic nonlinear and linear with residual strain cases [9]. Using the geometry created from the histology specimen, a mesh was generated using quadrilateral, nine-node, plane-strain elements (figure 2). These elements have a local dimension of 0.03 mm, thereby allowing for accuracy particularly near material interfaces [1]. Mesh refinement by doubling the number of elements in vicinity of the rupture point produced results that were generally within 0.4% of those from the original mesh. For the anisotropic model, displacement-based elements were used and for the isotropic model, displacement/ pressure (u/p) based elements were used to avoid locking as ν approached 0.5 [10].

Residual strains were applied to the isotropic model in order to produce a model with smaller radial stress gradients at normal arterial pressure, as typically found in normal, healthy arteries [3,12]. Strain values from the inflated isotropic model were averaged over 15 degree segment. This average value per segment was then subtracted from each of the original (inflated) strain values in that segment, node by node (done repetitively for each of the 15 degree segments). These differences were then applied to the model as nodal initial strains (figure 3)

Orthotropic axes were defined for each element, roughly corresponding to the circumferential and radial directions. Once the model was defined, the load was then ramped to an intraluminal

static pressure of 14.6 kPa (110 mmHg); external pressure was assumed to be zero. The resulting mesh contained 44450 nodes, 681 elements, 110 surfaces, and had an average solution time of 27 seconds on a 600 MHz DEC alpha workstation.

Maximum principal stress and maximum principal strain are determined at three points of interest: (1) an element between a lipid pool and the lumen, (2) an element where the plaque is relatively homogeneous, and (3) the node where plaque rupture occurred *in vivo* (figure 2).

VII.3.4 Sensitivity Analysis

To observe the sensitivity of these material parameters, the models were first analyzed at the average values of each parameter for each material. Analyses were then conducted in which one of the five defining parameters of each orthotropic material, or one of the two defining parameters of each isotropic material, was varied by $\pm$10%. An exception was made for the Young's modulus of lipid which was varied over its known range; 35% to 260% of its initial value [8].

It is important to note that because some parameters were specified in relation to others as described above, when one was varied by 10%, the other related parameters were altered as well.

VII.4. Results and Discussion

VII.4.1. Mean stress and strain levels.

Stress distributions for the four types of analysis, isotropic (linear elastic, nonlinear, linear with residual strains) and anisotropic, are shown in figures 4 (a), (b), (c) and 5 respectively. Whereas the distributions are generally similar, there are several differences of note. The maximum level of stress in the isotropic case is located at the site of rupture, while the anisotropic model predicts peak stress at a remote site where the vessel wall seems to exhibit a sharp corner. This is presumably artifactual but illustrates an important potential source of error in this type of calculation.

The maximum principal stress levels when all parameters are fixed at their calculated values serve as the baseline conditions for the sensitivity analysis. These values are provided in table 4.

	Isotropic Linear		w/ Residual Strains		Isotropic Nonlinear	
	Stress (kPa)	**Strain**	**Stress (kPa)**	**Strain**	**Stress (kPa)**	**Strain**
RUP	424.093	0.158	222.896	0.088	417.624	0.103
TP1	56.281	0.020	62.282	0.022	50.053	0.017
TP2	12.335	0.005	14.642	0.005	13.048	0.005

(a)

	Anisotropic Linear	
	Stress (kPa)	**Strain**
RUP	552.334	0.196
TP1	77.345	0.032
TP2	9.942	0.003

(b)

Table 4 Maximum principal stress and strain values at baseline parameters for (a) Isotropic cases, and (b) Anisotropic case.

The isotropic (anisotropic) level of stress at the rupture site is approximately 1.5 times (2 times) that previously used as a threshold value for plaque rupture [1]. Although values at the three sites are generally consistent, stress at the site of rupture is significantly reduced by the addition of residual strain.

VII.4.2. Isotropic Analysis

Sensitivity results in the form of the percentage change in stress or strain are presented in table 5 for the isotropic linear and nonlinear analyses. As can be seen, when the modulus, or **a**, the

nonlinear material analog, is varied, changes in stress are generally small. The changes in strain, however, are comparable to the variation in E. This reflects the fact that the stresses must balance the average loads. Thus changes in stress can only result from changes in the distribution of stress across the wall, and these are apparently small. Strain, however, must directly reflect any change in modulus.

Effects due to changes in arterial wall properties are particularly small since the points of interest lie within fibrous plaque and the arterial wall contributes little in supporting the overall load. The effects of varying **b** in the nonlinear model were generally very small throughout all materials. The results also show little sensitivity to changes in Poisson's ratio, with the exception of ν approaching 0.5 in the calcified region or lipid pool (results not shown). This effect is greatest at the point of rupture, decreasing peak stress by 5.6% when ν=0.495, and is therefore of some concern. Note, however, that the possible range of ν is smaller than the range of uncertainty for E, with ν varying between about 0.25 and 0.5 according to estimates in the literature [5,11]. The isotropic linearly elastic model with residual strains showed in general lower sensitivity to changes in E and ν.

	Isotropic Linear				With Residual Strains			
	E (-10%)		ν (-10%)		E (-10%)		ν (-10%)	
	% Stress	% Strain	% Stress	% Strain	% Stress	% Strain	% Stress	% Strain
ARTERY RUP	-0.005	-0.004	-0.001	-0.001	0.000	0.000	0.000	0.000
TP1	0.149	0.147	0.039	0.038	0.165	0.161	0.041	0.040
TP2	-0.066	-0.083	-0.021	-0.026	-0.047	-0.060	-0.013	-0.019
FIBROUS RUP	-0.421	10.669	-0.147	3.662	-2.151	8.881	-1.001	1.545
TP1	0.345	11.496	0.011	4.470	0.872	11.808	0.195	4.382
TP2	-0.403	10.558	-0.248	2.392	-2.577	8.411	-1.233	1.949
CALCIFIED RUP	0.418	0.393	0.196	0.198	0.565	0.499	0.286	0.272
TP1	-0.573	-0.564	-0.008	-0.007	-0.649	-0.628	0.058	0.057
TP2	0.475	0.590	0.320	0.411	0.373	0.443	0.254	0.307
	E (-65%)		ν (-10%)		E (-65%)		ν (-10%)	
LIPID RUP	0.170	0.168	0.088	0.087	0.579	0.591	0.298	0.309
TP1	0.135	0.086	0.072	0.043	0.579	0.388	0.318	0.204
TP2	-0.057	-0.061	-0.036	-0.038	-0.242	-0.262	-0.153	-0.164

(a)

	Isotropic Nonlinear			
	a (-10%)		b (-10%)	
	% Stress	% Strain	% Stress	% Strain
ARTERY RUP	-0.001	0.000	0.000	0.000
TP1	0.096	0.231	0.000	0.000
TP2	-0.038	4.234	0.000	0.000
FIBROUS RUP	0.620	6.378	-1.532	1.667
TP1	0.012	10.989	-0.010	0.174
TP2	-0.038	8.669	0.084	0.000
CALCIFIED RUP	0.231	0.097	-0.004	0.000
TP1	-0.713	-0.636	-0.006	0.000
TP2	0.383	0.403	0.008	0.000
	a (-65%)		b (-10%)	
LIPID RUP	0.106	0.068	0.001	0.004
TP1	0.060	0.000	-0.096	-3.686
TP2	-0.008	0.000	0.000	-0.044

(b)

Table 5 Sensitivity of maximum principal stress and strain for the (a) isotropic linear (with and without residual strains), and (b) the nonlinear model. RUP represents the rupture site,

TP1, test point one, and TP2, test point two (see figure 2). The region (artery, fibrous, etc.) identifies in which portion of the model the parameters were changed in a given test (color coded in figure 2). Values for the nonlinear isotropic model were calculated using the refined mesh.

VII.4.3. Anisotropic Analyses

The anisotropic trials (table 6) are generally consistent with the isotropic ones. For both cases, the variation of stress is similar across material parameters and test points. Also, the normal arterial wall material properties have little effect on maximum principal stress or strain, and the variation of ν for the lipid trials exhibits a tendency for greater deviation as ν approaches the incompressible limit of 0.5.

		E_θ (-10%)		E_r (-10%)		$G_{r\theta}$ (-10%)	
		% Stress	% Strain	% Stress	% Strain	% Stress	% Strain
ARTERY	RUP	-0.003	0.0003	0.000	0.000	0.000	0.000
	TP1	0.063	0.060	0.007	0.007	0.008	0.007
	TP2	-0.037	-0.033	-0.003	-0.001	-0.004	-0.001
FIBROUS	RUP	0.326	10.756	0.326	10.756	0.326	10.756
	TP1	0.218	11.358	0.218	11.358	0.218	11.358
	TP2	-0.625	10.257	-0.625	10.257	-0.625	10.257
		E (-10%)					
CALCIFIED	RUP	-0.299	0.293				
	TP1	-0.369	-0.350				
	TP2	0.668	0.809				
		E (-65%)					
LIPID	RUP	-0.199	0.194				
	TP1	0.279	0.170				
	TP2	-0.138	-0.020				

		$\nu_{r\theta}$ (-10%)		$\nu_{\theta z}$ (-10%)	
		% Stress	% Strain	% Stress	% Strain
ARTERY	RUP	0.000	0.000	-0.001	0.000
	TP1	-0.004	-0.004	0.007	0.007
	TP2	0.002	0.001	-0.005	-0.005
FIBROUS	RUP	0.348	1.691	0.400	1.498
	TP1	-0.919	-1.103	-0.426	1.007
	TP2	-1.676	1.889	0.150	1.744
		ν (-10%)			
CALCIFIED	RUP	-0.180	0.177		
	TP1	-0.039	-0.031		
	TP2	0.473	0.532		
		ν (-10%)			
LIPID	RUP	-0.105	0.113		
	TP1	0.157	0.808		
	TP2	-0.082	-6.501		

Table 6 Sensitivity of maximum principal stress and strain for the anisotropic model. RUP represents the rupture site, TP1, test point one, and TP2, test point two (see figure 2). The region (artery, fibrous, etc.) identifies in which portion of the model the parameters were changed in a give test (color coded in figure 2).

For both trials, the sensitivity between positive and negative variations were symmetric throughout with the exception of the change in ν for calcified and lipid materials.

While we are confident of the broad conclusions reached in this study, it is important to recognize several limitations. Clearly, the real diseased artery is a complex three-dimensional structure that can only be captured in an approximate sense with a two-dimensional model. Also, the partitioning of the wall into four uniform zones is obviously a gross simplification. It will be some time before we can more accurately portray the true geometry and structure, however, and this remains an active area of investigation.

VII.5. Conclusion

Based on these results, the currently known parameters of the arterial wall, fibrous plaque, calcified plaque, and lipid pool parts of plaque have low sensitivities for a $\pm$10% variation in Young's modulus. This insensitivity to variations in E is true for both isotropic , for linear with and without residual strains, and nonlinear materials, and transversely orthotropic models. Therefore, stress analysis may be used with confidence that the material properties contribute relatively small errors, recognizing, however, that the magnitude of uncertainty in strain is of the same order as uncertainties in elastic modulus of the fibrous plaque region. Images need to be closely scrutinized, however, to ensure that artifactual stress concentrations do not arise due to unrealistically sharp corners. Either isotropic or anisotropic models provide useful estimates, however the predictions in regions of stress concentration (e.g., the site of rupture) are somewhat more sensitive to the specific model used, increasing by up to 30% from the isotropic to orthotropic model in the present example and almost halving when residual stresses are included.

VII.6. References

1. Cheng, G.C., Loree, H.M., Kamm, R.D., Fishbein, M.C., and Lee, R.T., 1993, "Distribution of Circumferential Stress in Ruptured and Stable Atherosclerotic Lesions," *Circulation,* pp. 1179-1187.
2. Richardson, P.D., Davies, M.J., and Born, G.V.R., 1989, "Influence of Plaque Configuration and Stress Distribution on Fissuring of Coronary Atherosclerotic Plaques," *The Lancet*, pp. 941-944.
3. Humphrey, J.D., 1995, "Mechanics of the Arterial Wall: Review and Directions," *Critical Reviews in Biomedical Engineering.* Vol. 23, pp. 82-90.
4. Loree, H.M., Grodzinsky, A.J., Park, S.Y., Gibson, L.J., and Lee, R.T.,1994, "Static Circumferential Tangential Modulus of Human Atherosclerotic Tissue," *Journal of Biomechanics*. Vol. 27, pp. 195-204.
5. Patel, D.J., Janicki, J.S. and Carew, T.E., 1969, "Static anisotropic elastic properties of the aorta in living dogs," *Circulation Research.* Vol. 25, pp.765-779.
6. Jones, R.M., 1975, "Macromechanical Behavior of a Lamina," in *Mechanics of Composite Materials*. New York, McGraw-Hill Book Co., pp 31-47
7. Loree, H.M., Kamm, R.D., Stringfellow, R.G., and Lee, R.T., 1992, "Effects of Fibrous Cap Thickness on Peak Circumferential Stress in Model Atherosclerotic Vessels," *Circulation Research,* Vol. 71, pp. 850-858.
8. Loree, H.M., Tobias, B.J., Gibson, L.J., Kamm, R.D., Small, D.M., and Lee, R.T., 1994, "Mechanical Properties of Model Atherosclerotic Lesion Lipid Pools," *Arteriosclerosis and Thrombosis,* Vol.14, pp. 230-234.
9. ADINA: Automatic Dynamic Incremental Nonlinear Analysis, Watertown, MA.

10. Bathe, K.J.: *Finite Element Procedures.* Saddle River, New Jersey, Prentice Hall, Inc, 1996, p 290.
11. Dobrin, P.B., 1986, "Biaxial Anisotropy of Dog Carotid Artery: Estimation of Circumferential Elastic Modulus," *Journal of Biomechanics.* Vol. 19, pp. 351-358.
12. Delfino, A., Stergiopulos, N., Moore, J. E., Jr. and Meister, J. J., 1997, "Residual strain effects on the stress field in a thick wall finite element model of the human carotid bifurcation." *Journal of Biomechanics.* Vol. 30, pp. 777-86.
13. Holzapfel, G. A., Gasser, T.C., and Ogden, R.W., 2000, "A New Constitutive Framework for Arterial Wall Mechanics and a Comparative Study of Material Models." *Journal of Elasticity.* Vol. 61, pp. 1-48.

VII.7. Figures

VII.7.1 Figure Captions

Figure 1. Histology of the post mortem specimen obtained from the coronary artery.

Figure 2. Computational mesh with the model test points labeled. Red indicates normal arterial wall (media and adventitia combined), blue, fibrous plaque, purple, calcified plaque, and green, lipid pools.

Figure 3. Diagram of residual stress calculation and application.

Figure 4. Maximum principal stress band plot (in Pa) for isotropic trials using average parameters. The triangle indicates the location of maximum stress while the star indicates the location of minimum stress. Linear isotropic (a), Linear isotropic with residual stresses (b), Non-linear isotropic (c). In the isotropic runs, the location of maximum stress is also the rupture site.

Figure 5. Maximum principal stress band plot (Pa) for a transversely isotropic trial of average parameters. The triangle indicates the point of maximum stress while the star indicates the point of minimum stress. In the transversely isotropic runs, the point of maximum stress is in an area of artificial stress concentration.

VII.7.2 Figures

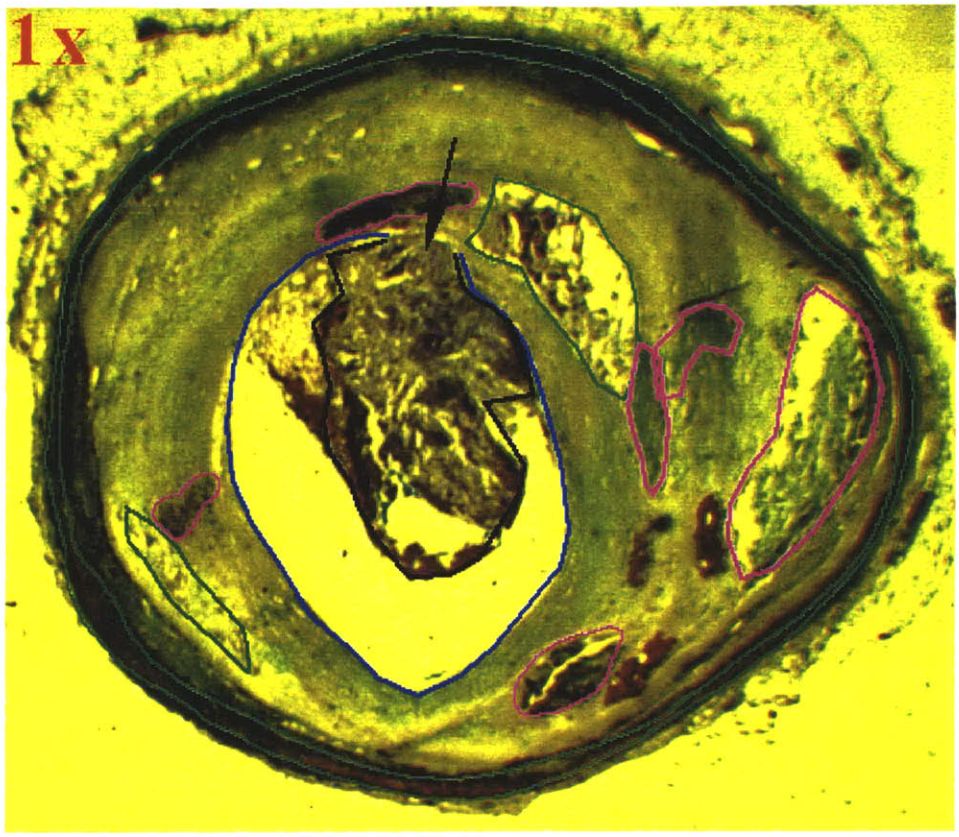

Figure 1

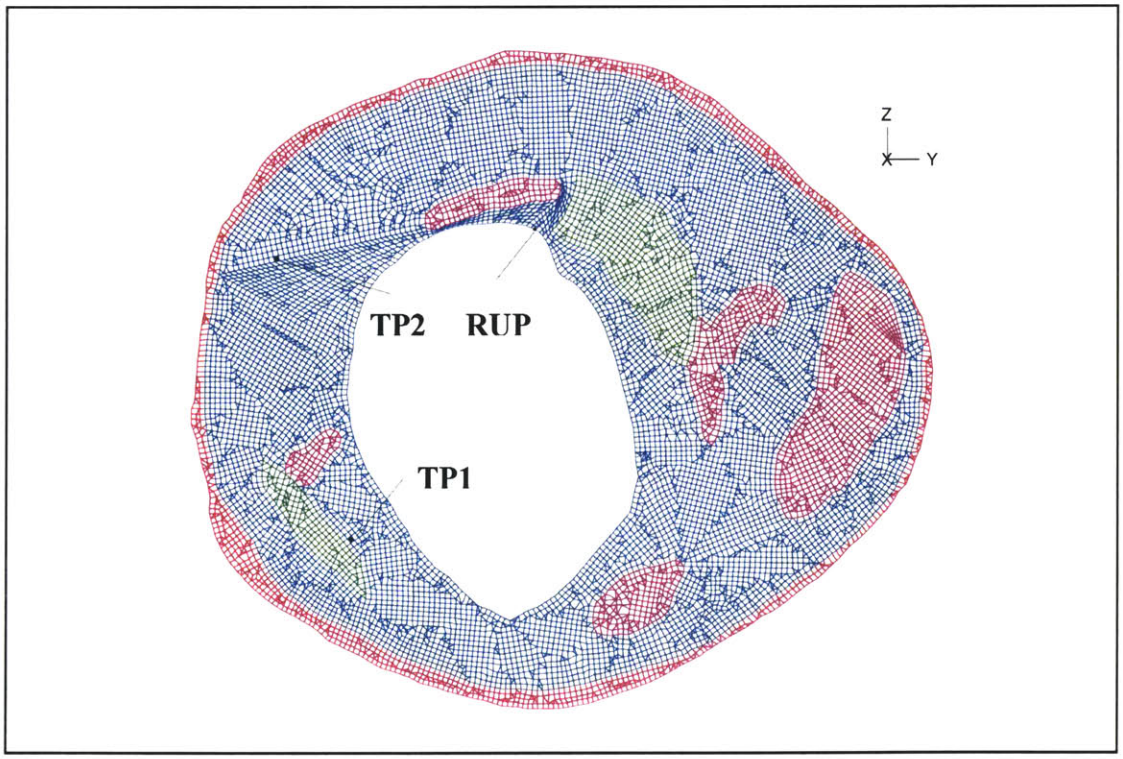

Figure 2

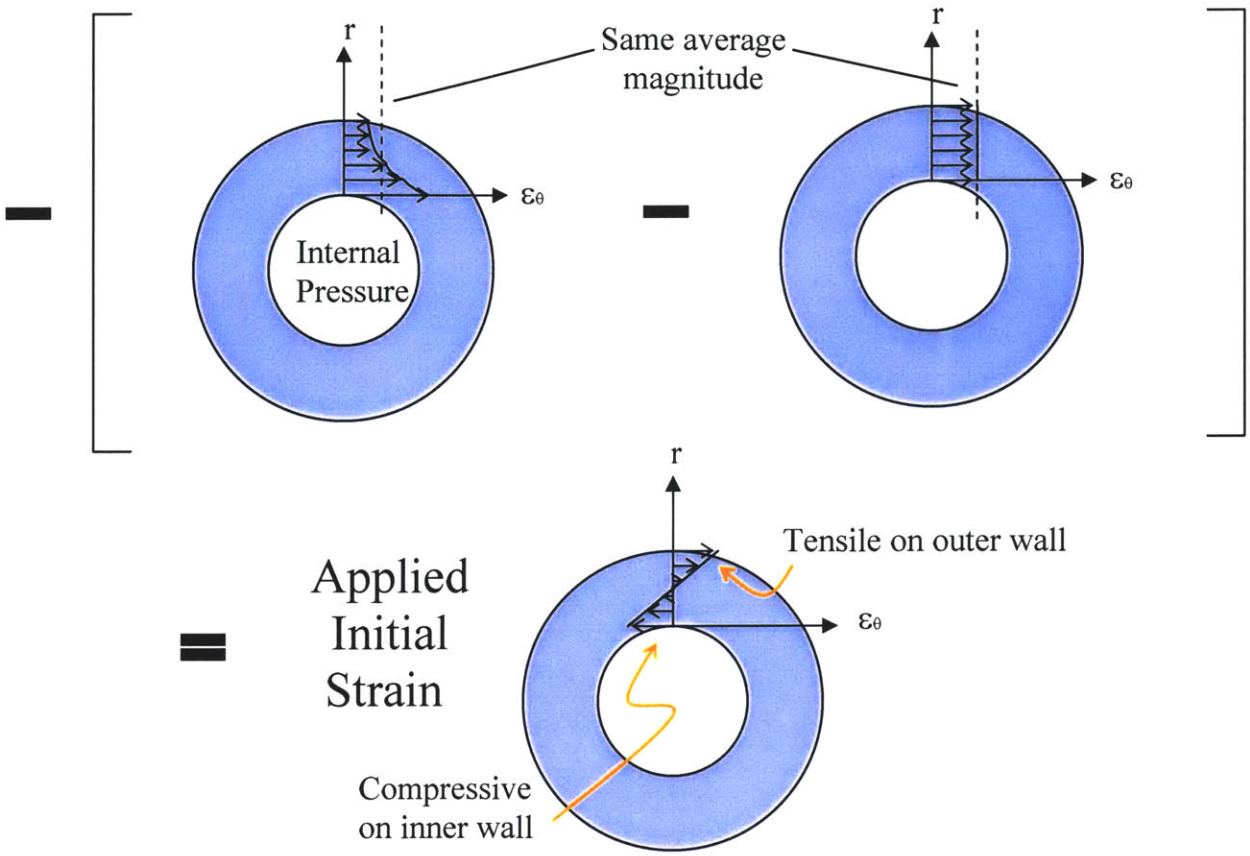

Figure 3

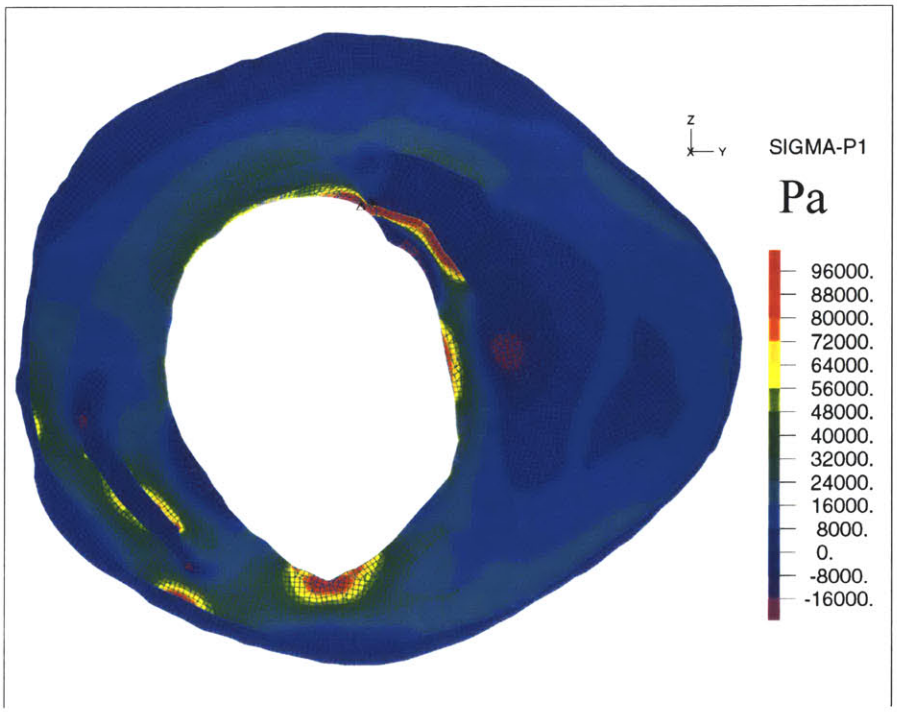

Figure 4 (a)

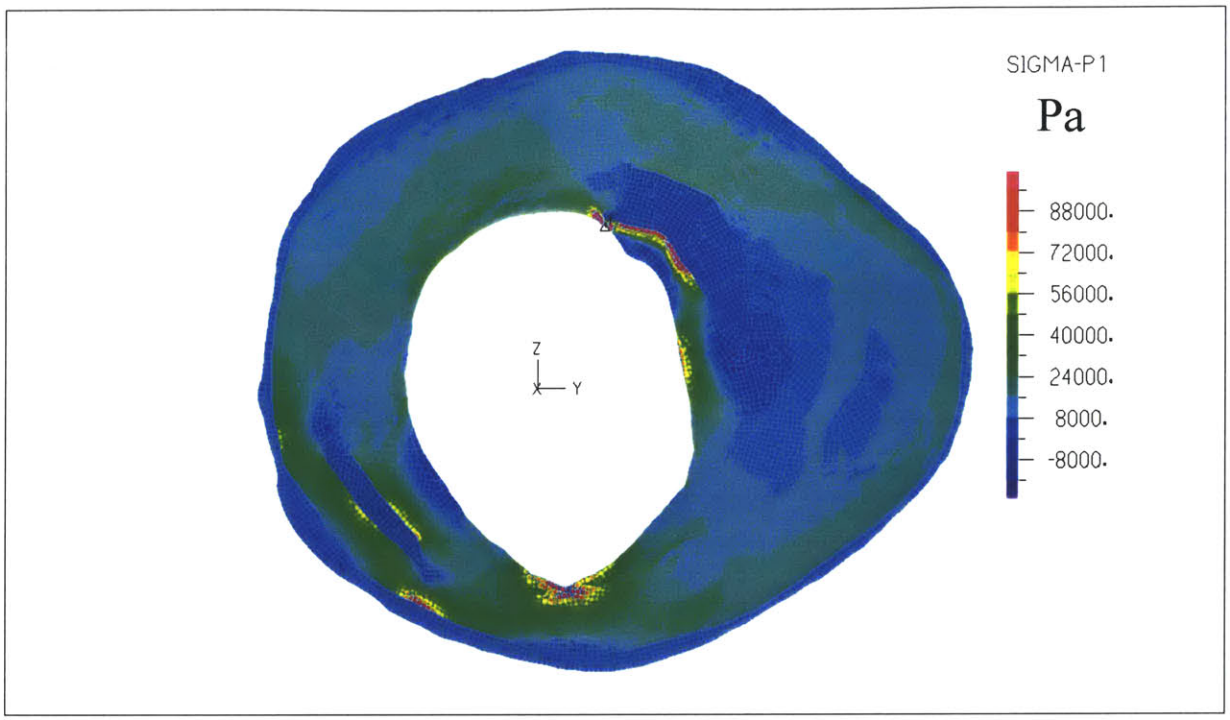

Figure 4(b)

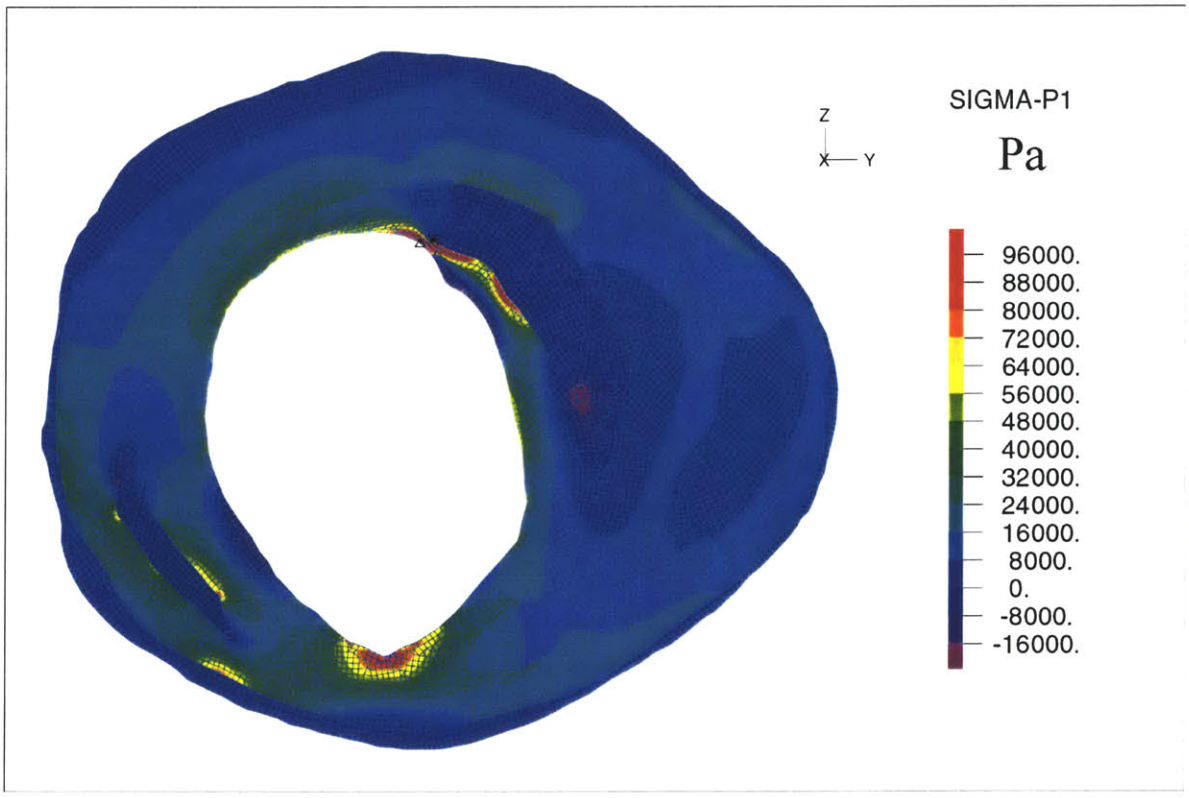

Figure 4(c)

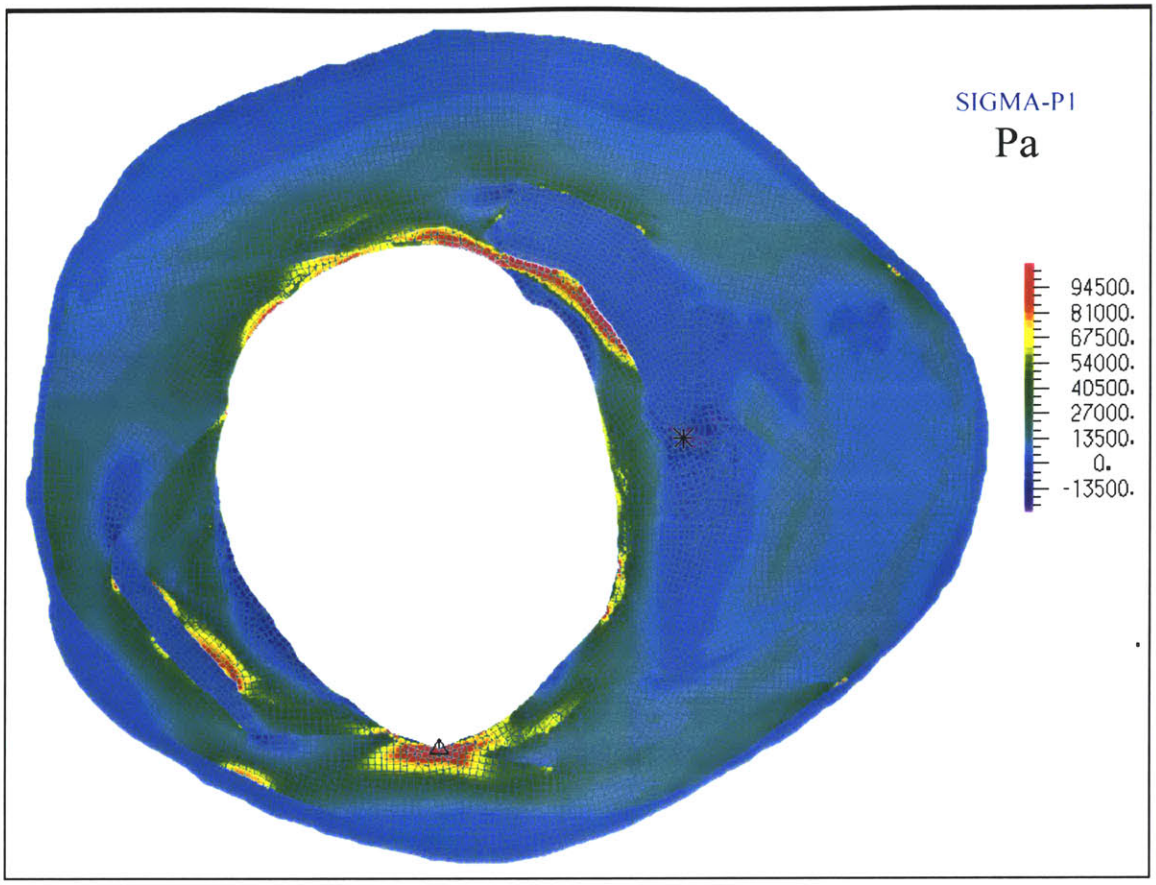
SIGMA-P1
Pa
94500.
81000.
67500.
54000.
40500.
27000.
13500.
0.
-13500.

Figure 5